



TRANSIENT SIMULATIONS OF
SUPERCONDUCTING FAULT CURRENT LIMITERS

Wescley Tiago Batista de Sousa

Tese de Doutorado apresentada ao Programa de Pós-graduação em Engenharia Elétrica, COPPE, da Universidade Federal do Rio de Janeiro, como parte dos requisitos necessários à obtenção do título de Doutor em Engenharia Elétrica.

Orientadores: Rubens de Andrade Júnior
Alexander Polasek

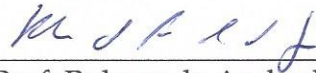
Rio de Janeiro
Março de 2015

TRANSIENT SIMULATIONS OF
SUPERCONDUCTING FAULT CURRENT LIMITERS

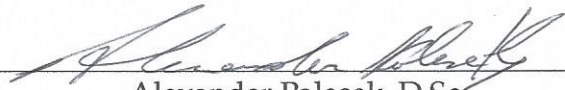
Wescley Tiago Batista de Sousa

TESE SUBMETIDA AO CORPO DOCENTE DO INSTITUTO ALBERTO LUIZ
COIMBRA DE PÓS-GRADUAÇÃO E PESQUISA DE ENGENHARIA (COPPE)
DA UNIVERSIDADE FEDERAL DO RIO DE JANEIRO COMO PARTE DOS
REQUISITOS NECESSÁRIOS PARA A OBTENÇÃO DO GRAU DE DOUTOR EM
CIÊNCIAS EM ENGENHARIA ELÉTRICA.

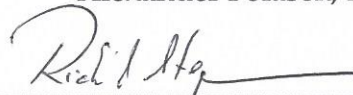
Examinada por:



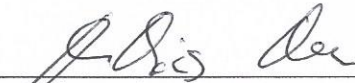
Prof. Rubens de Andrade Jr., D.Sc.



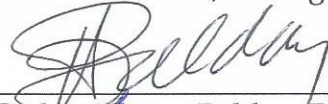
Alexander Polasek, D.Sc.



Prof. Richard M. Stephan, Dr.-Ing.



Prof. Mathias Noe, Dr.-Ing.



Prof. Carlos Alberto Baldan, D.Sc.



Prof. José Albino Oliveira de Aguiar, D.Sc.

RIO DE JANEIRO, RJ – BRASIL
MARÇO DE 2015

Sousa, Wescley Tiago Batista de

Transient Simulations of Superconducting Fault Current Limiters/Wescley Tiago Batista de Sousa. – Rio de Janeiro: UFRJ/COPPE, 2015.

XX, 194 p.: il.; 29, 7cm.

Orientadores: Rubens de Andrade Júnior

Alexander Polasek

Tese (doutorado) – UFRJ/COPPE/Programa de Engenharia Elétrica, 2015.

Bibliografia: p. 160 – 174.

1. Applied Superconductivity. 2. Fault Current Limiters. 3. Transient Simulations. I. Andrade Júnior, Rubens de *et al.* II. Universidade Federal do Rio de Janeiro, COPPE, Programa de Engenharia Elétrica. III. Título.

*To Nágela, my love.
To Johannes, my son.*

Acknowledgements

It was impossible for me to accomplish this D.Sc. study without the numerous help I received from all kind people around me. I would like to take this opportunity to thank you all, even if you are not personally mentioned here.

First of all, I would like to express my sincere appreciation to Prof. D.Sc. Rubens de Andrade Jr. and D.Sc. Alexander Polasek for their courage and patience in advising me. Their scientific knowledge and life experiences were essential in my journey.

I could not finish this thesis without the help from my colleagues at Federal University of Rio de Janeiro. I would like to thank my colleagues at LASUP Laboratory, in no particular order, Felipe Sass, Flávio Goulart, Vagner Santos, Felipe Costa, Vina Guedes and Prof. Dr.-Ing. Richard Sthephan.

My sincere gratitude to the colleagues at Karlsruhe Institute for Technology, Oliver Näckel, Patthabi Vishnuvardhan Gade, Sebastian Hellman, Florian Erb, Marion Gilliar, Dr. Rainer Gehring and Dr.-Ing. Kai Bauer. A very special thanks to my office colleague Herr Dustin Kottonau for his huge gentleness in helping me to improve my German skills as well as MatLab programming.

I would like to extend my sincerest thanks to Herr Prof. Dr.-Ing. Mathias Noe for very important advices about SFCL modeling and for giving me the opportunity of working at KIT/ITEP.

Next, I would like to thank my beautiful wife, Nágela, for her support, guidances, patience and love throughout this project and for accompanying me in my journey in Germany.

To my friend at the Superconductivity Laboratory in the Electric Power Research Center, Rodrigo Dias, thank you for full assistance and friendship. DSc. Carlos Frederico Matt for fruitful discussions and collaboration on mathematical aspects behind the Electro-Thermal Model.

I gratefully acknowledge the financial support and generosity of CEPTEL and the agencies CNPq and DAAD, without which the present study could not have been completed.

Last but not least, I thank God, for never leaving me alone even when I am on my own.

Resumo da Tese apresentada à COPPE/UFRJ como parte dos requisitos necessários para a obtenção do grau de Doutor em Ciências (D.Sc.)

SIMULAÇÕES DE REGIME TRANSITÓRIO DE LIMITADORES DE CORRENTE DE CURTO-CIRCUITO SUPERCONDUTORES

Wesley Tiago Batista de Sousa

Março/2015

Orientadores: Rubens de Andrade Júnior
Alexander Polasek

Programa: Engenharia Elétrica

Este trabalho apresenta os conceitos fundamentais a respeito da modelagem de dispositivos Limitadores de Corrente de Curto-Circuito Supercondutores além de contribuir com novos métodos de simulação. Três diferentes tipos de limitadores supercondutores foram testados a fim de validar os resultados das simulações através de sua comparação com dados experimentais. Cada dispositivo limitador foi testado em três diferentes níveis de corrente de curto-circuito. Os ensaios foram realizados em laboratórios no Brasil e Alemanha. Os novos métodos de simulação apresentados são baseados no método da analogia eletro-térmica (TEA) e também no método de diferenças finitas (FDM). Este último tem suas soluções obtidas por meios da rotina da direção implícita alternada (ADI) combinada com o uso de malha variável. Além disso, através dos métodos TEA e FDM, análises a respeito de condições adiabáticas, variações das propriedades físicas, mudanças na troca convectiva de calor e heterogeneidades também foram realizadas. Uma boa concordância entre resultados de simulação e resultados de ensaios foi obtida neste trabalho. Não obstante, aumento de temperatura e desenvolvimento de resistência durante o transiente de curto-circuito também foram estimados através dos modelos propostos e se encontram dentro do esperado.

Abstract of Thesis presented to COPPE/UFRJ as a partial fulfillment of the requirements for the degree of Doctor of Science (D.Sc.)

TRANSIENT SIMULATIONS OF
SUPERCONDUCTING FAULT CURRENT LIMITERS

Wescley Tiago Batista de Sousa

March/2015

Advisors: Rubens de Andrade Júnior
Alexander Polasek

Department: Electrical Engineering

This work presents fundamental notions regarding modeling of Superconducting Fault Current Limiters (SFCL) devices besides introducing new simulation methods. Three different SFCL concepts were tested in order to validate simulation results by comparing it with measured data. Each SFCL device was tested under three different fault current levels. Tests were carried out in laboratories in Brazil and Germany. New simulation models are based on the thermal-electrical analogy method (TEA) and also on the finite difference method (FDM). The last one is solved by means of the alternating direction implicit routine (ADI) combined with variable mesh. Furthermore, by means of TEA and FDM methods, analysis concerning adiabatic conditions, variations on physical properties, changes on the convective heat transfer and inhomogeneities have been also performed. A good agreement between simulations and tests has been found in the present work. Moreover, increase of temperature and resistance development during the fault transient were also predicted by proposed models and lie within the expected values.

Kurzfassung, die für die COPPE/UFRJ vorgestellt wurde, als Bestandteil der zu erfüllenden Voraussetzungen zur Erlangung des akademischen Grades Doktor der Wissenschaften (D.Sc.)

Simulationen des transienten Verhaltens von supraleitenden Strombegrenzern

Wescley Tiago Batista de Sousa

März/2015

Betreuer: Rubens de Andrade Júnior

Alexander Polasek

Abteilung: Elektrotechnik

In dieser Arbeit werden grundlegende Begriffe der Modellierung von supraleitenden strombegrenzenden Betriebsmitteln neben der Einführung neuer Simulationsmethoden präsentiert. Drei verschiedene Arten von supraleitenden Strombegrenzern (SSB) wurden theoretisch und experimentell untersucht, mit dem Ziel Ergebnisse aus Simulationen durch Vergleiche mit gemessenen Ergebnissen zu bestätigen. Jeder Strombegrenzer wurde auf drei verschiedenen Kurzschlussstromniveaus getestet. Die Messungen wurden in brasilianischen und in deutschen Labors (URFJ, KIT) durchgeführt. Die neuen Simulationsmodelle basieren auf der thermoelektrischen Analogie (TEA) und der Finite-Differenzen-Methode (FDM). Das FDM Modell wird mit Hilfe der Alternating-Direction-Implicit-Methode (ADI), kombiniert mit variablen Gittergrößen, berechnet. Des Weiteren konnten mit TEA- und FDM-Methoden Untersuchungen bezüglich adiabatischer Bedingungen, veränderlicher physikalischer Eigenschaften, Änderungen an Wärmeübergangskoeffizienten und Inhomogenitätseinflüssen durchgeführt werden. Es konnte eine gute Übereinstimmung zwischen Simulationen und Tests in der gegenwärtigen Arbeit gefunden werden. Auch der Temperaturanstieg und die Widerstandsentwicklung im Moment des Kurzschlusses entsprachen den Vorhersagen aus den herangezogenen Modellen.

Contents

List of Figures	xii
List of Tables	xvi
List of Symbols	xvii
List of Abbreviations	xix
1 Introduction	1
2 Superconductivity and Superconducting Fault Current Limiters	3
2.1 Superconductivity	3
2.1.1 Coherence Length and Penetration Depth	5
2.1.2 Types of Superconductors	7
2.1.2.1 High Temperature Superconductors	9
2.1.3 Critical Current Density in HTS Superconductors	11
2.1.3.1 The E-J Characteristic of HTS Superconductors	12
2.2 Superconducting Fault Current Limiters	13
2.2.1 Resistive Type (R-SFCL)	15
2.2.1.1 MCP-BSCCO-2212	17
2.2.1.2 ENSYSTROB	18
2.2.2 Magnetic Field Assisted (MF-SFCL)	20
2.2.3 Shielded Iron Core (L-SFCL)	20
2.2.4 Diode Bridge Type (D-SFCL)	21
2.2.5 Saturated Core (SC-SFCL)	22
2.2.6 Air Coil SFCL (AC-SFCL)	24
2.2.7 Comparative Evaluation	26
3 Tests, Experimental Data and Inhomogeneity Representation	28
3.1 Tested Components	28
3.2 Measurements Circuits and Tests	30
3.2.1 Tests Results	32

3.2.1.1	MCP-BSCCO-2212 Tests	32
3.2.1.2	YBCO 2G Coil Tests	34
3.2.1.3	Air Coil SFCL Tests	36
3.3	Inhomogeneity Representation	38
3.3.1	I_c Distribution for the MCP-BSCCO-2212 Assembly	39
3.3.2	I_c Distribution for the YBCO 2G Coil	40
3.3.3	I_c Distribution for the Air Coil SFCL	40
4	Introductory Models	43
4.1	Introduction	43
4.2	Time Dependent Model	44
4.3	Two Branches Model	47
4.3.1	Results of Case Example	50
4.3.1.1	First Discussions	51
4.4	SFCL Modeling - Brief Review	53
5	Thermal-electrical Analogy Method	56
5.1	Introduction	56
5.2	Mathematical Justification	57
5.3	Electro-Thermal Model for SFCL	61
5.3.1	Electrical Equivalents	61
5.3.2	Thermo-Electrical Equivalents	64
5.3.2.1	Adiabatic Model (TEA-MA)	66
5.3.2.2	Non-Adiabatic Model (TEA-MB)	66
5.3.2.3	Non-Adiabatic Model with Variable Parameters (TEA-MC)	71
5.4	Solution Routine	72
5.5	Results	74
5.5.1	MCP-BSCCO-2212 Results	74
5.5.2	YBCO 2G Coil Results	80
5.5.3	Air Coil Results	85
5.6	Summary and Discussions	91
6	Finite Difference Method - ADI Routine	95
6.1	Finite Difference Basics	95
6.2	Implicit Schemes	98
6.2.1	2D FDM Implicit Method	99
6.3	Model for SFCLs	100
6.3.1	Thermal Problem Description	101
6.4	Alternating Direction Implicit (ADI)	104

6.4.1	First Half-Timestep	105
6.4.2	Second Half-Timestep	106
6.5	Solution Routine	111
6.6	Results	113
6.6.1	MCP-BSCCO-2212 Results	114
6.6.2	YBCO 2G coil Results	121
6.6.3	Air Coil SFCL Results	129
6.7	Summary and Discussions	137
7	Final Comparisons	140
7.1	MCP-BSCCO-2212 - TEA \times FDM Results	140
7.2	YBCO 2G Coil - TEA \times FDM Results	144
7.3	Air Coil SFCL - TEA \times FDM Results	148
7.4	Computational Efforts and Error Values	152
7.5	Discussions	154
8	Conclusions	156
	Bibliography	160
A	Critical Current Measurements	175
A.1	MCP-BSCCO-2212 Modules	175
A.2	Air Coil SFCL tapes	177
B	Physical Properties	181
B.1	Electrical Resistivity ρ	181
B.2	Specific Heat ς	182
B.3	Thermal Conductivity k	183
B.4	Convective heat transfer h_c	185
C	Mathematical Procedures - ADI parameters	186
C.1	Boundary Conditions at the First half-timestep	186
C.2	Boundary Conditions at the Second half-timestep	188
	Curriculum Vitae	192

List of Figures

2.1	Electrical resistance of Hg	4
2.2	Diagram of the Meissner-Ochsenfeld effect	4
2.3	Superconductivity requirements	5
2.4	Screening currents, penetration depth λ and coherence length ξ	6
2.5	Magnetic phase diagrams	7
2.6	Mixed state in applied magnetic field	8
2.7	Representation of the layered structures	10
2.8	Lorentz force in a superconductor in mixed state	11
2.9	E-J Characteristic curve for HTS materials	12
2.10	Operation modes of SFCL.	14
2.11	Expected installations locations of SFCL	16
2.12	Resistive SFCL	17
2.13	Stages of production of the MCP-BSCCO-2212	18
2.14	YBCO tapes sizes	19
2.15	The ENSYSTROB component	20
2.16	Magnetic Field Assisted SFCL	20
2.17	Shielded-Core SFCL	21
2.18	Diode Bridge Type SFCL	22
2.19	Saturated Core SFCL	23
2.20	Iron core curves	24
2.21	Geometrical sizes of the 2G YBCO tapes	25
2.22	Air Coil SFCL	25
3.1	Design of the tested R-SFCL	29
3.2	Design of the tested AC-SFCL	29
3.3	Test Circuit configuration	30
3.4	Equivalent circuit diagram of the measurement setup to test the Air Coil SFCL.	32
3.5	Comparison between fault and limited current for test t1-mcp	33
3.6	Comparison between fault and limited current for test t2-mcp	33
3.7	Comparison between fault and limited current for test t3-mcp	34

3.8	Comparison between fault and limited current for test t1-coil	34
3.9	Comparison between fault and limited current for test t2-coil	35
3.10	Comparison between fault and limited current for test t3-coil	35
3.11	Comparison between fault and limited current for test t1-acsfcl . . .	36
3.12	Comparison between fault and limited current for test t2-acsfcl . . .	37
3.13	Comparison between fault and limited current for test t3-acsfcl . . .	37
3.14	Sketch critical current inhomogeneity distribution	38
3.15	Critical current distribution for each module	40
3.16	Critical current distribution for each tape of the YBCO 2G SFCL . .	41
3.17	Simplified measurement system to determine I_c	41
3.18	Critical current distribution for each tape of the Air Coil SFCL . . .	42
4.1	Time dependency variation of the SFCL resistance.	44
4.2	Equivalent circuit diagram of the Air Coil SFCL.	45
4.3	Schematic diagram of the time dependent simulation model. . . .	45
4.4	Time Dependent Model results	46
4.5	Two branches model describes	47
4.6	Schematic diagram of the two branches model	48
4.7	Schematic diagram of the current iteration method.	49
4.8	Two Branches Model results - Current and Voltage	51
4.9	Two Branches Model results - Resistance and Temperature	52
5.1	Thermal-electrical Analogy principles	57
5.2	Finite-difference discretization	59
5.3	Equivalent circuit of the measurements - CEPTEL/BRAZIL	62
5.4	Electric representation of the R-SFCL	62
5.5	Equivalent circuit of the measurements - KIT/GERMANY	63
5.6	Electric representation of the AC-SFCL	64
5.7	Employed geometry for simulations	65
5.8	Thermal-electric circuit - MCP-BSCCO-2212	68
5.9	Thermal-electric circuit - YBCO 2G Coil	69
5.10	Thermal-electric circuit - AC-SFCL	70
5.11	Convective heat transfer coefficient curve	72
5.12	Simulation routine flowchart	73
5.13	Results of simulation test t1-mcp	75
5.14	Temperature rise in t1-mcp	75
5.15	Equivalent resistances of assembly t1-mcp	76
5.16	Results of simulation test t2-mcp	76
5.17	Temperature rise in t2-mcp	77
5.18	Equivalent resistances of assembly t2-mcp	78

5.19	Results of simulation test t3-mcp	78
5.20	Temperature rise in t2-mcp	79
5.21	Equivalent resistances of assembly - t3-mcp	79
5.22	Results of simulation test t1-coil	80
5.23	Temperature rise in t1-coil	81
5.24	Equivalent resistances of YBCO 2G coil - t1-coil	82
5.25	Results of simulation test t2-coil	82
5.26	Temperature rise in t2-coil	83
5.27	Equivalent resistances of YBCO 2G coil - t2-coil	83
5.28	Results of simulation test t3-coil	84
5.29	Temperature rise in t3-coil	85
5.30	Equivalent resistances of YBCO 2G coil - t3-coil	85
5.31	Results of simulation test t1-acsfcl	86
5.32	Temperature rise in t1-acsfcl	86
5.33	Equivalent resistances of the HTS tapes in the AC-SFCL - t1-acsfcl .	87
5.34	Results of simulation test t2-acsfcl	88
5.35	Temperature rise in t2-acsfcl	89
5.36	Equivalent resistances of the HTS tapes in the AC-SFCL - t2-acsfcl .	89
5.37	Results of simulation test t3-acsfcl	90
5.38	Temperature rise in t3-acsfcl	90
5.39	Equivalent resistances of the HTS tapes in the AC-SFCL - t3-acsfcl .	91
6.1	Finite Difference Basics	96
6.2	Effects of parameter Fo on the stability of FDM method	98
6.3	Discretization for the 2D FDM scheme.	99
6.4	Geometry for FDM simulations	101
6.5	Boundary conditions for SFCL	103
6.6	Discretization for the 2D FDM scheme	104
6.7	Schema to satisfy boundary conditions	107
6.8	Fictitious nodes concept; $T_{j,0}$ and T_{j,n_z+1}	108
6.9	Flowchart of the simulation routine	111
6.10	Results of simulation test t1-mcp	114
6.11	Temperature rise in t1-mcp	115
6.12	Equivalent resistances of assembly t1-mcp	116
6.13	Results of simulation test t2-mcp	117
6.14	Temperature rise in t2-mcp	118
6.15	Equivalent resistances of assembly t2-mcp	119
6.16	Results of simulation test t3-mcp	119
6.17	Temperature rise in t3-mcp	120

6.18	Equivalent resistances of assembly t3-mcp	121
6.19	Results of simulation test t1-coil	122
6.20	Temperature rise in t1-coil	123
6.21	Equivalent resistances of assembly t1-coil	124
6.22	Results of simulation test t2-coil	124
6.23	Temperature rise in t2-coil	126
6.24	Equivalent resistances of assembly t2-coil	127
6.25	Results of simulation test t3-coil	127
6.26	Temperature rise in t3-coil	128
6.27	Equivalent resistances of assembly t3-coil	129
6.28	Results of simulation test t1-acsfcl	130
6.29	Temperature rise in t1-acsfcl	131
6.30	Equivalent resistances of HTS tapes in test t1-acsfcl	132
6.31	Results of simulation test t2-acsfcl	132
6.32	Temperature rise in t2-acsfcl	133
6.33	Equivalent resistances of HTS tapes in test t2-acsfcl	134
6.34	Results of simulation test t3-acsfcl	135
6.35	Temperature rise in t3-acsfcl	136
6.36	Equivalent resistances of HTS tapes in test t3-acsfcl	137
7.1	Results of simulation test t1-mcp	141
7.2	Results of simulation test t2-mcp	142
7.3	Results of simulation test t3-mcp	144
7.4	Results of simulation test t1-coil	145
7.5	Results of simulation test t2-coil	147
7.6	Results of simulation test t3-coil	148
7.7	Results of simulation test t1-acsfcl	149
7.8	Results of simulation test t2-acsfcl	150
7.9	Results of simulation test t3-acsfcl	151
A.1	Critical current measurements - modules 01 to 04	175
A.2	Critical current measurements - modules 05 to 08	176
A.3	Critical current measurements - module 09 to 12	176
A.4	Critical current measurements - tapes 01 to 04	177
A.5	Critical current measurements - tapes 05 to 08	178
A.6	Critical current measurements - tapes 09 to 12	178
A.7	Critical current measurements - tapes 13 to 16	179
A.8	Critical current measurements - tapes 17 to 20	179
A.9	Critical current measurements - tapes 21 and 22	180

List of Tables

2.1	Critical magnetic flux density B_c	9
2.2	Comparative Evaluation of the main characteristics between the SFCL concepts [34, 46, 48].	27
3.1	Parameters of the AC-SFCL ($\omega = 2\pi f$).	30
3.2	Short-circuit tests for both R-SFCL.	31
3.3	Short-circuit tests for the AC-SFCL.	32
3.4	Measured critical current values of the MCP-BSCCO-2212 modules.	39
3.5	Measured critical current values of the YBCO 2G coil.	40
3.6	Measured critical current values of the Air Coil SFCL.	42
5.1	Analogous elements of thermal and electrical systems	61
5.2	Developed Models	65
6.1	Developed Models	102
6.2	Γ and Θ values originated from the boundary conditions	106
6.3	Parameters of discretization for each MCP-BSCCO-2212 module.	112
6.4	Parameters of discretization for each tape of the YBCO 2G Coil.	113
6.5	Parameters of discretization for each tape of the Air Coil SFCL.	113
7.1	Time of Simulation	152
7.2	Maximum Error values - Current error Voltage error (%)	153
A.1	Measured critical current values for the tapes of the Air Coil SFCL.	180

List of Symbols

c	Speed of light
e	Electron charge
J_c	Critical Current Density
J_d	Depairing Current density
I_c	Critical Current
I_{cm}	Average of the critical current of a tape or module
B_c	Magnetic Critical Field
Φ	Quantum of flux (<i>fluxon</i>)
n_s	Density of Superelectrons
ξ	Coherence Length
λ	Penetration depth
κ	Ginzburg-Landau parameter
T_c	Critical Temperature
E_c	Electric field criteria
n	Index of transition
ϵ	Defines a range of I_c values to be selected
σ	Standart deviation
Vo	Applied voltage over the SFCL terminals
X	Inductive reactance
ρ	Electrical resistivity

R	Resistance
f	Frequency
ω	$2\pi f$
i	Electrical current
u	Iteration number
β	Current iteration process adjustment factor
T	Temperature
Fo	Fourier number
Q	Rate of heat flow
S	Heat exchange surface
V	Volume
α	Thermal diffusivity
γ	Volumetric density
ς	Specific heat
k	Thermal conductivity
\dot{g}	Internal heat generation volume rate
h_c	Convective heat transfer coefficient
τ	Aleatory time-step
ν	Layer thickness
η	Layer number
ℓ	Length
a	Cross section area
j	Aleatory element (x -direction)
m	Aleatory element (z -direction)
n_x	Number of elements in x -direction
n_z	Number of elements in z -direction

List of Abbreviations

UFRJ	Universidade Federal do Rio de Janeiro
LASUP	Laboratório de Aplicações de Supercondutores
CEPEL	Centro de Pesquisas de Energia Elétrica
KIT	Karlsruher Institut für Technologie
ITEP	Institut für Technische Physik
CNPq	Conselho Nacional de Desenvolvimento Científico e Tecnológico
DAAD	Deutscher Akademischer Austauschdienst
SFCL	Superconducting Fault Current Limiters
R-SFCL	Resistive SFCL
MF-SFCL	Magnetic Field Assisted SFCL
SC-SFCL	Saturated Core SFCL
D-SFCL	Diode Bridge SFCL
L-SFCL	Shielded Iron Core SFCL
AC-SFCL	Air Coil SFCL
BCS	Bardeen-Cooper-Schrieffer Theory
HTS	High Temperature Superconductors
BSCCO	Bismuth-Strontium-Calcium-Copper-Oxide Supercond.
YBCO	Yttrium-Barium-Copper-Oxide Superconductor
MCP-BSCCO-2212	Melt Casting Process - $Bi_2Sr_2CaCu_2O_8$ SFCL
FRP	Fiber Reinforced Plastics

1G	First generation superconducting tapes
2G	Second generation superconducting tapes
TEA	Thermal Electrical Analogy
FDM	Finite Difference Method
ADI	Alternating Direction Implicit
LN ₂	Liquid Nitrogen
PIT	Power in Tube
CFL	Courant-Friedrichs-Lewy Condition

Chapter 1

Introduction

Before application of a superconducting fault current limiter in a power system, it can be useful to confirm its performance through simulation studies. There are different approaches for modeling SFCL devices, whereas testing procedures have been under discussion aiming at standardization. Computational simulations of these devices are necessary in order to understand its behavior before installing it in power systems and to estimate results of hard experimental access. Different methodologies have been proposed in order to predict the thermal and electrical behaviors of SFCL devices as, for example, detailed and computationally-intensive 3-D finite element models and less computationally-intensive, but also quite accurate, 1-D models with nonlinear resistance.

This work aims to introduce new approaches to predict both the electrical and thermal behaviors of SFCL devices. The main contribution and innovative aspect of the present work is related to the use of a thermal-electrical analogy and finite difference method (combined with ADI routine and variable mesh) to solve heat transfer equations within each layer of tapes and components constituting SFCL devices.

Simulations have been developed with basis on three different SFCL concepts: the MCP-BSCCO-2212 SFCL, the YBCO 2G coil similar to the ENSYSTROB and the Air Coil SFCL. MCP-BSCCO-2212 modules and the YBCO 2G coil were acquired from *Nexans Superconductors GmbH* and tested in Brazil. The Air Coil SFCL demonstrator is presently under development at KIT /ITEP, in Germany.

In addition, each limiting device was tested under different fault current levels aiming to validate simulation results for different cases.

This work is organized as follows.

- Chapter 2 briefly describes basic concepts of superconductivity and introduces main concepts of SFCL devices. A comparative evaluation is done at the end of this chapter;

- Chapter 3 shows measurements setup used in each test for each device. Experimental results of current limitation are presented. Furthermore a statistical representation of inhomogeneities is done in this chapter;
- Chapter 4 introduces the main concepts regarding SFCL modeling. A brief review of usual simulation methods found in literature is available.
- Chapter 5 describes the computational model based on the thermal-electrical analogy method (TEA) to predict both the thermal and electrical behaviors of SFCL devices. Comparisons of simulation results are done with experimental data.
- Chapter 6 presents the basic concepts of finite difference method (FDM) and its application on SFCL modeling. A deep description of the FDM method integrated with the alternating direction implicit (ADI) routine combined with variable mesh is given. Comparisons of simulation results are done with experimental data
- Chapter 7 compares numerical results obtained by models TEA and FDM.
- Chapter 8 sets the main conclusions of the current work forth.

Chapter 2

Superconductivity and Superconducting Fault Current Limiters

Superconductivity is a phenomenon whereby some materials, when cooled down under low temperature, present zero resistivity. Since its discovery in 1911 by the Dutch physicist Heike Kamerlingh Onnes, many efforts have been done aiming to develop a theory to describe all the physical phenomena behind it. The first part of this chapter is a brief summary of the superconductivity basics, where different regimes of a superconductor material are defined. The second part presents the main concepts and types of Superconducting Fault Current Limiters (SFCL).

2.1 Superconductivity

Superconductivity was discovered by Heike Kamerlingh Onnes in 1911 following his success in liquefying helium three years earlier [1]. Researching about the resistivity of material at very low temperatures, Onnes observed that the resistivity of mercury suddenly decreased to a very low value when the temperature reached 4.2 K, as shown in figure 2.1a. Since then, the temperature at which an element loses its resistivity is called critical temperature T_c .

Following this discovery, a big number of superconducting elements with different values of T_c were discovered. Nowadays one knows that among the elements of the periodic table, more than twenty become superconducting at sufficiently low temperature, several semiconductors can become superconducting under suitable conditions, whereas the number of alloys with superconducting properties is in the order of thousands [2]. In 1986 the physicists Johannes Georg Bednorz e Karl Alexander Müller discovered the superconductivity above 30 K

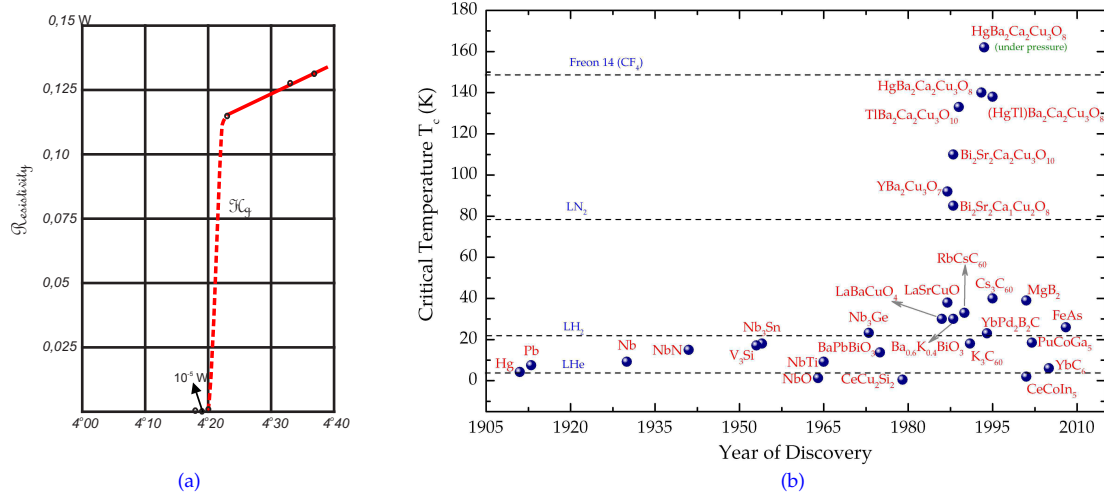


Figure 2.1: (a) Electrical resistance of Hg at low temperature which showed a transition temperature at 4.2 K (adapted from [1]) and (b) Chronological evolution of T_c over the years.

in the ceramic compound *LaBaCuO* [3]. Only one year after, the physicists Maw-Kuen Wu, Ching-Wu (Paul) Chu and co-workers announced superconductivity at 92 K in the *YBaCuO* compound system [4]. In 1988 the systems based on *Bi* and *Tl* were discovered, becoming superconductors at 110 K and 125 K, respectively [5–7]. Figure 2.1b shows the chronological evolution of T_c over the years. The horizontal dashed lines indicate the required coolant to bring each system to its superconducting state. The discovery of systems with T_c value above the liquid nitrogen temperature (LN_2) increased the potentiality of the applied superconductivity.

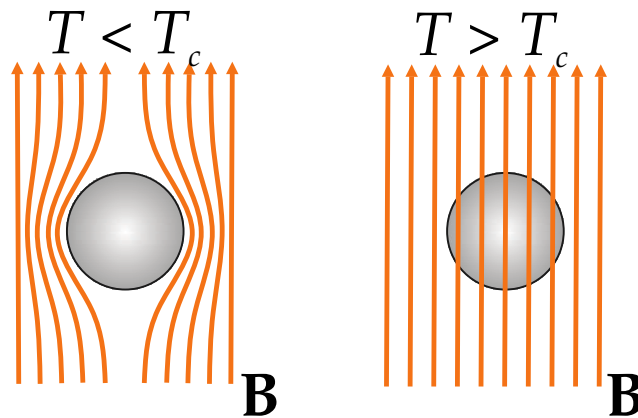


Figure 2.2: Diagram of the Meissner-Ochsenfeld effect. Magnetic flux lines are excluded from a superconductor when it is below its critical temperature T_c .

Only the loss of resistivity, however, is not enough to define the superconducting state. Onnes also observed that the superconductivity could be destroyed by exposing a superconducting material to a certain value of magnetic field. It means that the superconducting state cannot exist in the presence of a magnetic

flux greater than a critical value B_c , even at absolute zero. Indeed, in 1933, the German physicists Walther Meissner and Robert Ochsenfeld found out that superconductors are perfect diamagnets [8].

By applying a magnetic flux density B , so that $B < B_c$, in a superconducting material ($T < T_c$), one observes a complete exclusion of this flux by the superconductor material, as shown in figure 2.2. It is the nature of superconductors to exclude magnetic fluxes so long as the applied flux does not exceed their critical magnetic flux B_c . Such phenomena is called Meissner-Ochsenfeld effect.

Superconducting materials are not able to transport infinity value of electrical current. Although a superconductor can transport current without resistance, its ability is limited. It also loses its superconductivity if the transport current increases above a certain value, called critical current I_c . In practical applications, it is more convenient to use current density ($J = I/a$) than transport current, so that the corresponding current density is defined as critical current density J_c .

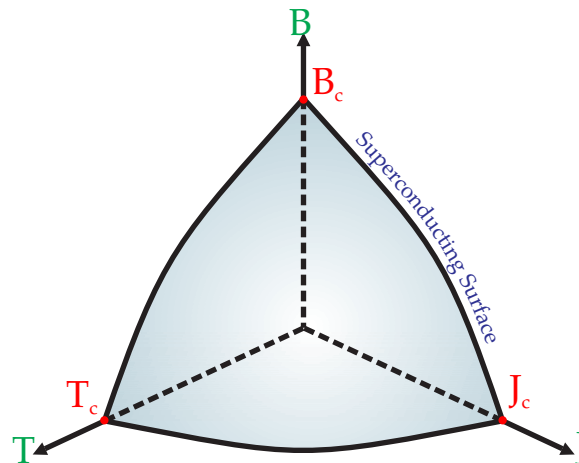


Figure 2.3: The conditions required for a material to exhibit superconductivity.

The three basic critical parameters T_c , B_c , and J_c are not independent of each other. A strong correlation between them does exist. Figure 2.3 shows the relationship between these three critical parameters. Any point within the volume enclosed by the curved surface (T_c , B_c , and J_c) is in superconducting state; any point outside the volume is in normal state.

2.1.1 Coherence Length and Penetration Depth

In 1957 the physicists J. Bardeen, L. N. Cooper and J. R. Schrieffer proposed the microscopic theory of superconductivity, the BCS theory [9]. The BCS theory, considers energy gaps and excitation spectrum for the electrons and predicts that the conducting superelectrons form so-called *Cooper pairs* since electrons interact with the mechanical vibrations in the crystalline lattice. This atom movement in

the lattice has a tendency to neutralize the normal repulsion between electrons and instead generates an attraction between them, which is only possible below a certain critical temperature T_c . Such combination of electrons in pairs determines also the coherence length ξ , which is a measure of how likely it is that a Cooper pair is formed, and corresponds to the distance between the electrons within the Cooper pair [10]. Figure 2.4 illustrates the coherence length ξ at the boundaries of a superconducting material, as well as the number of superelectrons per unit volume n_s .

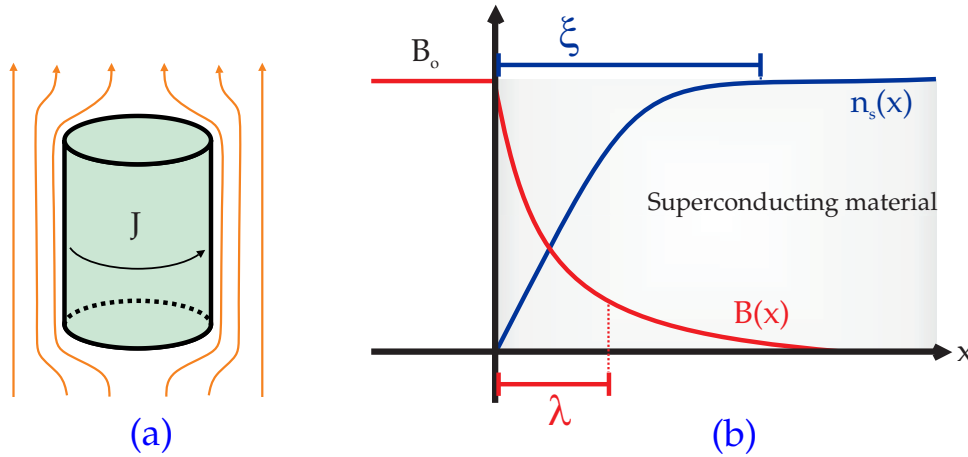


Figure 2.4: (a) Screening currents at the surface of a superconducting material and (b) penetration depth λ and coherence length ξ of superconductors at their interfaces.

In order to clearly explain the classification of superconductors in section 2.1.2, another important microscopic parameter, the penetration depth λ , must be defined. In an applied field, a superconductor material excludes all magnetic flux (Meissner-Ochsenfeld effect). It does this by setting up electric currents near its surface, as shown in figure 2.4a. The magnetic field of these surface currents cancels the applied magnetic flux within the superconductor. Consequently, the flux density does not fall abruptly to zero at the boundary of the material but decreases exponentially towards the core of a superconductor, as shown in figure 2.4b. For this reason the depth within which the screening currents flow is called London penetration depth λ , because it is the depth to which the flux of the applied magnetic field appears to penetrate [11]. The magnitude of the penetration depth is directly related to the number of superelectrons per unit volume n_s as

$$\lambda^2 = \frac{m^* c^2}{4\pi e^2 n_s} \quad (2.1)$$

where m^* is the effective mass of the charge carriers, e is the electron charge, and c is the speed of light in vacuum [11].

2.1.2 Types of Superconductors

It was experimentally found that some superconductors in magnetic fields do not allow penetration of magnetic flux with magnetic field increase before they lose superconductivity. Conversely, other superconductors allow partial penetration of magnetic fields into the bulk region, resulting in local interlacement with the normal state and the superconducting state simultaneously, even though their resistance remains zero. Thus, superconductors are classified into two types. The Ginzburg-Landau theory of the superconductivity predicts that superconductors can be classified into two categories based on the ratio of penetration depth to coherence length [10]. By defining the Ginzburg-Landau parameter κ as:

$$\kappa = \lambda/\xi \quad (2.2)$$

if $\kappa < 1/\sqrt{2}$, superconductors are called Type-I superconductors. Conversely, if $\kappa > 1/\sqrt{2}$, superconductors are defined as Type-II superconductors.

The main difference between these two types of superconductors is that they can show different responses to an external magnetic field. While Type-I superconductors expels magnetic flux completely from their interior, Type-II superconductors do it completely only at small magnetic field magnitudes, but partially in higher external fields.

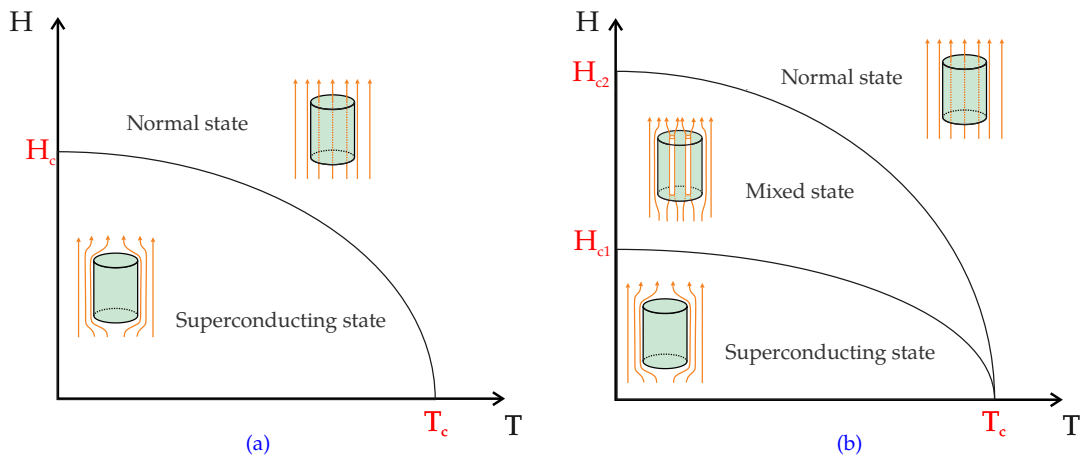


Figure 2.5: Magnetic phase diagram for (a) Type-I superconductors and (b) Type-II superconductor.

There are two critical fields for Type-II superconductors: the lower critical field H_{c1} and the upper critical field H_{c2} , as shown in figure 2.5b. In applied fields less than H_{c1} , the superconductor completely expels the field, just as a Type-I superconductor does below H_c (figure 2.5a). At fields just above H_{c1} , flux, however, begins to penetrate the superconductor in microscopic filaments called vortices which form a regular (triangular) lattice, as shown in figure 2.6a. Each vortex

consists of a normal core in which the magnetic field is large, surrounded by a superconducting region, and can be approximated by a long cylinder with its axis parallel to the external magnetic field. Moreover, each vortex carries a quantum of flux (*fluxon*) Φ equals to [12]:

$$\Phi = \frac{h}{2e} = 2.07 \times 10^{-15} \text{ Wb} \quad (2.3)$$

The vortex state of a superconductor, discovered experimentally by Shubnikov and theoretically by Abrikosov [13, 14], is known as the mixed state. It exists for applied fields between H_{c1} and H_{c2} . At H_{c2} , the superconductor becomes normal, and the field penetrates completely.

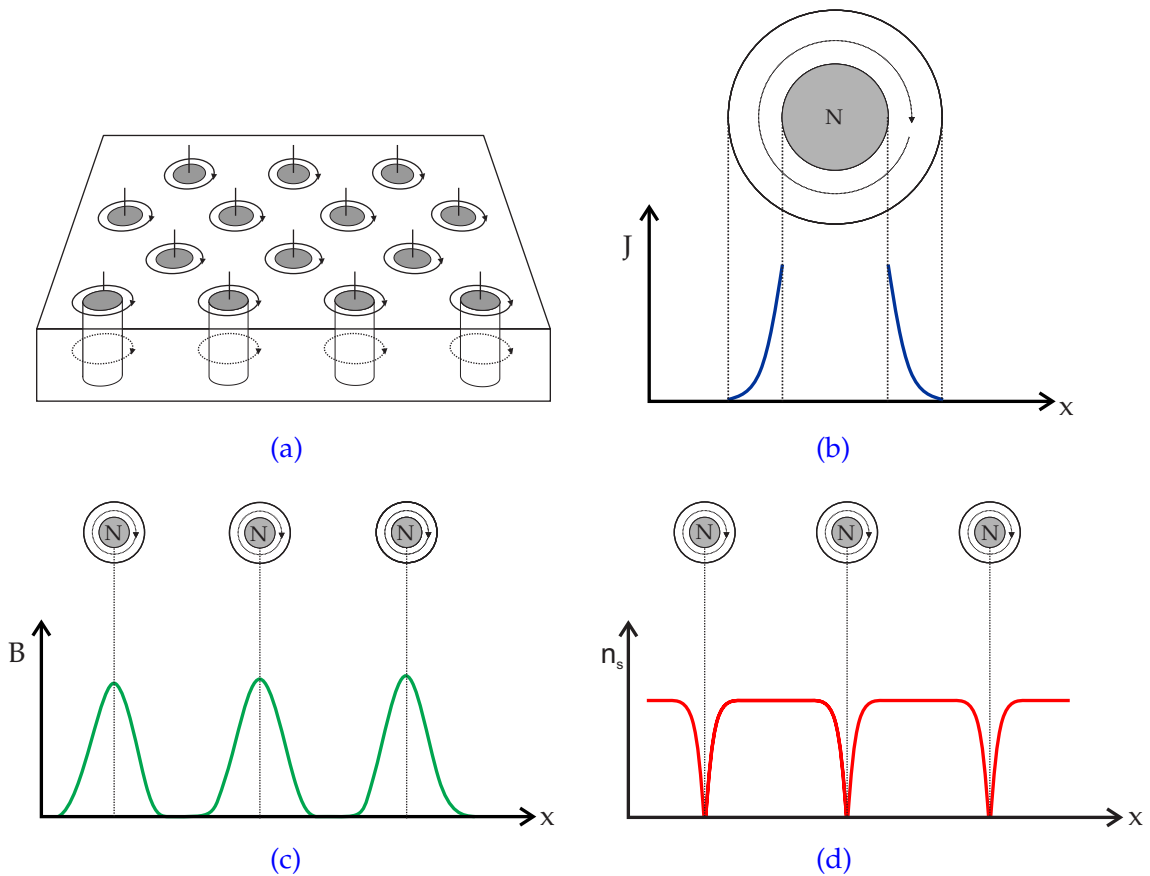


Figure 2.6: Mixed state in applied magnetic field of strength just greater than H_{c1} : (a) lattice of cores and associated vortices, (b) distribution of current density in a unit consisting of normal and superconducting regions, (c) variation of magnetic flux inside the material and (d) the variation with position of concentration n_s of superelectrons (Cooper pairs).

Figure 2.6b presents a unit consisting of normal and superconducting regions in the mixed state, in which the normal region (N) is located in the central section. A magnetic field can pass through the normal area, and the vortex screening current forms outside of the central region. The magnetic field gradually decreases

until it reduces to zero outwards from the central region of the vortex, as shown in figure 2.6c. Furthermore, towards the center of each vortex the concentration n_s of superelectrons falls to zero, as shown in figure 2.6d.

When the external magnetic field H further increases, superconducting region gradually reduces and the normal area (N) expands; if $H > H_{c2}$, the superconducting state completely returns into the normal state (N).

Table 2.1 lists the critical magnetic flux density of several superconducting materials at 0 K.

Table 2.1: Critical magnetic flux density B_c

Material	B_c (T)	Material	B_c (T)
Hg	0.04	LaBaCuO	30
Nb	0.2	La _{2-x} Sr _x CuO ₄	40
NbN	16	YBa ₂ Cu ₃ O ₃	180
Nb ₃ Sn	24	Bi ₂ Sr ₂ Ca ₁ Cu ₂ O ₈	225
NbAl	33	Tl ₂ Ca ₂ Ba ₂ Cu ₃ O ₁₀	>130
NbTi	14	HgBa ₂ Ca ₂ Cu ₂ O ₈	162

2.1.2.1 High Temperature Superconductors

The BCS theory predicts that superconductivity can only appear below a critical temperature of about 32 K. So it was a big surprise to the scientific world when Bednorz and Müller in 1986 discovered the *LaBaCuO* system which becomes superconducting at a critical temperature above 30 K. This discovery of high temperature superconductors (HTS) started the search for even higher critical temperatures and soon new materials had been discovered. Currently, there is critical temperatures up to 135 K.

The ceramic superconductors consists of layered crystal structures (figure 2.7), where copper-oxide planes are responsible for the current transport. The layered structure is further the explanation why high temperature superconductors exhibit an extreme anisotropy in critical magnetic fields and critical current. The material, being a ceramic, is also mechanically brittle, which complicates its application. Furthermore, the crystal grains are difficult to make large and the coupling between them is fairly poor, which reduces the ability of carrying a transport current, especially when the temperature approaches its critical value for the material. It has also turned out that the conductivity is further diminished when the grains are at an angle [15].

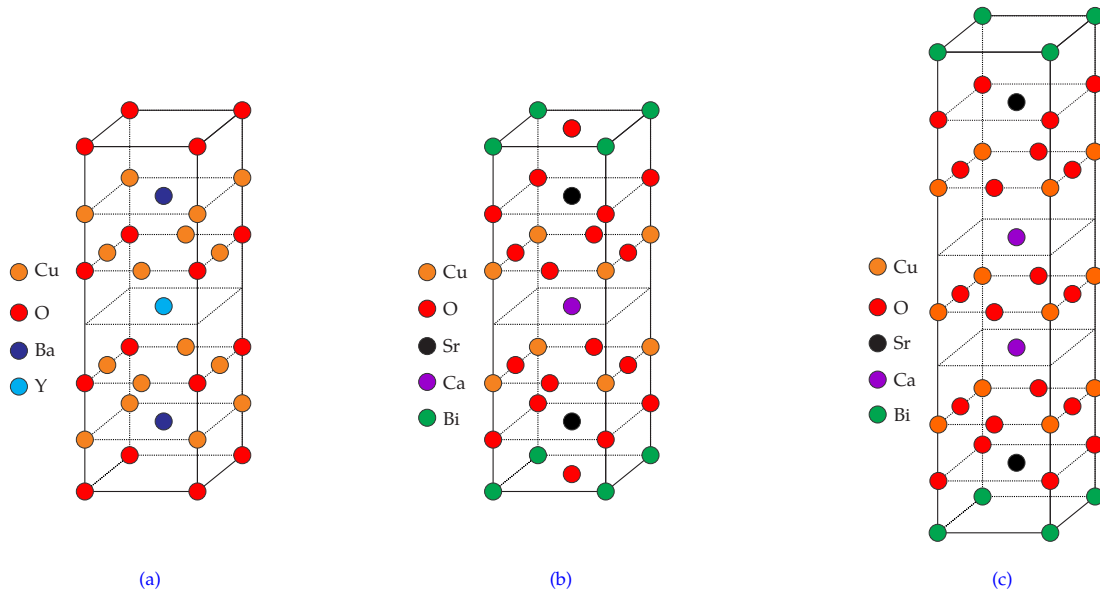


Figure 2.7: Representation of the layered structures for (a) $YBa_2Cu_3O_7$, (b) $Bi_2Sr_2CaCu_2O_8$ and (c) $Bi_2Sr_2Ca_2Cu_3O_{10}$.

There are in principle two types of high temperature superconducting materials: those that include rare earths and those that do not. The most common from the former group is Yttrium-Barium-Copper-Oxide ($YBa_2Cu_3O_7$) or YBCO for short (figure 2.7a). It has a critical temperature of 92 K and is best suited for thin films. YBCO exhibits a relatively good performance under magnetic fields, but possesses weak links between grains. A widespread material from the latter group is Bismuth-Strontium-Calcium-Copper-Oxide, which is abbreviated to BSCCO. BSCCO comes in two different mixtures, $Bi_2Sr_2CaCu_2O_8$ (Bi-2212, figure 2.7b) and $Bi_2Sr_2Ca_2Cu_3O_{10}$ (Bi-2223, figure 2.7c) that have a critical temperatures of about 90 K and 110 K, respectively. BSCCO compounds can be shaped more easily into composite wires due to the shearing along the Bismuth-oxide planes, which makes it useful to produce tapes that contain one (mono-) or several (multi-) filaments of superconducting material within a silver matrix. A well-developed production method helps also to align the crystals, and so increases the conducting ability.

High temperature superconductors have a very short coherence length and a very deep penetration depth, which makes them extreme samples of Type-II superconductors. The Ginzburg-Landau ratio κ is therefore very large, and so the first critical magnetic field H_{c1} is very low and H_{c2} can be extremely high (see table 2.1).

2.1.3 Critical Current Density in HTS Superconductors

When it comes to high temperature superconductors, the definition of critical current density J_c may be different. By critical current density, J_c means the maximum lossless current density which a superconductor can sustain before voltage increase (i.e. when a resistance appears). The current density responsible for breaking the Cooper pairs, and consequently destroying the superconducting state, is called "depairing current" density J_d [16].

If one passes a transport current in a HTS material in the mixed state, flux lines will experience a Lorentz force \vec{F} and will move it in perpendicular direction to the current flow direction, as shown in figure 2.8. Such vortices movement creates an electric field along the superconductor in the direction of current flow and the material appears to have a resistance even though there is a continuous superconducting path between the fluxons from one end to the other.

To stop or prevent this motion, a pinning force \vec{F}_p of magnitude at least equal to \vec{F} is necessary. When $|F| < |F_p|$ the flux-line lattice will be at rest, whereas the lattice will move if $|F| > |F_p|$. This is the conceptual definition of J_c : the maximum value of current density which a HTS material can transport without moving the flux lattice, i.e, without presenting resistance [17].

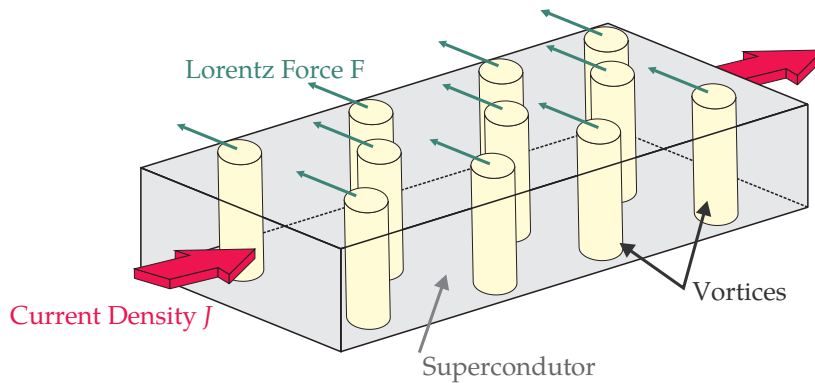


Figure 2.8: Lorentz driving force acting in a current carrying superconductor in mixed state.

Pinning force \vec{F}_p can occur through their interaction with various types of microstructural inhomogenities, such as dislocation networks, different types of inter- and intra-grain boundaries, composition fluctuations, precipitates of a second phases, etc. They give rise to local variations in superconducting properties either through "core interaction" or the "magnetic interaction" with a flux vortex, characterized by normal core radius (ξ) and supercurrent circulation spread (λ) respectively [16].

If the density of the current flowing in HTS exceeds the critical current density J_c under T_c , resistance begins to appear. The temperature of the HTS goes up by

the joule heat produced by the resistance. When the temperature reaches T_c , a transition to the normal state of the superconductor takes place [18].

2.1.3.1 The E-J Characteristic of HTS Superconductors

At very low current densities J , the Lorentz force \vec{F} is smaller than the maximum pinning force \vec{F}_p , hence all flux is pinned and the electric field E along the material is zero. If J increases and the value of J_c is exceeded, the flux line lattice starts to move. This stage of the E-J curve is highly nonlinear, as shown in figure 2.9a. At sufficiently high J (J_d) the system becomes normal and an ohmic behavior is expected.

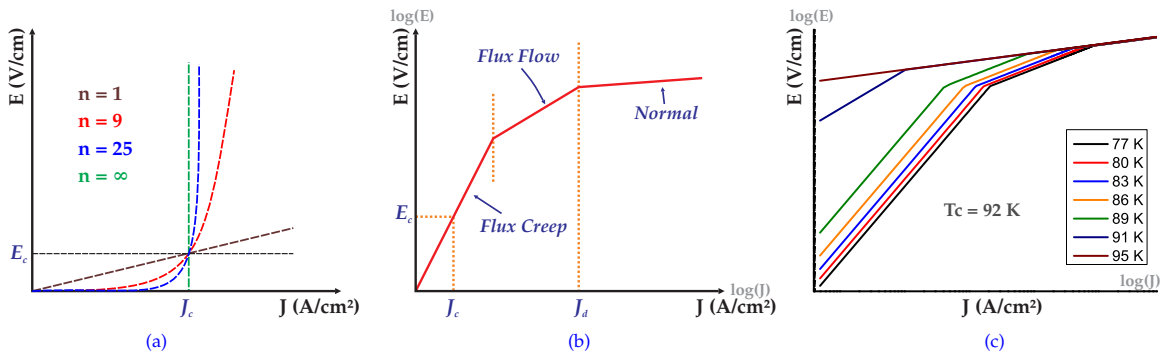


Figure 2.9: (a) The E-J Characteristic curve for HTS materials at the vicinity of J_c , (b) logarithmic E-J curve showing the three stages of transition under T_c and (c) the dependence on temperature under self field.

The E_c parameter, shown in figure 2.9, is the criteria used to determining J_c . Normally such criterion is adopted as $1 \mu\text{V}/\text{cm}$ [19]. The transport current is equals to J_c when the electric field reaches the E_c value along the material.

Figure 2.9b shows the main stages of the logarithmic E-J characteristic curve of HTS materials. If there is no applied field, the electric field strength can be considered a function of current density and temperature. Equation 2.4 describes all stages of the E-J curve. It is called power law.

$$E(J) = E_c \left[\frac{J}{J_c(T)} \right]^n \quad (2.4)$$

In equation (2.4), J_c is function of temperature. If the temperature T increases, J_c decreases and consequently the value of electric field E increases. Figure 2.9c shows the E-J curve described by equation (2.4) for different values of temperature considering a HTS material with $T_c = 92\text{K}$. The values of J_c at 77 K and index n are usually obtained experimentally when the electric field reaches the E_c criteria ($1 \mu\text{V}/\text{cm}$).

The n parameter is called "index of transition" [19] and can vary widely for various HTS materials, as well for the stage of transition. A real superconductor lies between the normal conductor linear characteristic ($n = 1$) and the case of superconducting material at 0 K ($n = \infty$) [20]. The E-J curve can be divided into three stages [21, 22]:

1. *Flux Creep* \Rightarrow The vortices movement in this stage occurs due to the transport current in the HTS material. The generated Lorentz force \vec{F} presents almost the same magnitude of the pinning force \vec{F}_p , leading to a slow motion of the flux lattice. The index of transition value n lies between 5 and 15 for the Bi-2212 material [23] and between 20 and 30 for YBCO coated conductors [24, 25].
2. *Flux Flow* \Rightarrow The movement in this stage is also caused by the transport current. However, the Lorentz force \vec{F} generated by such current is much greater than the pinning force \vec{F}_p , leading to a free motion of the flux lattice. The index of transition n varies between 2 and 4 for Bi-2212 and YBCO compounds [23, 25].
3. *Normal* \Rightarrow In this stage the vortices no longer exists and the superconducting state is completely destroyed. Therefore, the HTS material behaves essentially as a normal conductor, presenting linear resistance. The n value is 1 for this stage.

Although different approaches for the E-J characteristic curve may be found in the literature [26–30], equation (2.4) is enough to provide satisfactory results of HTS materials.

The dependence on temperature of J_c can be modeled as a linear function if the system operates between 77 K and T_c [31, 32]. In the case of working at low temperatures, a quadratic function will be more suitable.

2.2 Superconducting Fault Current Limiters

In the last years there has been a large amount of researches concerning about frequencies and magnitudes of destructive currents arising from short-circuits, also called fault currents, that can occur in the electrical network. The current generated due to a short-circuit can be 100 times greater than the rated current of the system [23] and can be caused by poor or aging insulation, lightning or even objects (branches, animals, etc.) [33].

Power systems are experiencing an increase of the fault current levels. Several factors have contributed to increasing these levels, such as new power plants that

were not foreseen in the long term planning of the power system. Power plants close to urban centers and the increasing interconnections in the electrical grid can also contribute to raising short-circuit current levels.

Since the electromagnetic forces on current-carrying conductors increase with the square of the current, the thermal, magnetic and physical stresses caused by fault currents are very high and it can literally tear equipments in the network apart (transformers, busbars and circuit breakers).

The need to manage the high levels of fault currents has prompted groups around the world to develop economical ways to avoid damages and blackouts. Measures, like splitting into subgrids and splitting of busbars as topological measures and choosing a higher transformer impedance, all lead to a permanent increase of the impedance not only at fault operation but also at nominal operation. The latter is in contradiction to the growing demand for a higher power quality and decreases the power system stability [34]. Some groups propose the development of an equipment with small impedance at nominal operation and fast increase of impedance at fault conditions. This one is called *fault current limiter*, FCL for short.

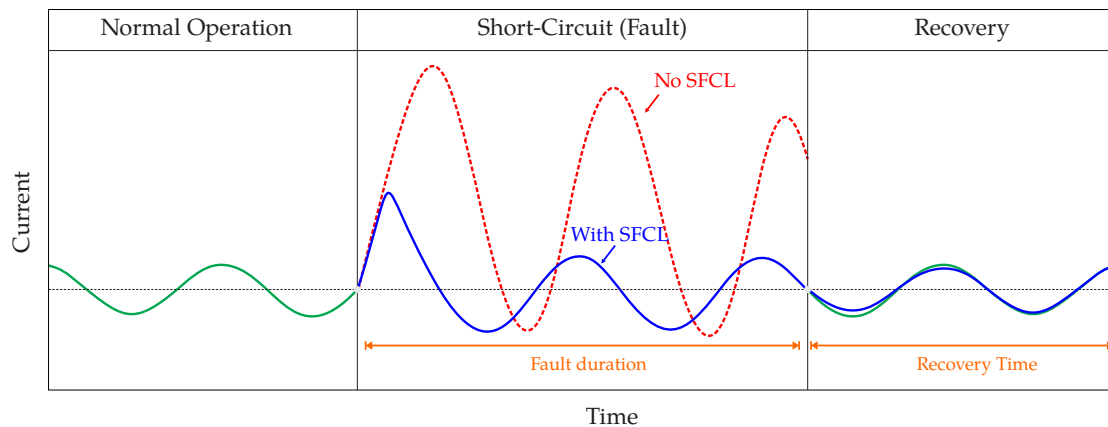


Figure 2.10: Operation modes of SFCL.

A fault current limiter is not intended to completely suppress the fault current, but rather reducing the fault current to such a level that already existing equipments and devices can handle it [35]. By using HTS materials, one can build *superconducting fault current limiters* (SFCL) devices having impedance only when a fault occurs, as shown in figure 2.10. Some concepts of SFCL are based on the quench of the superconductor material whereas others concepts are not. During normal operation, a SFCL is supposed to have zero impedance, just developing it during the fault period. After the clearance of the fault, the SFCL must recover its initial condition. Such period is called recovery time and it is defined as the time required to carry the nominal current again after fault clearance without quenching or thermal runaway [36].

SFCL has a number of advantages which are unique and not available with other limiting devices [37]:

- In the most types of SFCL, the systems are intrinsically safe. The change from zero resistance to nonzero resistance is self-triggering. The fault current itself activates the SFCL, being independent of external communications or triggers.
- The current flow is not interrupted so that the detection of the short circuit location is not hampered.
- The limited current can be adjusted according to the specifications.
- After a short circuit the system automatically recovers if cooling is provided, dependent on the system, in less than 1 min [38, 39].
- The reactive load under normal operation conditions is negligible.
- The SFCL offers special advantages in combination with the installation of a HTS cable, which does not need to be short-circuit-proof, allowing easier cable design and higher availability of the cable system.

As shown in figure 2.11, possible installations of SFCLs in the power grid include [40, 41]:

1. Generator feeder
2. Power station auxiliaries
3. Transformer feeder
4. Network coupling
5. Combination with other superconducting devices, especially cable
6. Outgoing feeder
7. Closing ring circuits
8. Busbar coupling
9. Shunting current limiting reactors
10. Coupling local generating units

There is a variety of SFCL types. The main types are described in the following sections.

2.2.1 Resistive Type (R-SFCL)

This is the concept that first comes to mind, and the simplest one in design. The FCL composed of a superconducting element is inserted in series with the system to be protected and immersed into a coolant bath (figure 2.12a). In nominal conditions, the element is in the superconducting state and passes the normal load

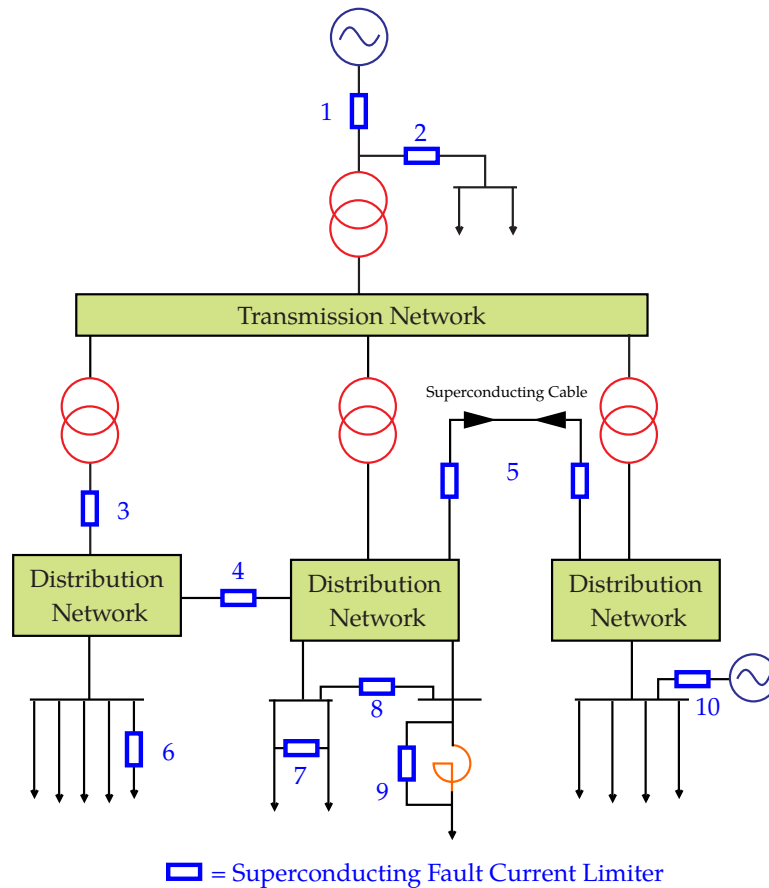


Figure 2.11: Some expected installations locations of SFCL in the power system.

current with theoretically no losses. In fault conditions, current rises and as soon as J_c is exceeded the superconductor transits to the normal state because of the joule heating and acts as a series resistor to reduce the fault current level.

Since this type of SFCL can have long length of HTS material, it is possible the occurrence inhomogeneities over the material, i.e., parts of the HTS material having different superconducting properties (T_c or J_c). As consequence, a uniform transition from the superconducting state to the normal state is difficult to achieve, since the HTS material may present distinct rates of heating under fault conditions. Hence, some part of the material may go to the normal state before others, generating the so called *hot-spots*. Hot-spot is nothing more than the overheating of one region over another [34, 42–45].

Appearance of hot-spots is completely unwelcome, since the region which early goes to the normal state will dissipate alone all the energy of the short-circuit. Obviously, excessive power over a unique region will result on damages, or even, on the total destruction of the superconducting material and device. To avoid appearance of hot-spots, it is usual the use of a *shunt* resistor over the length of the HTS material, as shown in figure 2.12b. In such way, most of the current is switched to the shunt during a fault. Furthermore, the shunt resistance adjusts

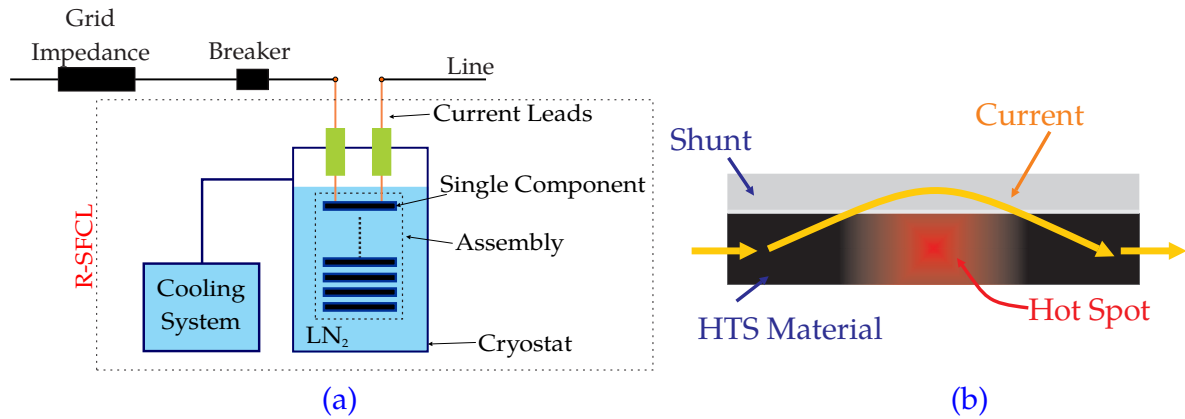


Figure 2.12: (a) The R-SFCL is connected in series with the system to be protected and (b) the use of a shunt resistance to protect the R-SFCL against hot-spots.

the limited current and avoids overvoltages that could occur if the resistance of the HTS material rises too fast. In order to not exceed the maximum temperature of the superconductor, fault must be cleared by a switch, typically within several half-cycles [34].

As already mentioned before, the main advantages of the R-SFCL lies on its simple design, since this device is connected in series with the system to be protected; low volume and weight of the components; negligible impedance under normal conditions of operation and fast triggering time. A drawback is the need for current leads from room to cryogenic temperature that cause heat losses due to heat conduction even in standby operation without current [34, 46–48].

Resistive SFCL can be found in diverse shapes: meander [24, 49], multifilar pancakes [50], spiral or bars [28] and coils. In this work two commercial R-SFCL are studied and simulated: the MCP-BSCCO-2212 and YBCO 2G tapes coils (similar to the coils employed in the ENSYSTROB project [51, 52]) both manufactured by the German company *Nexans Superconductors GmbH*.

2.2.1.1 MCP-BSCCO-2212

Fault current limiters and current leads are the most significant examples of the use of Bi-2212 superconductors (BSCCO-2212) in the form of bulk tubes. The very effective *Melt Casting Process - MCP* has been developed for BSCCO-2212 bulks, enabling processing of even large tubes with diameters between 25 and 200 mm and lengths up to 1 m [53]. This process consists of successive melting, centrifugal casting, heat treatment and oxygenation. Figure 2.13 illustrates some stages of the process. For centrifugal casting, the melt of a composition appropriate to the subsequent solidification of BSCCO-2212 is heated in a rotating metal cylinder, thereby becoming distributed over the inner wall. Solidification in air proceeds

from a temperature near 900°C under controlled cooling. Finally, the precise dimension is obtained by ceramics machining [54, 55].

Bifilar functional elements for fault current limiters are obtained from such tubes by cutting a spiral nearly to the end of the tube. A sophisticated technology is used to produce a 3-layer compound element containing also the metallic shunt (by soldering a CuNi or CuNiMn alloy onto the BSCCO-2212 tube) and additionally a tube of fiber-reinforced plastics. A 1 mm slot is cut precisely, with computer control, using either a disc saw or high-speed milling.

The components are connected in series and constitute each phase of the limiter (figure 2.13a). The series assemblies are immersed in liquid nitrogen cooled to below its boiling point. The nitrogen head pressure is below atmospheric pressure.

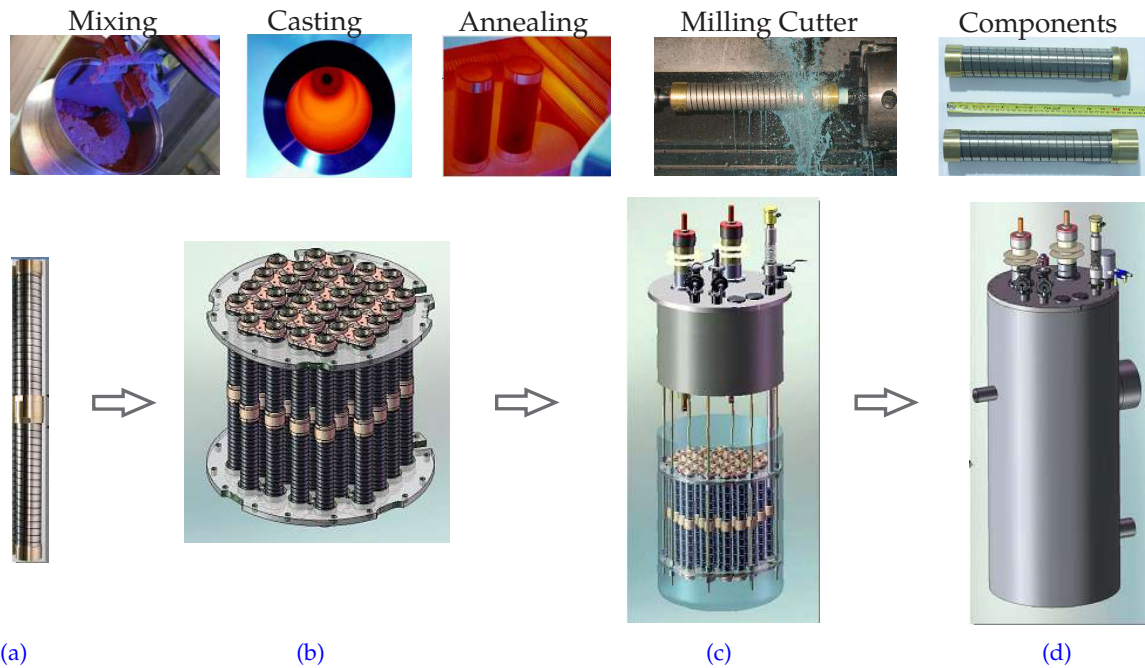


Figure 2.13: Main stages of production of the MCP-BSCCO-2212 SFCL, (a) connection of two components, (b) montage of an assembly, (c) set-up of a phase and (d) accommodation in a cryostat. Courtesy of Nexans Superconductors GmbH

2.2.1.2 ENSYSTROB

The next R-SFCL to be studied is similar to the ENSYSTROB. This one was recently designed (2009), built and installed in Germany for MV application [51]. Conversely to the MCP-BSCCO-2212, this limiter does not consist of bulk material, but of second generation YBCO based coated conductors [51, 52], YBCO 2G for short.

Compared with BSCCO based tapes (1G tapes), YBCO has superior electro-

magnetic characteristics with higher irreversible magnetic field. It also displays a higher critical current density J_c and weak anisotropy in high magnetic fields and at a liquid nitrogen temperature (77 K). Because of the weak link among YBCO grains, it is difficult to fabricate 2G YBCO tapes by PIT techniques. Preparation methods of 2G YBCO tapes, such as depositing and coating, are the main trend of fabricating practical HTS materials applied in electrical engineering. The *SF12100* tapes employed in the ENSYSTROB are manufactured by the Japanese company *SuperPower Inc.* by two high-throughput processes: IBAD-MgO for texture buffer and MOCVD for the HTS layer. Further details about manufacturing process can be found in [56–58]. The schematic geometrical structure of 2G YBCO tapes and sizes of components are displayed in figure 2.14 [59].

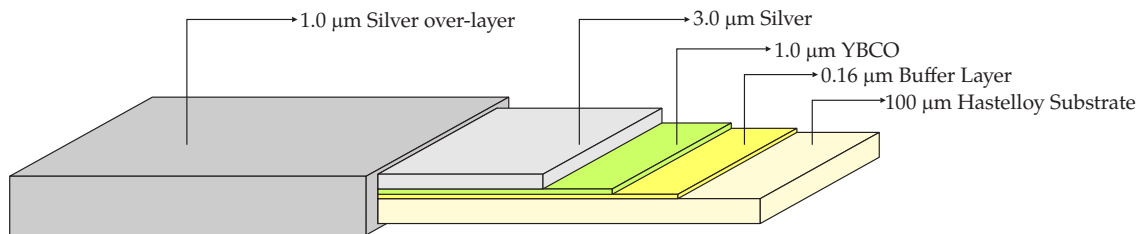


Figure 2.14: Geometrical sizes of the 2G YBCO tapes employed in the ENSYSTROB. Sizes refers to the *SF12100* tapes from *SuperPower Inc.* company.

The choose for the *SF12100* tapes relies on the availability with user defined thickness of the Ag protection, non-magnetic substrate (AC-losses) and the absence of soldering procedures which may lead to damage if the sample locally gets hot [52]. 2G YBCO tapes are disposed in a pan-cake arrangement to minimize the inductance of the component. Pairs of tapes ("twins") in a "back to face" configuration without insulation are wound to spirals [51].

All tapes are connected in a common center contact M, with the advantage that the tapes better protect each other in the case of hot spots. Contacts are made by pressing the YBCO sides of the tapes on clean Cu surfaces with some additional Indium-foil. The pancake is mounted on a 120° segment of fiber reinforced plastics (FRP), as displays figure 2.15a.

In order to enable the high specified limited currents an internal shunt had to be foreseen. A stack of several stainless steel tapes has been wound to a bifilar spiral and was also mounted on a 120° segment. Both, the superconducting and the shunt spiral, each on a FRP plate, are mounted on top of each other and connected in parallel [51]. Further details about the ENSYSTROB project can be found in [51, 52, 60].

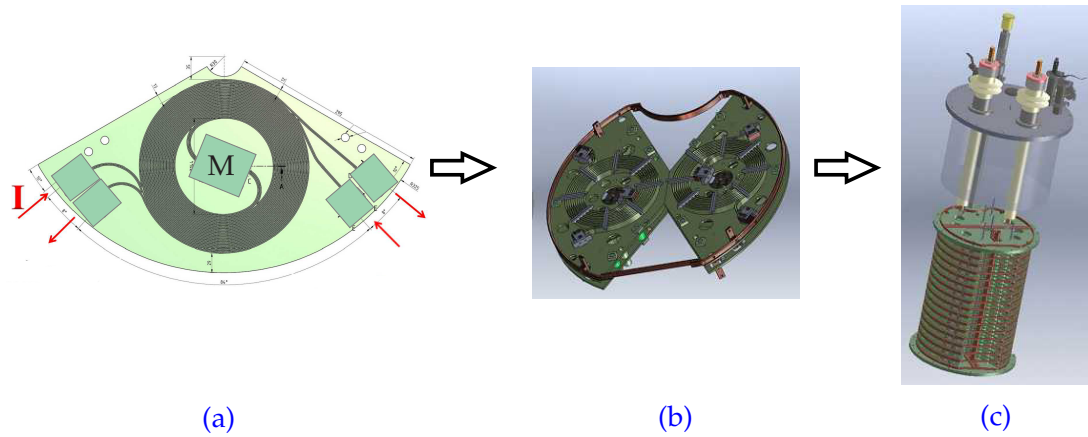


Figure 2.15: (a) Single component of the ENSYSTROB, (b) montage of an assembly and (c) set-up of a phase. Courtesy of Nexans Superconductors GmbH

2.2.2 Magnetic Field Assisted (MF-SFCL)

The MF-SFCL is similar to the R-SFCL. However, the quenching of the HTS material depends on the applied magnetic field. The HTS material is placed inside a conventional coil and during normal operation the current flows through it, as shown in figure 2.16.

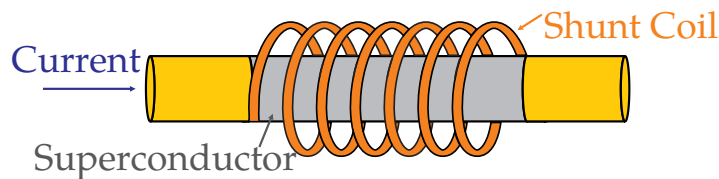


Figure 2.16: Schematic arrangement of the MF-SFCL.

Under fault conditions, quench starts at the weakest point of the superconductor and its growing resistance forces the current to flow in the parallel shunt coil [34]. The deviated current originates a magnetic flux that forces homogeneous and fast quench by reducing the critical current J_c in the remaining superconducting parts, thereby avoiding hot-spots.

The main advantages and drawbacks of the MF-SFCL are the same of the R-SFCL described in section 2.2.1. An additional advantage of the MF-SFCL is that the HTS material in use is able to withstand higher electric field during the fault period and thereby less amount of superconductor material is required [48].

2.2.3 Shielded Iron Core (L-SFCL)

The shielded iron core SFCL, or often called inductive SFCL [34], allows the HTS cryogenic environment to remain mechanically isolated from the rest of the circuit. An electrical connection is made between the line and the HTS element through

mutual coupling of AC coils via a magnetic field. Basically, the device resembles a transformer with a copper winding at the primary and with the secondary side composed by an HTS cylinder (figure 2.17). Under normal load conditions, the induced current in the superconducting cylinder is lower than the critical current density J_c , thus the magnetic flux is shielded by the superconductor and does not penetrate the iron. Hence the impedance is low.

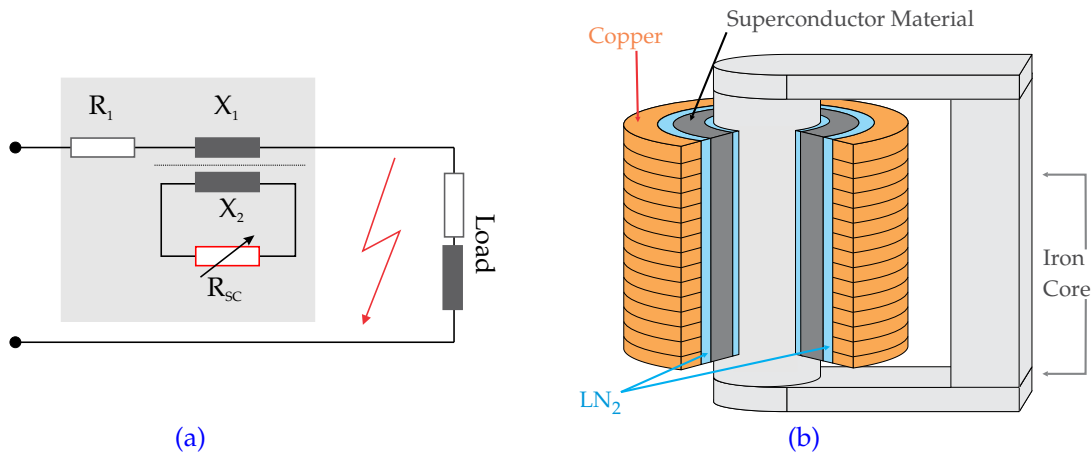


Figure 2.17: Shielded-Core SFCL Concept: (a) equivalent circuit and (b) design.

If the current in the copper winding increases because of a fault, the induced current in the superconducting cylinder becomes higher than J_c , increasing the resultant magnetic field. As consequence the flux lines start to penetrate the superconductor and then into the iron core. This brings a rise in the impedance seen from the primary side of the transformer, limiting the fault current.

Since the HTS material is not in series connection with the system to be protected, there are no current leads to cryogenic temperatures, that is, there is no heat transport into the cryogenic system. A major drawback of the shielded-core technology is its size and weight; it has much larger size and weight of the R-SFCL [26] and has volume and weight which is similar to a transformer of the same power rating [34, 46–48].

2.2.4 Diode Bridge Type (D-SFCL)

The Diode Bridge Type SFCL is based on the use of solid state switches, a superconducting coil and a DC voltage source. Switches can be diodes or thyristors arranged as a full bridge rectifier. Figure 2.18 shows the electrical circuit of the D-SFCL type.

Under normal conditions, the DC voltage source v supplies a current of amplitude i_o that is branched out in such way that a current of amplitude $i_o/2$ flows through the series connection of a pair of diodes (D1-D2 and D3-D4). The current

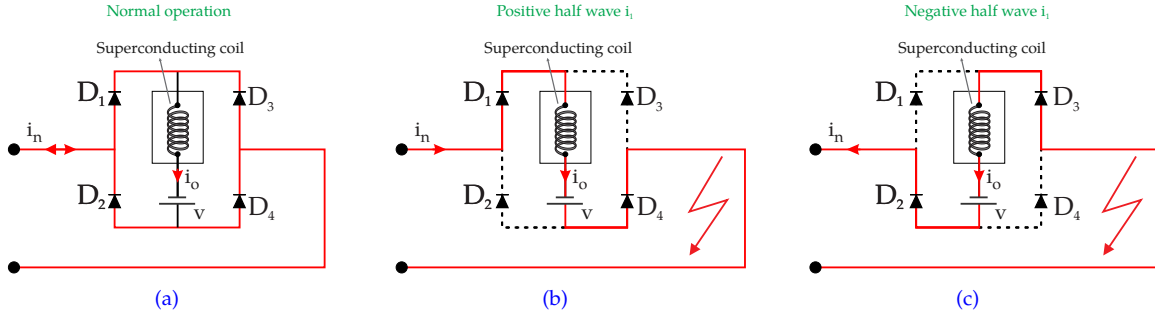


Figure 2.18: Electrical circuit of a D-SFCL (a) under normal operation, (b) during the positive half wave and (c) the negative half wave of the fault current.

i_n also branches out between each bridge of the limiter, that is, a current of amplitude $i_n/2$ flows through the D1-D3 and D2-D4 connections (see figure 2.18a). In that way the resulting current is $(i_o + i_n)/2$ through D1-D4 diodes and $(i_o - i_n)/2$ through D2-D3 diodes. Hence, all diodes are operating in the conducting mode since $i_o > i_n$, therefore the AC current bypasses the superconducting coil.

Under fault conditions, the amplitude of i_n gets higher than i_o and, depending on the half wave of i_n , a pair of diode will arrest: during the positive half wave diodes D2-D3 will arrest (figure 2.18b) and during the negative half wave diodes D1-D4 will arrest (figure 2.18c). The arrest of a pair of diodes in the bridges deviates the fault current to the superconducting coil and the current is limited [61–63].

Since the current in this coil only increases marginally over time the DC voltage source will not be stressed in any way. In principle the superconducting coil could be non-superconducting but this would result in larger coils and in higher losses due to the continuous current through the coil. The main advantages of the D-SFCL is no superconductor quench, immediate recovery after the fault period and adjustable current trigger. The drawbacks relies on the use of semiconductors: in the case of a diode fails the device will not limit the current, besides presenting relatively high losses under normal conditions[34].

2.2.5 Saturated Core (SC-SFCL)

Unlike resistive and shielded-core SFCL, which rely on the quenching of superconductors to achieve increased impedance, the SC-SFCL utilize the dynamic behavior of the magnetic properties of iron to change the inductive reactance on the system [64–66]. The concept (shown in figure) utilizes two iron cores and two AC windings for each phase. The AC windings are made of conventional conductors that are wrapped around the core to form an inductance in series with the AC line. The iron core also has a constant current superconductive winding that provides a magnetic bias.

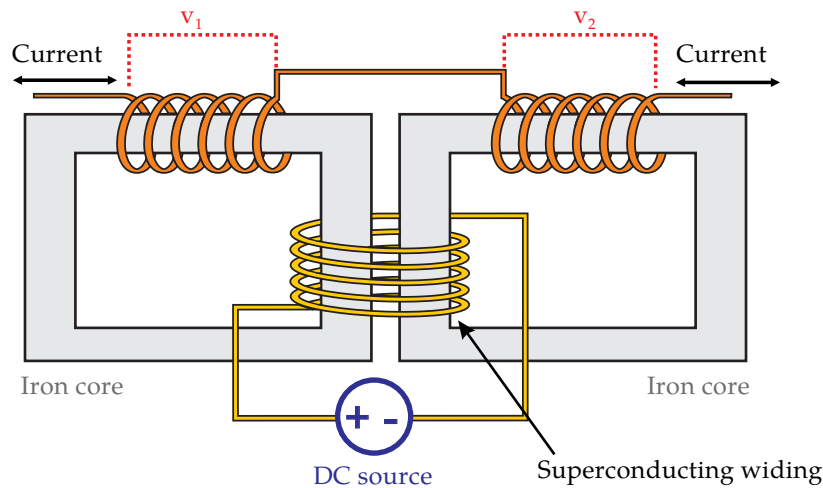


Figure 2.19: Design of the Saturable Core SFCL.

The nonlinear magnetic behavior of iron, as shown in the curves of figure 2.20, constitutes the physical basis for this SFCL. In normal operation, both iron cores are driven into saturation by the DC currents produced by the superconducting DC winding which cause the magnetic circuits to operate around the DC bias magnetic fields H_{DC1} and H_{DC2} , respectively.

Under fault conditions, the negative and positive current peaks force the core out of saturation, resulting in increased line impedance during part of each half cycle (see impedance graphs at top and bottom of figure 2.20). The result is a considerable reduction in peak fault current (20-50 %). During a limiting action, the dynamic action of the core moving instantaneously in and out of saturation produces harmonics in the current waveform (see $B \times H$ graphs in figure 2.20). However, under normal conditions, the voltage and current waveforms are basically unaffected by the saturable core SFCL [34, 66, 67].

Essentially, the SC-SFCL is a variable-inductance iron-core reactor which has the impedance of an air core reactor under normal grid conditions and a very high impedance during fault events. Unlike the R-SFCL, which may require time between limiting actions to cool the superconducting components, the SC-SFCL approach can manage several actions in succession since the superconductor does not quench. In fact, saturable core FCL does not need to use a superconducting coil. However, the use of an HTS DC field winding reduces operating losses and makes the winding more compact.

The major disadvantage of the SC-SFCL is its huge size. It depends on prospective fault currents and limiting capability, but it will anyway be much larger than conventional three phase transformers of the same nominal power level.

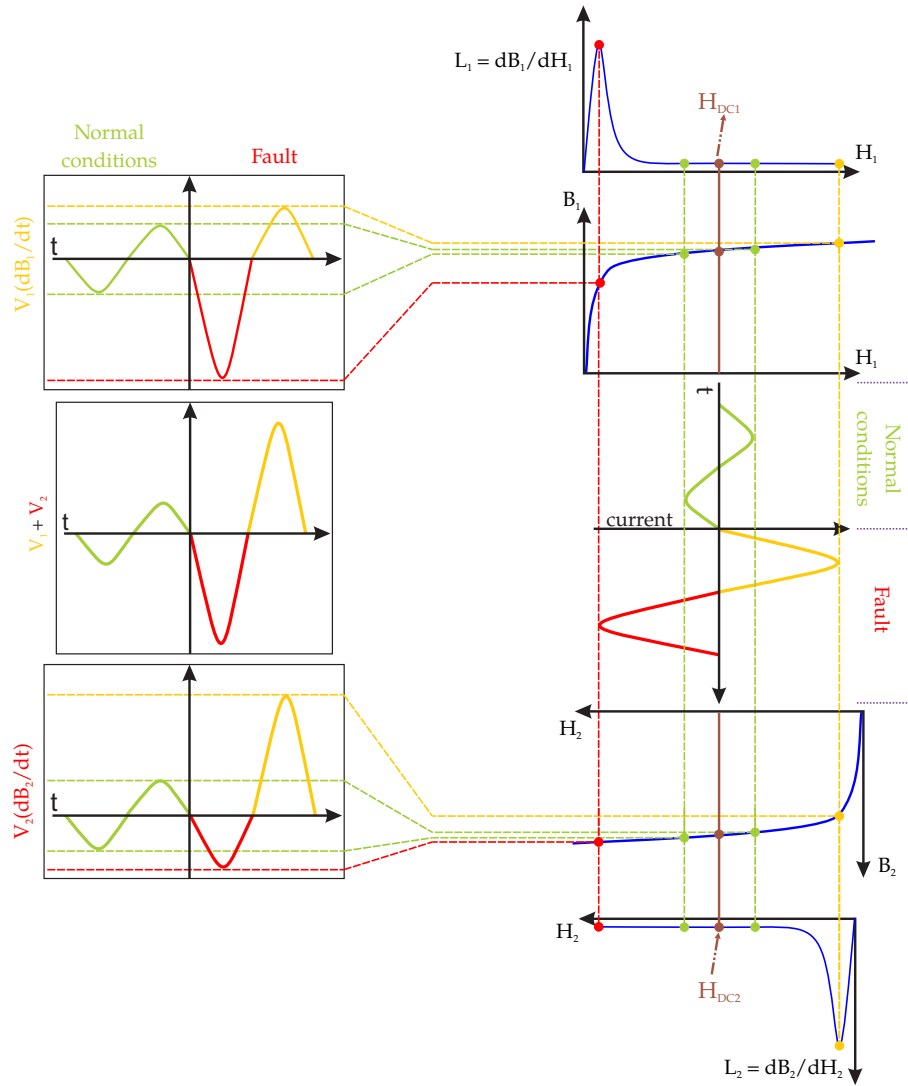


Figure 2.20: Iron core characteristic and current/voltage curves of a SC-SFCL.

2.2.6 Air Coil SFCL (AC-SFCL)

The air coil SFCL is a new concept of FCL under development in Germany (at Karlsruhe Institute of Technology) and, as the resistive MCP-BSCCO-2212 and ENSYSTROB, will be studied and simulated in this work.

The AC-SFCL consists of two concentric aligned solenoid coils, which act as primary and secondary winding. The primary winding is connected in series to the system, is made of copper and operates at room temperature. The secondary winding uses 2G YBCO tapes (SCS12050 manufactured by *SuperPower Inc.*, see figure 2.21) and is cooled with liquid nitrogen (77 K) [68, 69]. The design of the AC-SFCL is shown in figure 2.22a.

Under normal conditions of operation, the superconducting tapes at the secondary winding shields the magnetic field at the center of the coils. As consequence the impedance seen from the primary coil is low. Under fault conditions,

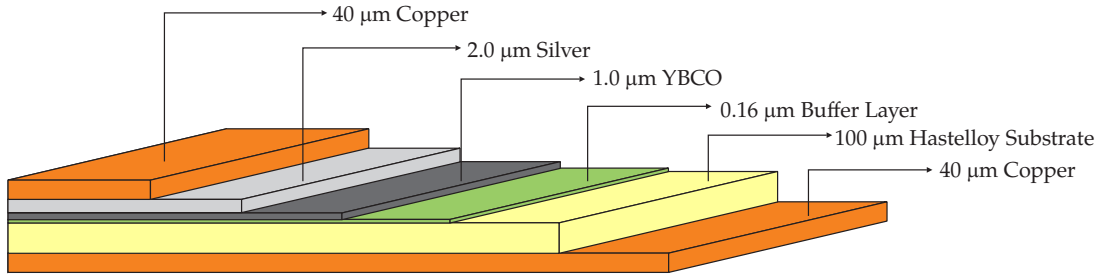


Figure 2.21: Geometrical sizes of the 2G YBCO tapes employed in the AC-SFCL. Sizes refers to the SCS12050 tapes from SuperPower Inc. company.

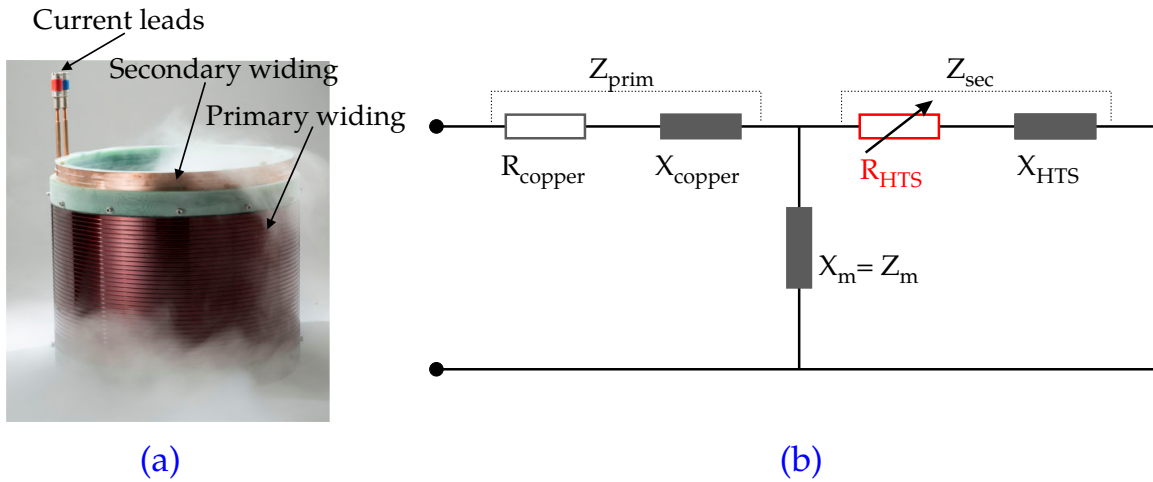


Figure 2.22: (a) Primary copper winding and secondary superconducting winding (pulled out) and (b) equivalent circuit diagram of the AC-SFCL.

the current in the copper winding (primary) increases and an induced current surges in the superconducting coil (secondary). Depending on how high is this induced current, a considerable impedance is now seen from the primary coil and the limitation of the fault current starts taking place.

A better understanding of the AC-SFCL can be achieved by analyzing its equivalent electrical circuit (figure 2.22b) which resembles that of a short circuited transformer. During normal operation the induced current in the secondary winding is lower than J_c and the HTS material is in the superconducting state. Hence $R_{HTS} \approx 0$ and Z_{sec} is lower than Z_m . Under fault conditions the HTS material quenches. In this case the resistance R_{sec} increases the impedance of the secondary winding Z_{sec} and most of the fault current is commuted to the parallel branch containing Z_m . therefore limiting it.

The main objective of the AC-SFCL is to improve installed air core reactors by retrofitting it with a secondary superconducting winding. The advantage of this approach is a SFCL, which allows to omit an iron core, thus reducing weight and costs compared to inductive type SFCL and to omit current leads, thus reducing losses compared to resistive type SFCL. Furthermore, in case of failure of

the secondary superconducting winding, the impedance of the shunt reactor is not affected. The impedance of the shunt reactor still takes effect during a fault current. The concept is therefore failsafe [68].

2.2.7 Comparative Evaluation

To finish this chapter, one presents a comparative evaluation between the described SFCL concepts. Table 2.2 summarizes the main advantages and drawbacks. The evaluated characteristics are:

- Fail safe;
- Superconductor quench;
- Current leads into the cryostat;
- AC losses;
- Voltage drop under normal operation;
- Maintenance;
- Volume, size and weight;
- Trigger by sensors;
- Recovery time;

Table 2.2: Comparative Evaluation of the main characteristics between the SFCL concepts [34, 46, 48].

	R-SFCL	MF-SFCL	DB-SFCL	SC-SFCL	L-SFCL	AC-SFCL
Fail Safe	Yes	Yes	No	Yes	Yes	Yes
Quench	Yes	Yes	No	No	Yes	Yes
Current leads into cryostat	Yes	Yes	Yes	Yes	No	No
AC losses	Yes	Yes	No	No	Yes	Yes
Voltage drop	Low	Low	Low	Middle	Low	Low
Maintenance	Middle	Low / Middle	Middle	Low	Middle	Low
Volume, size and weight	Small	Small / Middle	Middle	Heavy	Middle / Heavy	Small / Middle
Trigger by sensors	No	No	Yes	No	No	No
Recovery time	Sec. / Min	Sec. / Min.	Immediate	Immediate	Sec.	Sec.

Chapter 3

Tests, Experimental Data and Inhomogeneity Representation

SFCL devices were tested in order to obtain experimental data to validate simulations results. This chapter presents tested devices, measurements circuits and performed tests. Furthermore, a numerical model related to the inhomogeneity representation is presented in order to enhance the quality and capability of simulations.

3.1 Tested Components

The MCP-BSCCO-2212 SFCL, described in section 2.2.1.1, were supplied by *Nexans Superconductors GmbH*. In total, twelve modules were tested. Each one was designed for a maximum rated current of about $330 A_{rms}$, at 77 K and maximum rated voltage of $135 V_{rms}$. It consists of a shunted BSCCO-2212 monofilar coil with a total length of 270 cm (current path) and critical temperature T_c of about 92 K.

The geometry is that of a helicoidal tube. The shunt component consists of a CuNi alloy and it is soldered continuously over the whole length of the superconductor through a thin layer of a low melting solder. In order to compensate thermal stresses and mechanical forces in the case of a short-circuit, a thin tube of fiber reinforced plastics (FRP) is glued coaxially into the superconducting tube. The contact resistance of components is lower than $1 \mu\Omega$ [53]. Figure 3.1a illustrates the design of a MCP-BSCCO-2212 SFCL module.

Similarly to the ENSYSTROB components described in section 2.2.1.2, the YBCO 2G coil component was also supplied by *Nexans Superconductors GmbH* and consists of shunted coils of 2G tapes. Eight tapes with a length of 4.3 m each compose the component. There is an additional central contact connecting the tapes. These are arranged in an anti-parallel manner as shown in the figure 3.1b result-

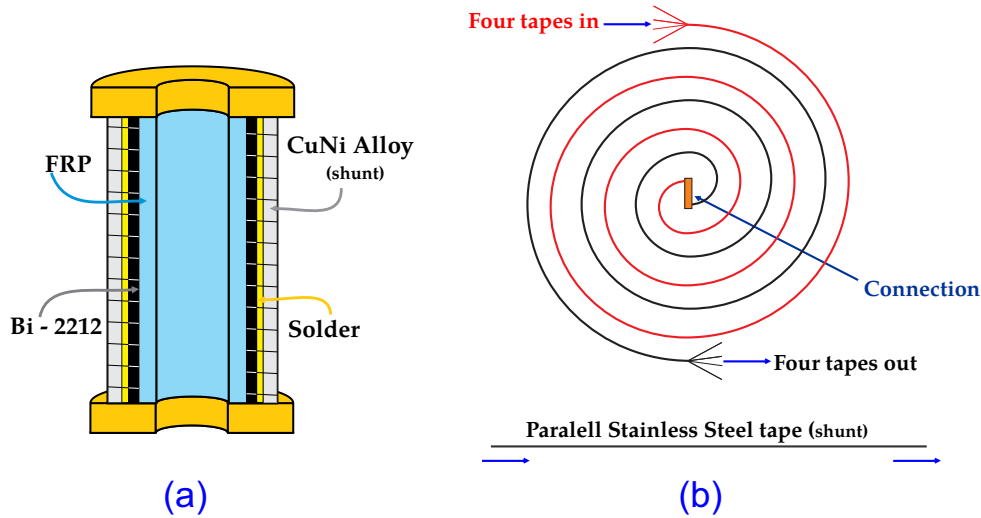


Figure 3.1: Design of the tested R-SFCL: (a) MCP-BSCCP-2212 and (b) YBCO 2G Coil.

ing in both field compensation and AC losses reduction. The red path goes inside and the black path outside. The contact resistance of the component is approximately $3 \mu\Omega$. Its nominal current is $600 A_{rms}$ at 77 K and the maximum voltage is $400 V_{rms}$.

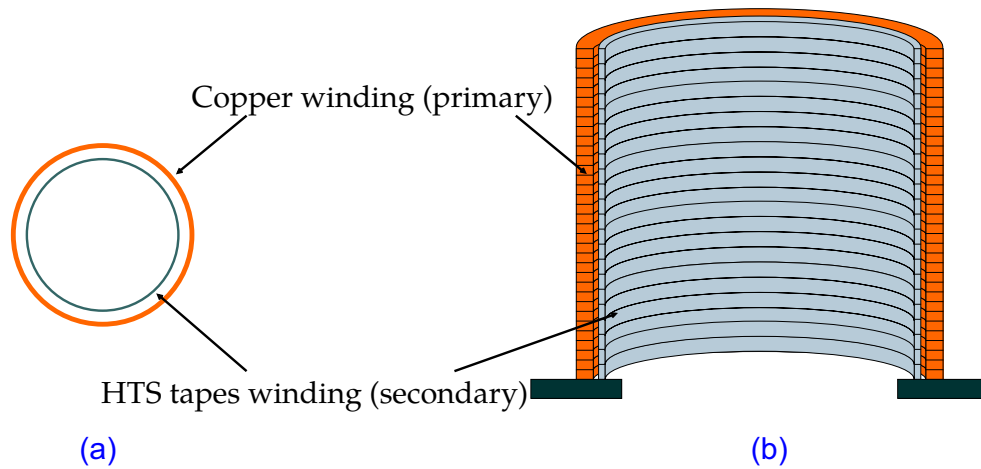


Figure 3.2: Design of the tested AC-SFCL: (a) upper view and (b) cross section view of the device.

The Air Coil SFCL has a copper winding with 34 turns as primary and operates at room temperature. The secondary winding is composed of 22 short circuited multilayer HTS tapes manufactured by SuperPower Inc (SCS12050). These tapes in the secondary winding have total length of 147 cm and are all assumed to be in parallel and therefore acting electromagnetically as a winding with only one turn, as shown in figure 3.2. The inner and outer radius of the device are 48 cm and 49.4 cm respectively [68, 69].

The nominal current and voltage of the device are $150 A_{rms}$ at 77 K and 400

V_{rms} respectively. Table 3.1 lists the main parameters of the AC-SFCL at 50 Hz: X_{cu} and R_{cu} are the values of inductive reactance and resistance of the primary coil, X_m is the value of the magnetizing reactance, X_{Sec} represents the inductive reactance of the secondary coil [70].

Table 3.1: Parameters of the AC-SFCL
($\omega = 2\pi f$).

Parameter	Value (Ω)	Parameter	Value (Ω)
$X_{cu} = \omega L_{cu}$	0.011	R_{cu}	0.0002
$X_m = \omega L_m$	0.155	$X_{Sec} = \omega L_{Sec}$	0.007

3.2 Measurements Circuits and Tests

The resistive MCP-BSCCO-2212 SFCL modules (in series connection) and the YBCO 2G Coil were submitted to single-phase short-circuit tests in the High Current Laboratory of the Electric Power Research Center (CEPEL - ELETROBRAS System) in Brazil. Such Lab can achieve source voltages as high as 6 kV_{rms} (single-phase) or 3.5 kV_{rms} (three-phase) and currents up to 50 kA_{rms} (steady state) and up to 200 kA_{rms} (or 500 kA_{peak}). Its maximum short-circuit times is 5 s.

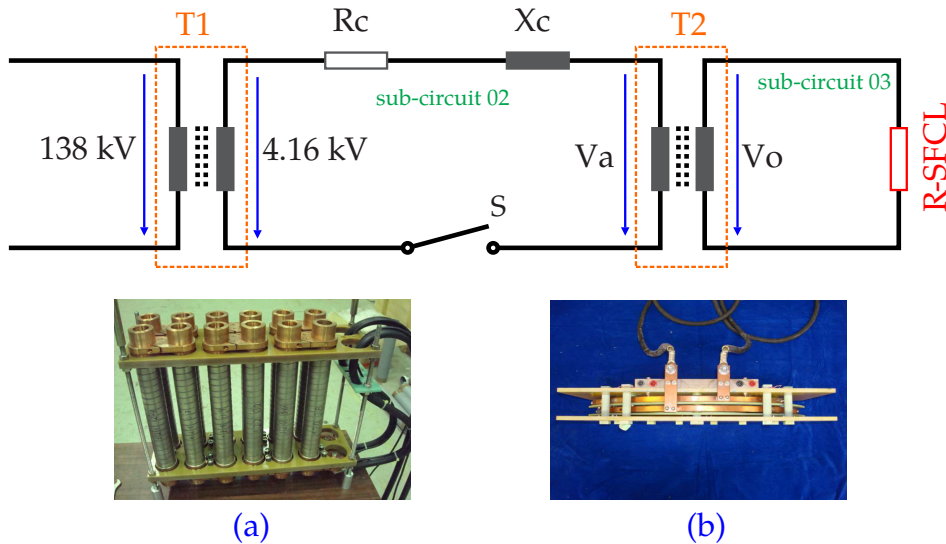


Figure 3.3: Configuration used in the present work to test resistive SFCL. The resistance R-SFCL indicates (a) the MCP-BSCCO-2212 SFCL modules and (b) the YBCO 2G Coil SFCL.

The Lab is fed by a high voltage transmission line (138 kV) and is composed of two transformers: T1 and T2. The first one (T1) lowers the high voltage value

from 138 kV to 4.16 kV at the sub-circuit 02, as shown in figure 3.3. The value of the prospective fault current (without the SFCL) is controlled by the values of resistance R_c and reactance X_c connected to this sub-circuit. The second transformer (T2) lowers the voltage V_a to V_o at the sub-circuit 03. The SFCL modules were connected in series with the secondary of the transformer T2 in the sub-circuit 03. The short-circuit is triggered by closing the switch S in the sub-circuit 02.

The MCP-BSCCO-2212 assembly and the YBCO 2G Coil were tested in an open bath of liquid nitrogen (77 K). A resistive divider was used to measure the voltage drop between the SFCL terminals, whereas a current transformer enabled the measurement of current passing through the cables connected to the SFCL. Both resistive divider and current transformer were linked to a data acquisition system.

In order to calibrate the testing set-up, the prospective fault current was measured by connecting a copper bar in the place of the R-SFCL components. Afterwards, the copper bar was replaced by the SFCL components. The test circuit of figure 3.3 was configured to carry out fault currents during 60 ms at 60 Hz. Several short-circuit tests have been carried out, but for modeling purposes only those listed in table 3.2 will be simulated.

Table 3.2: Short-circuit tests for both R-SFCL.

R-SFCL	Voltage (V_o)	Fault Current	Components	Current Waveform	Test key
MCP-BSCCO 2212	$1.0 \text{ kV}_{\text{rms}}$	$5 \text{ kA}_{\text{rms}}$ $25 \text{ kA}_{\text{rms}}$ $67 \text{ kA}_{\text{rms}}$	12	Symmetrical	t1-mcp t2-mcp t3-mcp
YBCO 2G Coil	$200 \text{ V}_{\text{rms}}$	$5 \text{ kA}_{\text{rms}}$ $20 \text{ kA}_{\text{rms}}$ $30 \text{ kA}_{\text{rms}}$	01	Asymmetrical	t1-coil t2-coil t3-coil

The air coil SFCL (AC-SFCL) described in section 2.2.6 was also submitted to single-phase short-circuit tests at the Institute for Technical Physics (ITEP) of the Karlsruhe Institute of Technology (KIT), in Germany. The Lab of ITEP is fed by a 400 kVA variable transformer set to $400 \text{ V}_{\text{rms}}$ on the primary and secondary side serves as power supply for the whole setup, as shown in figure 3.4.

Two branches with two anti-parallel thyristors allow triggering the nominal current as well as the fault current individually at a specified phase angle and for a specified duration of half cycles. This approach allows negative and positive half cycles to pass independently and short-circuiting during normal operation (with load). The currents for load and fault operation can be adjusted to the desired value by the resistances R_l (for load) and R_f (for fault). The resistance R_p functions as protection for the thyristors in case of an accidentally short-circuit without any

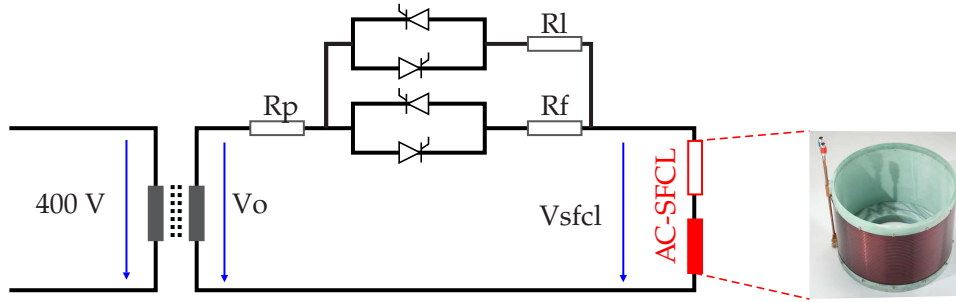


Figure 3.4: Equivalent circuit diagram of the measurement setup to test the Air Coil SFCL.

other resistance.

All measured signals are acquired by a transient recorder and transmitted to the computer for evaluation. A synchronization box enables triggering the switches and releasing the fault current at any desired point in time. This approach allows exact adjustment of desired duration in half cycles as well as short-circuiting at a specific phase angle.

The AC-SFCL was also submitted to several short-circuit tests, but only three cases have been simulated and are listed in table 3.3. The test circuit of figure 3.4 was configured to carry out single-phase short-circuits for 40 ms at 50 Hz.

Table 3.3: Short-circuit tests for the AC-SFCL.

SCFCL	Voltage (Vo)	Fault Current	Components	Current Waveform	Test key
Air Coil SFCL	400 V _{rms}	450 A _{rms}	01	Symmetrical	t1-acsfcl
		1.05 kA _{rms}			t2-acsfcl
		2.55 kA _{rms}			t3-acsfcl

3.2.1 Tests Results

3.2.1.1 MCP-BSCCO-2212 Tests

Results of the short-circuit tests with the MCP-BSCCO-2212 assembly are now presented. Figure 3.5 shows results of test t1-mcp. The first current peak without the MCP-BSCCO-2212 assembly (fault current) of 7.6 kA_{peak} was limited to 6.1 kA_{peak}. One also observes the voltage drop between the assembly terminals.

Figure 3.5 also shows that the last two cycles of limited current present a quasi steady-state regime because of the transition of superconductor material to the normal state (quench). After the transition of superconductor material, its resistance becomes much higher than the resistance of the CuNi alloy (shunt resistor). Since the shunt is soldered throughout the whole superconducting coil length, the current flows almost completely through it after the quench.

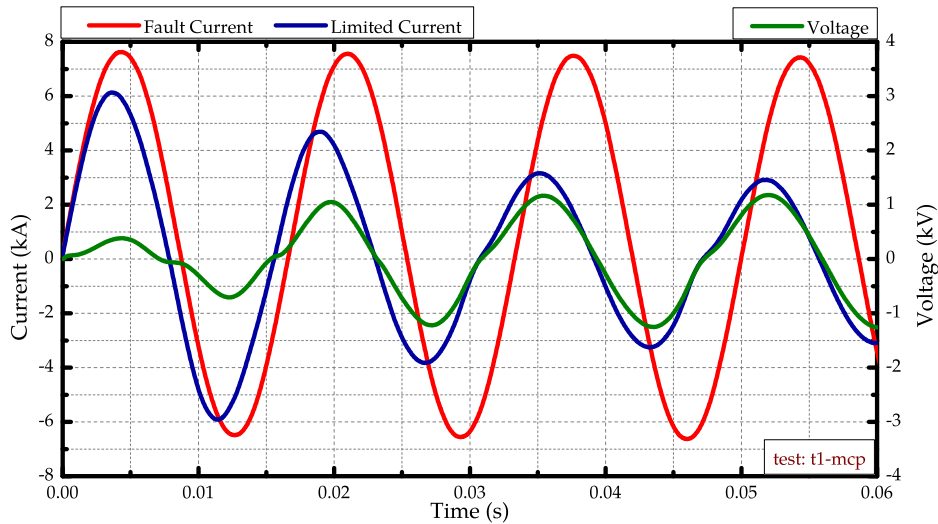


Figure 3.5: Comparison between fault and limited current for test t1-mcp with fault current = 5.0 kA_{rms} under 1.0 kV_{rms} and voltage drop over the SFCL terminals.

In the case of higher fault currents, faster transitions to the normal state can be observed. Figure 3.6 illustrates results of test t2-mcp where the quench is complete after the first current cycle. In this case the first current peak without the presence of the limiter was 38.24 kA_{peak} and it was limited to 10.03 kA_{peak} with the SFCL. The subsequent current peaks after the quench are about 3.6 kA_{peak} .

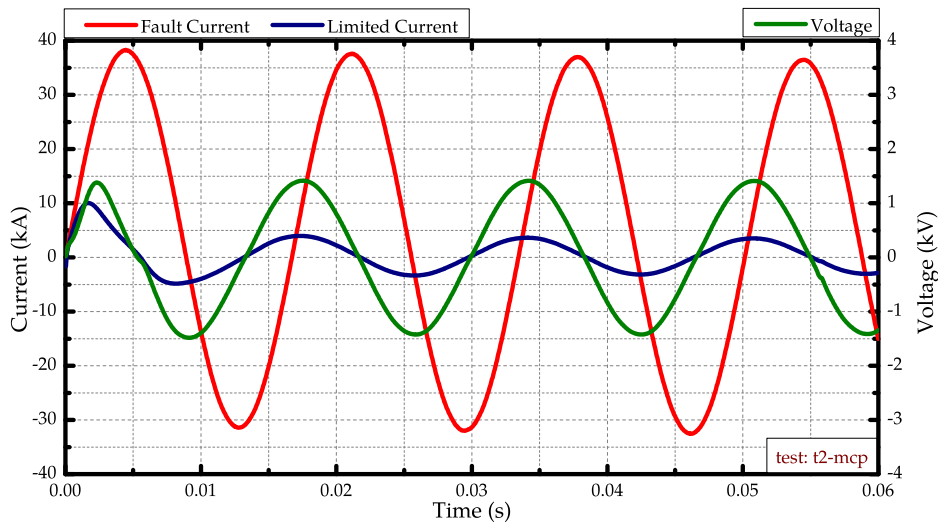


Figure 3.6: Comparison between fault and limited current for test t2-mcp with fault current = 25.0 kA_{rms} under 1.0 kV_{rms} and voltage drop over the SFCL terminals.

Figure 3.7 shows results of test t3-mcp. The first current peak without the MCP-BSCCO-2212 assembly of 98.8 kA_{peak} was limited to 11.0 kA_{peak} . Subsequent current peaks are about 3.15 kA_{peak} when the current attains a quasi steady-state regime.

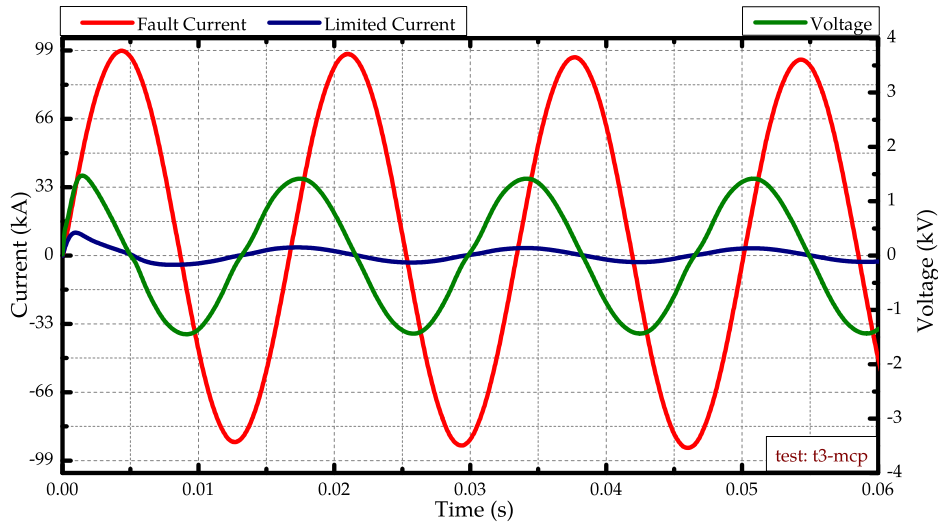


Figure 3.7: Comparison between fault and limited current for test t3-mcp with fault current = 67.0 kA_{rms} under 1.0 kV_{rms} and voltage drop over the SFCL terminals.

The limitation of the fault current by the MCP-BSCCO-2212 assembly becomes more efficient for high currents.

3.2.1.2 YBCO 2G Coil Tests

Figure 3.8 shows results of short circuit test t1-coil performed with the YBCO 2G Coil.

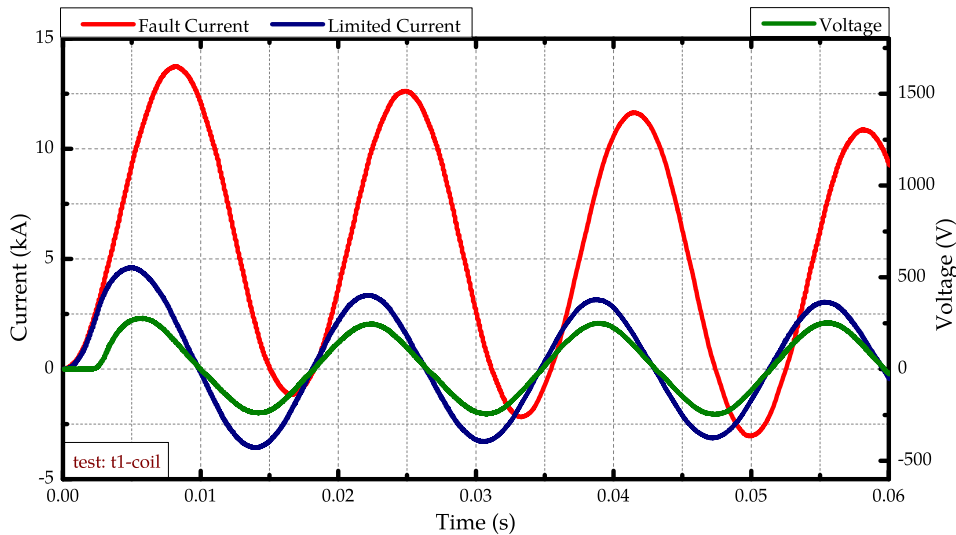


Figure 3.8: Comparison between fault and limited current for test t1-coil with fault current = 5.0 kA_{rms} under 200 V_{rms} and voltage drop over the SFCL terminals.

The first peak of the asymmetrical fault current of 13.7 kA_{peak} was limited to 4.6 kA_{peak} . Subsequent current peaks decreases smoothly to about 3.0 kA_{peak} . The voltage drop between the coil terminals is also observed.

Figure 3.9 shows results of short circuit test t2-coil. The first peak of the asymmetrical fault current of 53.5 kA_{peak} was limited to 4.6 kA_{peak} . Subsequent current peaks decreases smoothly to about 3.0 kA_{peak} .

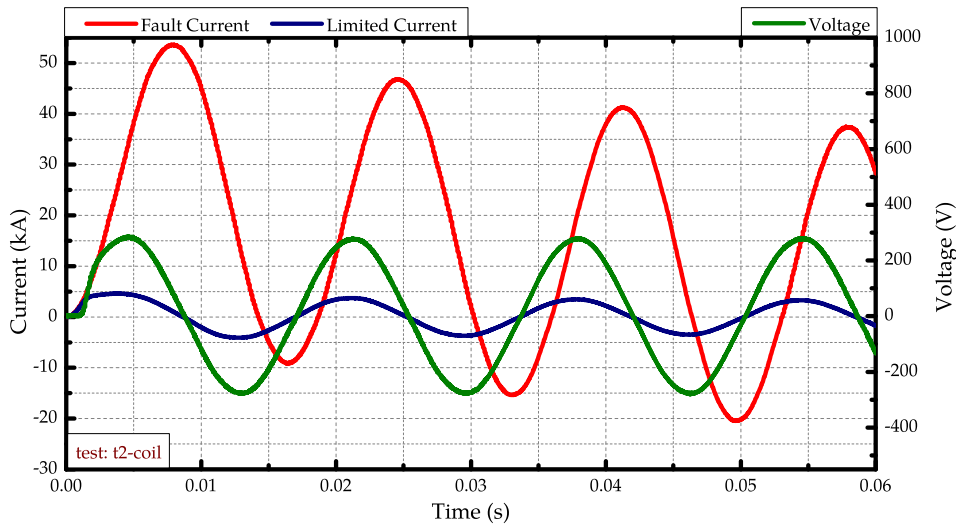


Figure 3.9: Comparison between fault and limited current for test t2-coil with fault current = 20 kA_{rms} under 200 V_{rms} and voltage drop over the SFCL terminals.

Finally, the fault current, limited current and voltage drop between the coil terminals of test t3-coil are shown in figure 3.10. The first peak of the asymmetrical fault current of 80.5 kA_{peak} was limited to 4.5 kA_{peak} . Subsequent current peaks also decreases smoothly to about 3.0 kA_{peak} .

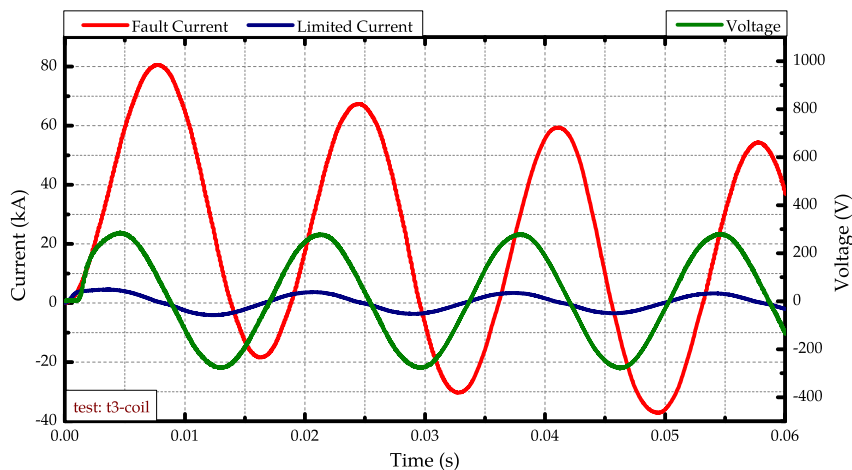


Figure 3.10: Comparison between fault and limited current for test t3-coil with fault current = 30 kA_{rms} under 200 V_{rms} and voltage drop over the SFCL terminals.

For all results of the YBCO 2G Coil tests, the quench is complete in the first half cycle of current. After the quench, resistance of the 2G tapes becomes higher than the shunt resistance (stainless steel tapes), therefore the current flows almost

completely in the shunt after quenching. The current flowing in the shunt heats it up. For this reason one observes smoothly decrease in all current peaks after the quench of the 2G tapes.

An important feature of the limitation behavior presented by the YBCO 2G coil is the waveform of the limited current. In the three carried out tests the fault current had an asymmetrical waveform (inductive circuit) coming from the ratio X/R , where R and X are respectively the resistance and reactance of the system. By connecting the YBCO 2G coil in the system, its resistance rapidly increases, reducing the X/R ratio. That is why phase shift and asymmetry effects are not observed in the limited current. The symmetrical waveform of the limited current may avoid damaging circuit breakers. This is a typical behavior of R-SFCL.

3.2.1.3 Air Coil SFCL Tests

Figure 3.11 shows results of short circuit test t1-acsfcl performed with the Air Coil SFCL. The peak of current was limited from $651 A_{peak}$ to $618 A_{peak}$ in the first half cycle and from $652 A_{peak}$ to $603 A_{peak}$ in the second half cycle. In the third and fourth half cycle the limitation remains the same as in the second half cycle. One does not observe a high limitation in this case, since the peak of fault current is just about two times the critical current value. Furthermore one also observes distortions on the voltage curve, suggesting that the quench may not have occurred in such test.

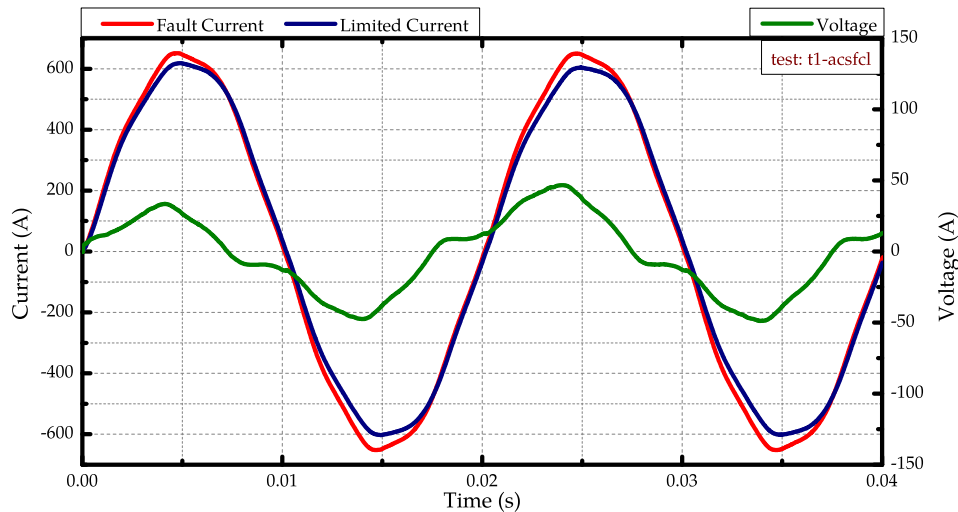


Figure 3.11: Comparison between fault and limited current for test t1-acsfcl with fault current = $450 A_{rms}$ under $400 V_{rms}$ and voltage drop over the SFCL terminals.

Observing results of test t2-acsfcl (shown in figure 3.12), one notes smaller distortions on the voltage curve, indicating once again that the quench may not have occurred. In the same test, the current peak was limited from $1.5 kA_{peak}$ to

1.28 kA_{peak} in the first half cycle and from 1.52 kA_{peak} to 1.2 kA_{peak} in the second half cycle. In the third and fourth half cycle the limitation remains the same as in the second half cycle.

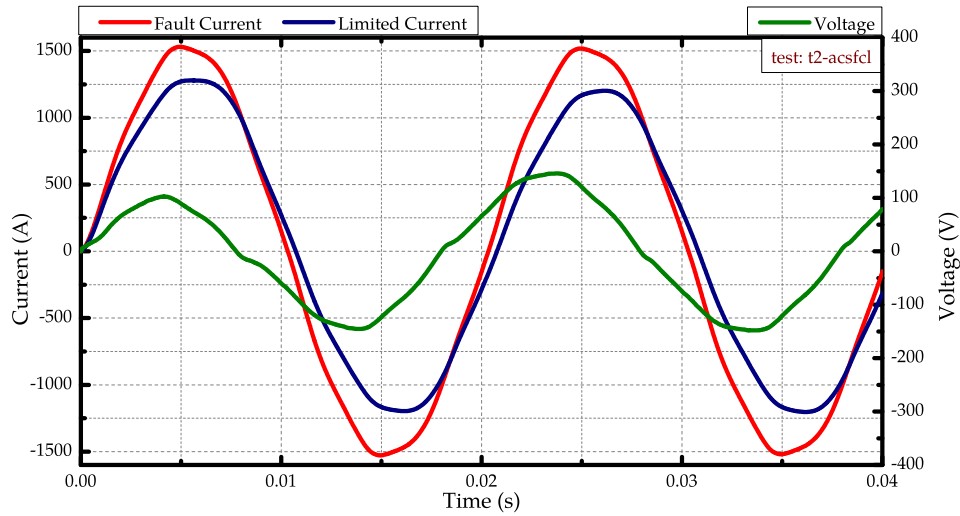


Figure 3.12: Comparison between fault and limited current for test t2-acsfcl with fault current = 1.05 kA_{rms} under 400 V_{rms} and voltage drop over the SFCL terminals.

In the case of test t3-acsfcl the peak of fault current was limited from 3.6 kA_{peak} to 2.4 kA_{peak} in the first half cycle and from 3.5 kA_{peak} to 2.0 kA_{peak} in the second half cycle, as shown in figure 3.13. Limitations remains approximately the same as in the second half cycle for the subsequent current peaks.

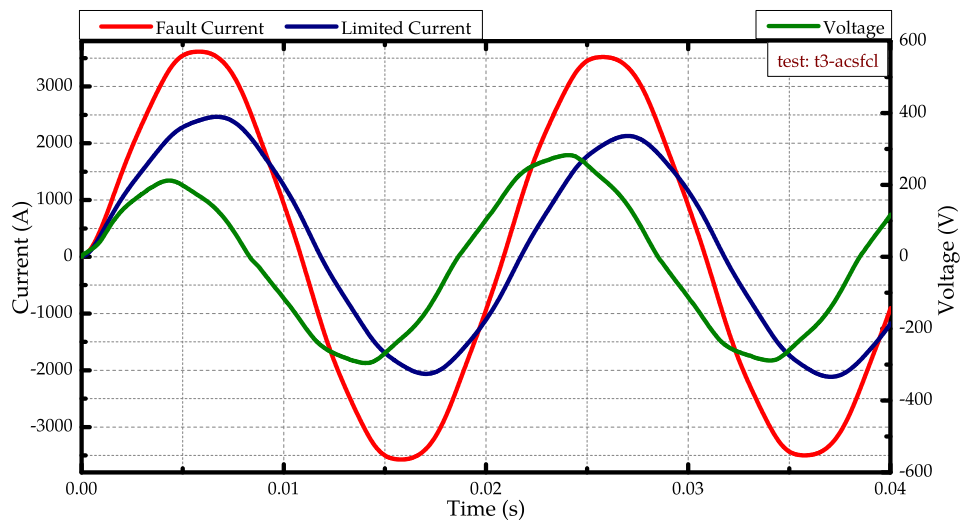


Figure 3.13: Comparison between fault and limited current for test t3-acsfcl with fault current = 2.55 kA_{rms} under 400 V_{rms} and voltage drop over the SFCL terminals.

In all results of the Air Coil SFCL tests, voltage drop curves show a phase shift in relation to the current curves, indicating a mainly inductive current limitation.

3.3 Inhomogeneity Representation

A HTS element is never strictly homogeneous over its full length. Even a HTS material produced by an ideal production process may present variations of the critical current value I_c along the length (inhomogeneity) [71]. Macroscopic defects can lead to local decrease of I_c . These defects may emerge because of several factors, such as processing effects on the material, as well as handling and storage conditions. The consequences of such inhomogeneities are of prime importance and must be studied with great care, since they can generate hot-spots in the superconducting material, or even, lead a small region of the HTS material to quench. The previous quench of just a small part of the superconducting material might result in an unwanted intervention of the limiter or in permanent damages of the device, as already described in section 2.2.1. Furthermore, conductor cost increases with the requirements in terms of homogeneities [72].

The inhomogeneities of HTS materials may be modeled by a Gaussian distribution, which is function of the average critical current I_{cm} and the standard deviation σ , as proposed in [20, 73, 74]:

$$P(I_c, \sigma, I_{cm}) = \frac{1}{\sigma\sqrt{2\pi}} e^{-\frac{I_c - I_{cm}}{2\sigma^2}} \quad (3.1)$$

where $P(I_c, \sigma, I_{cm})$ denotes the probability, to find the critical current I_c along the tape length.

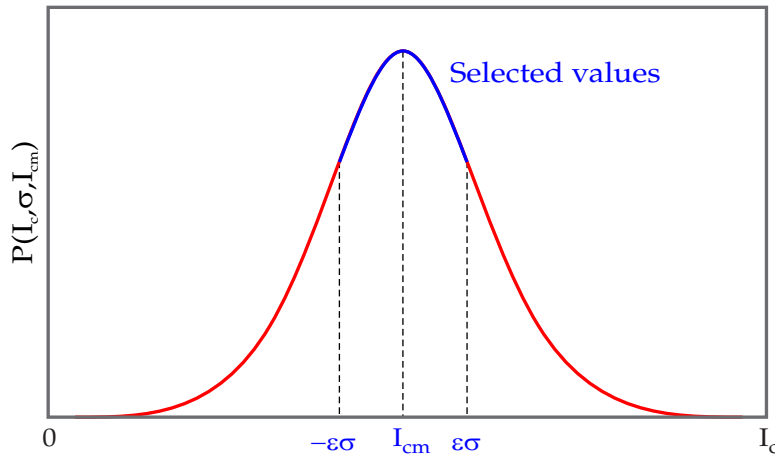


Figure 3.14: Sketch of critical current inhomogeneity distribution. The Gaussian distribution P has an average critical current I_{cm} with standard deviation σ .

Using equation (3.1), different values of critical current I_c between $-\epsilon\sigma$ and $\epsilon\sigma$ have been generated. The ϵ value was adapted in order to select I_c values with high probability to be found along length, as shown in figure 3.14. Afterward, I_c values were distributed through a random permutation along the length of the

tapes of the AC-SFCL and of the YBCO 2G Coil SFCL and along the length of modules composing the MCP-BSCCO-2212 assembly. The random permutation is done in such way that different I_c values can be found at each 1.0 cm length.

In the next sections, average critical current I_{cm} and standard deviation σ values are presented, as well as the final distribution of the I_c for each tape and module of each limiter to be simulated.

3.3.1 I_c Distribution for the MCP-BSCCO-2212 Assembly

The critical current value I_c of each component of the MCP-BSCCO-2212 assembly was measured at the Superconductivity Laboratory of the Electric Power Research Center, in Brazil.

Critical current I_c values were obtained by a voltage-current measurements (VxI curve) by using the four points method and the $1 \mu\text{V}/\text{cm}$ criteria. A DC current source and a digital multimeter were used. Thus, obtained VxI curves were corrected by subtracting the voltage signal of all contact resistances introduced by electric connections like clamps and cable connections. Measured data agree well with nominal I_c values provided by the manufacturer. Results are shown in figures A.1, A.2 and A.3 (Appendix A, section A.1). Table 3.4 lists I_c values obtained for each MCP-BSCCO-2212 module.

Table 3.4: Measured critical current values of the MCP-BSCCO-2212 modules.

Module	I_c (A)	Module	I_c (A)
01	515	07	533
02	515	08	518
03	525	09	530
04	530	10	531
05	535	11	529
06	532	12	506

According to [22] and [53], one can have deviations of about $\pm 5\%$ on the critical current values for each MCP-BSCCO-2212 module. Therefore the value $\epsilon = 0.5$ have been chosen for these distributions. Figure 3.15 illustrates the superconducting layer of each component with its respective distribution of critical current values.

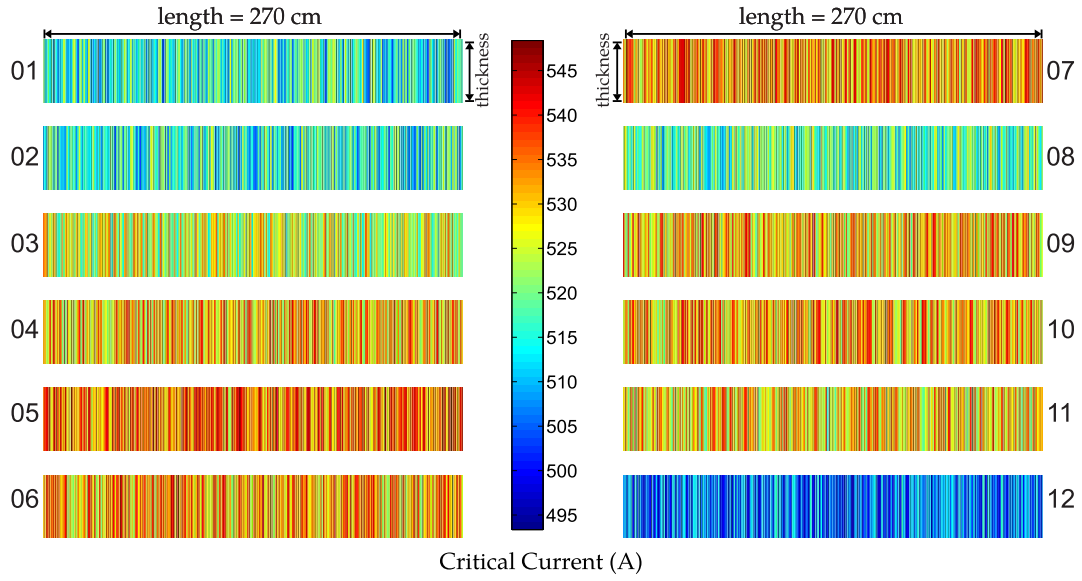


Figure 3.15: Critical current distribution for each module. The directions x (length) and y (thickness) are out of scale. Only the superconducting layers are shown.

3.3.2 I_c Distribution for the YBCO 2G Coil

Table 3.5 presents I_c values of the YBCO 2G coil. These values were provided by the manufacturer. Such limiter is constituted by two branches of four tapes in parallel connection (as shown in figure 3.1b).

Table 3.5: Measured critical current values of the YBCO 2G coil.

Tape	I_c (A)	Tape	I_c (A)
01	310	05	302
02	295	06	287
03	305	07	292
04	307	08	297

Figure 3.16 illustrates the superconducting layer of each tape of the YBCO 2G coil with its respective distribution of critical current values. According to [73] and [20], 2G tapes SF12100 may present a standard deviation of 6.59% in the values of critical current and once more the value $\epsilon = 0.5$ has been chosen for these distributions.

3.3.3 I_c Distribution for the Air Coil SFCL

The critical current values of each tape of the Air Coil SFCL were measured at the Institute for Technical Physics (ITEP) of the Karlsruhe Institute of Technology

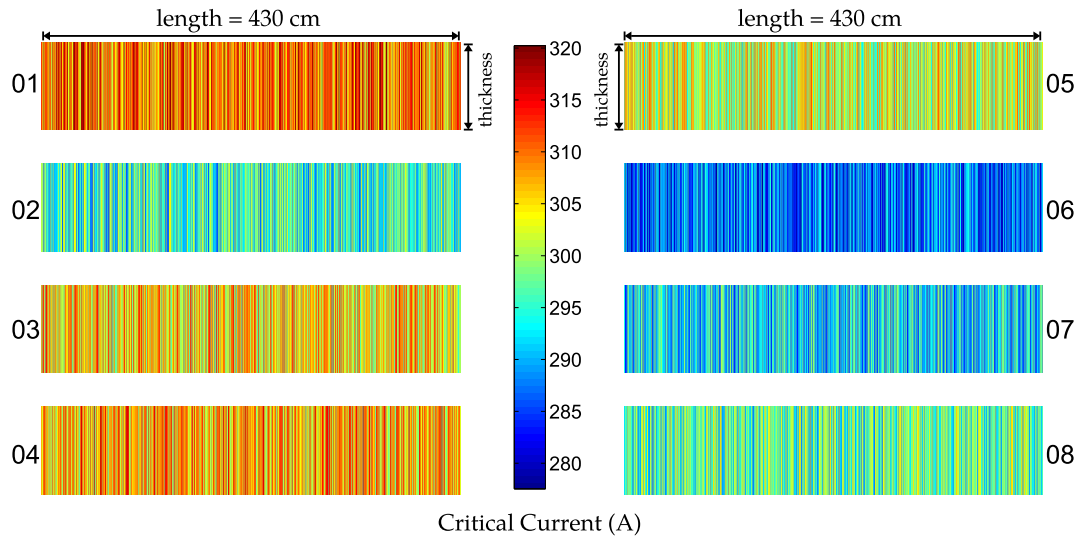


Figure 3.16: Critical current distribution for each tape of the YBCO 2G SFCL (*SuperPower SF12100* tapes). The directions x (length) and y (thickness) are out of scale. Only the superconducting layers are shown.

(KIT), in Germany.

As in the case of the MCP-BSCCO-2212 components, I_c values were determined by voltage-current measurements. The tapes were connected to a DC current source, that provides growing current pulses. As shown in figure 3.17, each tape was divided into ten equal sections. For each current pulse, one tracks ten voltage drops along the tape length by means of a nanovoltmeter. In that way, ten different values of I_c for a single tape can be determined. Further details about the measurement system can be found in [75, 76]. Graphs with measurements results are shown in section A.2 of appendix A.

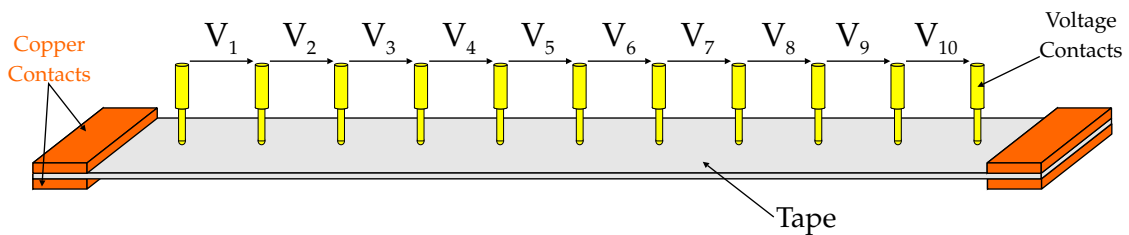


Figure 3.17: Simplified measurement system to determine I_c values along the length of the 22 tapes of the Air Coil SFCL.

With experimental values of I_c for each tape, it is possible to determine an average value I_{cm} and the standard deviation σ for each tape. Table 3.6 is based on graphs A.4-A.9 and table A.1 (see appendix A, section A.2). Values of σ have been obtained by means of equation (3.2).

$$\sigma_{tape} = \sqrt{\frac{1}{10} \sum_{i=1}^{10} (I_{c,i} - I_{cm,tape})^2} \quad (3.2)$$

Table 3.6: Measured critical current values of the Air Coil SFCL.

Tape	I_{cm}	σ (A)	Tape	I_{cm}	σ (A)	Tape	I_{cm}	σ (A)
01	379.0	0.9	09	359.7	1.6	17	267.1	2.8
02	342.9	4.6	10	354.0	1.8	18	265.8	2.6
03	358.8	1.2	11	362.8	1.7	19	350.0	2.8
04	351.6	2.2	12	372.7	2.5	20	353.3	2.5
05	267.5	1.9	13	362.8	2.7	21	343.6	2.8
06	265.8	2.5	14	358.1	4.0	22	348.3	3.0
07	272.3	2.2	15	351.7	4.7			
08	356.3	3.0	16	263.5	3.2			

Based on the σ values listed in table 3.6, the value $\epsilon = 1.5$ have been chosen in order to select the most probable values of critical current. Figure 3.18 illustrates the superconducting layer of each tape of the Air Coil SFCL with its respective distribution of critical current values.

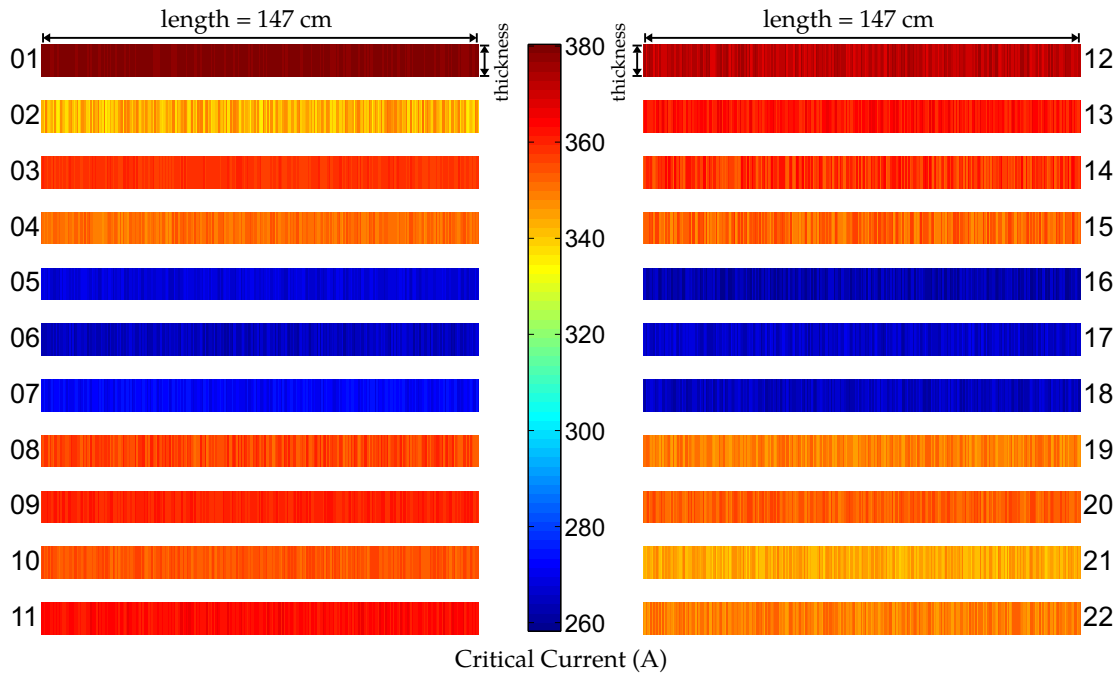


Figure 3.18: Critical current distribution for each tape of the Air Coil SFCL (*SuperPower SCS12050* tapes). The directions x (length) and y (thickness) are out of scale. Only the superconducting layers are shown.

Chapter 4

Introductory Models

The way in which a superconducting fault current limiter works makes prediction of its behavior quite complex due to the number of variables which can change during the fault period. In particular, since a large proportion of the supply power is absorbed by the superconductor material during limiting, there will be a significant amount of heating in the superconductor. This chapter presents an introduction to elementary concepts for developing models describing the transient behavior of SFCL devices. The presented models will clarify the main aspects of simulations and introduce the first methodologies. Furthermore a brief review about SFCL modeling is presented.

4.1 Introduction

The research and development progress with the use of superconductor materials has already shown its technical feasibility for the commercial deployment of SFCL devices. For the further commercialization of these devices many simulations models have been developed, in order to optimize the design of SFCL for applications and to study the limiters integration in the network. It is of utmost importance to control the physical properties of the superconducting structures in real scenarios operating at different voltage rates and fault levels. The process of quenching is not easy to model as it takes the superconductor through transient states with high electric fields where it is impossible to measure their local physical properties. Nevertheless, some theoretical assumptions can be made in order to understand and predict some relevant features for the operating a SFCL. The following sections analyze which simulation tools have been proposed to study and optimize SFCL devices.

4.2 Time Dependent Model

The behavior of a SFCL device must be modeled as a nonlinear resistance because of the sharp changes on the resistivity of the superconducting material during the fault transient. All models to be presented in this work are nonlinear. There are many ways to describe a nonlinear resistance. The simplest one represents a SFCL as a time dependent resistance which start to increase exponentially at the moment of fault occurrence, as shown in equation 4.1 and figure 4.1.

$$R_{sfcl} = \begin{cases} 0 \ \Omega, & \text{for } t < t_1 \\ cte [1 - e^{-q(t-t_1)}], & \text{for } t > t_1 \end{cases} \quad (4.1)$$

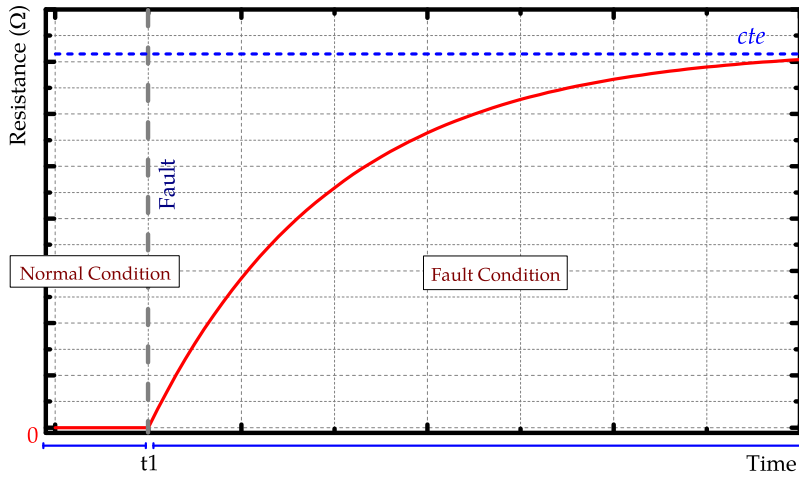


Figure 4.1: Time dependency variation of the SFCL resistance.

In equation 4.1, the parameters cte and q are constants; q defines how fast the resistance increases to an approximated value cte . Normally, one defines the cte value as the resistance value R_{RT} of the device at room temperature, that is, the equivalent resistance of the SFCL device when the superconducting material is in the normal state. Constant q may be extracted from experimental results by analyzing the limited current curve; when it reaches a steady state one may assume that the quench is complete and most of the current no longer flows in the superconductor material. In that way, equation 4.1 should sketch a transient behavior of a SFCL device under fault conditions.

In order to investigate the model efficiency, test t1-acsfcl¹ carried out with the AC-SCFL has been chosen. One assumes different values for q , in order to compare simulations with experimental data. The value of cte was extracted from [68, 69] ($cte = 0.726\Omega$).

¹Fault current = 450 A_{rms} under 400 V_{rms}

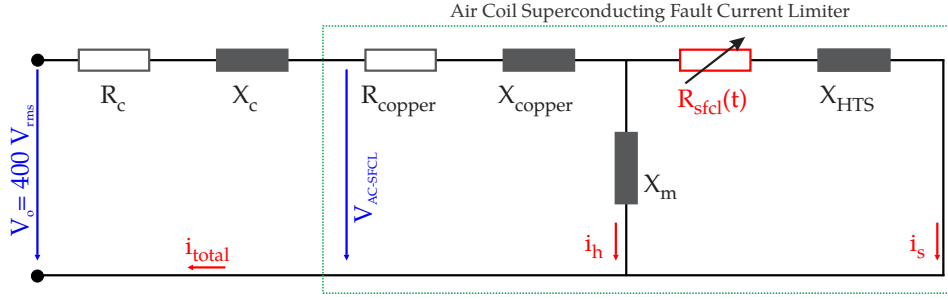


Figure 4.2: Equivalent circuit diagram of the Air Coil SFCL.

Figure 4.2 illustrates the equivalent circuit diagram of the AC-SFCL connected to the equivalent circuit diagram of the measurement setup. The following system of differential equations must be solved to obtain the limitation behavior:

$$\begin{bmatrix} \dot{i}_s \\ \dot{i}_h \end{bmatrix} = \begin{bmatrix} L_c + L_{cu} + L_{Sec} & L_c + L_{cu} \\ L_c + L_{cu} & L_c + L_{cu} + L_m \end{bmatrix}^{-1} \left\{ V_o \begin{bmatrix} 1 \\ 1 \end{bmatrix} - \begin{bmatrix} R_c + R_{cu} + R_{sfcl}(t) & R_c + R_{cu} \\ R_c + R_{cu} & R_c + R_{cu} \end{bmatrix} \begin{bmatrix} i_s \\ i_h \end{bmatrix} \right\} \quad (4.2)$$

Here, i_s represents the current in the secondary coil of the transformer and i_h represents the excitation current, required to produce the resultant mutual flux in a transformer. These differential equations are solved numerically by means of classical Runge-Kutta fourth-order method (RK4) [77]. A schematic diagram of such simulation model is presented in figure 4.3.

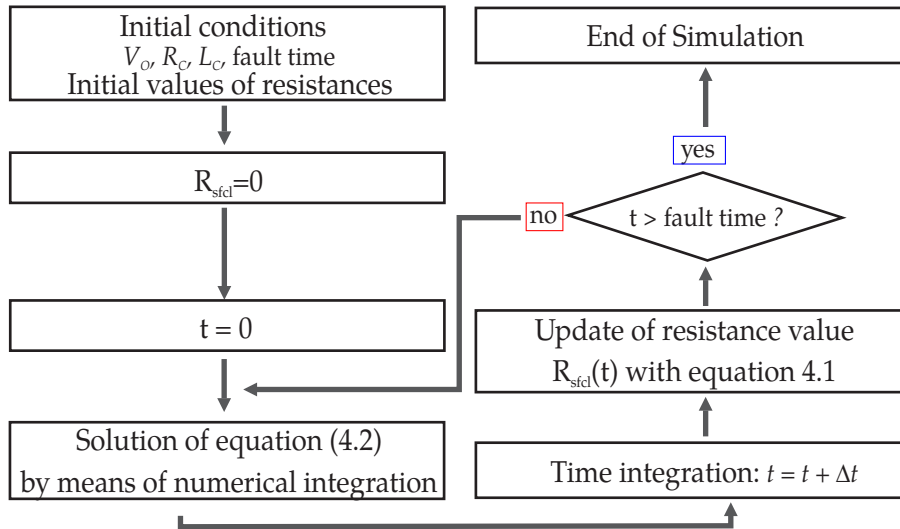


Figure 4.3: Schematic diagram of the time dependent simulation model.

The process illustrated in figure 4.3 does not require high computational effort to be performed and therefore it runs fast. One must only concern about the timestep Δt used in the Runge-Kutta method.

This model however presents some drawbacks. One of them is that in such approach the SFCL does not react to fault currents automatically; it must be programmed to enter the resistive state at a specific time in a simulation. This is inconvenient besides driving into uncertainty concerning how to precisely define when the quenching should be initiated relative to the inception of the fault, for each phase. If the type of fault or the fault impedance is changed, the SFCL model must be reconfigured.

Another important drawback is the accuracy of the simulated results. As shown in figure 4.4a, simulated results for limited current are close to the measurements but results for the voltage drop over the device terminals do not match with the measured values (figure 4.4b). It comes from the assumption that the final value of the resistance is equal to the equivalent resistance R_{RT} of the SFCL at room temperature, i.e., one assumes that a complete quench takes place. As will be demonstrated in forthcoming chapters, this may not be completely true.

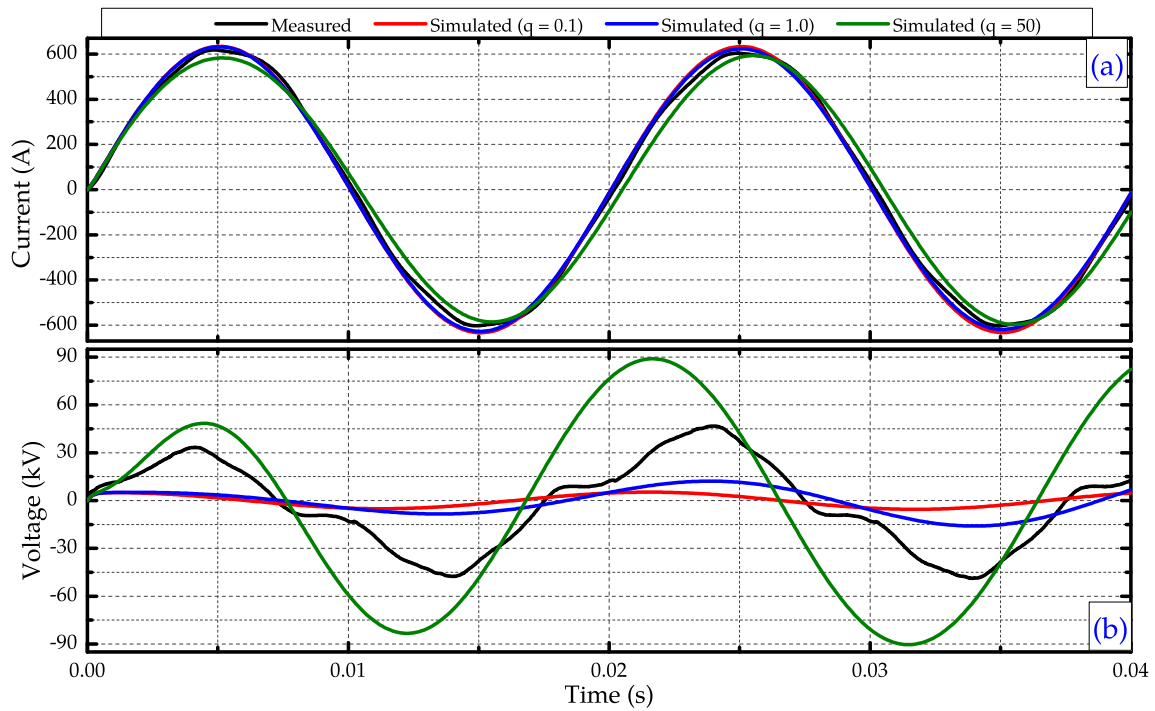


Figure 4.4: Time Dependent Model results: comparison between measured and simulated results of (a) limited current of the circuit and (b) voltage drop over the AC-SFCL device for test t1-acsfcl with fault current = $450 A_{rms}$ under $400 V_{rms}$.

In addition, this model requires informations from performed tests to be used. It means this model may be able to reproduce a transient behavior of a SFCL device and not to predict it. In addition, the time dependent model does not provide any information about heating of the materials composing the limiting device either.

In order to correctly predict the simulated transient behavior, one must consider the E-J characteristics of the HTS material during the fault current period.

4.3 Two Branches Model

The two branches model considers two resistances in parallel connection. One of the resistances is the equivalent resistance R_{RT} . The another one is the HTS material, which is modeled according to the E-J characteristics, shown in figure 4.5. By means of E-J curve, one can obtain the resistivity ρ of the superconducting material just by dividing E by J ($\rho = E/J$). Hence, a HTS material of length ℓ and cross section area a , has a resistance equal to:

$$R_{HTS} = \rho \frac{\ell_{hts}}{a_{hts}} \quad (4.3)$$

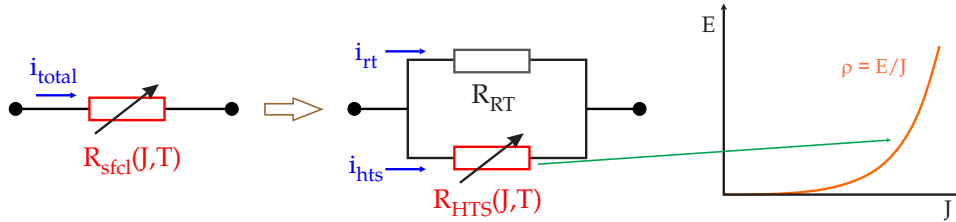


Figure 4.5: Two branches model describes the SFCL by means of a parallel connection between the HTS material and a constant resistance. The EJ characteristics was introduced in section 2.1.3.1.

Since the resistivity of the HTS material is dependent on electrical current, at each timestep the current flowing in it must be calculated. That can be made by means of the current divider rule, i.e., a general formula for the current in a resistor that is in parallel with a combination of other resistors [78]. Thus, equations 4.4 and 4.5 calculate the current flowing in each resistor shown in figure 4.5.

$$i_{rt} = \frac{R_{sfcl}}{R_{RT}} i_{tot} \quad (4.4)$$

$$i_{hts} = \frac{R_{sfcl}}{R_{HTS}} i_{tot} \quad (4.5)$$

Parameter i_{tot} denotes the total current entering the combined network of R_{RT} in parallel with R_{HTS} and R_{sfcl} denotes the equivalent value between both resistances.

The critical current density $J_c(T)$ is dependent on temperature therefore the E-J curve is also temperature dependent, as show in figure 2.9c. Hence at each timestep the temperature of the superconducting material must also be updated. At first instance, one can consider an adiabatic case, where there is no heat exchange with the surrounding environment. In that way, the temperature rise can

be calculated as:

$$V \gamma \varsigma \frac{dT_{HTS}}{dt} = R_{HTS} i_{hts}^2 \quad (4.6)$$

where, γ is the volumetric density (kg/m^3), ς denotes the specific heat ($\text{J}/\text{kg}\cdot\text{K}$), V is volume, R_{HTS} is the electric resistance and i_{hts} is the current flowing in the HTS material. Equation 4.6 can be solved numerically by means of explicit Euler method [77].

The dependence on temperature of the critical current density $J_c(T)$ must also be taken into account. It is possible to find in literature numerous equations representing the dependence on temperature of the critical current. However, in this work a linear dependence has been adopted (equation 4.7), since the SFCL devices studied in the present work operated above 77 K [31, 32].

$$J_c(T) = J_c(77) \left(\frac{T_c - T_{HTS}}{T_c - 77} \right) \quad (4.7)$$

As shown in figure 4.6, the insertion of a current dependent resistance (E-J power law) in the circuit of figure 4.2 changes the solution process for the equations of equivalent circuit shown in figure 4.3 (test t1-acsfcl is still adopted as case example).

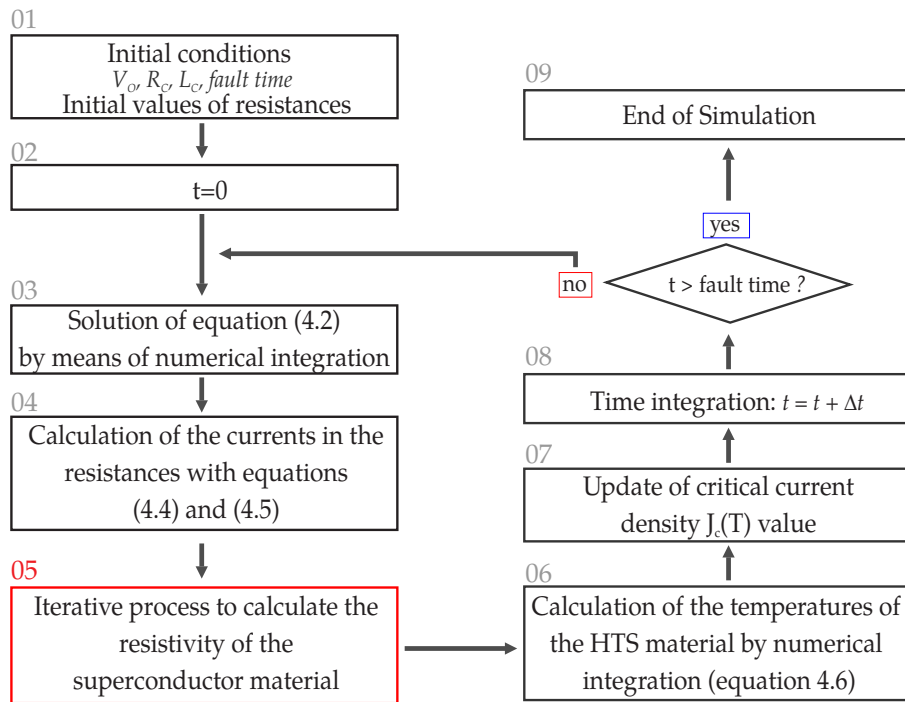


Figure 4.6: Schematic diagram of the two branches model. The red box (number 05) denotes the current-iterative process.

Due the high non-linearity of the superconductor material, solution of equation (4.2) may require very sophisticated numerical methods, since it becomes a

stiff problem². For example, in reference [38] the power law was employed and the implicit Trapezoidal Rule with the second order Backward Difference Formula integration scheme (TR-BDF2) [80] was necessary to deal with the stiff differential equations. Although the TR-BDF2 method ensures numerical stability of the solution, it may be very complicated to be implemented besides limiting the capabilities of further improvements in the simulation algorithm. For this reason a current-iterative process has been used. This method is fully detailed in figure 4.7.

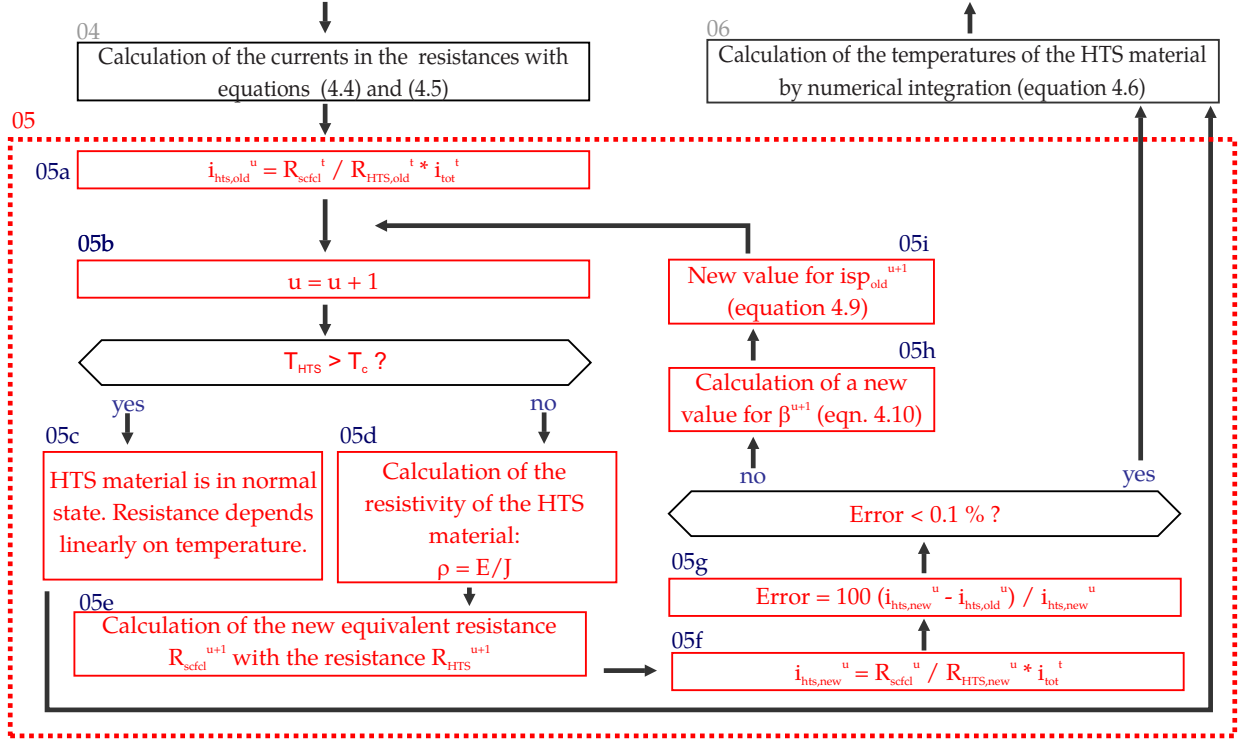


Figure 4.7: Schematic diagram of the current iteration method.

The current-iterative process starts at iteration $u = 1$ after calculating the current in each resistor of the SFCL component (box number 04). At this point, the current in the HTS material is assigned as $i_{hts,old}$ (box 05a). If the temperature of the superconductor material is above T_c , there is no dependency on current and the resistivity can be calculated as a normal conductor (box 05c). Conversely, if the temperature is lower than T_c the current dependency must be considered (box 05d). In this case the old value of current ($i_{hts,old}$) is used to calculate a new value of resistivity and resistance ($R_{HTS,new}$) of the superconductor material by means of equation 4.3. Having the new resistance value, one calculates a new value for the equivalent resistance R_{scfd} considering the parallel connection between $R_{HTS,new}$ and R_{RT} (box 05e).

²Stiff equations are problems for which the conventional explicit methods do not work, unless the step size is taken to be extremely small [79].

With the new values of $R_{HTS,new}$ and R_{scfcl} it is possible to calculate new value of current ($i_{hts,new}$) in the superconductor material (box 05f). This value will be compared with the old value $i_{hts,old}$ with an error equation defined as (box 05g):

$$ERROR^u = 100 \left[\frac{i_{hts,new}^u - i_{hts,old}^u}{i_{hts,new}^u} \right] \quad (4.8)$$

If the calculated ERROR is lower than 0.1%, the simulation follow to the calculation of the temperature rise, solving numerically equation 4.6. In case of the calculated ERROR be higher than 0.1%, than the value of $i_{hts,old}$ must be adjusted to the next iteration ($u = u + 1$) (box 05i). The adjustment is done using equation 4.9:

$$i_{hts,old}^{u+1} = i_{hts,old}^u + \beta^{u+1}(i_{hts,new}^u - i_{hts,old}^u) \quad (4.9)$$

In equation 4.9, β^{u+1} is called adjustment factor. Such factor is also variable and depends on the previous value of the ERROR function. If $ERROR^{u-1}$ and $ERROR^u$ values present same signal, the adjustment is being done in the correct "direction" and a pre-defined value of β (defined by the user) can be raised by a δ amount. If that is not the case, then previous value of β must be kept (box 05h). Equation 4.10 shows the conditions for the adjustment of the β values.

$$\beta^{u+1} = \begin{cases} \beta^u + \delta, & \text{for } |ERROR^{u-1}| > 0 \text{ and } |ERROR^u| > 0 \\ \beta^u, & \text{for } otherwise \end{cases} \quad (4.10)$$

Normally, values of the pre-defined β lies between 0.01 and 0.5, whereas values of δ lies between 0.01 and 0.1. Such values can be adjusted in order to obtain smaller times of simulation and fast convergence in the current iteration loop.

The presented current iterative process is continued until the changes between $i_{hts,old}$ and $i_{hts,new}$ drop below a pre-set error criterion (0.1%). Such process is also fully detailed in [29, 81, 82].

It is worth noting that the two branches model automatically reacts to fault currents, i.e, the quench process is triggered by the increase of the current over I_c .

4.3.1 Results of Case Example

Figure 4.8 compares measured data with simulated ones for test t1-acsfcl with the Air Coil SFCL. As those ones simulated by the time dependent model, results of the two branches model gives a good approximation for the limited current (figure 4.8a).

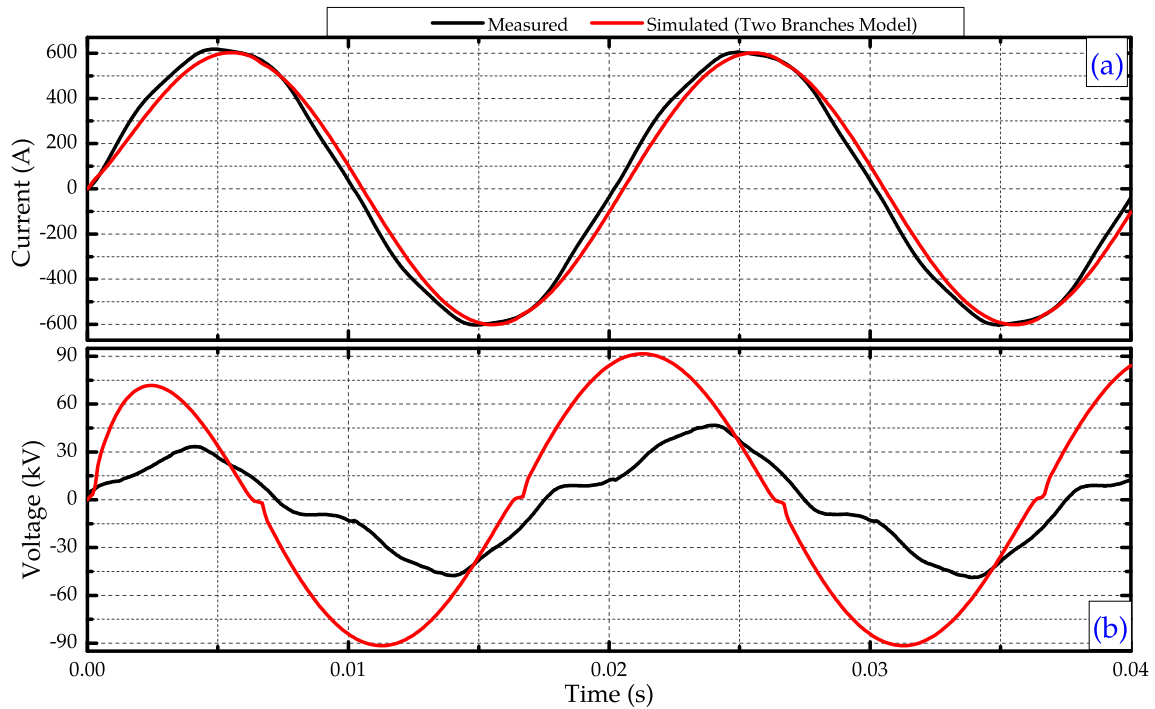


Figure 4.8: Two Branches Model results: comparison between measured and simulated results of (a) limited current of the circuit and (b) voltage drop over the AC-SCFCL device for test t1-acsfcl with fault current = $450 A_{rms}$ under $400 V_{rms}$.

Simulated results for the voltage drop over the AC-SCFCL terminals does not match, as show in figure 4.8b. It can be observed that simulated data reaches values up to almost twice the measured ones. Such erroneous result comes from the resistance modeling of the SFCL device. As shown in figure 4.9 its resistance is highly nonlinear during the fault period. Although the E-J curve has already been included, the thermal model should still be improved.

Figure 4.9 also shows the temperature rise of the HTS material during the fault period. It reaches 81 K at the end of the fault period, that is, the quench does not take place in this case ($T_c = 92$ K). However, in this case only the heating of the HTS material has been calculated. The heat transfer of the HTS material with the adjacent layers as well as the heat exchanges with the surrounding environment (LN_2 cooling bath) must also be taken into account in order to improve the simulation model.

4.3.1.1 First Discussions

Based on the results of figures 4.4, 4.8 and 4.9 it is clear that the presented models (time dependent model and two branches model) may not be suitable to properly simulate the transient behavior of a SFCL device.

The time dependent model may provide reasonable simulation results being useful for a first approximation. It runs very fast (≈ 2 s), since it does not require

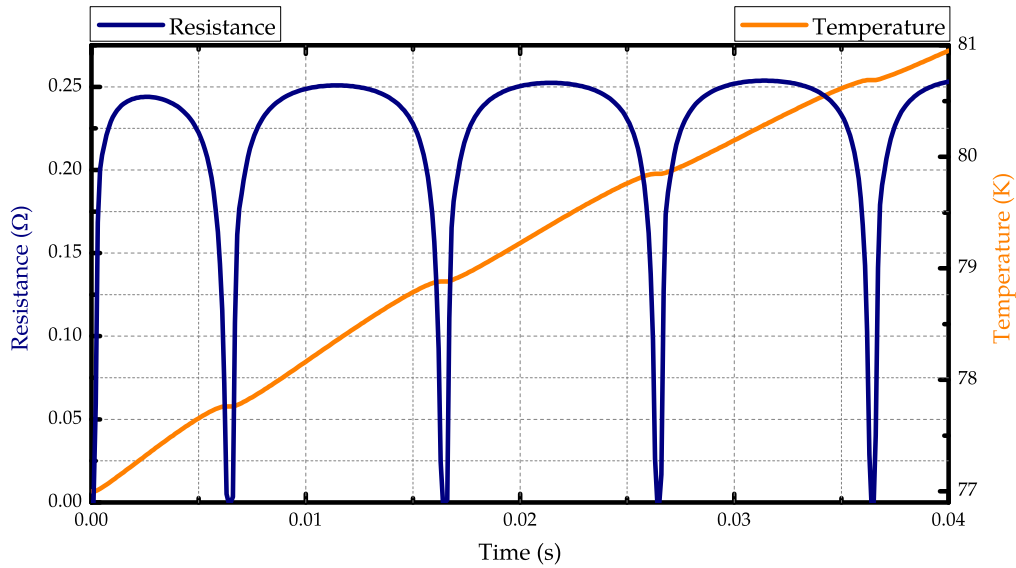


Figure 4.9: Two Branches Model results: Resistance and Temperature rise during the transient of fault current for test t1-acsfcl with fault current = $450 A_{rms}$ under $400 V_{rms}$.

high computational effort, besides having a easy simulation algorithm (see figure 4.3). However, this model works if (and only if) one knows exactly values of the constant parameters cte and q . As already mentioned, these values can be obtained by means of analyzing tests results in laboratory.

The time dependent model may also be performed by different time functions: linear, polynomial, composite, power, logarithm and so on. Nevertheless there will be always constant parameters that must be extracted from experimental tests in order to run the simulation. In that way one may conclude that such model might be suitable to reproduce experimental tests and not to predict the transient behavior.

The two branches model is a more sophisticated method that automatically reacts to fault currents by means of the E-J curve, resulting in the high non linearity of the HTS material resistance. In order to deal with the stiff equations created by insertion of the E-J curve, this method requires a current iterative process, thus resulting in longer algorithm sequence (see figures 4.6 and 4.7) if compared with that of the time dependent model.

The inclusion of the E-J curve in the simulation model is not enough to simulate the SFCL transient behavior, as shown in figure 4.8. The thermal transient analysis of the SFCL device should also be improved in order to enhance simulated results. In the next chapters, different methodologies concerning improvement of the thermal transient model will be introduced. Forthcoming models however will inherit the proposed current iterative process, in order to be possible to deal with stiffness of the differential equations. The current iterative process enables

the capabilities of further simulation improvements.

In the next section a short literature review focusing in simulations of superconducting fault current limiters will be presented.

4.4 SFCL Modeling - Brief Review

In spite of the recent advances achieved with superconducting fault current limiters, modeling and simulation of such devices are still important issues. There are different approaches for modeling SFCL, whereas computational simulations provide a better understanding of the behavior of such devices. In addition, results of hard experimental access may be achieved by means of computational simulation.

Accurate analytical calculations are difficult, if not impossible, to solve and this has required development of computer simulations [83]. The main goal of such studies is the further development of tools for simulating full size SFCLs.

As shown in section 4.2, simplified approaches as the time dependent model are possible and have been published in [84–88] for stability studies purposes, but it is still necessary to include as many effects as possible if the computer solutions are to compare with experimental data.

Improved models (similar to the two branches model one) have been published in order to obtain a better understanding of SFCL devices during the transient of fault [26, 31, 32, 89–93]. Into this framework, most models have been developed customarily by simulation packages such as: ATP/EMTP [31, 93–96], PSCAD/EMTDC [47, 97–99], MATLAB/Simulink [38, 73, 100–102], PsPice [103] and Wolfram Mathematica [104]. Despite providing satisfactory results in some cases, such models may fail if one desires a deep investigation of the SFCL dynamics. For example, it is not possible to obtain correct values of temperature rise in each component of a SFCL if one uses the two branches model (or similar ones). This requires taking into account all existing heat transfer phenomena during the fault period.

The insertion of the heat transfer effects in the simulation model makes solution processes even harder to be solved since electrical and thermal equations becomes coupled to each other. Hence softwares with advanced features for thermal transient analysis have been employed. For dealing with 2D and 3D symmetries, numerical modeling of SFCL based on finite element methods (FEM) has been more extensively used due to the availability of commercial computational packages [25, 105–110].

The FEM model has shown to be a powerful tool for simulations of SFCL not only due to the possibility of studying thermal transient problems but also for

electromagnetic analysis. FEM softwares are capable to use different mathematical formulations for solving the Maxwell equations. Most of the 2D and 3D analysis performed by FEM are based on current vector potentials [111–113].

Usually the models can be enclosed in a single framework regarding the mathematical formulation for solving the Maxwell equations, that is, the so called H -formulation. In this case, the partial differential equations system defined by the classical Maxwell equations are solved by imposing boundary conditions for the expected pattern of magnetic field H at some regions of the space. This method, although very powerful, does not allow to ensure a unique solution for large scale nonlinear systems. It creates major difficulties to assure that all the physical phenomena inside of the superconducting material are being properly described when the boundary conditions for H are usually imposed far away of the material. However, for 2D systems with J constrained to flow in only one direction, reliable solutions for the electromagnetic problem can be achieved, whilst the heat transfer problem is solved via the transient conduction equation [109, 114–116]. FEM models have also taken a leader role for evaluating AC losses in SFCL devices [117–122].

The most common packages used for simulations of SFCL by means of FEM models are: FLUX2D [123], COMSOL [20, 124], FEMLAB [125] and ANSYS [126].

In summary, models based on FEM methods offer a more accurate (and local) description of the superconducting effects, but they usually require high computational effort, being more suitable for simulating short length tapes. Moreover, the interface of FEM models with other conventional circuit elements (transformers, non-linear inductors, generators, etc) is complicated [20]. Furthermore, due to the time consuming process of implementing such model, the specialized software which is needed, and the relatively long simulation times, this approach is not suitable for power system simulation studies.

Even non traditional methods have been utilized for simulations of SFCL. Due to the complexity and great dependency on the properties as type and size of the devices and also physical properties of the HTS materials, simulations based on modular neural networks using a constructive multilayer neural network have been proposed [127]. One drawback of the method is that the criterion of adding new neurons must be determined carefully so that neither the number of neurons overgrow, nor the speed of learning process reduces. Furthermore, the model must be trained with suitable data. Obtaining data may be difficult, and the neural networks may have to be re-trained for different parameters, for example, for different values of superconductor length. These models are thereby impractical for power system studies.

The methods presented in this chapter are the basis concerning the SFCL mod-

eling. In the next chapters two different simulation models will be presented; both concerns about heat exchanges existing during the transient period. Electromagnetic analysis will be put aside, since the magnetic field influence in the superconducting properties of the studied SFCL devices may be neglected [46].

Chapter 5

Thermal-electrical Analogy Method

This chapter introduces a simple computational model to predict electrical and thermal behaviors of SFCL devices. Its main contribution is the use of a thermal-electrical analogy to solve heat transfer equations inside the layers of the SFCL, which enables one to handle with relative ease the strong and nonlinear coupling between thermal and electrical phenomena. The most important features of this chapter have been already published in [128].

5.1 Introduction

The basic aspects of simulation models have been introduced in chapter 4. As has been shown, heat exchanges existing during the transient period play a fundamental role on the SFCLs modeling.

The aim of this chapter is to present a simple computational model to predict electrical and thermal behaviors of SFCL devices. For the heat transfer analysis, it is assumed one-dimensional transient heat conduction across each layer of the tapes and modules. For the electric circuit analysis, the SFCL devices are modeled as variable nonlinear resistances, whose magnitude depends on the temperature of the superconductor layer. This temperature is in turn obtained from the solution of the heat transfer equations subjected to internal heat generation and to appropriate boundary and initial conditions.

The main contribution and innovative aspect of this model is related to the use of a thermal-electrical analogy to solve heat transfer equations for each layer of the SFCL device. There is a lack of published papers employing this method to simulating SCFCL devices, though some works employed the thermal-electrical analogy to investigate the thermal behavior of SFCL devices [47, 48, 129, 130]. As will be demonstrated, by employing the thermal-electrical analogy the strong coupling between thermal and electrical phenomena becomes easier to be han-

dled since the heat transfer equations become mathematically equivalent to an RC electric circuit equations. The thermal-electrical analogy have been used for some authors to predict the thermal behavior of some electrical equipments and devices [131–134].

5.2 Mathematical Justification

The main goal of this section is to provide a mathematical basis for the thermal-electrical analogy that will be employed in the simulations of the studied SFCL devices. Further details about the method formulation can be found in [135] and [136].

Consider the transient one-dimensional heat flow within the infinitesimal volume element illustrated in figure 5.1a of unit dimensions along the Cartesian coordinate axes x and y , and of length dz along the z -axis. One is assuming that heat flows only along the z direction. Let us denote by \dot{Q}_z the rate of heat flow into the volume element along the z -axis. The rate of heat flow out of the volume element through the surface located at $z + dz$ may be approximated as $\dot{Q}_z + (\partial\dot{Q}_z/\partial z) dz$. Hence, the net rate of heat flow into the volume element is:

$$\dot{Q}_z - \left[\dot{Q}_z + \left(\frac{\partial\dot{Q}_z}{\partial z} \right) dz \right] = - \left(\frac{\partial\dot{Q}_z}{\partial z} \right) dz \quad (5.1)$$

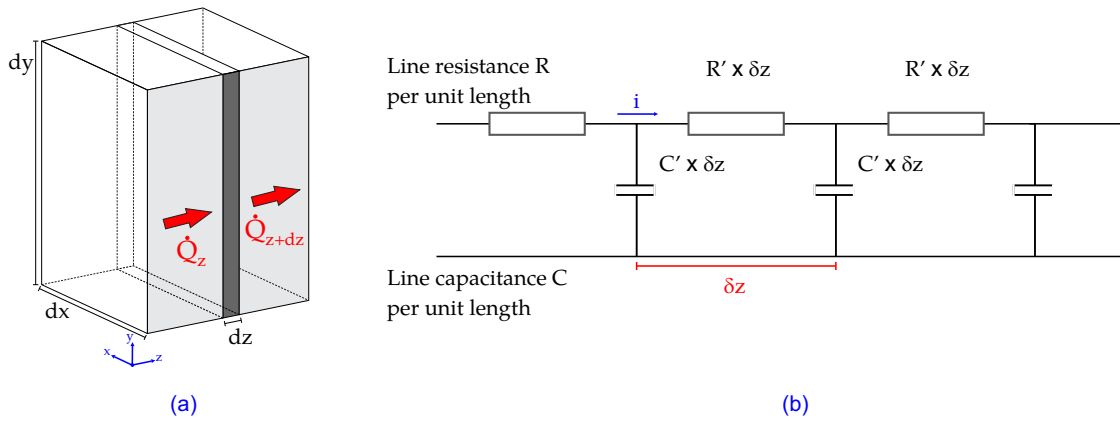


Figure 5.1: (a) Differential volume element for derivation of the heat conduction equation. (b) A distributed transmission line system with uniform resistance R' and uniform capacity C' per unit length.

The energy balance principle (the first law of Thermodynamics [137]) states that the net rate of heat flow into the volume element plus the rate at which energy is generated within it must be equal to the rate of increase of the internal thermal energy stored by the material occupying the volume element. Denoting by \dot{q} the

rate of internal heat generation per unit of volume, the energy balance principle yields

$$-\frac{\partial \dot{Q}_z}{\partial z} dz + \dot{g} dV = \gamma \varsigma dV \frac{\partial T}{\partial t}. \quad (5.2)$$

where $dV = dy dx dz$ denotes the volume of the infinitesimal element. Assuming that the material occupying the volume element obeys Fourier's law of heat conduction, the net rate of heat flow \dot{Q}_z may be related to the temperature gradient along the z -axis as follows

$$\dot{Q}_z = -k da \frac{\partial T}{\partial z} \quad (5.3)$$

where $da = dy dx$ is the surface area of heat exchange, orthogonal to the z -axis. Substituting equation (5.3) into equation (5.2) and assuming a constant thermal conductivity k yields

$$\frac{\partial T}{\partial t} = \frac{k}{\gamma \varsigma} \frac{\partial^2 T}{\partial z^2} + \frac{\dot{g}}{\gamma \varsigma} \quad (5.4)$$

which is the classical one-dimensional transient heat conduction equation (a parabolic partial differential equation).

Consider now a transmission line having an uniform resistance per unit length denoted by R' and an uniform capacity per unit length denoted by C' . Consider an infinitesimal element of length dz along the transmission line, as illustrated in figure 5.1b. Let us denote, respectively by i and v , the current and voltage at the left end of the infinitesimal element. The voltage change along the length dz is $v - [v + (\partial v/\partial z) dz] = -(\partial v/\partial z) dz$. The change in current flow along the length dz is $i - [i + (\partial i/\partial z) dz] = -(\partial i/\partial z) dz$.

Ohm's law states that the voltage change is directly proportional to the current flowing through the element with the proportionality constant being its total resistance. Hence, for the infinitesimal element shown in figure 5.1b Ohm's law may be mathematically stated as:

$$-\frac{\partial v}{\partial z} dz = R' dz i \quad \therefore i = -\frac{1}{R'} \frac{\partial v}{\partial z} \quad (5.5)$$

Kirchhoff's law gives the following relationship between the change in current flow and the shunt-capacity C' :

$$-\frac{\partial i}{\partial z} dz = C' dz \frac{\partial v}{\partial t} \quad \therefore \frac{\partial i}{\partial z} = -C' \frac{\partial v}{\partial t} \quad (5.6)$$

Combining equations (5.5) and (5.6) one arrives at the following two partial differential equations:

$$\frac{\partial v}{\partial t} = \frac{1}{R'C'} \frac{\partial^2 v}{\partial z^2} \quad (5.7)$$

$$\frac{\partial i}{\partial t} = \frac{1}{R'C'} \frac{\partial^2 i}{\partial z^2} \quad (5.8)$$

which are mathematically identical to the one-dimensional transient heat conduction equation (equation (5.4)), except for an additional source term on the right-hand side of the latter. Nevertheless, additional source terms may also be added to equations (5.7) and (5.8) if there is a voltage or a current source in the transmission line. Hence, any one-dimensional transient heat conduction problem admits an RC electric circuit representation as the one illustrated in 5.1b [135]. In the next paragraphs, we also justify the thermal-electrical analogy for a semi discrete version of the heat conduction equation.

Let us consider the transient heat conduction equation with internal heat generation for a layered structure, as shown in figure 5.2a. Consider the η^{th} -layer, with thickness ν_η :

$$\gamma_\eta \varsigma_\eta \frac{\partial T_\eta(z, t)}{\partial t} = k_\eta \frac{\partial^2 T_\eta(z, t)}{\partial z^2} + \dot{g}_\eta \quad \text{for } z_{\eta-1} < z < z_\eta, t > 0. \quad (5.9)$$

For our specific heat conduction problem, \dot{g}_η depends on the temperature $T_\eta(z, t)$ making the above partial differential equation nonlinear and precluding a purely analytical solution. Hence, one must resort to numerical methods for its solution as, for example, the finite-difference method.

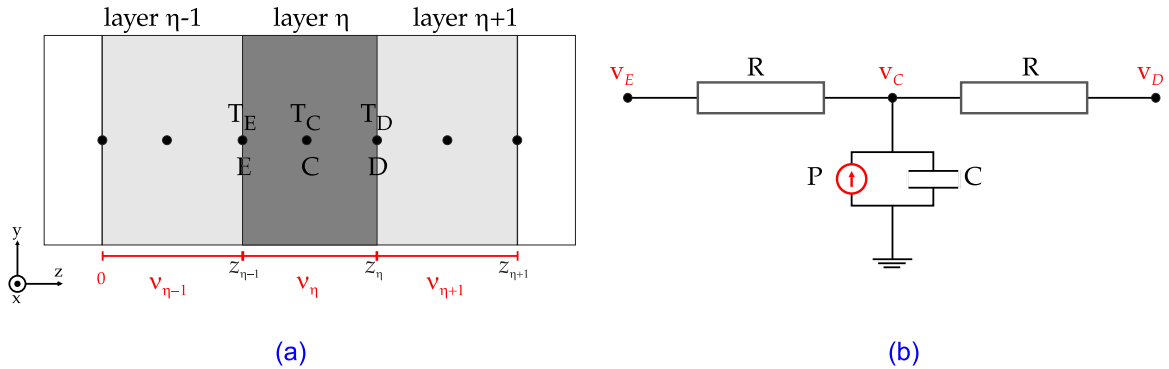


Figure 5.2: (a) Finite-difference discretization of the heat conduction equation within the layered composite medium and (b) discrete RC circuit equivalent to the transmission line shown in figure 5.1b with a current source P .

A particular finite-difference mesh for spatial discretization of the first term on the right-hand side of equation (5.9) (the diffusive term) is schematically illustrated in figure 5.2a. This particular finite-difference mesh comprises only one

node within the η^{th} -layer placed at its midpoint. There are also two other nodes, each one placed at the boundary shared by the η^{th} -layer and the two adjoining layers, namely, $\eta - 1$ and $\eta + 1$. Let us denote, respectively by T_C , T_E and T_D , the temperature at the midpoint node, the temperature at the node on the boundary shared by layers η and $\eta - 1$, and the temperature at the node on the boundary shared by η and $\eta + 1$ (see figure 5.2a).

Using a second-order central finite-difference scheme to approximate the first term on the right-hand side of equation (5.9) allows one to write the following approximate equation for the midpoint node:

$$\gamma_\eta \varsigma_\eta \frac{\partial T_\eta(z_C, t)}{\partial t} = k_\eta \frac{T_\eta(z_C - \Delta z_\eta, t) - 2T_\eta(z_C, t) + T_\eta(z_C + \Delta z_\eta, t)}{\Delta z_\eta^2} + \dot{g}_\eta \quad (5.10)$$

where $\Delta z_\eta = \nu_\eta/2$ denotes the finite-difference mesh size and $z_C = z_{\eta-1} + \Delta z_\eta$ denotes the position of the midpoint node. Referring to figure 5.2a and using the notation previously defined, equation (5.10) may be rewritten as

$$\frac{dT_C}{dt} = \frac{k_\eta}{\gamma_\eta \varsigma_\eta} \frac{T_E - 2T_C + T_D}{\Delta z_\eta^2} + \frac{\dot{g}_\eta}{\gamma_\eta \varsigma_\eta}. \quad (5.11)$$

Equation (5.11) is commonly referred to as the semidiscrete form of the partial differential equation (5.9) because only the independent space variable z has been discretized; notice that the independent variable t remains continuous.

Let us now consider the discrete counterpart of the distributed system shown in figure 5.1b. The discrete RC circuit equivalent to the transmission line is illustrated in figure 5.2b. Notice that R and C denote, respectively, the resistance and the shunt-capacity for each finite length of the circuit. There is also included in figure 5.2b a current source denoted by P . Applying Kirchhoff's law to the central node shown in figure 5.2b (equivalent to the midpoint node shown in figure 5.2a) one arrives at

$$\frac{v_E - v_C}{R} + \frac{v_C - v_D}{R} + P = C \frac{dv_C}{dt} \quad (5.12)$$

or, alternatively,

$$\frac{dv_C}{dt} = \frac{1}{C} \frac{v_E - 2v_C + v_D}{R} + \frac{P}{C} \quad (5.13)$$

Notice that equations (5.11) and (5.13) are mathematically identical. Hence, T-shape RC circuits such as those illustrated in figure 5.2b may be employed to solve equation (5.11). The thermal-electrical analogy is thus justified for the semi discrete form of the heat conduction equation.

To close up this section, the following remarks are worthwhile. The finite-difference discretization procedure described in the foregoing paragraphs must be repeated for all layers of the medium. For a layer whose boundary tempera-

ture is prescribed, either T_E or T_D appearing in equation (5.11) becomes a known function and thus need not be computed. For our specific heat conduction problem, the first and the last layers possess a boundary surface which exchanges heat by convection with LN₂ (a boundary condition of the third-kind). For those layers, one may perform an energy balance at their boundaries in contact with LN₂ and rewrite equation (5.11) as a function of the LN₂ temperature and the convective heat transfer coefficient h_c instead of the unknown boundary temperatures (either T_E or T_D). The end result is a system of (coupled) ordinary-differential equations that may be cast in a general matrix form, i.e.,

$$\frac{d\mathbf{T}}{dt} = \mathbf{A} \mathbf{T} + \mathbf{f} \quad (5.14)$$

$$\mathbf{T}(0) = \mathbf{T}_0 \quad (5.15)$$

where \mathbf{T} denotes the vector of unknown temperatures (temperatures at all mid-point nodes and at boundary nodes on which no prescribed temperature is enforced) and \mathbf{T}_0 denotes the vector of initial temperatures. The coefficient matrix \mathbf{A} accounts for the geometry and material properties of the layers whereas the vector \mathbf{f} comprises any source (e.g., the internal heat generation) or known boundary terms (e.g., known temperatures and/or heat fluxes prescribed at the boundaries of the medium).

Table 5.1 has been prepared to list the properties of thermal and electrical systems in analogous form [136].

Table 5.1: Analogous elements of thermal and electrical systems

Thermal Property	Symbol	Unit	Electrical Property	Symbol	Unit
Temperature	T	K	Voltage	V	volt
Power	P	watt	Current	i	ampere
Heat capacity	$\gamma \varsigma \nu S$	$J/m^3.K$	Capacitance	C	farad
Conductivity	k	$W/m.K$	Resistance	R	Ohm

5.3 Electro-Thermal Model for SFCL

5.3.1 Electrical Equivalentents

To simulate the electrical behavior of the MCP-BSCCO-2212 assembly and the YBCO 2G coil, the model schematically sketched in figure 5.3 have been used.

This electric circuit reproduces quite well the short-circuit tests described in section 3.2 (see figure 3.3).

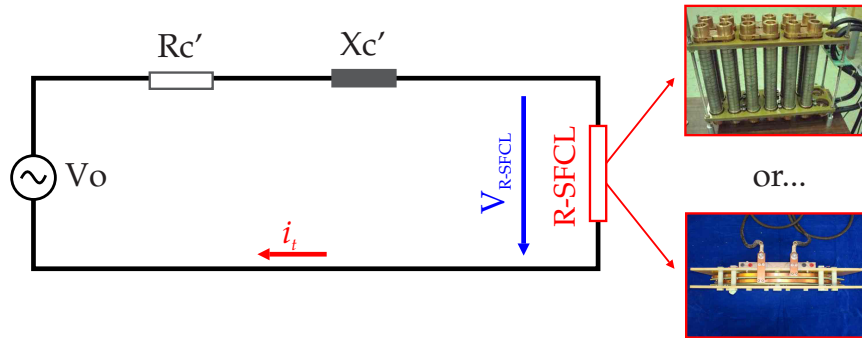


Figure 5.3: Equivalent circuit of the measurements setup for the MCP-BSCCO-2212 assembly and the YBCO 2G coil (see figure 3.3).

Values of R'_c and X'_c shown in figure 5.3a are adjusted according to the desired value of the fault current to be simulated. These values are obtained from R_c and X_c (refer to figure 3.3a), by means of equations (5.16) and (5.17).

$$R'_c = \left[\frac{V_o}{V_a} \right]^2 R_c \quad (5.16) \quad X'_c = \left[\frac{V_o}{V_a} \right]^2 X_c \quad (5.17)$$

Each MCP-BSCCO-2212 module was modeled as four variable resistors in parallel connection, since they are temperature dependents (figure 5.4a). These resistors represent the following layers: CuNi alloy (shunt resistor), the solder between the superconductor material and CuNi layer, HTS material (BSCCO-2212) and FRP tube (refer to figure 3.1a).

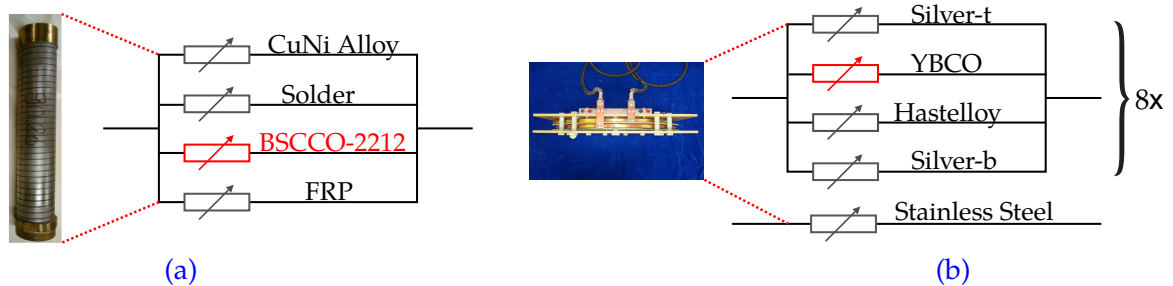


Figure 5.4: (a) Electric representation of the sub-components of each module of the MCP-BSCCO-2212 assembly and (b) electric representation of the YBCO 2G Coil.

Each tape of the YBCO 2G coil was also modeled as four variable resistors in parallel connection (figure 5.4b). They represent the silver layer at top (silver-t = $3\mu\text{m} + 1\mu\text{m}$), HTS material (YBCO), Hastelloy substrate and the silver layer at

bottom (silver-b = 1 μ m) (refer to figure 2.14). The effect of buffer layer is expected to be negligible and thus not considered in the model. Since the YBCO 2G coil is composed by eight tapes, the parallel connection illustrated in figure 5.4b must be created eight times. Furthermore, an extra resistor in parallel must be added, in order to represent the shunt of the coil (stainless steel tapes) (refer to figure 3.1b).

The dependence on temperature of the resistivity of all materials is presented in B.1 of appendix B.

The computational model for the electric circuit analysis makes use of the power law E-J curve characteristic of the superconductor material composing both limiters, thereby the current iterative process is necessary. According to [27], for the BSCCO-2212 material the n value is equal to 9 in the flux-creep stage and 3 in the flux-flow stage. For the YBCO material, n is 30 in the flux-creep and 2 in the flux-flow stage. In the normal state, the resistances is of the YBCO and BSCCO-2212 are modeled by means of equations (B.3) and (B.7) (see appendix B, section B.1).

The computational model for the electric circuit sketched in figure 5.3 comprises the following nonlinear ordinary differential equation ¹:

$$\frac{di_t}{dt} = \frac{1}{L_c} [V_o - (R_c + R_{r-sfcl})i_t] \quad (5.18)$$

where R_{r-sfcl} represents the equivalent resistance of the SFCL device (MCP-BSCCO-2212 assembly or the YBCO 2G coil), V_o is a sinusoidal voltage source and i_t is the total current of the circuit.

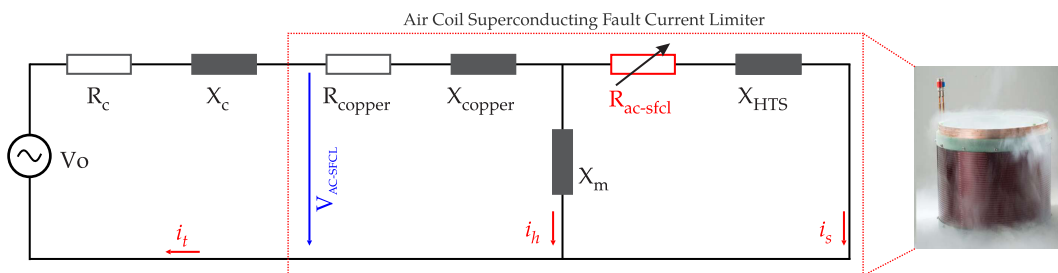


Figure 5.5: Equivalent circuit of the measurements setup for the AC-SFCL (see figure 3.4).

The model of the electrical behavior of the AC-SFCL is similar to that one already presented in figure 4.1 (section 4.2 of chapter 4), repeated here in figure 5.5 for convenience. For this circuit, the following system of differential equations must be solved:

¹ $L_c = X'_c/\omega$ ($\omega = 2\pi f$)

$$\begin{bmatrix} \dot{i}_s \\ \dot{i}_h \end{bmatrix} = \begin{bmatrix} L_c + L_{cu} + L_{Sec} & L_c + L_{cu} \\ L_c + L_{cu} & L_c + L_{cu} + L_m \end{bmatrix}^{-1} \left\{ V_o \begin{bmatrix} 1 \\ 1 \end{bmatrix} - \begin{bmatrix} R_c + R_{cu} + R_{ac-sfcl} & R_c + R_{cu} \\ R_c + R_{cu} & R_c + R_{cu} \end{bmatrix} \begin{bmatrix} \dot{i}_s \\ \dot{i}_h \end{bmatrix} \right\} \quad (5.19)$$

Once again, i_s represents the current in the secondary coil of the transformer, i_h represents the excitation current, required to produce the resultant mutual flux in a transformer and $R_{ac-sfcl}$ represents the equivalent resistance of the secondary coil of the AC-SFCL device.

In the circuit of figure 5.5, each tape of the AC-SFCL is represented by a parallel connection containing five resistors whereby each one represents a layer of a single tape (refer to figure 2.21). Since the AC-SFCL is composed by 22 short-circuited tapes at the secondary winding, the parallel connection illustrated in figure 5.6 must be created 22 times.

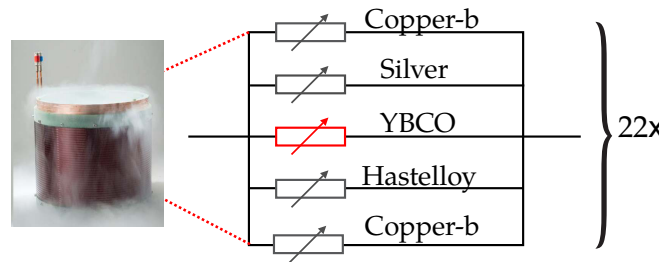


Figure 5.6: Electric representation of the layers of each tape of the AC-SFCL.

Resistances of the layers which composes the tapes are also represented by variable resistors since their resistivity are temperature dependent (see appendix B, section B.1).

5.3.2 Thermo-Electrical Equivalents

Before describing how thermal-electrical equivalents are employed to solve heat conduction equations, some assumptions about layers and configuration of each SFCL component must be introduced. For the sake of simplicity, the composites plane wall geometry with layers depicted in figure 5.7 were used to perform the thermal analysis of the SFCL devices. It shows a simplified schematic drawn of the layers for each limiter (figure out of scale).

Heat transfers along x and y directions are neglected (length and width respectively), since one assumes homogeneous materials along the x direction and negligible temperature gradient along the y direction. Hence, only temperature

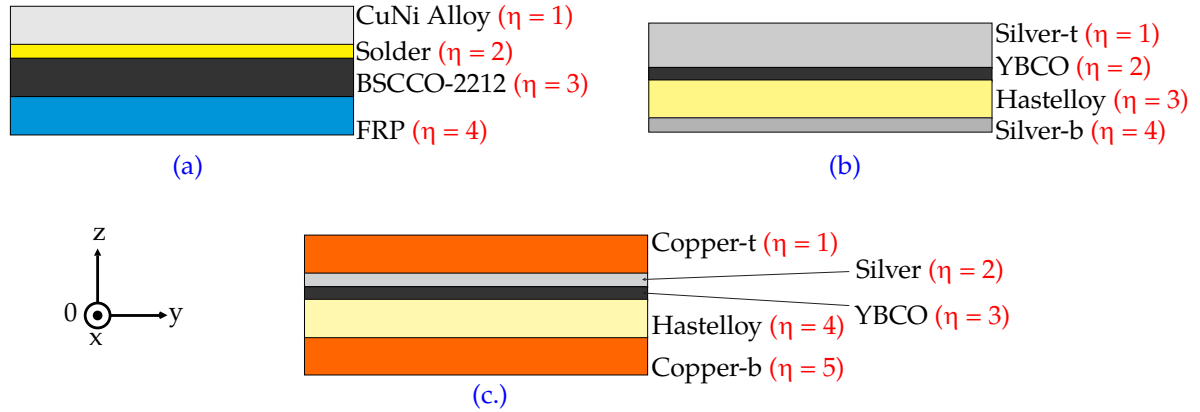


Figure 5.7: Cross section of the employed geometry for simulations of the (a) each MCP-BSCCO-2212 module, (b) each tape of the YBCO 2G coil and (c) each tape of the AC-SFCL.

gradients across each layer thickness (z -direction) are taken into account. Henceforth, the subscripts 1, 2, 3... η_e will designate quantities associated with the layers of the tapes and modules ².

Solutions of equations 5.18 and 5.19 are used to calculate the dissipated power in each layer and the resistivity of the HTS material.

To investigate the influence of the heat exchanges and also the influence of variable and constant physical properties, three different models were developed and compared. Table 5.2 summarizes the considered models.

Table 5.2: Developed Models

Model	Heat Exchange	ς and k	h_c
TEA-MA	no	constant	null
TEA-MB	yes	constant	0.2 W/K.cm^2
TEA-MC	yes	temperature dependent	

- TEA-MA \rightarrow Adiabatic model with no heat exchanges between layers and between external surface and LN2. In this model, physical properties are considered at 100 K;
- TEA-MB \rightarrow Model with heat exchanges between layers of the tapes and modules and heat exchange between surfaces and the liquid nitrogen bath. Once again, all the physical properties are assumed constant at 100 K;

² η_e denotes the last layer of the tape or module. For the MCP-BSCCO-2212 modules $\eta_e = 4$. For the tapes of the YBCO 2G Coil $\eta_e = 4$ and for the tapes of the AC-SFCL $\eta_e = 5$

- TEA-MC → Model with heat exchanges as for TEA-MB and temperature dependent physical properties (specific heat ς , thermal conductivity k and the convective heat transfer coefficient h_c).

5.3.2.1 Adiabatic Model (TEA-MA)

Many models that not consider heat exchanges in SFCL during fault period can be found in literature. That means that such models have no consideration of the heat exchanges between layers or with the liquid nitrogen bath. In order to investigate what kind of results an adiabatic approximation can provide, one proposes a model to analyze such conditions. In this case the following partial differential equation is solved separately for each layer:

$$\gamma_\eta \varsigma_\eta \frac{\partial T_\eta(z, t)}{\partial t} = \dot{g}_\eta \quad \text{for } z_{\eta-1} < z < z_\eta, t > 0 \quad (5.20)$$

γ_η , ς_η , k_η and \dot{g}_η denote, respectively, specific mass (kg/m³), specific heat (J/kg.K), thermal conductivity (W/m.K) and internal heat generation (per unit volume) (W/m³) of the η^{th} layer. The internal heat generation is given by:

$$\dot{g}_\eta = \frac{R_\eta \times i_\eta^2}{V_\eta} \quad (5.21)$$

where V_η is the volume, R_η is the electric resistance of the layer η and i_η is the current flowing in the respective layer. The solution of equation 5.20 may be solved numerically by means of explicit Euler method [77].

5.3.2.2 Non-Adiabatic Model (TEA-MB)

To simulate the temperature rise of each layer of the HTS tapes and each MCP-BSCCO-2212 module, the presented analogy between thermal and electrical systems was used. The temperature distribution within each layer, $T_\eta(z, t)$, $\eta = 1, 2, 3 \dots \eta_e$, is governed by the following partial differential equation:

$$\gamma_\eta \varsigma_\eta \frac{\partial T_\eta(z, t)}{\partial t} = k_\eta \frac{\partial^2 T_\eta(z, t)}{\partial z^2} + \dot{g}_\eta \quad \text{for } z_{\eta-1} < z < z_\eta, t > 0 \quad (5.22)$$

The partial differential equation (5.22) is subjected to third-kind boundary conditions at $z = 0$ and at $z = z_{\eta_e}$ given by

$$k_1 \frac{\partial T_1}{\partial z} \Big|_{z=0} = h_c [T_1(0, t) - T_{LN_2}] \quad \text{at } z = 0 \quad (5.23)$$

$$-k_{\eta_e} \frac{\partial T_{\eta_e}}{\partial z} \Big|_{z=z_{\eta_e}} = h_c [T_{\eta_e}(z_{\eta_e}, t) - T_{LN_2}] \quad \text{at } z = z_{\eta_e}, \quad (5.24)$$

and also to the following interface conditions, which express continuity of temperature and heat flux at common boundaries shared by adjoining layers

$$T_{\eta-1}(z_{\eta-1}, t) = T_{\eta}(z_{\eta-1}, t) \quad \text{at } z = z_{\eta-1} \quad (5.25)$$

$$-k_{\eta-1} \left. \frac{\partial T_{\eta-1}}{\partial z} \right|_{z=z_{\eta-1}} = -k_{\eta} \left. \frac{\partial T_{\eta}}{\partial z} \right|_{z=z_{\eta-1}} \quad \text{at } z = z_{\eta-1} \quad (5.26)$$

for $\eta \in \{2, 3 \dots \eta_{\rho}\}$. To complete the mathematical formulation, temperatures $T_{\eta}(z, t)$, $\eta = 1, 2 \dots \eta_{\rho}$ are also subjected to the initial condition $T_{\eta}(z, 0) = T_{LN_2}$. In the boundary conditions given by equations (5.23) and (5.24), h_c and T_{LN_2} denote, respectively, convection heat transfer coefficient and the liquid nitrogen temperature. The internal heat generation $\dot{q}_{\eta} = E_{\eta}(T_{\eta}(z, t)) J_{\eta}$ (Joule heating effect) depends on both the temperature and electrical current flowing through the η^{th} layer, which makes the above boundary and initial value problem highly nonlinear and coupled to the electrical circuit differential equation, precluding a purely analytical solution.

As have been shown, the one-dimensional transient heat conduction problem across the composite plane wall depicted in figure 5.7 may be represented by the equivalent thermal circuits. The designed equivalent thermal circuits shown in the next paragraphs comprises a network of T sections. For these networks, thermal resistances R_{η} , $\eta = 1, 2, 3 \dots \eta_{\rho}$, are associated with the resistance to heat flow by conduction inside the η^{th} layer, while the capacitors C_{η} are related to the volumetric heat capacity of the material inside the η^{th} layer. The convective heat transfer with liquid nitrogen is also represented by the thermal resistance R_{conv} . Such parameters are calculated as follows [133–136, 138]:

$$R_{\eta} = \frac{\nu_{\eta}}{k S} \quad (5.27) \quad R_{conv} = \frac{1}{h_c S} \quad (5.28)$$

$$C_{\eta} = \gamma_{\eta} \varsigma_{\eta} \nu_{\eta} S \quad (5.29) \quad P_{\eta} = \dot{q}_{\eta} V_{\eta} \quad (5.30)$$

where S denotes the surface of heat exchange (orthogonal to the z -axis). The remaining symbols have been previously defined.

At each equivalent thermal circuit, the temperature rise of each layer of the SFCL devices is calculated as the voltage drop between the midpoint node at that layer and g , i.e., $T_{\eta}(\nu_{\eta}/2, t) - g$. For example, the temperature rise of the BSCCO-2212 layer in the modules of the MCP-BSCCO-2212 assembly is calculated as the voltage drop between the points $T_{bscco} = T_3(\nu_3/2, t)$ and g (see figure 5.8). The DC voltage source g is set to 77 V in order to simulate the constant liquid nitrogen bath temperature T_{LN_2} (77 K). Taking the conductances G between each layer, it

is possible to show for each SFCL that the proposed analog electrical networks (as the ones illustrated in figures 5.8, 5.9 and 5.10) may be cast in matrix form, as demonstrated in equation (5.14), in order to obtain the solutions of the thermal problem in SFCL devices by solving systems of differential equations.

Matrix form of the MCP-BSCCO-2212 modules - With basis in figure 5.8, one can write the following matrix for each module of the MCP-BSCCO-2212 assembly³.

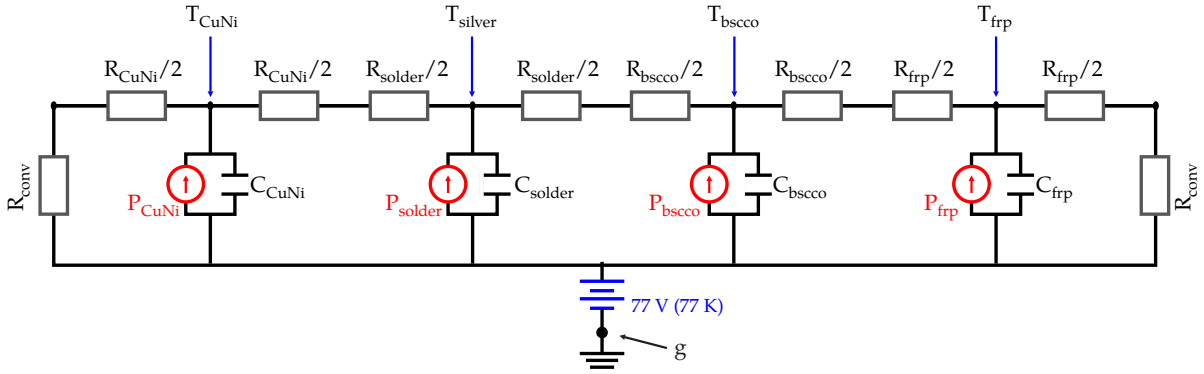


Figure 5.8: Thermal-electric circuit to solve the thermal behavior for each MCP-BSCCO-2212 module.

$$\begin{bmatrix} C_{frp} & 0 & 0 & 0 \\ 0 & C_{bscco} & 0 & 0 \\ 0 & 0 & C_{solder} & 0 \\ 0 & 0 & 0 & C_{CuNi} \end{bmatrix} \begin{bmatrix} \dot{T}_{frp} \\ \dot{T}_{bscco} \\ \dot{T}_{solder} \\ \dot{T}_{CuNi} \end{bmatrix} = \begin{bmatrix} P_{frp} \\ P_{bscco} \\ P_{solder} \\ P_{CuNi} \end{bmatrix} - \begin{bmatrix} G_{frpn} + G_{frpsp} & -G_{frpsp} & 0 & 0 \\ -G_{frpsp} & G_{frpsp} + G_{spsl} & -G_{spsl} & 0 \\ 0 & -G_{spsl} & G_{spsl} + G_{slsh} & -G_{slsh} \\ 0 & 0 & -G_{slsh} & G_{slsh} + G_{shn} \end{bmatrix} \begin{bmatrix} T_{frp} \\ T_{bscco} \\ T_{solder} \\ T_{CuNi} \end{bmatrix} + T_{LN_2} \begin{bmatrix} G_{frpn} \\ 0 \\ 0 \\ G_{shn} \end{bmatrix} \quad (5.31)$$

where

$$G_{frpn} = \left(R_{conv} + \frac{R_{frp}}{2} \right)^{-1} \quad (5.32) \quad G_{frpsp} = \left(\frac{R_{frp}}{2} + \frac{R_{bscco}}{2} \right)^{-1} \quad (5.33)$$

$$G_{spsl} = \left(\frac{R_{bscco}}{2} + \frac{R_{solder}}{2} \right)^{-1} \quad (5.34) \quad G_{slsh} = \left(\frac{R_{solder}}{2} + \frac{R_{CuNi}}{2} \right)^{-1} \quad (5.35)$$

³ $\dot{T}_\eta = \frac{\partial T_\eta(z, t)}{\partial t}$

$$G_{shn} = \left(R_{conv} + \frac{R_{CuNi}}{2} \right)^{-1} \quad (5.36)$$

Matrix form of the YBCO 2G Coil - With basis in figure 5.9, one can write the matrix shown in equation (5.37) for each tape of the YBCO 2G Coil. In this model the effect of buffer layer is expected to be negligible and thus not considered.

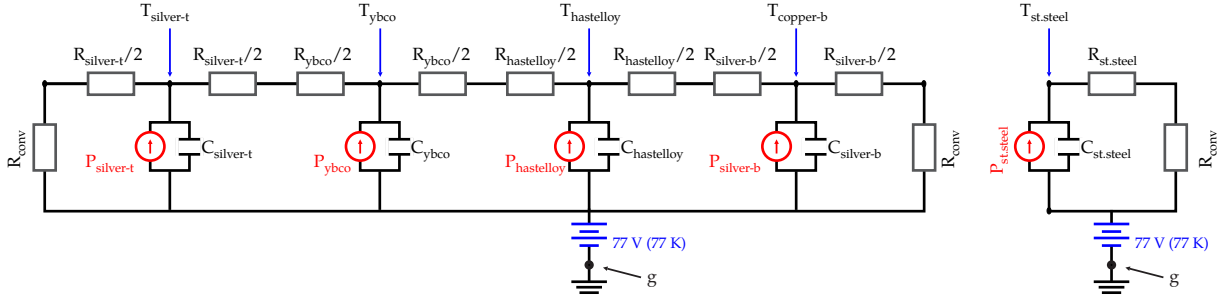


Figure 5.9: Thermal-electric circuit to solve the thermal behavior for each tape of the YBCO 2G Coil and the stainless steel tape (shunt).

$$\begin{bmatrix} C_{silver-t} & 0 & 0 & 0 \\ 0 & C_{ybco} & 0 & 0 \\ 0 & 0 & C_{hastelloy} & 0 \\ 0 & 0 & 0 & C_{silver-b} \end{bmatrix} \begin{bmatrix} \dot{T}_{silver-t} \\ \dot{T}_{ybco} \\ \dot{T}_{hastelloy} \\ \dot{T}_{silver-b} \end{bmatrix} = \begin{bmatrix} P_{silver-t} \\ P_{ybco} \\ P_{hastelloy} \\ P_{silver-b} \end{bmatrix} - \begin{bmatrix} G_{agtn} + G_{agsp} & -G_{agsp} & 0 & 0 \\ -G_{agsp} & G_{agsp} + G_{sphy} & -G_{sphy} & 0 \\ 0 & -G_{sphy} & G_{sphy} + G_{hyagb} & -G_{hyagb} \\ 0 & 0 & -G_{hyagb} & G_{hyagb} + G_{agbn} \end{bmatrix} \begin{bmatrix} T_{silver-t} \\ T_{ybco} \\ T_{hastelloy} \\ T_{silver-b} \end{bmatrix} + T_{LN_2} \begin{bmatrix} G_{agtn} \\ 0 \\ 0 \\ G_{agbn} \end{bmatrix} \quad (5.37)$$

Since stainless steel tapes are in parallel connection with the HTS tapes in the YBCO 2G coil (acting as shunt), the following equation must be solved independently (but simultaneously) of the equation (5.37):

$$\dot{T}_{st.steel} = \frac{1}{C_{st.steel}} [P_{st.steel} - G_{st.steel} (T_{st.steel} - T_{LN_2})] \quad (5.38)$$

Conductances of equations (5.37) and (5.38) are defined as follows:

$$G_{agt n} = \left(R_{conv} + \frac{R_{silver-t}}{2} \right)^{-1} \quad (5.39) \quad G_{agsp} = \left(\frac{R_{silver-t}}{2} + \frac{R_{ybco}}{2} \right)^{-1} \quad (5.40)$$

$$G_{sphy} = \left(\frac{R_{ybco}}{2} + \frac{R_{hastelloy}}{2} \right)^{-1} \quad (5.41) \quad G_{hyagb} = \left(\frac{R_{hastelloy}}{2} + \frac{R_{silver-b}}{2} \right)^{-1} \quad (5.42)$$

$$G_{agbn} = \left(R_{conv} + \frac{R_{silver-b}}{2} \right)^{-1} \quad (5.43) \quad G_{st.steel} = (R_{conv} + R_{st.steel})^{-1} \quad (5.44)$$

Matrix form of the Air Coil SFCL - With basis in figure 5.10, one can write the matrix shown in equation (5.45) for each tape of the Air Coil SFCL. Once again, the effect of buffer layer is expected to be negligible and thus not considered in the model.

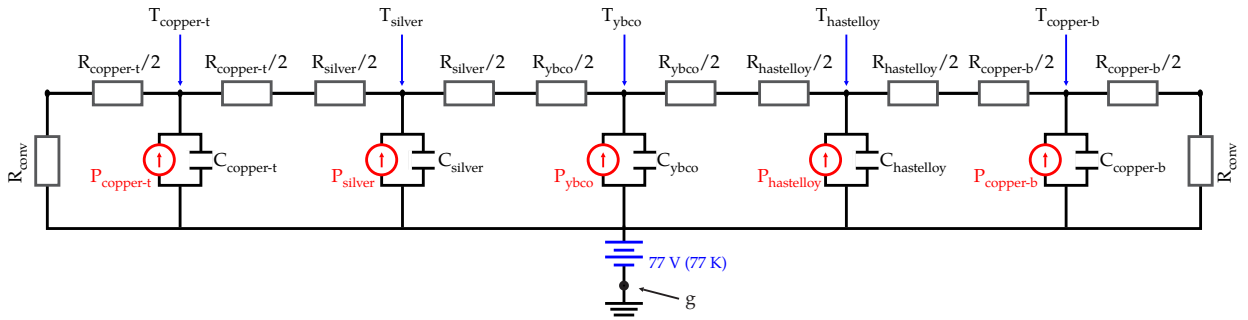


Figure 5.10: Thermal-electric circuit to solve the thermal behavior for each tape of the Air Coil SFCL.

$$\begin{bmatrix} C_{copper-t} & 0 & 0 & 0 & 0 \\ 0 & C_{silver} & 0 & 0 & 0 \\ 0 & 0 & C_{ybco} & 0 & 0 \\ 0 & 0 & 0 & C_{hastelloy} & 0 \\ 0 & 0 & 0 & 0 & C_{copper-b} \end{bmatrix} \begin{bmatrix} T_{copper-t} \\ T_{silver} \\ T_{ybco} \\ T_{hastelloy} \\ T_{copper-b} \end{bmatrix} = \begin{bmatrix} P_{copper-t} \\ P_{silver} \\ P_{ybco} \\ P_{hastelloy} \\ P_{copper-b} \end{bmatrix} - \begin{bmatrix} G_{kptn} + G_{kpag} & -G_{kpag} & 0 & 0 & 0 \\ -G_{kpag} & G_{kpag} + G_{agsp} & -G_{agsp} & 0 & 0 \\ 0 & -G_{agsp} & G_{agsp} + G_{sphy} & -G_{sphy} & 0 \\ 0 & 0 & -G_{sphy} & G_{sphy} + G_{hykpb} & -G_{hykpb} \\ 0 & 0 & 0 & -G_{hykpb} & G_{hykpb} + G_{kpb n} \end{bmatrix} \begin{bmatrix} T_{copper-t} \\ T_{silver} \\ T_{ybco} \\ T_{hastelloy} \\ T_{copper-b} \end{bmatrix} + T_{LN_2} \begin{bmatrix} G_{kptn} \\ 0 \\ 0 \\ 0 \\ G_{kpb n} \end{bmatrix} \quad (5.45)$$

Conductances shown in equation (5.45) are defined as follows:

$$G_{kptn} = \left(R_{conv} + \frac{R_{copper-t}}{2} \right)^{-1} \quad (5.46) \quad G_{kpag} = \left(\frac{R_{copper-t}}{2} + \frac{R_{silver}}{2} \right)^{-1} \quad (5.47)$$

$$G_{agsp} = \left(\frac{R_{silver}}{2} + \frac{R_{ybco}}{2} \right)^{-1} \quad (5.48) \quad G_{sphy} = \left(\frac{R_{ybco}}{2} + \frac{R_{hastelloy}}{2} \right)^{-1} \quad (5.49)$$

$$G_{hykp} = \left(\frac{R_{hastelloy}}{2} + \frac{R_{copper-b}}{2} \right)^{-1} \quad (5.50) \quad G_{kpbn} = \left(R_{conv} + \frac{R_{copper-b}}{2} \right)^{-1} \quad (5.51)$$

5.3.2.3 Non-Adiabatic Model with Variable Parameters (TEA-MC)

Model TEA-MC analyzes influence of the temperature dependency of the physical properties during the fault period (specific heat ς , the thermal conductivity k and the convection heat transfer coefficient h_c). Sections B.2 and B.3 in appendix B present the dependency on temperature of the physical properties of each material (ς_η and k_η).

Although the physical properties are dependent on temperature in the TEA-MC model, the electrical-thermal equivalents shown in figures 5.8, 5.9 and 5.10 do not change significantly. One must only attempt that in this case all resistors and capacitors are no longer constants and must be replaced by variable components. There are no significant changes in the form of equations (5.31), (5.37) and (5.45), therefore these differential equations remain the same since at each timestep of the solution routine, temperatures inside each layer of the SFCL are taken as constant. The physical properties are updated at the end of each timestep according with the current value of temperature. Further details about the solution routine are given in section 5.4.

The convective heat transfer coefficient h_c is dependent on the temperature difference ΔT between the external surfaces of the tapes or modules and liquid nitrogen, pressure and heat capacity of LN₂. In fact, according to [139], the heat transfer coefficient h_c can present different behaviors for stationary and transient regimes. In this work the most usual curve for h_c according to [140] has been adopted. Such curve is shown in figure 5.11 and can be often divided into three phases; free convection, bubble boiling and the film boiling. At the bubble boiling phase there is a significant increase on the value of convective heat transfer coefficient during the heating. This speeds up the convective heat transfer process during the heating process. At the last stage, i.e., film boiling regime, the h_c coefficient reaches its lowest value and, therefore, the convective heat transfer process

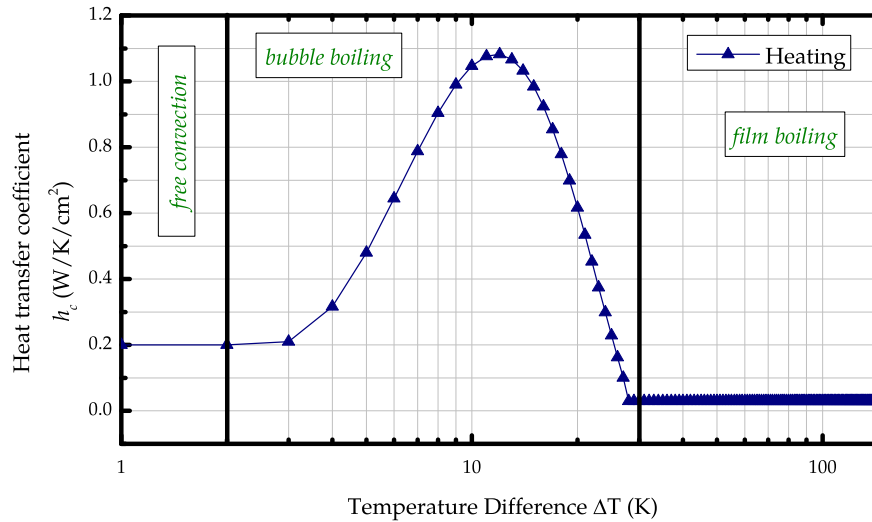


Figure 5.11: Convective heat transfer coefficient curves between the SFCLs surfaces and liquid nitrogen at room pressure for heating. Adapted from [140]

reduces severely.

Section B.4 in appendix B provides a mathematical description of the curve shown in figure 5.11.

5.4 Solution Routine

Figure 5.12 shows the complete routine of the solution for the methods presented in this chapter. Basically, the routine uses the outputs from the electrical solution as inputs to the thermal solution. The first part of the routine obtains the solution of the electrical system by solving equations (5.18) and (5.19) by means of classical Runge-Kutta 4th order (box 03). After obtaining the values of current flowing in the circuit one calculates current flowing at each layer of each tape and module using the current divider rule⁴ (box 04).

At box 05, the current in the HTS layer is used in the current iterative process to calculate the resistivity of the HTS material. It is important mentioning that the current iterative process must be done for each tape or module of the SFCL since each one has its own value of critical current I_c . In this model average values presented in tables 3.4, 3.5 and 3.6 are used. The inhomogeneity representation (I_c distribution) can not be considered because the thermal-electrical analogy does not provide local values for each tape or module.

The product indicated in the equation (5.30) provides the heat generated in each layer. That is represented in the thermal equivalents as a current source (P_η), i.e, the energy dissipated within a layer is inputted in the thermal circuit as elec-

⁴Refer to equations (4.4) and (4.5) as example

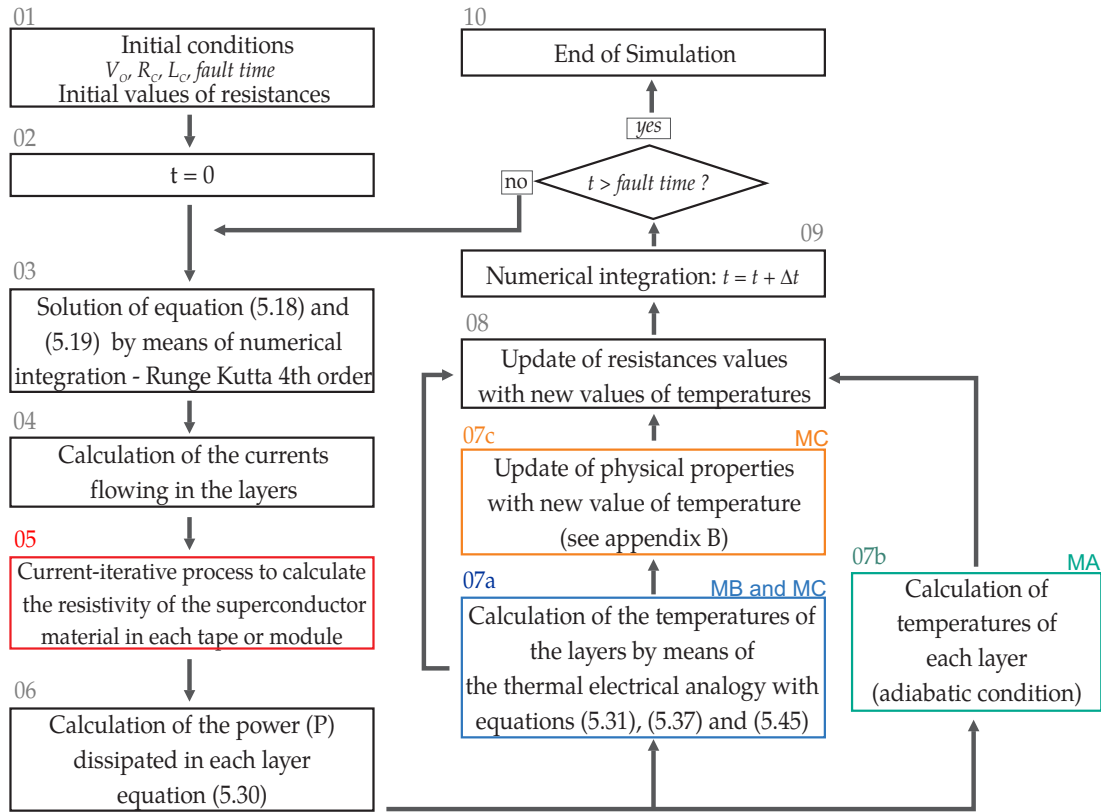


Figure 5.12: Flowchart of the simulation routine. The blue box (07a) runs only for models TEA-MB and TEA-MC; the green box (07b) runs only for model TEA-MA and the orange box (07c) runs only for model TEA-MC.

trical current (box 06). At this point, the routine may follow different procedures: if one does not take into account heat exchanges (model TEA-MA) the routine falls into box 07b; otherwise it falls into box 07a (common to models TEA-MB and TEA-MC). In the box 07a, differential equations of the thermal analogy (equations (5.31), (5.37) and (5.45)) are solved numerically for each tape or module by means of implicit Euler method in order to guarantee the numerical stability of the solution [77].

From box 07b the routine will follow to box 08, in order to update the resistance value of each layer. Nonetheless, departing from box 07a, the routine will follow to box 07c, to update the physical properties (model TEA-MC), or directly to box 08 (model TEA-MB). At box 08 the routine follows to the next timestep ($t = t + \Delta t$, box 09) and the whole process starts again if the fault period is not achieved.

The routines were performed under OS Windows 7 by means of a MATLAB® Script-File (m-file) using a conventional machine (3.4GHz, i4 processor, 8Gb RAM).

5.5 Results

In order to validate the simulation models, test results presented in section 3.2.1 were compared with the results of simulations. For all simulated cases, comparisons between simulated models and experimental results for limited current and voltage drop over the SFCL terminals are presented. Such comparisons also show the percentage error $\%E$, defined in equation (5.52), related only to the error of the waveform peaks.

$$\%E = \frac{|Measured - Simulated|}{Measured} \times 100 \quad (5.52)$$

Further errors regarding the phase shift between the curves are possible to exist. However, that errors may not be directly associated to the simulations since there may be unknown parameters and effects in the test circuits. For this reason, only errors associated to the peak values have been taken.

For each model, temperature rise of tapes and modules with the highest and lowest I_c values are presented. The other ones present always intermediate values of temperature. For a given module or set of modules (assembly), the "quench" is defined as the transition of the tape or module presenting the highest I_c value. Finally, comparisons between equivalent resistance of the simulated SFCL are shown in order to analyze the transient behavior of each model.

5.5.1 MCP-BSCCO-2212 Results

Results of simulations for the MCP-BSCCO-2212 assembly have been performed using the thermal-electric circuit shown in figure 5.8. Figure 5.13 compares measured data with simulated ones for test t1-mcp.

For all models, simulated results of limited current and voltage drop follow the same behavior of the measured ones. Model TEA-MA (adiabatic model) however presents higher values of $\%E$ for voltage drop curve. In most cases, there is not a huge difference between models TEA-MB (constant physical properties) and TEA-MC (physical properties dependent on temperature).

Figure 5.14 shows results of simulated temperature rise of each model. Temperature of the modules with lowest and highest value of critical current I_c are shown. In this case, modules number 12 and 05 respectively (see table 3.4). Comparing the three models one notes that model TEA-MA presents the highest values of temperature for all layers of the modules since in this model no considerations about heat exchange between the layers as well with liquid nitrogen bath have been taken into account. Consequently, the quench occurs faster in this model, approximately at 0.041 s, whereas in the models TEA-MB and TEA-MC it occurs

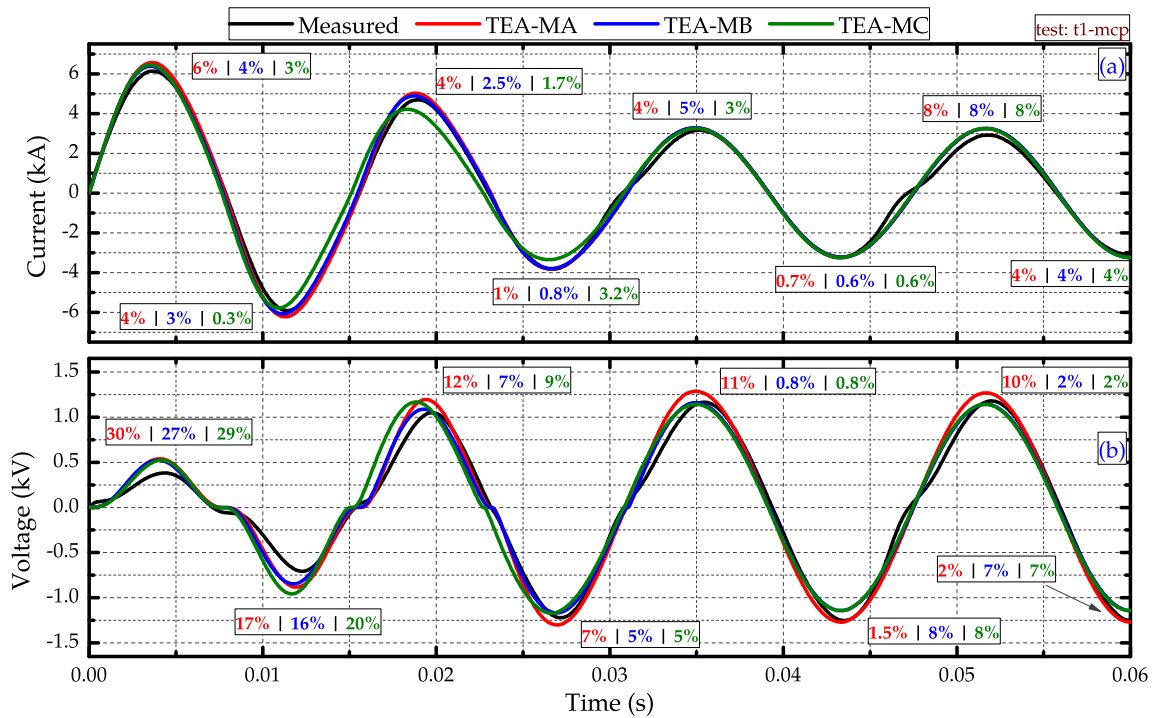


Figure 5.13: Comparison between measured and simulated results of the TEA model for a) limited current and b) voltage drop over the MCP-BSCCO-2212 assembly for test t1-mcp (fault current = 5.0 kA_{rms} under 1.0 kV_{rms}).

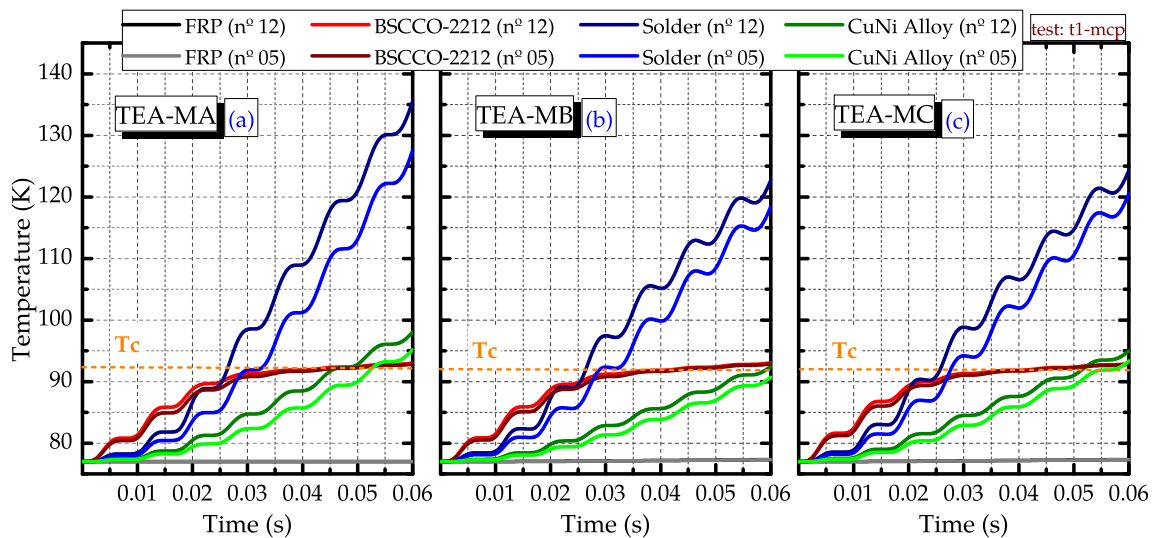


Figure 5.14: Temperature rise predicted by models TEA-MA, TEA-MB and TEA-MC during the fault period for test t1-mcp.

at approximately 0.045 s.

Figure 5.15 shows the behavior of the equivalent resistance of the assembly during the transient. As stated before and expected, it is highly nonlinear due to the E-J characteristic of the superconductor material.

Results of simulation for test t2-mcp are compared with measured data in figure 5.16. The behavior of the simulated curves agree well with measured data of

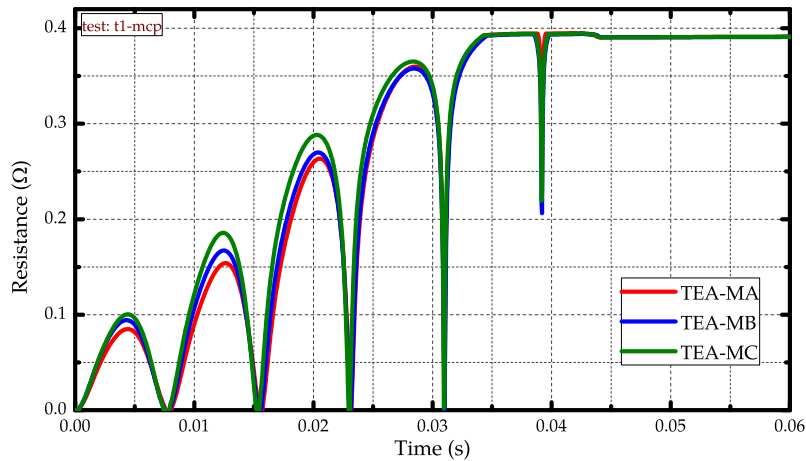


Figure 5.15: Comparison between equivalent resistances of the MCP-BSCCO-2212 assembly according to the models TEA-MA, TEA-MB and TEA-MC during the fault period in test t1-mcp.

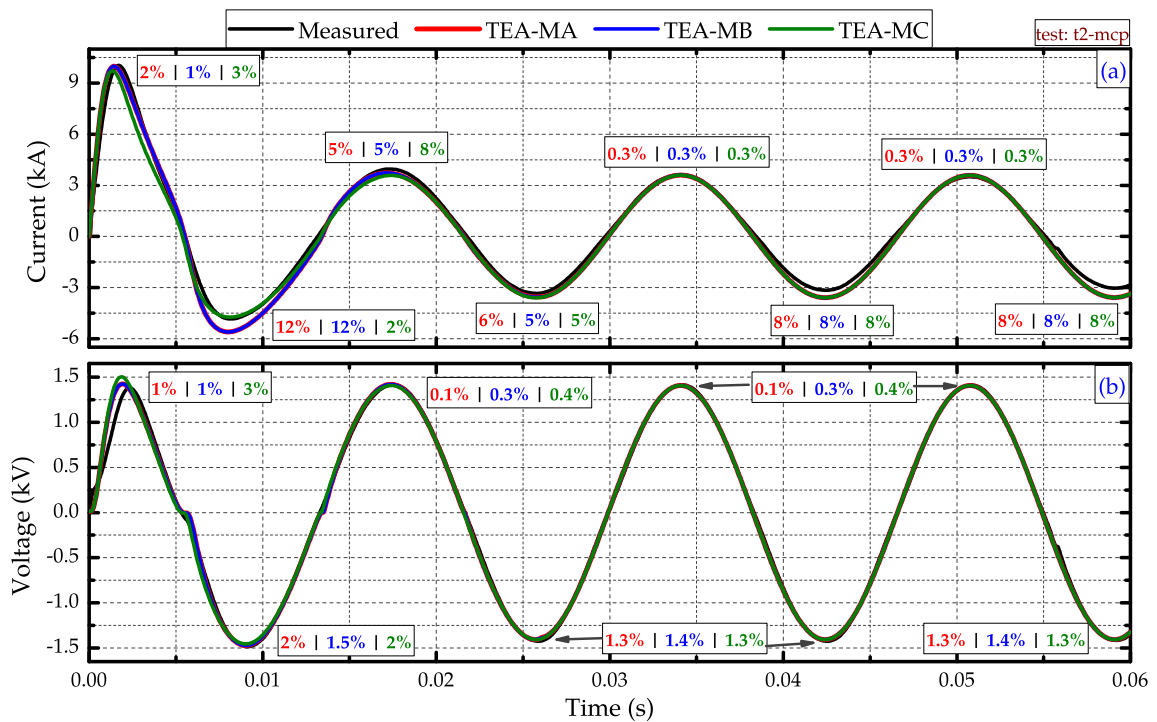


Figure 5.16: Comparison between measured and simulated results of the TEA model for a) limited current and b) voltage drop over the MCP-BSCCO-2212 assembly for test t2-mcp (fault current = 25.0 kA_{rms} under 1.0 kV_{rms}).

limited current and voltage drop over the assembly terminals.

Models TEA-MA and TEA-MB presents almost the same behavior and error values in the limited current and voltage drop curves. After the first current peak, the three models provide voltage curves with close error values.

As shown in figure 5.17, full quench takes place at approximately 0.026 s in models TEA-MA and TEA-MB whereas in the model TEA-MC it takes place at 0.020 s. The early quench in the model TEA-MC is accredited to the initial con-

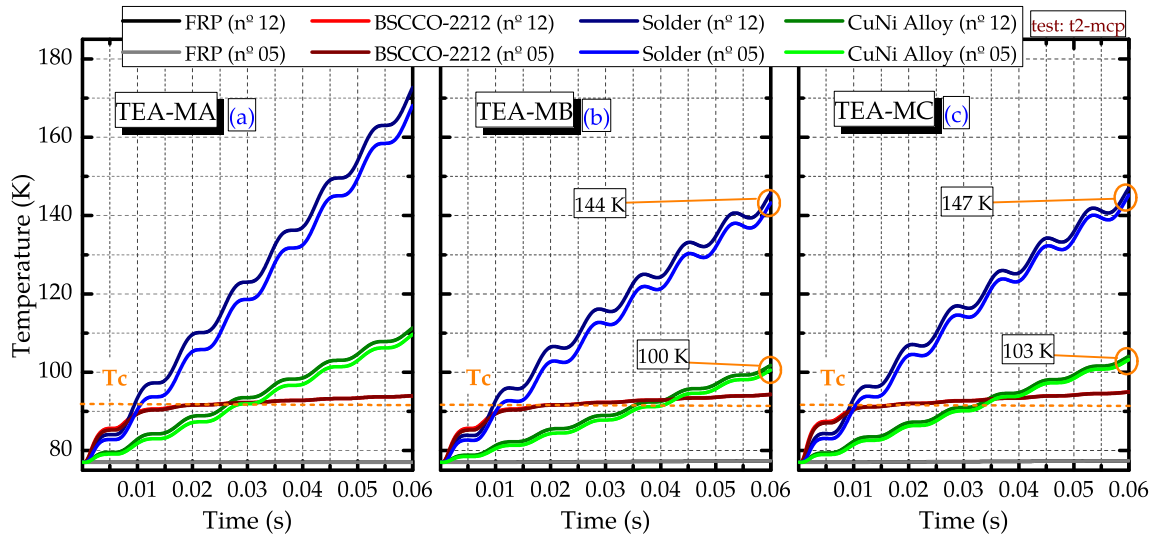


Figure 5.17: Temperature rise predicted by models TEA-MA, TEA-MB and TEA-MC during the fault period for test t2-mcp.

ditions of the modules; at the beginning of the fault period, model TEA-MC considers physical properties at 77 K whereas model TEA-MA and TEA-MB consider physical properties at 100 K during the fault period.

In other words, modules having physical properties at 77 K at the beginning of the fault (TEA-MC) have lower thermal inertia ⁵ in relation to those ones having physical properties at 100 K. That means the modules in model TEA-MC are easier heated than in models TEA-MA and TEA-MB at the beginning of the fault period.

Since the quench is faster in TEA-MC, current will start to flow earlier in CuNi layer than in TEA-MA and TEA-MB models. For this reason, final values of temperature calculated by model TEA-MC for that layers are slightly higher than those ones calculated by model TEA-MB. Final values of temperature calculated by model TEA-MA are the highest ones because of the absence of heat exchanges in the respective model.

Figure 5.18 presents the nonlinear behavior of the equivalent resistance during the fault period of test t2-mp for the three models. Models TEA-MA and TEA-MB present quit similar results, justifying the similar behavior in the limited current and voltage drop curves. Model TEA-MC present higher resistance values during the transient period, since in this model the heating rate is higher due the lower thermal inertia.

Figure 5.19 shows the results of simulations of the last performed test with the MCP-BSCCO-2212 assembly, t3-mcp. Limited current and voltage drop curves of

⁵One can roughly refer to thermal inertia as a measure of how fast the temperature of a material can be changed. It is dependent on its specific heat, its thermal conductivity, its dimensions, and other factors. Materials with a high volumetric heat capacity present high thermal inertia, consequently such materials will show small changes in temperature through a cycle.

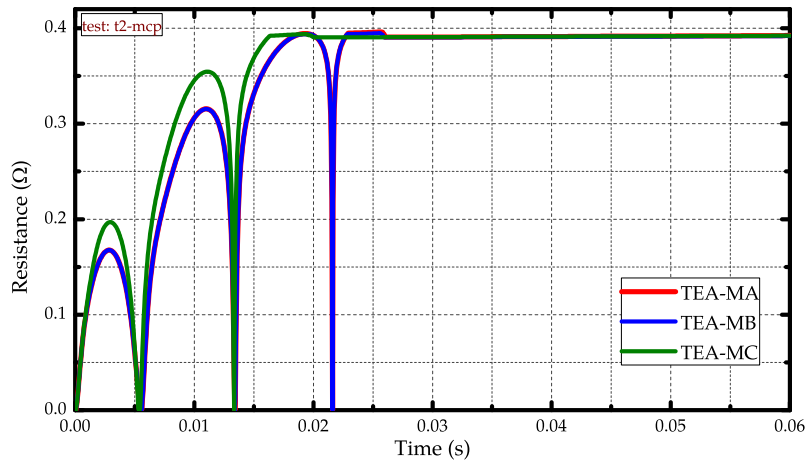


Figure 5.18: Comparison between equivalent resistances of the MCP-BSCCO-2212 assembly according to the models TEA-MA, TEA-MB and TEA-MC during the fault period in test t2-mcp.

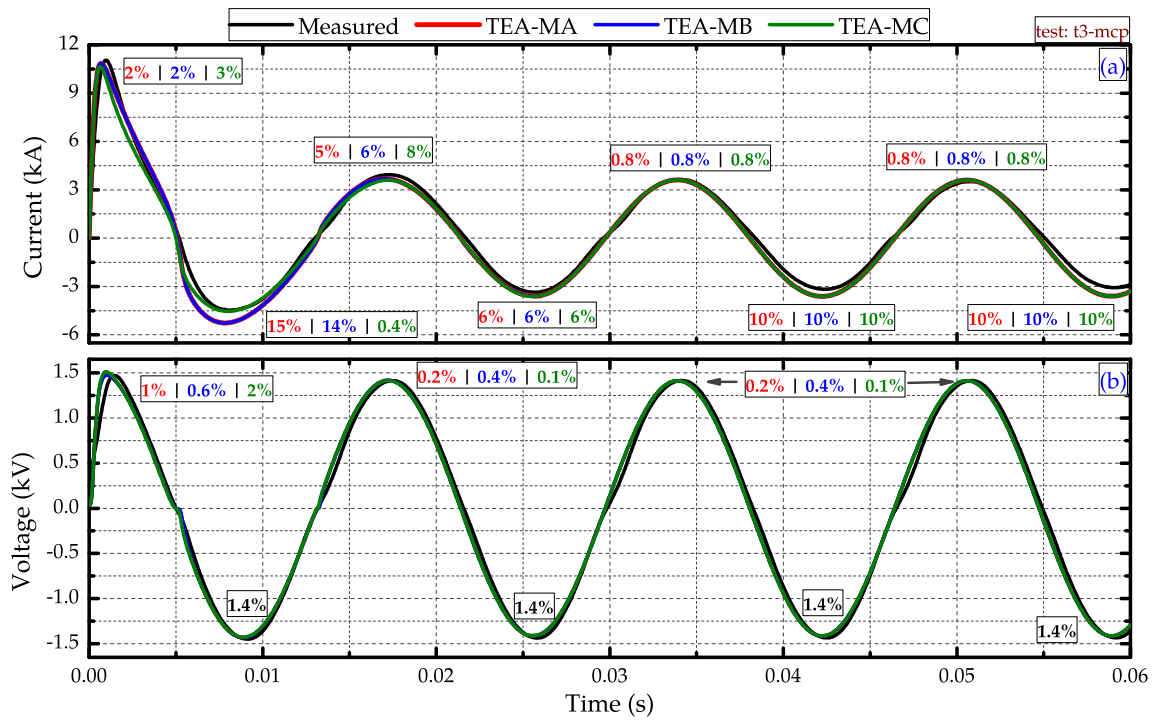


Figure 5.19: Comparison between measured and simulated results of the TEA model for a) limited current and b) voltage drop over the MCP-BSCCO-2212 assembly for test t3-mcp (fault current = 67.0 kA_{rms} under 1.0 kV_{rms}).

simulation follow the same behavior of the measured ones. Once again, models TEA-MA and TEA-MB present similar behaviors and close error values during. The highest error value occurs for model TEA-MA at the third current peak (15%) whereas the lowest value occurs for all models at fifth and seventh current peaks.

Errors involved in the simulation of voltage drop over the assembly terminals are small, since there is a good agreement between measured and simulated results

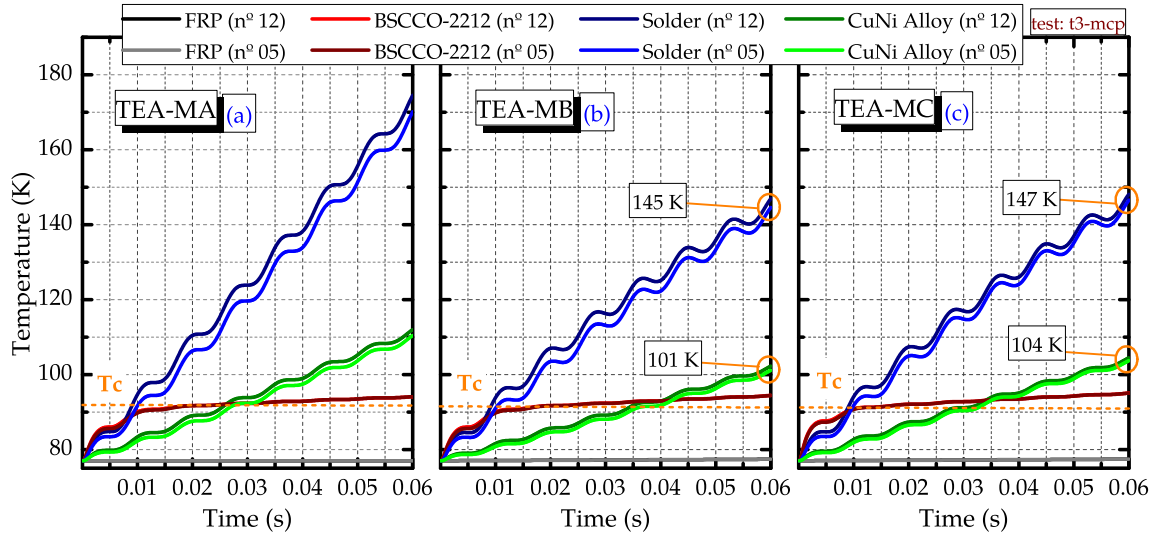


Figure 5.20: Temperature rise predicted by models TEA-MA, TEA-MB and TEA-MC during the fault period for test t3-mcp.

The temperature behavior of the three models for the test t3-mcp is shown in figure 5.20. According to the results, full quench takes place at 0.025 s for model TEA-MA, 0.026 s for model TEA-MB and 0.020 for model TEA-MC. As in the two previous cases, temperature values calculated by model TEA-MA present higher values during the fault period since all generated heat is not exchanged between the layers and with liquid nitrogen bath.

Because of the initial conditions at 77 K, final values of temperature for model TEA-MC are slightly higher than those ones of model TEA-MB.

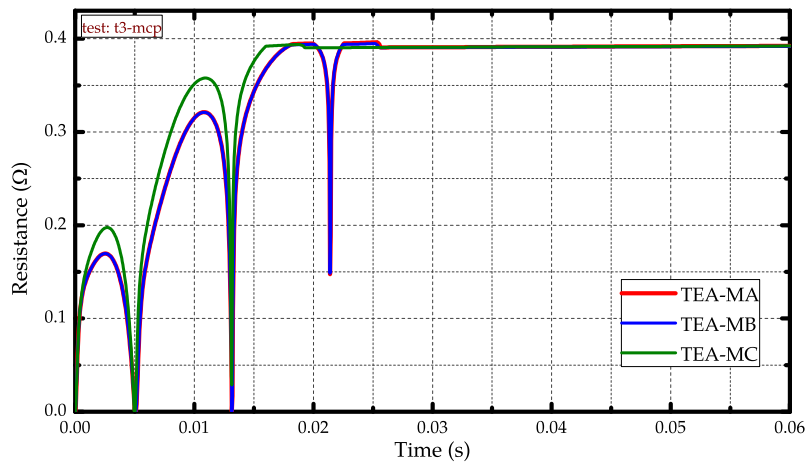


Figure 5.21: Comparison between equivalent resistances of the MCP-BSCCO-2212 assembly according to the models TEA-MA, TEA-MB and TEA-MC during the fault period in test t3-mcp.

Figure 5.21 shows resistance values during the transient of fault. These curves behave similarly to the resistance curves of tests t1-mcp and t2-mcp; it is highly non linear and models TEA-MA and TEA-MB show similar results.

5.5.2 YBCO 2G Coil Results

Results of simulation for the YBCO 2G coil have been performed using the thermal-electric circuit shown in figure 5.9. Figure 5.22 compares results obtained by means of models TEA-MA, TEA-MB and TEA-MC with measurements. Model TEA-MA presents highest values of error $\%E$ for the simulated limited current. Conversely, models TEA-MB and TEA-MC achieved small errors.

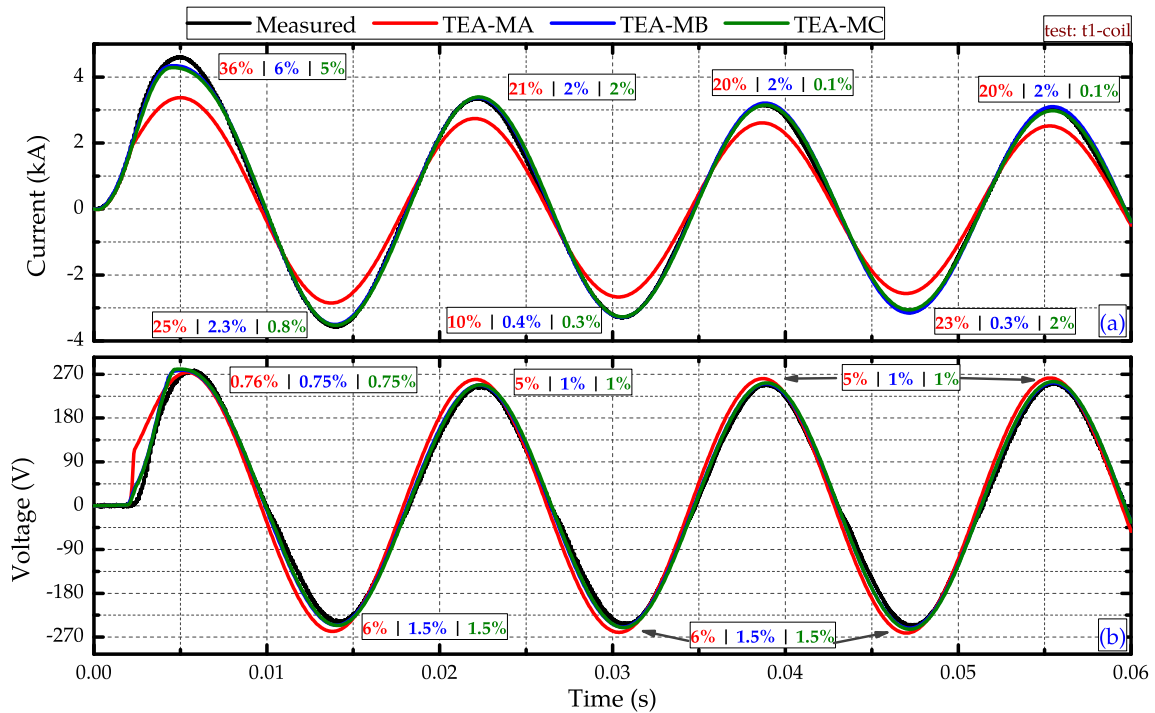


Figure 5.22: Comparison between measured and simulated results of the TEA model for a) limited current and b) voltage drop over the YBCO 2G coil for test t1-coil (fault current = 5.0 kA_{rms} under 200 V_{rms}).

Results of voltage drop over the coil terminals present small error values for the three models. However, the curve obtained by model TEA-MA presents large discrepancy in relation to the measured data at the first semi cycle of current. Such behavior suggests an abrupt quench of the superconducting material at the beginning of the fault period. Indeed, as show by results of temperature rise for model TEA-MA in figure 5.23a, temperature of YBCO layer quickly reaches T_c (92 K at 0.002 s.), resulting in an abrupt change in the voltage curve.

Figure 5.23 illustrates the temperature increase during test t1-coil. The temperatures of tape 06 (lowest I_c) and tape 01 (highest I_c) are presented (see table 3.5).

Differences in the temperature increase between models TEA-MB and TEA-MC are noticeable. Final values of temperature calculated by model TEA-MC are higher than those ones calculated by model TEA-MB.

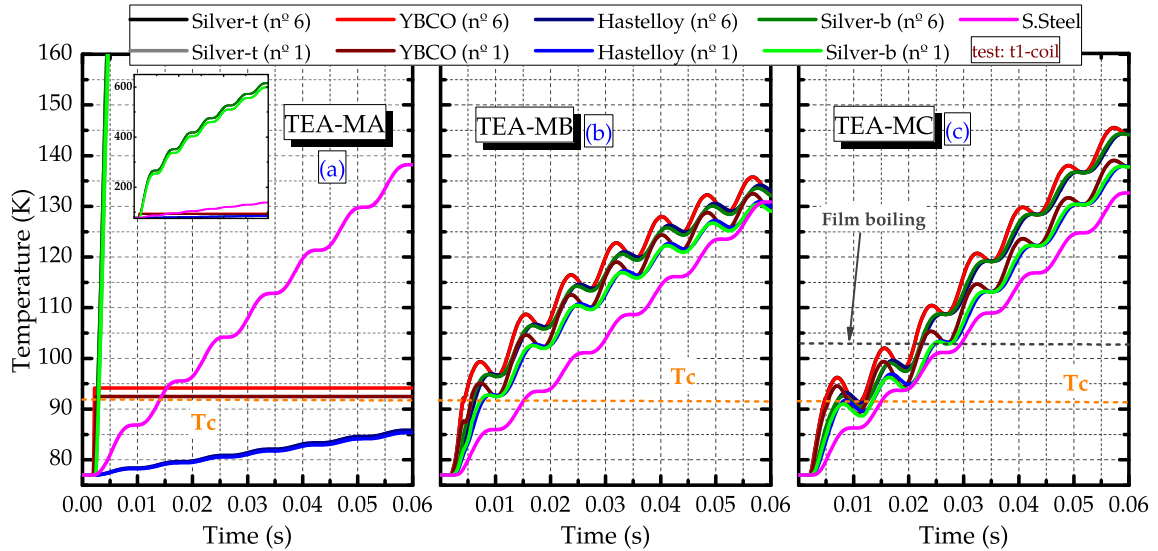


Figure 5.23: Temperature rise predicted by models TEA-MA, TEA-MB and TEA-MC during the fault period for test t1-coil.

Not only the initial conditions at 77 K of model TEA-MC have influence over this result, but also the convective heat exchange coefficient h_c . Model TEA-MC considers its dependence on temperature difference ΔT between the surfaces of the tapes and the LN_2 bath, as shown in figure 5.11 and section B.4 of appendix B. Highest values of h_c are found in the bubble boiling regime, that is, in the interval $2K > \Delta T > 26.5K$ (or, between $79K > T > 103.5K$). For temperatures higher than 103.5 K, h_c decreases to its lowest value, i.e., $0.03 W/K.cm^2$. As shown in figure 5.23c, between 20 ms and 30 ms, temperature values calculated by model TEA-MC reach 103.5 K. In that way, the convective heat transfer to the liquid nitrogen bath becomes hampered, leading to higher values of temperature.

Temperatures calculated by model TEA-MB do not suffer influence of changes in the h_c coefficient. Therefore, differences of temperature between the tapes in this simulation are only due to different values of critical current I_c .

The abrupt quench presented by model TEA-MA can be also noted in the resistance behavior. As shown in figure 5.24, the resistance calculated by means of TEA-MA promptly increases at the beginning of the fault period. Furthermore, these resistances values are higher than those ones calculated by models TEA-MB and TEA-MC. The fast quench, high value of temperature (see inset in figure 5.23a) and high resistance value presented by model TEA-MA are strongly related to the absence of heat exchanges in the model.

Still on figure 5.24, models TEA-MB and TEA-MC present almost the same behavior. However, because of the lower temperature values obtained by model TEA-MB at the end of the fault period, its calculated resistance is also lower than that one calculated by model TEA-MC at the same instant.

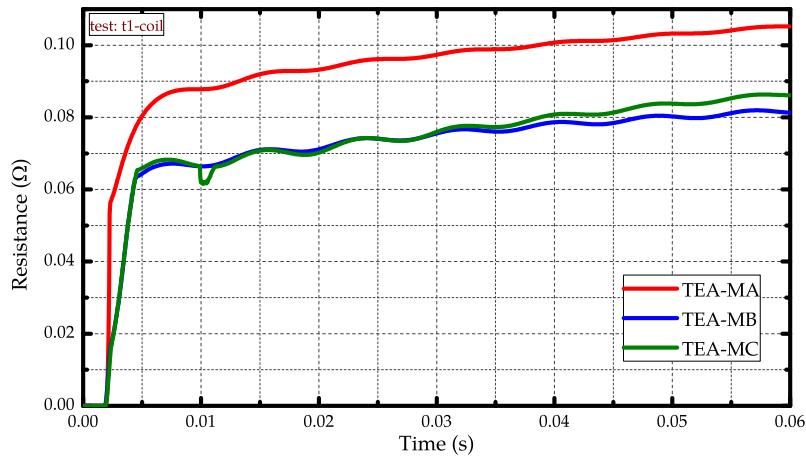


Figure 5.24: Comparison between equivalent resistances of the YBCO 2G coil according to the models TEA-MA, TEA-MB and TEA-MC during the fault period in test t1-coil.

Results obtained by means of model TEA-MA also presents high errors in the simulation of test t2-coil, as shown in figure 5.25.

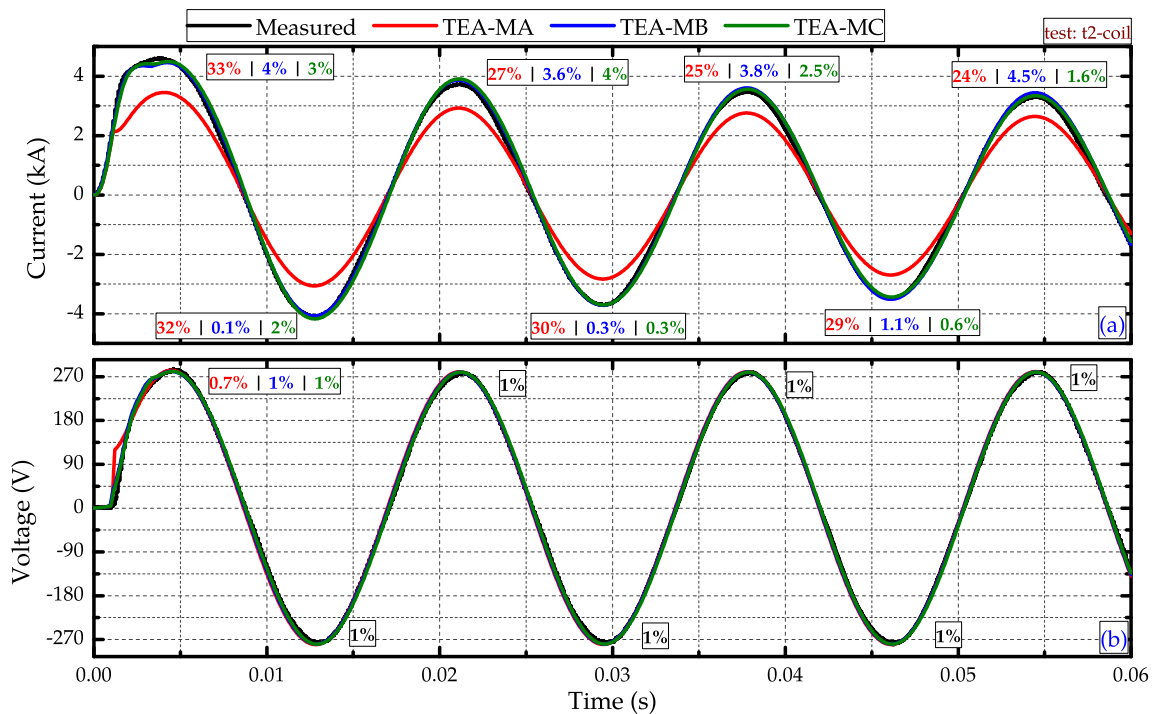


Figure 5.25: Comparison between measured and simulated results of the TEA model for a) limited current and b) voltage drop over the YBCO 2G coil for test t2-coil (fault current = 20.0 kA_{rms} under 200 V_{rms}).

On the other hand, models TEA-MB and TEA-MC provides tolerable errors in both curves. Errors involved in the voltage drop results calculated by model TEA-MA are also tolerable, but its behavior still presents discrepancies regarding the measured data at the first semi cycle of current.

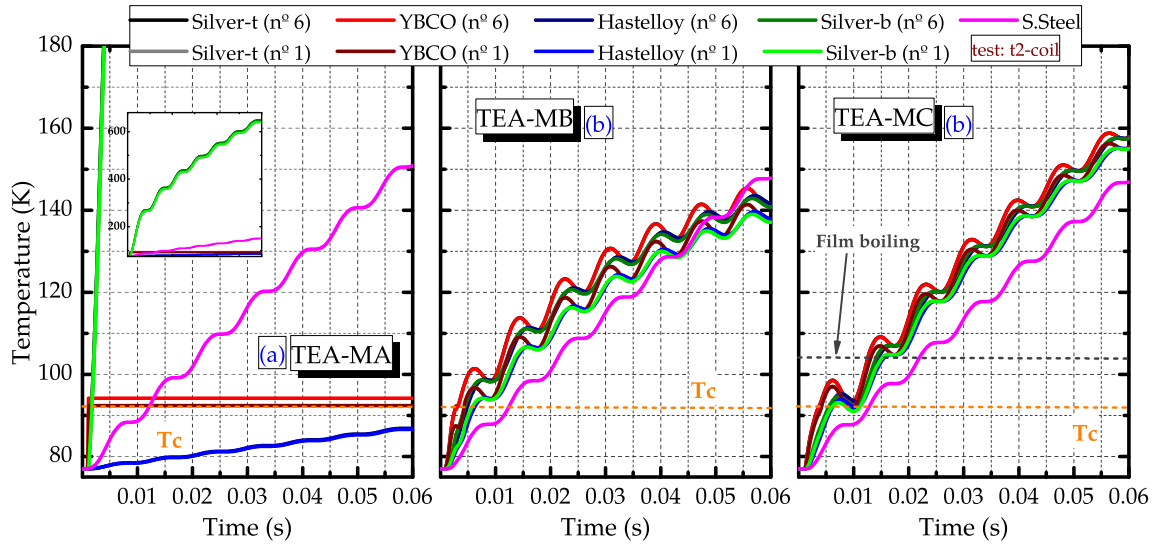


Figure 5.26: Temperature rise predicted by models TEA-MA, TEA-MB and TEA-MC during the fault period for test t2-coil.

As already discussed for the results of test t1-coil, calculated data may not match experimental results if heat exchange phenomena are ignored. In the case of test t2-coil, calculated temperature values also presents an abrupt increase for the YBCO material and overheating for the silver-b layer (inset in figure 5.26a).

Temperature results of models TEA-MB and TEA-MB presents the same characteristics discussed in test t1-coil. As shown in figure 5.26c, temperatures calculated by model TEA-MC quickly reach 103.5 K, leading the h_c coefficient to its lowest value and, consequently, hampering the convective heat transfer from the tapes to the LN_2 bath.

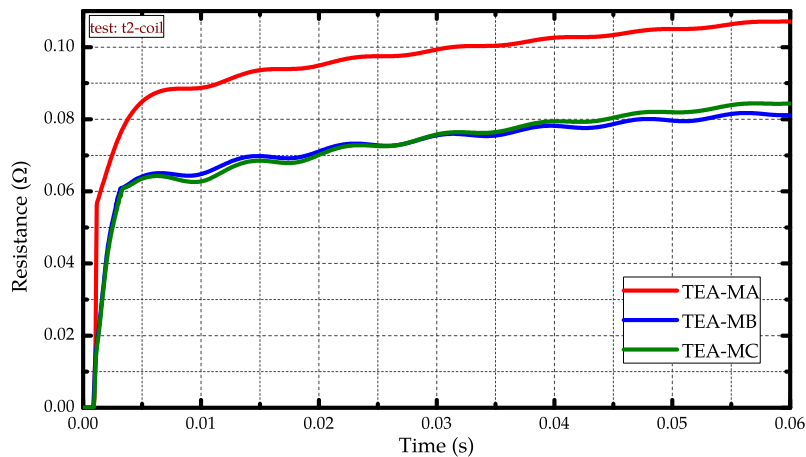


Figure 5.27: Comparison between equivalent resistances of the YBCO 2G coil according to the models TEA-MA, TEA-MB and TEA-MC during the fault period in test t2-coil.

Figure 5.27 shows the resistance behavior obtained by the three models. Model TEA-MA presents the highest values since there is not heat flux to LN_2 bath, lead-

ing to an overheating of all layers and, consequently, to higher values of resistance. Models TEA-MB and TEA-MC differs slightly from each other. Comparing both behaviors however, higher resistance values for model TEA-MB at the beginning of the linear behavior can be noted, since at this time there is an increase on the h_c coefficient in model TEA-MC. At about 0.025 s. both models provides the same value of resistance because the h_c coefficient is dropping at this moment in model TEA-MC. Final resistance value calculated by model TEA-MC becomes higher than that one calculated by model TEA-MB because the h_c coefficient reached its lowest value.

Comparisons between measured data and simulated ones for test t3-coil are shown in figure 5.28.

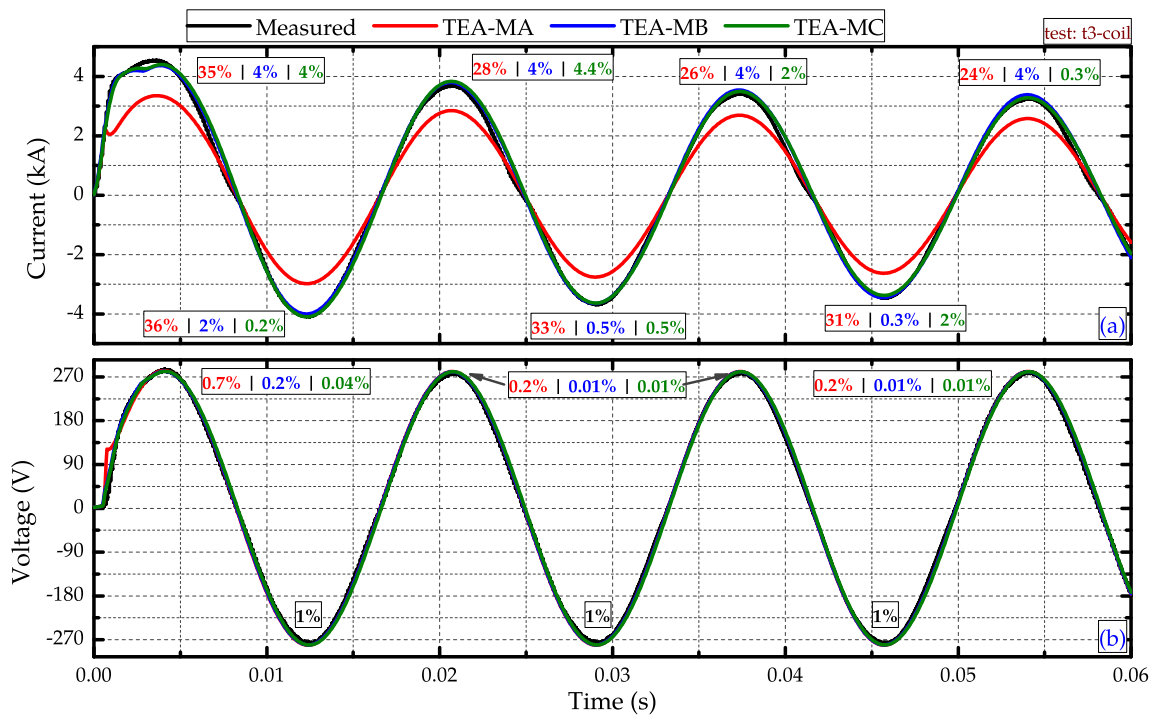


Figure 5.28: Comparison between measured and simulated results of the TEA model for a) limited current and b) voltage drop over the YBCO 2G coil for test t3-coil (fault current = 30.0 kA_{rms} under 200 V_{rms}).

The same characteristics of the previous tests can be found. Model TEA-MA presents the highest values of error in the limited current whereas models TEA-MB and TEA-MC present the lowest ones. In the voltage drop curves, the three models present lower error values, but model TEA-MA still has a discrepancy at the beginning of the fault period related to the fast quench of the YBCO material.

Values of temperature shown in figure 5.29a show similar behavior of those ones shown in figures 5.23a and 5.26a; a fast increase in the YBCO temperature and overheating of layer silver-b (see inset in figure 5.29 for model TEA-MA).

Temperatures calculated by models TEA-MB and TEA-MC do not present

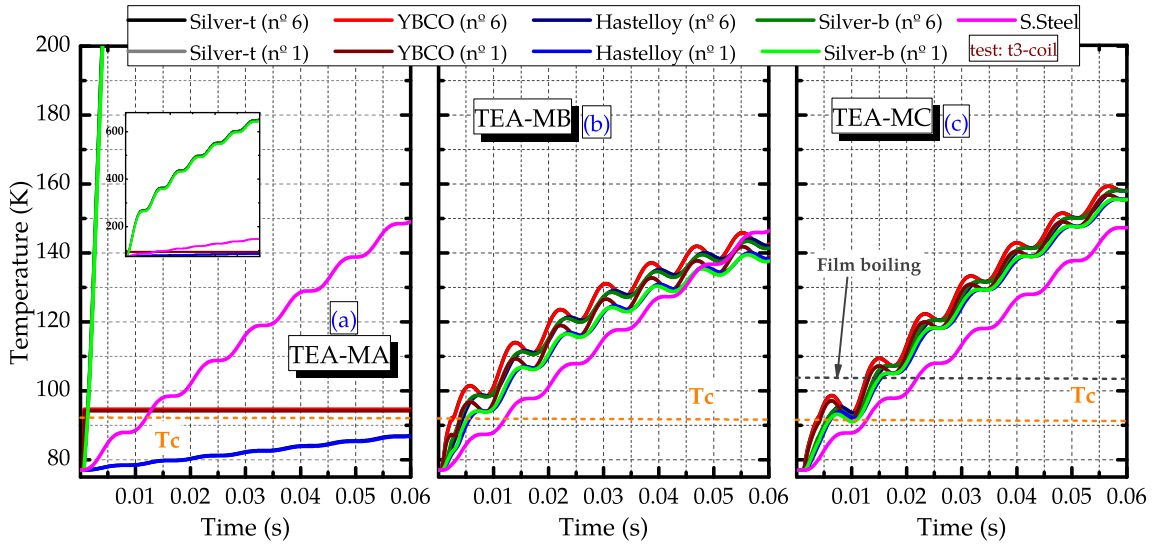


Figure 5.29: Temperature rise predicted by models TEA-MA, TEA-MB and TEA-MC during the fault period for test t3-coil.

overheating. However, model TEA-MC provides higher values in comparison to model TEA-MB since the film boiling regime of h_c coefficient is fast reached.

Figure 5.30 shows the resistance behavior for test t3-coil. The differences between TEA-MB and TEA-MC can be still attributed to the film boiling regime of the h_c coefficient in the TEA-MC model, as previously suggested in test t2-coil.

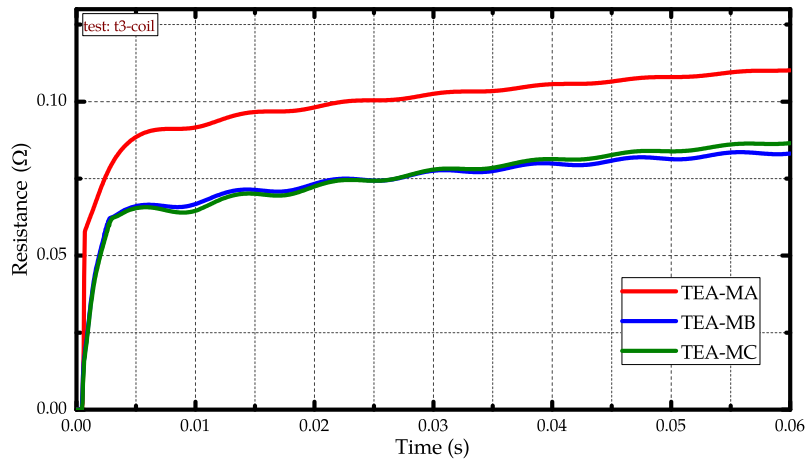


Figure 5.30: Comparison between equivalent resistances of the YBCO 2G coil according to the models TEA-MA, TEA-MB and TEA-MC during the fault period in test t3-coil.

5.5.3 Air Coil Results

Results of simulation for the AC-SFCL have been achieved using the thermal-electric circuit shown in figure 5.10. Figure 5.31 compares measured data with simulation results for the t1-acsfcl.

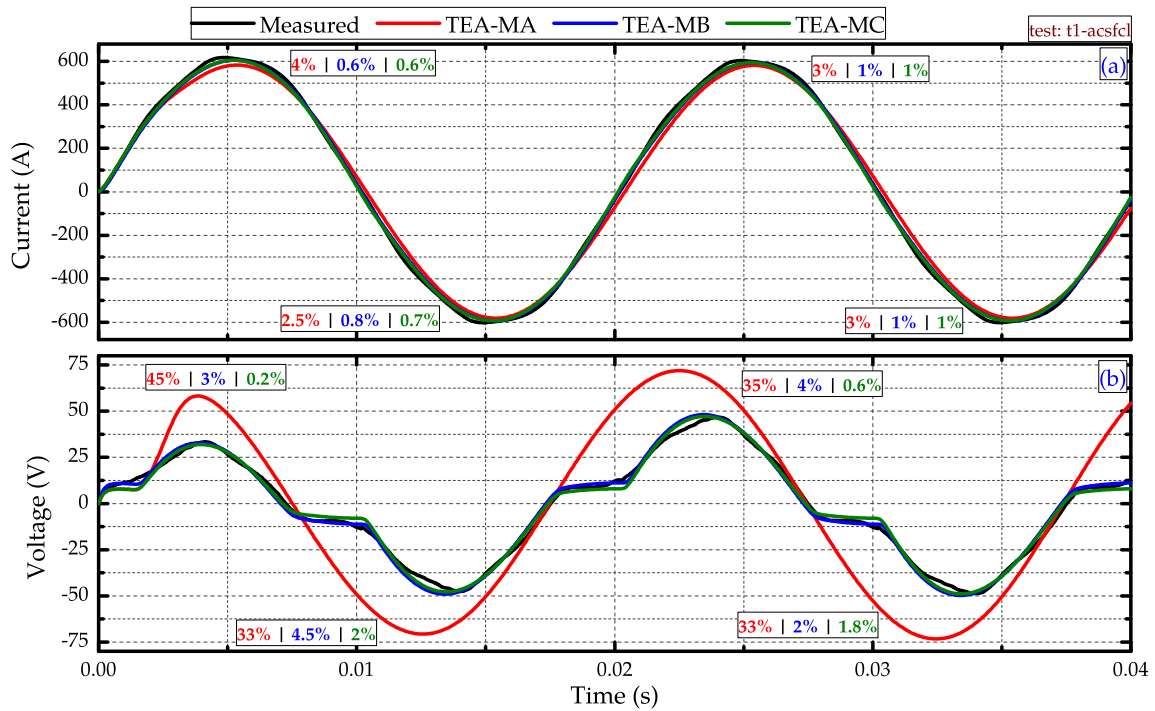


Figure 5.31: Comparison between measured and simulated results of the TEA model for a) limited current and b) voltage drop over the Air Coil SFCL for test t1-acsfcl (fault current = $450 A_{rms}$ under $400V_{rms}$).

Although the developed models agree well with the measured data for limited current, model TEA-MA presents a high discrepancy with the measured voltage drop in the air-coil SFCL, having a maximum percentage error equals to 45% at the first current peak. Models TEA-MB and TEA-MC present just small deviations from measured data for the voltage drop, with only 4.5% of maximum percentage error for model TEA-MB.

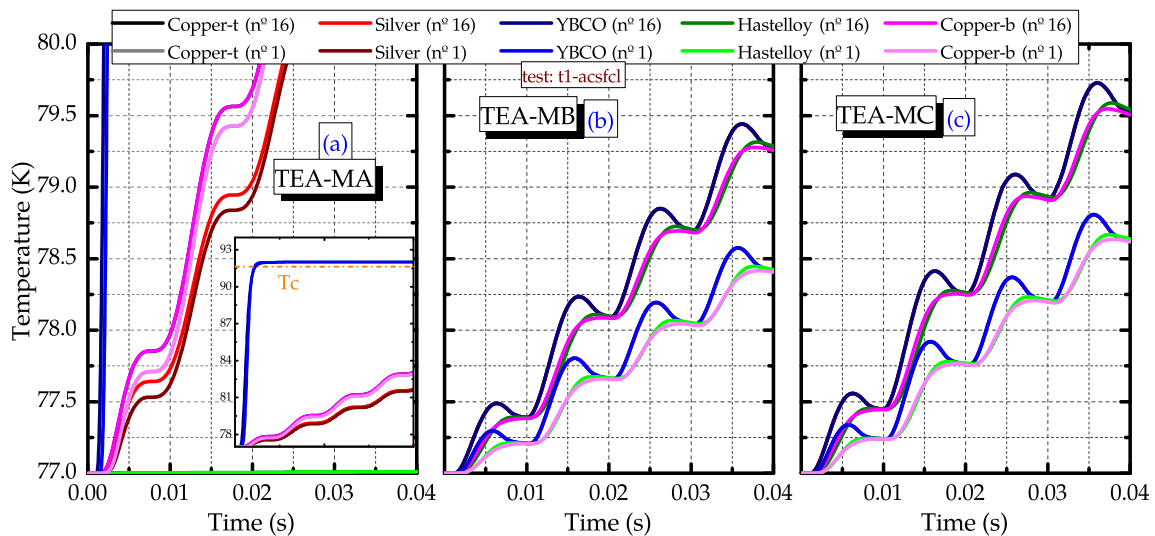


Figure 5.32: Temperature rise predicted by models TEA-MA, TEA-MB and TEA-MC during the fault period for test t1-acsfcl.

Figure 5.32 presents the behavior of temperature for the three models. Temperature of the modules with lowest and highest value of critical current I_c are presented. In this case, tapes number 16 and 01 respectively (see table 3.6). The absence of heat exchanges in model TEA-MA causes a fast heating of the tapes, as shown in figure 5.32a.

It is also possible to note in figure 5.32 higher values of temperature calculated by model TEA-MC in comparison with those ones calculates by model TEA-MB. Final temperature values do not go up 80 K, indicating that h_c coefficient barely comes into the bubble boiling regime in the case of model TEA-MC. Hence, the h_c coefficient present same value in models TEA-MB and TEA-MC for this test. The higher heating predicted by model TEA-MC is explained by the initial conditions of the models; in the model TEA-MB all physical properties are assumed constants at 100 K whereas in model TEA-MC they are temperature dependent, as already discussed in test t2-mcp.

An important feature to be noted in this test is that the YBCO layer does not quench; according to models TEA-MB and TEA-MC, the temperature of the YBCO layer does not reach the critical temperature T_c (92 K), supporting the presumption made in section 3.2.1.3.

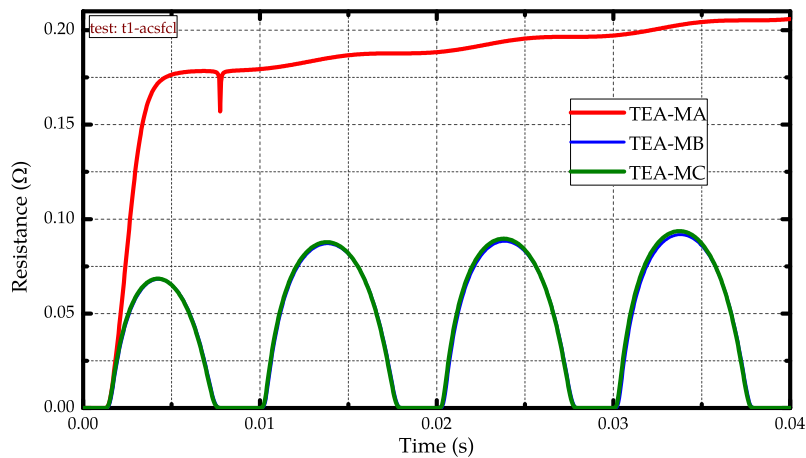


Figure 5.33: Comparison between equivalent resistances of the HTS tapes in the AC-SFCL according to the models TEA-MA, TEA-MB and TEA-MC during the fault period in test t1-acsfcl.

Figure 5.33 presents the results for the equivalent resistance of the HTS tapes in the AC-SFCL for the three models. The high voltage presented by model TEA-MA is due the high equivalent resistance developed during the fault period. Differences between model TEA-MB and TEA-MC are small and also present a highly non linear behavior in comparison with that one presented by model TEA-MA. According to the data calculated by model TEA-MA, there is occurrence of quenching of the superconducting material due the absence of heat exchanges

(see inset in figure 5.32a).

Figure 5.34 presents comparisons between measured and simulated data for test t2-acsfcl. All models present almost the same behavior for the limited current. Errors presented by model TEA-MA are smaller than those ones presented in test t1-acsfcl, but are still higher than those ones presented by models TEA-MB and TEA-MC.

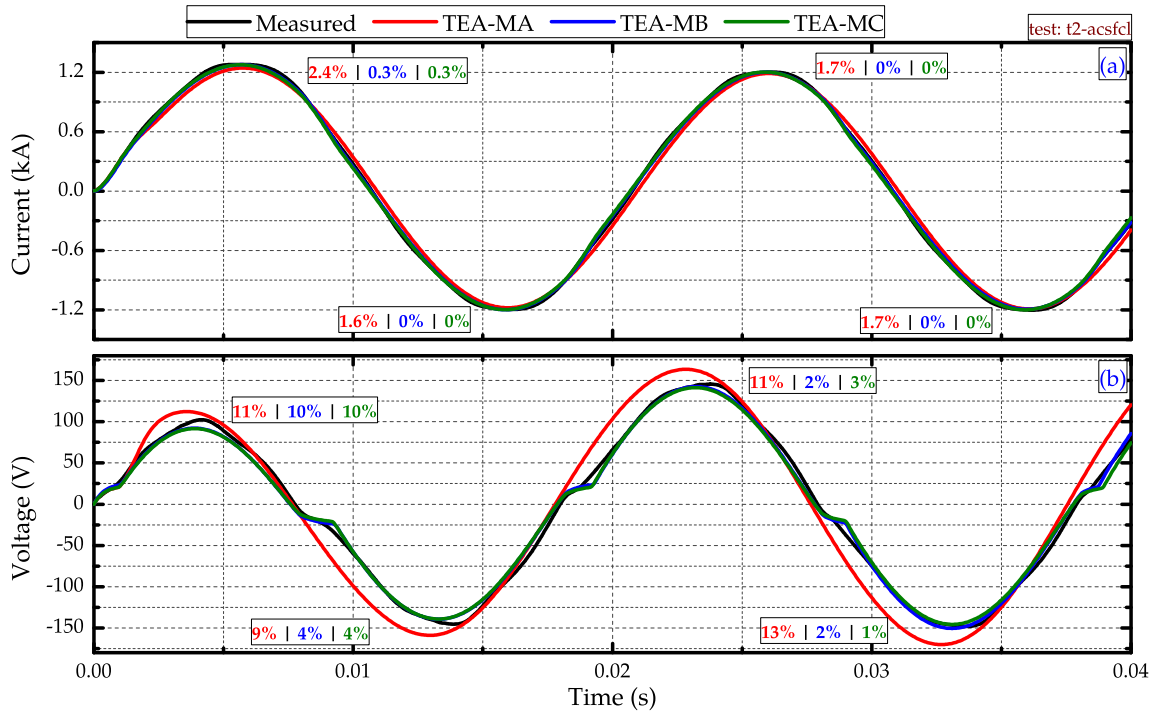


Figure 5.34: Comparison between measured and simulated results of the TEA model for a) limited current and b) voltage drop over the Air Coil SFCL for test t2-acsfcl (fault current = 1.05 kA_{rms} under 400V_{rms}).

Errors presented by model TEA-MA for the voltage drop curve are also smaller than those ones presented in test t1-acsfcl, but simulated data for test t2-acsfcl still does not follow the behavior of the measurements. Models TEA-MB and TEA-MC present small errors, however, small disagreements regarding the measured data around zero crossing can be noted.

Figure 5.35 presents the calculated temperature for each model. As in the previous test, TEA-MA present the highest temperature values. Moreover, TEA-MA predicts the quench of the YBCO material, what is not predicted by models TEA-MB and TEA-MC.

According to models TEA-MB and TEA-MC the quench does not take place in this test. Model TEA-MB however presents temperature values higher than those ones presented by model TEA-MC. In this case, the initial values of the model TEA-MC does not play a significant role, since the h_c coefficient in the model TEA-MC coefficient fast reaches the bubble boiling regime, increasing the convective

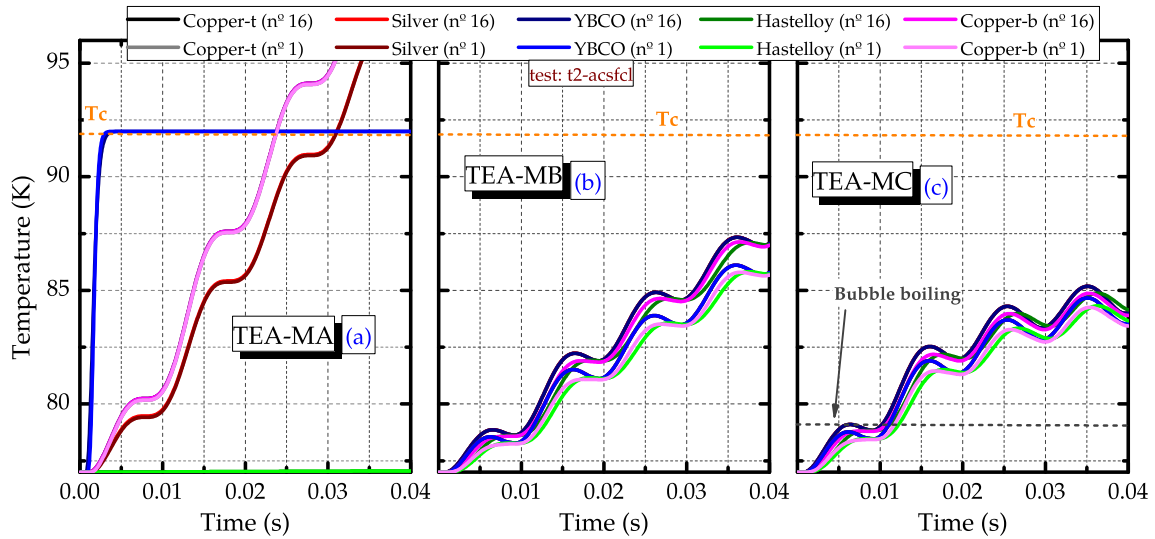


Figure 5.35: Temperature rise predicted by models TEA-MA, TEA-MB and TEA-MC during the fault period for test t2-acsfcl.

heat transfer to the LN_2 bath. Consequently, final temperature values calculated by TEA-MC are lower.

The non linear behaviors of resistance of the HTS tapes in the AC-SFCL for test t2-acsfcl are shown in figure 5.36. At the end of the fault period, one can note slightly differences between models TEA-MB and TEA-MC. Values presented by model TEA-MC are slightly lower at the end of the fault period, because of the lower temperature values. Values obtained by model TEA-MA are the highest ones, since it predicts the quench of the superconducting material.

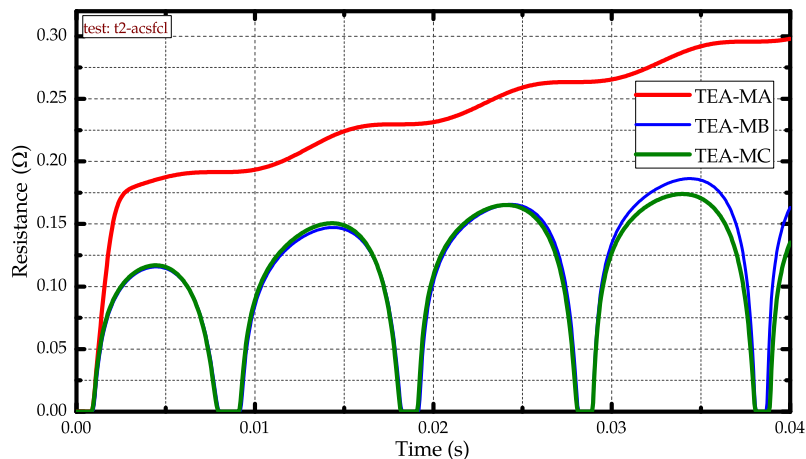


Figure 5.36: Comparison between equivalent resistances of the HTS tapes in the AC-SFCL according to the models TEA-MA, TEA-MB and TEA-MC during the fault period in test t2-acsfcl.

Figures 5.37 shows comparisons between measured and simulated results for test t3-acsfcl. Models TEA-MB and TEA-MC still presents lowest values for limited

current as well as for the voltage drop curves (excluding the first voltage peak where the lowest error value was obtained by model TEA-MA).

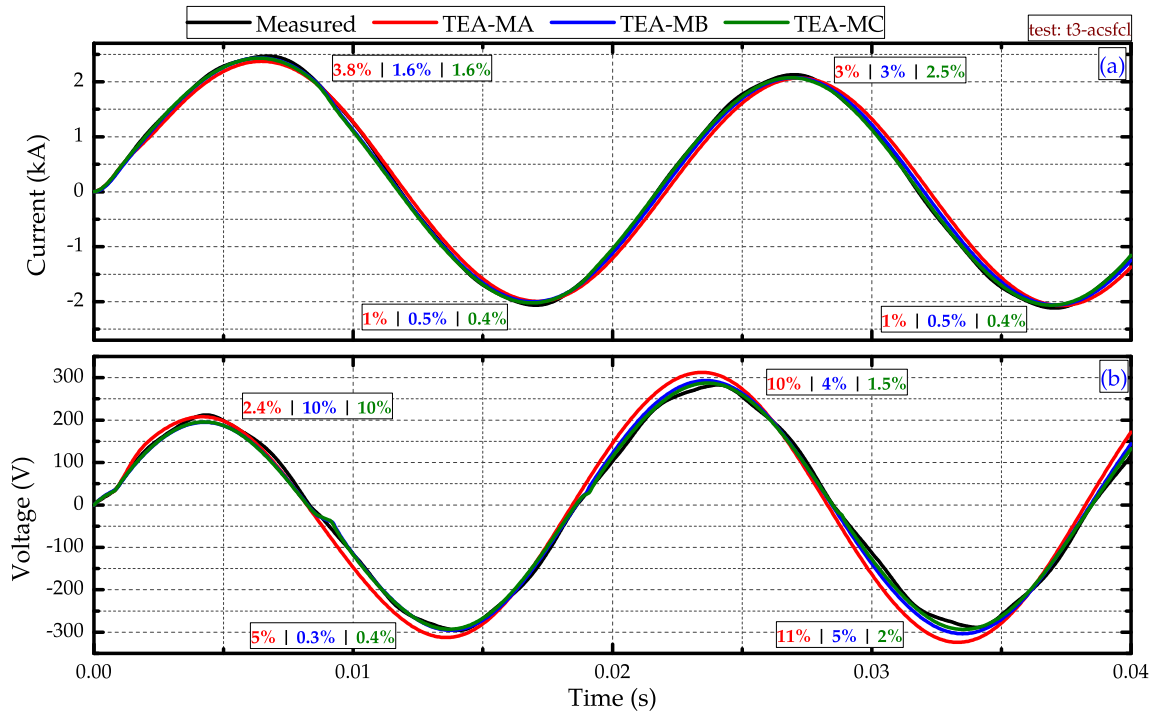


Figure 5.37: Comparison between measured and simulated results of the TEA model for a) limited current and b) voltage drop over the Air Coil SFCL for test t3-acsfcl (fault current = 2.55 kA_{rms} under 400V_{rms}).

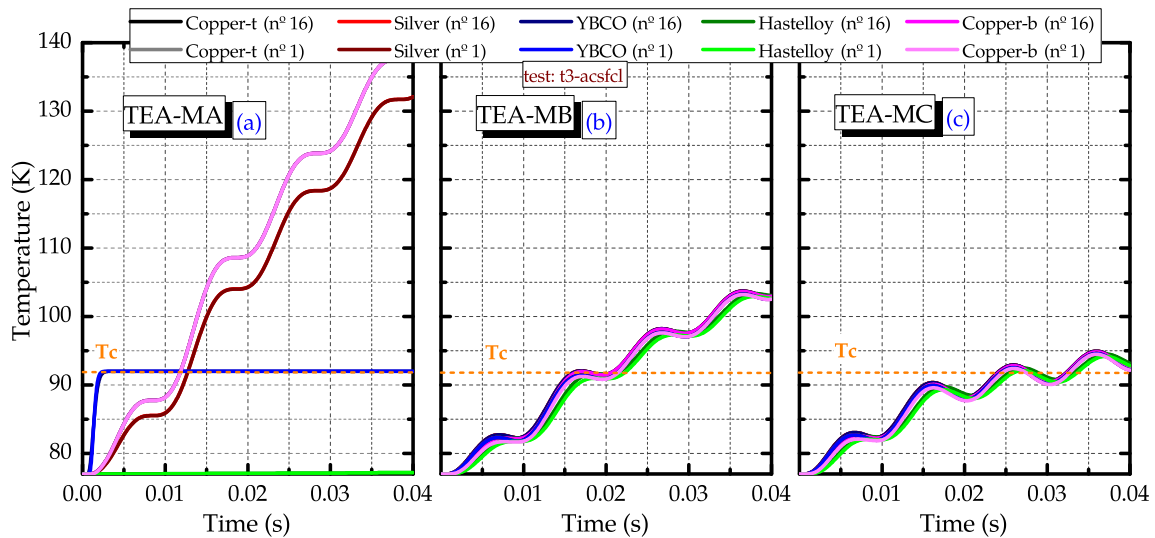


Figure 5.38: Temperature rise predicted by models TEA-MA, TEA-MB and TEA-MC during the fault period for test t3-acsfcl.

Differently than tests t1-acsfcl and t2-acsfcl, the quench is predicted for all the three models in the test t3-acsfcl. As shown in figure 5.38, not only in model TEA-MA the YBCO layer is quenched, but also in models TEA-MB and TEA-MC.

As discussed in test t2-acsfcl, the final values of temperature are higher in model TEA-MB than in model TEA-MC, since in the model TEA-MC, the h_c coefficient fast reaches the bubble boiling phase, increasing the heat losses to the LN_2 bath.

Figure 5.39 illustrates the evolution of equivalent resistance of the HTS tapes in the secondary of AC-SFCL for the three models in case of test t3-acsfcl. The linear behavior presented by model TEA-MA suggests a early quench of the YBCO layer, as shown in figure 5.38a whereas model TEA-MB presents linear behavior from 0.02 s. Model TEA-MC predicts the latest quench, i.e, it starts presenting linear behavior from 0.03 s..

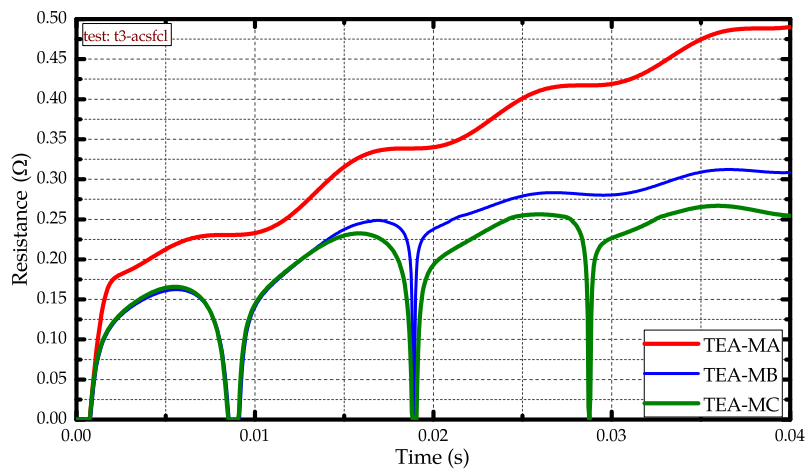


Figure 5.39: Comparison between equivalent resistances of the HTS tapes in the AC-SFCL according to the models TEA-MA, TEA-MB and TEA-MC during the fault period in test t3-acsfcl.

5.6 Summary and Discussions

This chapter has introduced the main concepts of the thermal-electrical analogy (TEA) method employed in simulations of superconducting fault current devices. The method allows to obtain good estimations of parameters that are experimentally of hard access, as temperature rise, quenching time and evolution of the equivalent resistance of the whole setup during the fault period. In addition, it was possible to insert individual values of I_c for each module and tape, making possible to develop a more realistic simulation.

By means of TEA method it was possible to investigate the influence of some parameters in the simulation results. Three different models have been created in order to analyze how much the results are affected by different considerations. Model TEA-MA was developed with no considerations about heat exchanges be-

tween the layers and the liquid nitrogen bath. Models like this one are frequently used in literature to simulate SFCL.

In the case of the MCP-BSCCO-2212 modules, model TEA-MA could reproduce almost the same behavior of measurements of limited current and voltage drop curves. In general, behaviors and errors of model TEA-MA are similar to those committed by model TEA-MB. Such similarities rise from the fact that heat exchanges do not play a fundamental role in the modules of MCP-BSCCO-2212 SFCL during the transient of high fault currents. In the case of low fault currents, as in the case of test t1-mcp, heat exchanges must be considered in order to reduce errors.

Model TEA-MA, however, may provide wrong heating rates. Absence of heat exchange in the modules means that each layer may store excessive thermal energy, leading to wrong information concerning temperature increase during fault. Indeed, a careful analyze of temperature values obtained by model TEA-MA always shows higher values compared to values obtained by the two other models.

Results obtained by means of model TEA-MA are worst in case of devices built with 2G tapes. The overheating of the layers creates resistance values higher than expected. In the case of the YBCO 2G coil, simulated data of limited current never matches with measured ones. For the AC-SCFL, voltage curves present high discrepancies between measurements and simulations as the fault current decreases.

A strong characteristic of model TEA-MA can be noted in its output behavior of temperature. For all simulated cases, temperature of the layers increases independently from each other, that is, according with TEA-MA model there will be always temperature gradient between the layers. In the case of the MCP-BSCCO-2212 modules, where considerable temperature gradients may exist due the mass and thickness of the layers, such feature plays a small role. Indeed, results obtained by models TEA-MB and TEA-MC (both take into account heat exchanges) for the MCP-BSCCO-2212 modules, show reasonable temperature gradient between the layers. That means, the adiabatic approximation (TEA-MA) may serve as a first approach for MCP BSCCO 2212 modules. But one must keep in mind that the adiabatic condition in case of MCP-BSCCO-2212 modules may provide temperatures higher than expected.

In the case of tapes, however, temperature gradients are very small since tapes are very thin. Indeed, such aspect could be predicted by models TEA-MB and TEA-MC; differences of temperature between layers of tapes are very small according to these models. Therefore, considering adiabatic conditions to simulate tapes of SFCL devices may not be a suitable choice since such condition may provide not only unrealistic temperature values, but also wrong temperature behavior during the fault period. As example, according to model TEA-MA, the YBCO

layer quickly quenches in test t1-acsfcl⁶ (figure 5.32a). It generates a wrong result of resistance (figure 5.33) that strongly affects the simulated voltage curve (figure 5.31b). According to the models considering heat exchanges (TEA-MB and TEA-MC), the superconducting material does not quench in this test.

Models TEA-MB and TEA-MC have provided results which agree well with measured data. Besides that, lower errors compared with those ones provided by adiabatic condition (TEA-MA model) in simulation of devices based on 2G tapes were committed. In general, these models could provide satisfactory results for all simulated cases. Differences on results obtained by these models are related to the convective heat transfer coefficient h_c as well as initial conditions of the modules and tapes. For the MCP-BSCCO-2212 modules, the rate of generated heat inside the layers are higher than the rate of heat flow to the liquid nitrogen bath. Thus, for the modules, increase and decrease of the h_c coefficient do not have a significant influence during the transient period. Small differences regarding temperature values between model TEA-MB and TEA-MB are mainly due different initial conditions set at each model. Since in model TEA-MC all materials are at 77 K at the beginning, they have a lower thermal inertia than those ones at 100 K in model TEA-MB. Modules with lower thermal inertia are faster heated. However, increasing the temperature also increases the thermal inertia. For this reason temperatures obtained by model TEA-MC does not reach huge values, but only slight differences of those ones obtained by means of model TEA-MB.

Influences of the convective heat transfer coefficient h_c are more noticeable when simulating tapes of limiting devices, as have been shown in the results of the YBCO 2G coil and AC-SFCL. Thermal inertia of the tapes are low (in comparison with modules) allowing a considerable influence of the h_c coefficient.

According to results of simulations performed to the YBCO 2G coil by means of model TEA-MC, tapes may be fast heated at the beginning of the fault period due its lower thermal inertia. Hence, the h_c coefficient fast reaches the film boiling regime, hampering the heat leakage to the LN_2 bath. This effect clearly generates higher temperatures than those ones obtained by model TEA-MB which does not consider the h_c curve illustrated in figure 5.11.

The convective heat transfer coefficient h_c plays a important role in the simulations of the tapes constituting the AC-SFCL device too. A careful comparison between behaviors of temperature calculated by models TEA-MB and TEA-MC for the tests t1-acsfcl and t2-acsfcl allows one to have a better understanding of the last mentioned aspects. According to model TEA-MC, temperature values in test t1-acsfcl increases faster than those ones of model TEA-MB. In this test, the h_c coefficient barely reaches the bubble boiling regime in model TEA-MC, remaining

⁶Test with AC-SFCL - fault current = 450 A_{rms} under 400V $_{rms}$

most of time in the free convection regime. Thus, for both models, the h_c coefficient has practically the same value (0.2 W/K.cm^2). Hence, higher values reached by model TEA-MC for test t1-acsfcl in comparison with values of TEA-MB model are due its initial conditions.

In the case of test t3-acsfcl however, h_c coefficient quickly reaches the bubble boiling regime. As shown in figure 5.35, the temperature behavior calculated by model TEA-MC is strongly affected by permanence of the h_c coefficient in this regime. It speeds up the heat flow to the liquid nitrogen bath, producing lower temperature values when compared with values of the TEA-MB model.

In a general way, one can consider the thermal electrical analogy method for further simulations of SFCL devices. In case of massive modules (as MCP-BSCCO-2212) the adiabatic condition can provide similar behavior to the measured ones. But in order to guarantee small errors of simulations and to obtain reliable estimation of temperature values and behavior, it is strongly recommended to employ simulations that take into account heat exchanges for modules and tapes. In case of simulating tapes, the influence of the h_c coefficient must not be neglected. Furthermore, the thermal electrical analogy method with heat exchanges was wearily tested in this chapter. It was tested under different conditions for three distinct SFCL concepts. The method was able to provide, in most of cases, satisfactory results with errors inside a tolerable margin. It is a powerful method which provides important and realist estimations that can not be achieved by means of the models presented in chapter 4, i.e, the time dependent and two branches models.

This method has been specially developed to take into account heat exchanges which do exist inside a SFCL device during the fault transient. Such feature makes possible transient analyzes, not only of the electrical network, but also of the inserted SFCL device. It is relatively easy inserting the TEA model in traditional power system simulations softwares, as for example, ATP/EMTP, MATLAB/Simulink, PsPice and PSCAD. Indeed, this model has been already used to investigate the installation of SFCL devices in electrical networks under fault conditions, as the work published in [141].

A drawback of the method is non possibility of inserting inhomogeneities of superconducting materials, as those ones shown in chapter 3. TEA model allows only one value of critical current per tape or module. Hence, a more detailed method is necessary to handle with inhomogeneity effects.

Chapter 6

Finite Difference Method

Alternating Direction Implicit Routine

Although the Thermal-electrical Analogy Method presents proper results to the transient behavior of the studied SFCLs, it does not allow the study of local variations of physical properties. In particular, it is not able to consider critical current inhomogeneities in the HTS material as well as variations of other properties along the material. In order to do so, a more advanced method is required. The Finite Difference Method (FDM) allows the study of inhomogeneities in each material composing a SFCL device. This chapter introduces the Alternating Direction Implicit Method (ADI) that consists of a FDM method for solving parabolic, hyperbolic and elliptic partial differential equations.

6.1 Finite Difference Basics

Finite difference methods offer a powerful technique for the solution of heat transfer problems. The domain in which solution is sought is replaced by a finite set of points and one tries to find approximate values for the temperature at these points. Values at these points are required to satisfy finite difference equations obtained either by replacing the governing partial differential equation in terms of partial difference quotients or by direct heat flow considerations.

The principle of finite difference methods is close to the numerical schemes used to solve ordinary differential equations. It consists in approximating the differential operator by replacing the derivatives in the equation using differential quotients. The domain is partitioned in space and in time and approximations of the solution are computed at the space or time points.

The main concept behind any finite difference scheme is related to the defini-

tion of the derivative of a smooth function φ at a point $x \in \mathbb{R}$:

$$\frac{\partial \varphi}{\partial x} = \lim_{\Delta x \rightarrow 0} \frac{\varphi(x + \Delta x) - \varphi(x)}{\Delta x} \quad (6.1)$$

When Δx tends to 0, the quotient on the right-hand side provides a good approximation of the derivative. In other words, Δx should be sufficiently small to get a good approximation. Considering the Taylor series expansion of the functions $\varphi(x + \Delta x)$ and $\varphi(x - \Delta x)$ around point x , as illustrated in figure 6.1a, one obtains [142]:

$$\varphi(x + \Delta x) = \varphi(x) + \Delta x \frac{\partial \varphi}{\partial x} + \frac{\Delta x^2}{2!} \cdot \frac{\partial^2 \varphi}{\partial x^2} + \frac{\Delta x^3}{3!} \cdot \frac{\partial^3 \varphi}{\partial x^3} + \dots \quad (6.2)$$

$$\varphi(x - \Delta x) = \varphi(x) - \Delta x \frac{\partial \varphi}{\partial x} + \frac{\Delta x^2}{2!} \cdot \frac{\partial^2 \varphi}{\partial x^2} - \frac{\Delta x^3}{3!} \cdot \frac{\partial^3 \varphi}{\partial x^3} + \dots \quad (6.3)$$

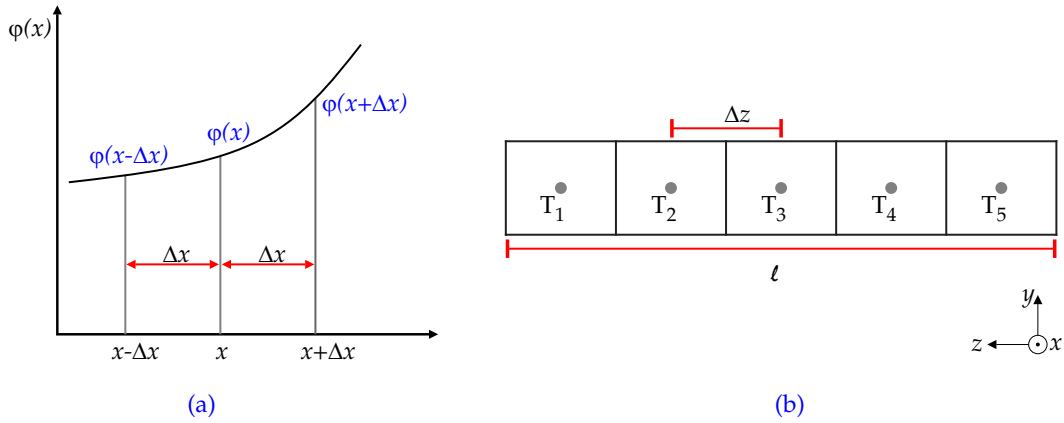


Figure 6.1: (a) Nomenclature for a Taylor series expansion and (b) a discretized material along the z -direction.

Now, solving equation (6.2) for $\partial\varphi/\partial x$, one obtains:

$$\frac{\partial \varphi}{\partial x} = \frac{\varphi(x + \Delta x) - \varphi(x)}{\Delta x} + O(\Delta x) \quad (6.4)$$

where $O(\Delta x)$ denotes the error involved in the local truncation of equation (6.2). One clearly sees that it is of order of step size Δx [143]. It measures the error by which the exact solution of a differential equation does not satisfy the difference equation at the grid points and are obtained by substituting the exact solution of the continuous problem into the numerical scheme. A necessary condition for the convergence of the numerical solutions to the continuous solution is that the local truncation error tends to zero as the step size goes to zero. In this case the method is said to be consistent.

In order to know the finite difference representation of the second derivative

$\partial^2\varphi/\partial x^2$, one sums equations (6.2) and (6.3), neglecting the 3th order terms, thus:

$$\varphi(x + \Delta x) + \varphi(x - \Delta x) = 2\varphi(x) + \Delta x^2 \frac{\partial^2\varphi}{\partial x^2}$$

$$\frac{\partial^2\varphi}{\partial x^2} = \frac{\varphi(x + \Delta x) - 2\varphi(x) + \varphi(x - \Delta x)}{\Delta x^2} \quad (6.5)$$

Consider now a material with length ℓ along the z-direction (figure 6.1b). In order to analyze the heat transfer along this direction, the one dimensional transient heat conduction equation must be taken into account:

$$\frac{\partial T}{\partial t} = \frac{k}{\gamma \varsigma} \frac{\partial^2 T}{\partial z^2} \quad (6.6)$$

Applying equations (6.4) and (6.5) in the derivatives of equation (6.6) yields

$$\frac{T_m^{\tau+1} - T_m^\tau}{\Delta t} = \frac{k}{\gamma \varsigma} \left[\frac{T_{m-1}^\tau - 2T_m^\tau + T_{m+1}^\tau}{\Delta z^2} \right] \quad (6.7)$$

Both τ and m are integers; τ varies from 1 to τ_f (total number of time steps) and m varies from 1 to n_z (total number of elements in z-direction). The next step is a rearrangement of the discretized equation, so that all known quantities (i.e. temperature at time τ) are on the right hand side and the unknown quantities on the left-hand side (properties at $\tau + 1$). This results in:

$$T_m^{\tau+1} = Fo T_{m-1}^\tau + (1 - 2Fo) T_m^\tau + Fo T_{m+1}^\tau \quad (6.8)$$

where Fo is a constant known as Fourier number and it is defined as [144]:

$$Fo = \frac{k}{\gamma \varsigma} \frac{\Delta t}{\Delta z^2} \quad (6.9)$$

Assuming that the temperature at the boundaries of the material illustrated in figure 6.1b are kept constant (T_1 and T_5), a matrix in the form $\mathbf{T}^{\tau+1} = \mathbf{A} \times \mathbf{T}^\tau$ can be written from equation (6.8):

$$\begin{bmatrix} T_1 \\ T_2 \\ T_3 \\ T_4 \\ T_5 \end{bmatrix}^{\tau+1} = \begin{bmatrix} 1 & 0 & 0 & 0 & 0 \\ Fo & 1 - 2Fo & Fo & 0 & 0 \\ 0 & Fo & 1 - 2Fo & Fo & 0 \\ 0 & 0 & Fo & 1 - 2Fo & Fo \\ 0 & 0 & 0 & 0 & 1 \end{bmatrix} \begin{bmatrix} T_1 \\ T_2 \\ T_3 \\ T_4 \\ T_5 \end{bmatrix}^\tau \quad (6.10)$$

6.2 Implicit Schemes

The major advantage of explicit finite difference methods, as that one shown in equation (6.10), is that they are relatively simple and computationally fast. However, the main drawback is that stable solutions are obtained only when the Courant-Friedrichs-Lewy (CFL) condition is satisfied [145]:

$$0 < Fo = \frac{k}{\gamma c} \frac{\Delta t}{\Delta z^2} < \frac{1}{2} \quad (6.11)$$

If the CFL condition is not satisfied, the solution becomes unstable and starts to wildly oscillate, as shown in figure 6.2. In order to guarantee the stability of the solution, one must concern about the choice of the time step Δt and the size of element Δz . For simulating 2G tapes, the value of Δz must be at maximum 1 μm , since this is the thickness of the HTS layer. In that way, in order to keep the Fourier number inside the stability limits, the highest time step Δt possible ¹ is 1.5×10^{-11} . It would hugely increase the time of simulation besides the computational requirements. For this reason an implicit method is more suitable.

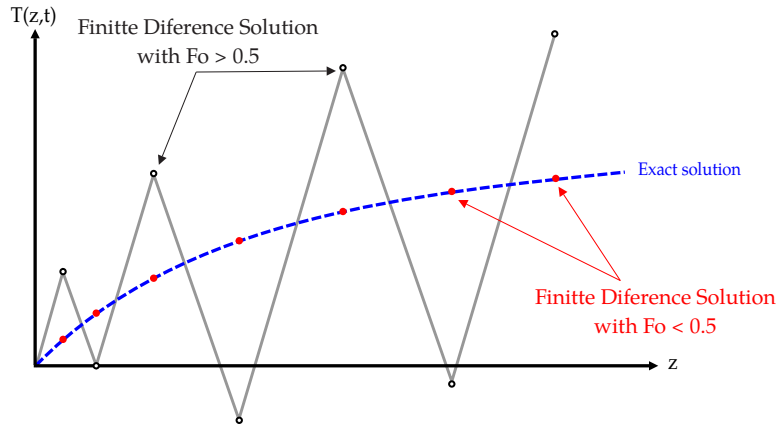


Figure 6.2: Effects of parameter Fo on the stability of FDM solution of the heat equation. Dots show the FDM solution for $Fo < 0.5$.

In implicit finite difference schemes, the spatial derivatives $\partial^2 T / \partial z^2$ are evaluated at the new time step ($\tau + 1$). The simplest implicit discretization of equation (6.6) is

$$\frac{T_m^{\tau+1} - T_m^\tau}{\Delta t} = \frac{k}{\gamma c} \left[\frac{T_{m-1}^{\tau+1} - 2T_m^{\tau+1} + T_{m+1}^{\tau+1}}{\Delta z^2} \right] \quad (6.12)$$

that can be rearranged so that unknown terms are on the left and known terms are on the right

$$-FoT_{m-1}^{\tau+1} + (1 + 2Fo)T_m^{\tau+1} - FoT_{m+1}^{\tau+1} = T_m^\tau \quad (6.13)$$

¹Considering the thermal conductivity and specific heat of YBCO at 100 K (see appendix B)

Adopting the discretization scheme for the material illustrated in figure 6.1b and still assuming the temperature at boundaries as constant, one has the following system of equations in the form $\mathbf{T}^{\tau+1} = \mathbf{A} \times \mathbf{T}^{\tau}$ to be implicitly solved:

$$\begin{bmatrix} T_1 \\ T_2 \\ T_3 \\ T_4 \\ T_5 \end{bmatrix}^{\tau+1} = \begin{bmatrix} 1 & 0 & 0 & 0 & 0 \\ -Fo & 1 + 2Fo & -Fo & 0 & 0 \\ 0 & -Fo & 1 + 2Fo & -Fo & 0 \\ 0 & 0 & -Fo & 1 + 2Fo & -Fo \\ 0 & 0 & 0 & 0 & 1 \end{bmatrix}^{-1} \begin{bmatrix} T_1 \\ T_2 \\ T_3 \\ T_4 \\ T_5 \end{bmatrix}^{\tau} \quad (6.14)$$

The main advantage of implicit finite difference methods described in equations (6.13) and (6.14) is that there are no restrictions on the time step Δt or in the element size Δz . Taking large time steps, however, may result in an inaccurate solution. Therefore it is always wise to check the results by decreasing the time step until the solution does not change anymore (converge check).

6.2.1 2D FDM Implicit Method

Since one aims to simulate the heat exchanges in the z -direction (along the thickness) and in the x -direction (along the length) of the tapes and modules of the studied SFCLs, it is worth analyzing the discretization of the heat equation by the implicit FDM method. Hence, for a 2D problem of heat transfer of a material with length ℓ and thickness ν (figure 6.3), the heat equation can be written as:

$$\frac{\partial T}{\partial t} = \frac{k}{\gamma \varsigma} \left[\frac{\partial^2 T}{\partial z^2} + \frac{\partial^2 T}{\partial x^2} \right] \quad (6.15)$$

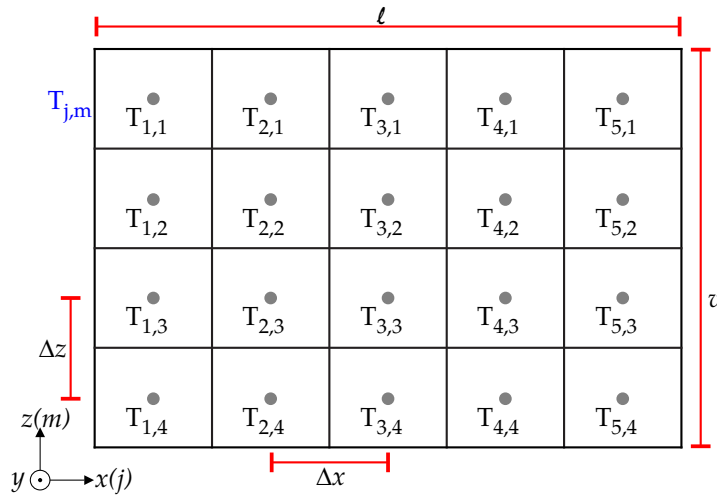


Figure 6.3: Discretization for the 2D FDM scheme.

One applies now equations (6.4) and (6.5) in the derivatives of equation (6.15)

in order to obtain its discretized version:

$$\frac{T_{j,m}^{\tau+1} - T_{j,m}^{\tau}}{\Delta t} = \frac{k}{\gamma \varsigma} \left[\frac{T_{j-1,m}^{\tau+1} - 2T_{j,m}^{\tau+1} + T_{j+1,m}^{\tau+1}}{\Delta x^2} + \frac{T_{j,m-1}^{\tau+1} - 2T_{j,m}^{\tau+1} + T_{j,m+1}^{\tau+1}}{\Delta z^2} \right] \quad (6.16)$$

Here j varies from 1 to n_x (total number of grid points in x -direction) and m varies from 1 to n_z (total number of grid points in z -direction). Rearranging to put terms with $\tau + 1$ on the left-hand-side and terms with τ on the right-hand-side gives

$$-Fo_z T_{j,m-1}^{\tau+1} + (1 + 2Fo_z + 2Fo_x) T_{j,m}^{\tau+1} - Fo_z T_{j,m+1}^{\tau+1} - Fo_x T_{j-1,m}^{\tau+1} - Fo_x T_{j+1,m}^{\tau+1} = T_{j,m}^{\tau} \quad (6.17)$$

where

$$Fo_z = \frac{k}{\gamma \varsigma} \frac{\Delta t}{\Delta z^2} \quad (6.18)$$

$$Fo_x = \frac{k}{\gamma \varsigma} \frac{\Delta t}{\Delta x^2} \quad (6.19)$$

Trying to write equation 6.17 in the matrix form $\mathbf{T}^{\tau+1} = \mathbf{A} \times \mathbf{T}^{\tau}$, as before, may be a bit more complicated than in the 1D case, since one must deal with book-keeping issues, that is, the nodes would have to be numbered continuously and it would entail in large matrices. For a 2D problem with $n_z \times n_x$ internal points, $(n_z \times n_x)^2 \times (n_z \times n_x)^2$ equations have to be solved at every time step. This quickly fills the computer memory.

Some methods have been proposed in order to solve the implicit form of the discretized heat equation (6.17). One of them is the so called alternating direction implicit (ADI) method [146, 147]. It is an attractive option to use in avoiding the Courant-Friedrichs-Lewy condition that limits the size of the time step required by explicit finite difference methods for stability.

Implicit methods like Crank-Nicholson offer the same advantages as ADI methods but they do not rely on simple, one-dimensional, tridiagonal system solvers for which there are well-known fast solution methods [148]. The ADI method for simulations of SFCLs is fully described in section 6.4.

6.3 Model for SFCLs

As the thermal-electrical analogy method, presented in the chapter 5, the routine of solution is divided into two parts. The first one remains the same of that one presented in section 5.3.1, i.e., it firstly obtains the solutions of equations (5.18) or (5.19) for the electrical equivalents illustrated in figures 5.3 and 5.5, respectively. Again, the electrical solution is obtained by numerical integration using the RK4 method and the outputs from the electrical solution serves as the inputs to the thermal solution.

The second part, related to the solution of the thermal problem, makes use of the described FDM method, in order to obtain a local solution for the temperature of all layers of the tapes and modules. It allows considerations of critical current I_c inhomogeneities along the HTS material.

6.3.1 Thermal Problem Description

Before describing the applied FDM method to solve the heat conduction equations, some new assumptions about layers and configuration of each SFCL component must be made. For the sake of simplicity, the layered geometries depicted in figure 6.4 were used to perform the local thermal analysis of the SFCLs devices. It shows a simplified schematic drawn of the layers of each limiter (figure out of scale).

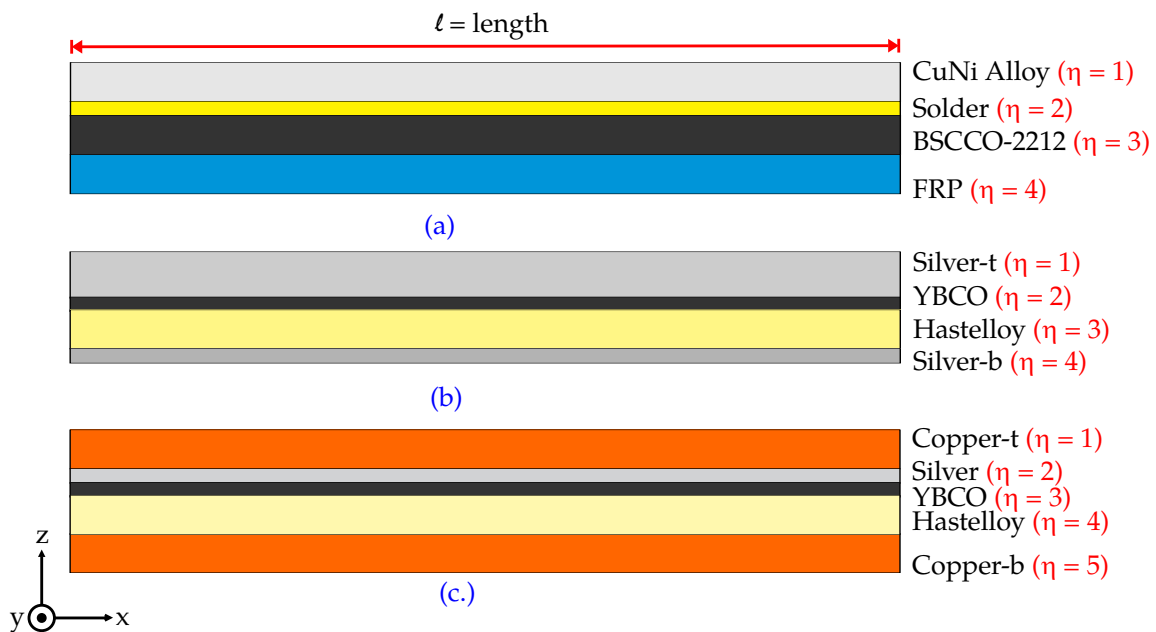


Figure 6.4: Geometry for FDM simulations of the (a) each MCP-BSCCO-2212 module, (b) each tape of the YBCO 2G coil and (c) each tape of the AC-SFCL.

This methodology considers all the heat transfer along the length (x -direction) and along the thickness (z -direction). The heat transfer along the width (y -direction) is neglected. The layers numbering is the same of that one presented in section 5.3.2.

Two different models have also been developed for the FDM methodology:

- FDM-MB → Model with heat exchanges between the layers of the tapes and modules and heat exchange between surfaces and liquid nitrogen bath. In this model, physical properties are considered constants at 100 K;

- FDM-MC → Model with heat exchanges as for FDM-MB and local temperature dependency of the physical properties (specific heat ς and thermal conductivity k , as well as the convection heat transfer coefficient h_c).

Table 6.1 summarizes the considered models.

Table 6.1: Developed Models

Model	Heat Exchange	ς and k	h_c
FDM-MB	yes	constant	0.2 W/K.cm^2
FDM-MC	yes	temperature dependent	

For all studied SFCLs, the temperature distribution within each layer, $T_\eta(z, x, t)$, $\eta = 1, 2, 3 \dots \eta_\varrho$, is governed by the following partial differential equation (Fourier heat conduction equation):

$$\gamma_\eta \varsigma_\eta \frac{\partial T_\eta(z, x, t)}{\partial t} = k_\eta \left(\frac{\partial^2 T_\eta(z, x, t)}{\partial z^2} + \frac{\partial^2 T_\eta(z, x, t)}{\partial x^2} \right) + \dot{g}_\eta \quad (6.20)$$

for $z_{\eta-1} < z < z_\eta$, $0 < x < \ell$ and $t > 0$

where ℓ denotes the length of one tape or module and γ_η , ς_η , k_η and \dot{g}_η denote, respectively, the specific mass, the specific heat, the thermal conductivity and the internal heat generation (per unit volume) for the η^{th} layer.

As the model presented in the section 5.3.2.2, the partial differential equation (6.20) is subjected to third-kind boundary conditions at $z = 0$ and at $z = z_{\eta_\varrho}$, related to the heat exchange with the liquid nitrogen bath:

$$k_1 \frac{\partial T_1}{\partial z} \Big|_{z=0} = h_c [T_{\text{LN}_2} - T_1(0, x, t)] \quad \text{at } z = 0 \quad (6.21)$$

$$-k_{\eta_\varrho} \frac{\partial T_{\eta_\varrho}}{\partial z} \Big|_{z=z_{\eta_\varrho}} = h_c [T_{\text{LN}_2} - T_{\eta_\varrho}(z_{\eta_\varrho}, x, t)] \quad \text{at } z = z_{\eta_\varrho} \quad (6.22)$$

and also to the following interface conditions (for $\eta \in \{2, 3 \dots \eta_\varrho\}$), which express continuity of temperature and heat flux at common boundaries shared by adjoining layers

$$T_{\eta-1}(z_{\eta-1}, t) = T_\eta(z_{\eta-1}, t) \quad \text{at } z = z_{\eta-1} \quad (6.23)$$

$$k_{\eta-1} \frac{\partial T_{\eta-1}}{\partial z} \Big|_{z=z_{\eta-1}} = k_\eta \frac{\partial T_\eta}{\partial z} \Big|_{z=z_{\eta-1}} \quad \text{at } z = z_{\eta-1} \quad (6.24)$$

To complete the mathematical formulation, temperatures $T_\eta(z, x, t)$, $\eta = 1, 2, \dots, \eta_\rho$, are also subjected to the initial condition $T_\eta(z, x, 0) = T_{LN_2}$.

Boundary conditions will now be set at $x = 0$ and $x = \ell$ for the three studied SFCL devices.

Boundary Conditions of the resistive SFCLs - The modules of the MCP-BSCCO-2212 assembly and the YBCO 2G coil are submitted to the same boundary conditions at $x = 0$ and $x = \ell$, since they are in direct contact with massive metal parts related to the electrical contacts of the devices, as described in equations (6.25) and (6.26) and shown in figure 6.5. For this reason one can consider that at $x = 0$ and $x = \ell$ the temperatures are kept constant at 77 K (temperature T_{LN_2} of the liquid nitrogen bath).

$$T_\eta(z, 0, t) = T_{LN_2} \quad \text{at } x = 0 \quad (6.25)$$

$$T_\eta(z, \ell, t) = T_{LN_2} \quad \text{at } x = \ell \quad (6.26)$$

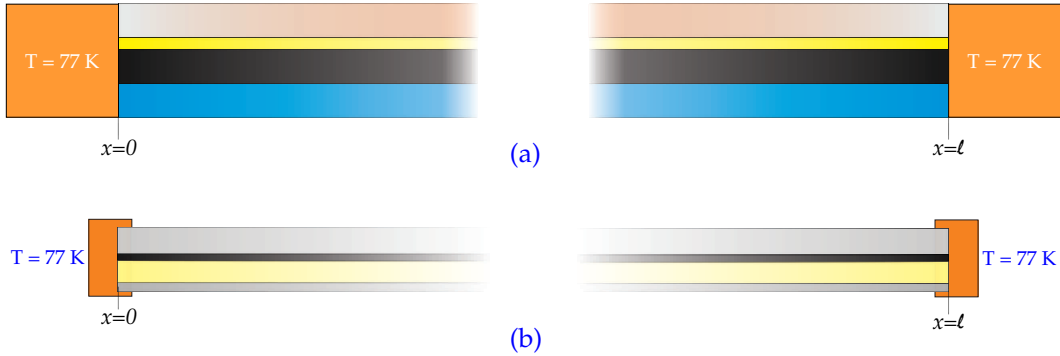


Figure 6.5: Boundary conditions for (a) each module of the MCP-BSCCO-2212 and (b) each tape of the YBCO 2G coil. The metal parts are related to the electrical contacts of the devices.

Boundary Conditions of the Air Coil SFCL - The tapes in the secondary coil of the AC-SFCL are short-circuited, as already shown in figure 3.2a of section 3.1 (see chapter 3). Hence, the following boundary conditions are valid:

$$T_\eta(z, 0, t) = T_\eta(z, \ell, t) \quad \text{at } x = 0 \quad (6.27)$$

$$T_\eta(z, \ell, t) = T_\eta(z, 0, t) \quad \text{at } x = \ell \quad (6.28)$$

6.4 Alternating Direction Implicit (ADI)

The principal advantage of the ADI method lies in the fact that the size of the matrix to be solved in each time step level is reduced at the expense of solving a reduced matrix many times[143]. The use of the ADI method allows the modeling of long lengths of HTS material, what can hardly be achieved by means of finite elements method (FEM) [20].

The ADI method has been already employed to simulate the behavior of the Air Coil SFCL and the results were published in [149] as a first version of this work. In that version a constant mesh, similar to that one illustrated in figure 6.3 was created. The results could be considered satisfactory, but the time of simulation was still huge using a conventional computer (about 30 hours).

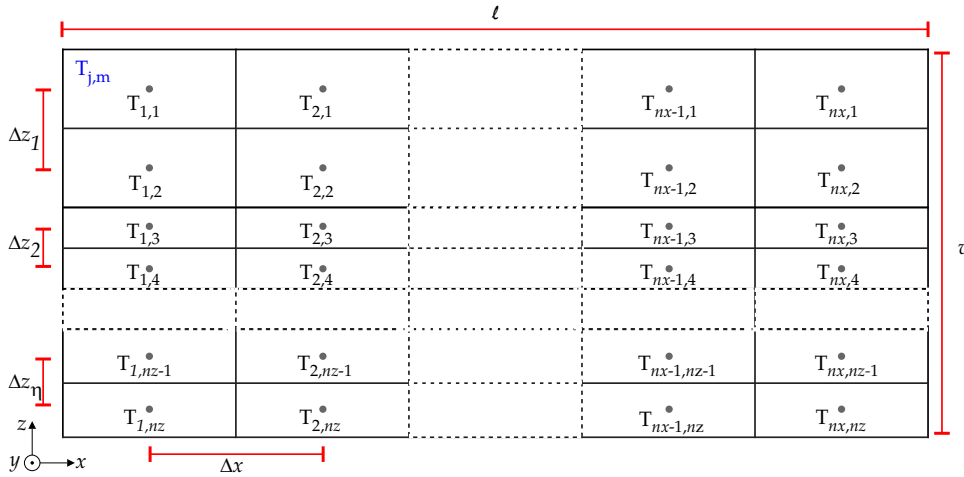


Figure 6.6: Discretization for the 2D FDM scheme with a variable mesh in z -direction.

With the purpose of reducing the simulation time, the ADI model with variable mesh is presented here. It means that the mesh presents different values of Δz along the thickness (z -direction) of the tape or module of the SFCL device, as shown in figure 6.6. It is also possible to create a variable mesh along the x -direction (length), however in this work it is used a constant Δx along the length since there are no different layers along this direction.

The ADI method basically consists in solving equation (6.20) half explicit and half implicit along 1D profiles. Each time step Δt is divided in two parts ($\Delta t/2$). In the first half-timestep equation (6.20) is solved implicitly in the x -direction while the z -direction is solved explicitly. In the second half-timestep the process is inverse.

6.4.1 First Half-Timestep

For the first half-timestep, equation 6.20 is solved implicitly in the x -direction.

$$\frac{T_{j,m}^{\tau+\frac{1}{2}} - T_{j,m}^{\tau}}{\Delta t/2} = \alpha_{j,m} \left[\frac{T_{j-1,m}^{\tau+\frac{1}{2}} - 2T_{j,m}^{\tau+\frac{1}{2}} + T_{j+1,m}^{\tau+\frac{1}{2}}}{\Delta x^2} + \frac{T_{j,m-1}^{\tau} - 2T_{j,m}^{\tau} + T_{j,m+1}^{\tau}}{\Delta z^2} \right] + k_{j,m} \frac{\dot{g}_{j,m}}{\alpha_{j,m}} \quad (6.29)$$

where $\alpha_{j,m} = k_{j,m} / (c_{j,m} \gamma_{j,m})$, known as thermal diffusivity [150]. For the sake of simplicity and computational purposes, one rewrites equation (6.29) so that at each time level, the unknown quantities (those at $\tau + 1$) appear on one side of the equality (say left) and the known (those at $\tau + 1/2$) quantities on the other side (say right).

$$\underbrace{-Fo_x T_{j-1,m}^{\tau+\frac{1}{2}} + (1 + 2Fo_x) T_{j,m}^{\tau+\frac{1}{2}} - Fo_x T_{j+1,m}^{\tau+\frac{1}{2}}}_{X_\eta} = \underbrace{Fo_z T_{j,m-1}^{\tau} + (1 - 2Fo_z) T_{j,m}^{\tau} + Fo_z T_{j,m+1}^{\tau}}_{SZ_j} + k_{j,m} \frac{\dot{g}_{j,m}}{\alpha_{j,m}} \frac{\Delta t}{2} \quad (6.30)$$

where

$$Fo_z = \alpha_{j,m} \frac{\Delta t}{2\Delta z^2} \quad (6.31)$$

$$Fo_x = \alpha_{j,m} \frac{\Delta t}{2\Delta x^2} \quad (6.32)$$

Here it is important mentioning that each layer η should have its own value of Fo_x and Fo_z , since the parameter $\alpha_{j,m}$ changes according with the material. Furthermore, the parameter Fo_z depends on the size of Δz that varies along the thickness.

One can cast equation (6.30) concerning to the first half-timestep in matrix form, as shown in equation (6.33). By analyzing equation (6.33) it is possible to note the matrix X_η must be created for each layer of the tapes or modules, because values of Fo_x depends on the layer material. It means that for the MCP-BSCCO-2212 modules and for the tapes of the YBCO 2G coil there are 4 different matrices X_η whereas for the tapes of the Air Coil SFCL there are 5 different matrices X_η ². Furthermore, a loop must be done (from $m = 1$ to $m = n_z$) at the first half-timestep in order to solve equation (6.33) for all rows of the discretized geometry.

²To remember: for the MCP-BSCCO-2212 modules and for the tapes of the YBCO 2G Coil, $\eta_\rho = 4$, and for the tapes of the AC-SFCL, $\eta_\rho = 5$

The creation of matrix SZ_j obeys the rule highlighted in equation (6.30).

$$\begin{aligned}
 & \overbrace{\begin{bmatrix} 1 + 2Fo_{x(\eta)} & -Fo_{x(\eta)} & 0 & 0 & \dots & \Gamma \\ -Fo_{x(\eta)} & 1 + 2Fo_{x(\eta)} & -Fo_{x(\eta)} & 0 & \dots & 0 \\ \vdots & \ddots & \ddots & \ddots & \ddots & \vdots \\ 0 & \dots & 0 & -Fo_{x(\eta)} & 1 + 2Fo_{x(\eta)} & -Fo_{x(\eta)} \\ \Gamma & \dots & 0 & 0 & -Fo_{x(\eta)} & 1 + 2Fo_{x(\eta)} \end{bmatrix}}^{X_\eta} \times \begin{bmatrix} T_{1,m} \\ T_{2,m} \\ \vdots \\ T_{n_x-1,m} \\ T_{n_x,m} \end{bmatrix}^{\tau+\frac{1}{2}} \\
 & - \begin{bmatrix} \Theta \\ 0 \\ \vdots \\ 0 \\ \Theta \end{bmatrix} = \overbrace{\begin{bmatrix} SZ_1 \\ SZ_2 \\ \vdots \\ SZ_{n_x-1} \\ SZ_{n_x} \end{bmatrix}}^{SZ_j}{}^\tau + \frac{k_\eta \Delta t}{\alpha_\eta} \frac{\Delta t}{2} \begin{bmatrix} \dot{g}_{1,m} \\ \dot{g}_{2,m} \\ \vdots \\ \dot{g}_{n_x-1,m} \\ \dot{g}_{n_x,m} \end{bmatrix}{}^\tau
 \end{aligned} \tag{6.33}$$

The values of Γ and Θ in equation (6.33) are determined by applying the boundary conditions at $x = 0$ and $x = \ell$ according with the specific boundary conditions of each device. In the discretized version, the boundary conditions are applied only at $j = 1$ and $j = n_x$. This procedure is fully described in appendix C, section C.1.

For the resistive SFCLs (MCP-BSCCO-2212 modules and YBCO 2G coil) the boundary conditions expressed in equations (6.25) and (6.26) are valid whereas for the Air Coil SFCL the boundary conditions are expressed in equations (6.27) and (6.28). Table 6.2 summarizes the values of Γ and Θ according with the SFCL device.

Table 6.2: Γ and Θ values originated from the boundary conditions

Parameter	MCP-BSCCO-2212	YBCO 2G Coil	Air Coil SFCL
Γ	0	0	$-Fo_{x(\eta)}$
Θ	$Fo_{x(\eta)}T_{LN2}$	$Fo_{x(\eta)}T_{LN2}$	0

6.4.2 Second Half-Timestep

For the second half-timestep the process is inverse, i.e, the z -direction is solved implicitly while the x -direction is solved explicitly, using the values of temperature

obtained at $\tau + 1/2$.

$$\frac{T_{j,m}^{\tau+1} - T_{j,m}^{\tau+\frac{1}{2}}}{\Delta t/2} = \alpha_{j,m} \left[\frac{T_{j-1,m}^{\tau+\frac{1}{2}} - 2T_{j,m}^{\tau+\frac{1}{2}} + T_{j+1,m}^{\tau+\frac{1}{2}}}{\Delta x^2} + \frac{T_{j,m-1}^{\tau+1} - 2T_{j,m}^{\tau+1} + T_{j,m+1}^{\tau+1}}{\Delta z^2} \right] + k_{j,m} \frac{\dot{g}_{j,m}}{\alpha_{j,m}} \quad (6.34)$$

Rewriting equation (6.34), yields:

$$\underbrace{-F_{Oz}T_{j,m-1}^{\tau+1} + (1 + 2F_{Oz})T_{j,m}^{\tau+1} - F_{Oz}T_{j,m+1}^{\tau+1}}_Z = \underbrace{F_{Ox}T_{j-1,m}^{\tau+\frac{1}{2}} + (1 - 2F_{Ox})T_{j,m}^{\tau+\frac{1}{2}} + F_{Ox}T_{j+1,m}^{\tau+\frac{1}{2}}}_{SX_m} + k_{j,m} \frac{\dot{g}_{j,m}}{\alpha_{j,m}} \frac{\Delta t}{2} \quad (6.35)$$

Before casting equation (6.35) in matrix form, it is mandatory analyzing the boundary conditions. In that way, one discretizes equations (6.23) and (6.24), related to the continuity of temperature and heat flux at common boundaries shared by adjoining layers as follows:

$$T_{j,m} + T_{ha} = T_{j,m+1} + T_{hb} \quad (6.36)$$

$$k_{j,m} \frac{T_{j,m} - T_{ha}}{\Delta z_{\eta}} = k_{j,m+1} \frac{T_{hb} - T_{j,m+1}}{\Delta z_{\eta+1}} \quad (6.37)$$

In equation (6.36), T_{ha} and T_{hb} are called auxiliary temperatures [81] and are created to satisfy the boundary condition expressed in equation (6.23). Figure 6.7 illustrates the schema for T_{ha} and T_{hb} .

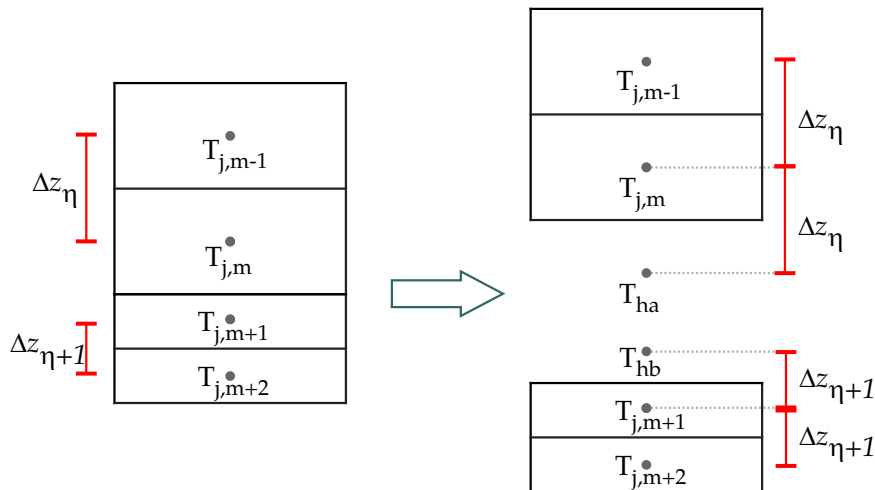


Figure 6.7: Created schema to satisfy boundary conditions between two adjoining sub-components where the mesh size changes.

Solving equations (6.36) and (6.37) for T_{ha} and T_{hb} one obtains:

$$T_{ha} = \left[\frac{2\psi}{1+\psi} \right] T_{j,m+1} + \left[\frac{1-\psi}{1+\psi} \right] T_{j,m} \quad (6.38)$$

$$T_{hb} = \left[\frac{2}{1+\psi} \right] T_{j,m} - \left[\frac{1-\psi}{1+\psi} \right] T_{j,m+1} \quad (6.39)$$

where:

$$\psi = \frac{k_{j,m+1}}{k_{j,m}} \cdot \frac{\Delta z_{\eta}}{\Delta z_{\eta+1}} \quad (6.40)$$

T_{ha} and T_{hb} values are inserted in equation (6.35) to satisfy the boundary condition at the interface between two layers. Such procedure is described in appendix C, section C.2.

The last boundary condition to be discretized is that one expressed in equations (6.21) and (6.22) related to the heat exchange with the liquid nitrogen bath. Such discretization is done using the fictitious node concept [143]. As shown in figure 6.8 the region $0 < z < v$ is extended outward by a distance Δz at both extremities giving rise to fictitious temperatures nodes $T_{j,0}$ and $T_{j,nz+1}$.

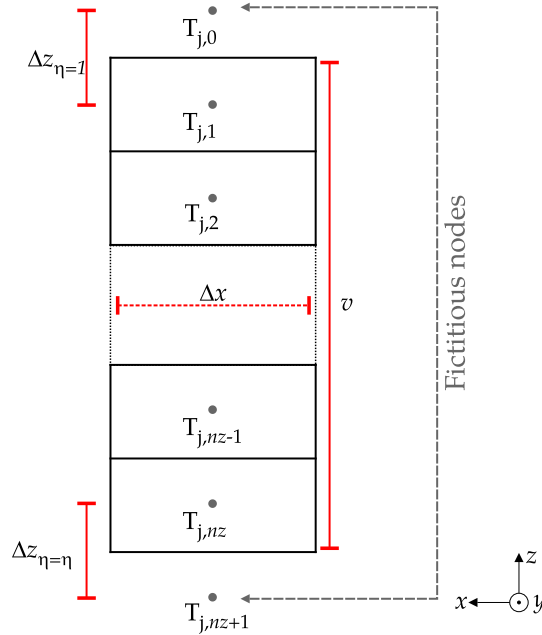


Figure 6.8: Fictitious nodes concept; $T_{j,0}$ and $T_{j,nz+1}$

Applying equation (6.4) in equations (6.21) and (6.22) yields:

$$k_{j,1} \frac{T_{j,0} - T_{j,2}}{2\Delta z} = h_c [T_{LN_2} - T_{j,1}] \quad (6.41)$$

$$-k_{j,nz} \frac{T_{j,nz-1} - T_{j,nz+1}}{2\Delta z} = h_c [T_{LN_2} - T_{j,nz}] \quad (6.42)$$

Solving equations (6.41) and (6.42) for $T_{j,0}$ and T_{j,n_z+1} yield

$$T_{j,0} = 2 \frac{h_c \Delta z}{k_{j,1}} [T_{LN_2} - T_{j,1}] + T_{j,2} \quad (6.43)$$

$$T_{j,n_z+1} = 2 \frac{h_c \Delta z}{k_{j,n_z}} [T_{LN_2} - T_{j,n_z}] + T_{j,n_z-1} \quad (6.44)$$

As in the previous case, the values of $T_{j,0}$ and T_{j,n_z+1} are inserted in equation (6.35) to satisfy the heat exchanges with the LN_2 bath. It must be done when $m = 1$ or $m = n_z$. This procedure is also described in appendix C, section C.2.

Finally, the matrix form for the second half-timestep can be written, as expressed in equation (6.46). For these equations the following relations are valid:

$$\beta = 1 + \frac{h_c \Delta y}{k} \quad \text{and} \quad \gamma = T_{LN_2} \frac{h_c \Delta z}{k} \quad (6.45)$$

The values of β and γ results from the discretization of the boundary conditions described in equations (6.43) and (6.44) when $m = 1$ and $m = n_z$, as well as matrix H . The parameter ψ satisfies the boundary conditions at the interface between two layers.

The matrix Z must be created just once, however the heat flux at adjoining layers must also be taken into account. The highlighted lines in matrix Z show the general rule for the heat flux at the interface between two layers. Such rule rises from the discretization of the boundary conditions described in equations (6.38) and (6.39). The creation of matrix SX_m obeys the rule highlighted in equation (6.35).

In order to solve equation (6.46) for all columns of the discretized geometry, a loop from $j = 1$ to $j = n_x$ is necessary.

Conversely to equation (6.33) that must be solved at the first half-timestep, equation (6.46) has the same form for all SFCLs studied in this work. That is because all SFCLs present a layered structure with heat exchanges with the liquid nitrogen bath at top and bottom of the geometry, as well as heat exchange between layers.

$$\underbrace{\begin{bmatrix}
 1 + 2\beta Fo_z(\eta=1) & -2Fo_z(\eta=1) & & & \\
 -Fo_z(\eta=1) & 1 + 2Fo_z(\eta=1) & & & \\
 \vdots & \vdots & \ddots & & \\
 -Fo_z(\eta) & 1 + 2Fo_z(\eta) - \left[\frac{1-\psi}{1+\psi} \right] Fo_z(\eta) & & & \\
 \vdots & \vdots & -\frac{2\psi Fo_z(\eta)}{1+\psi} & & \\
 \vdots & \vdots & \vdots & \ddots & \\
 1 + 2Fo_z(\eta+1) & -Fo_z(\eta+1) & & & \\
 \vdots & \vdots & \left[\frac{1-\psi}{1+\psi} \right] Fo_z(\eta+1) & & \\
 \vdots & \vdots & \vdots & \ddots & \\
 1 + 2Fo_z(\eta_e) & -Fo_z(\eta_e) & & & \\
 -2Fo_z(\eta_e) & 1 + 2\beta Fo_z(\eta_e) & & &
 \end{bmatrix}}_Z \times \begin{bmatrix}
 \dot{g}_{j,1} \\
 \dot{g}_{j,2} \\
 \vdots \\
 \dot{g}_{j,m} \\
 \dot{g}_{j,m+1} \\
 \vdots \\
 \dot{g}_{j,n_z-1} \\
 \dot{g}_{j,n_z}
 \end{bmatrix}^T$$

$$\begin{bmatrix}
 T_{j,1} \\
 T_{j,2} \\
 \vdots \\
 T_{j,m} \\
 T_{j,m+1} \\
 \vdots \\
 T_{j,n_z-1} \\
 T_{j,n_z}
 \end{bmatrix}^{\tau+1} - \begin{bmatrix}
 2\gamma Fo_z(\eta=1) \\
 0 \\
 \vdots \\
 0 \\
 0 \\
 \vdots \\
 0 \\
 2\gamma Fo_z(\eta_e)
 \end{bmatrix}^H = \begin{bmatrix}
 SX_1 \\
 SX_2 \\
 \vdots \\
 SX_m \\
 SX_{m+1} \\
 \vdots \\
 SX_{n_z-1} \\
 SX_{n_z}
 \end{bmatrix}^{\tau+\frac{1}{2}} + \alpha_{j,m} \frac{\Delta t}{2k_{j,m}}$$

(6.46)

6.5 Solution Routine

The complete solution routine is shown in figure 6.9. As can be seen, the first task of the algorithm (box 01) is to determine the number of elements from the length and thickness of the tape and modules of the SFCL devices. Hence, in this task the numbers of n_x and n_z are also defined. The subsequent box, the initial conditions are given.

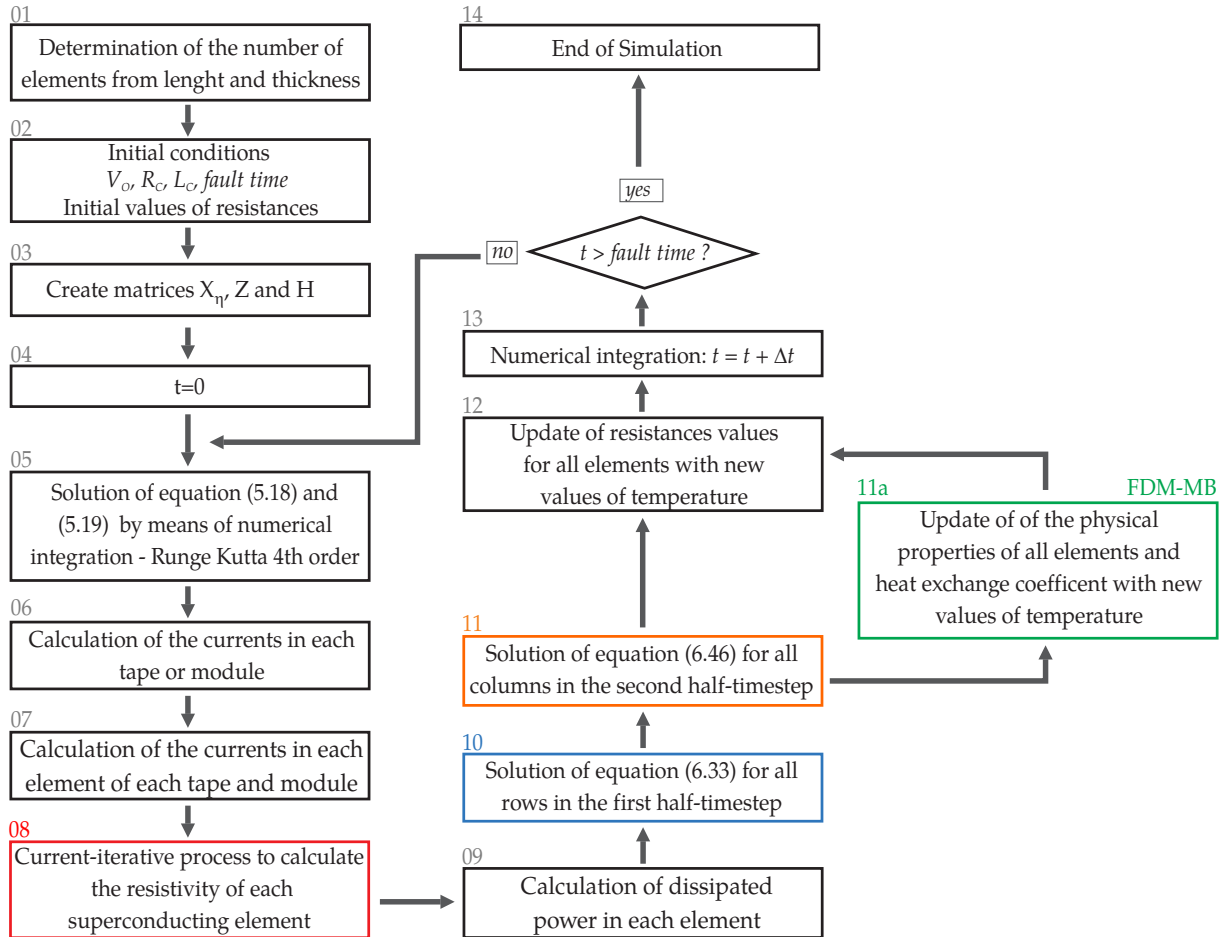


Figure 6.9: Flowchart of the simulation routine. The green box (11a) runs only for models FDM-MB. The red box (08) denotes the current iterative process.

In the box 03, the matrices X_η , Z and H are created for the further solution of equations (6.33) and (6.46). The solution in the time domain start in the box 04 and the solution of the electrical part of the problem is solved by means of the Runge-Kutta 4th order, as already described in section 5.4.

From the solutions of the electrical problem, one can calculate the current flowing in each layer of each tape and module (boxes 06 and 07) respectively. Box number 08 executes the current-iterative process for all superconducting elements since each one has its own value of critical current I_c , as shown in figures 3.15, 3.16 and 3.18. In that way, the inhomogeneities effects can be implemented in the

model and further analyzed, since it allows the local description of each tape and module.

In order to calculate the local temperature, box 09 calculates the power dissipated in each element, i.e., the respective values of $\dot{q}_{j,m}$. In the box 10 a loop from $m = 1$ to $m = n_z$ is done. For each value of m (for each row of the discretized geometry), a solution of the equation (6.33) is obtained. In the end of the this loop one has a temperature profile in the first half-timestep (at $\tau + 1/2$).

In box 11 a loop from $j = 1$ to $j = n_x$ is done, in order to obtain a solution for each column of the discretized geometry. In this step, the solutions obtained at $\tau + 1/2$ (box 10) are used as known quantities. In the end of this loop (second half-timestep), one has the temperature profile at $\tau + 1$.

In the case of applying the model FDM-MB (box 11a), the values of specific heat ς and thermal conductivity k of each element must be updated. As a consequence, matrices X_η , Z and H must be recreated for the next timestep, since such matrices are dependent on the physical properties of the materials. Moreover, values of the convection heat transfer coefficient h_c must also be updated in the FDM-MB model (see appendix B).

After updating the values of temperature, both models go to box 12, where the new value of resistance of each element for the next timestep is calculated. At box 13 the routine follows to the increase of the time step ($t = t + \Delta t$) and the whole process is started again if the fault period has not been achieved.

Table 6.3 presents the parameters of discretization for MCP-BSCCO-2212 modules. It shows the values of Δz for each layer of the modules, number of elements along the z -direction as well the value of the Δx and the number of elements along the x -direction. At the end the total number of elements for the whole assembly is shown.

Table 6.3: Parameters of discretization for each MCP-BSCCO-2212 module.

	Δz	n_z elements	Δx	n_x elements	Total
CuNi Alloy	0.0875 cm	4	1.0cm	270	1080
Solder	0.005 cm	2			540
BSCCO-2212	0.133 cm	3			810
FRP	0.075 cm	4			1080

Total of the assembly = $(1080 + 540 + 810 + 1080) \times 12 = 42120$ elements

Table 6.4 presents the same parameters for the tapes of the YBCO 2G coil.

Table 6.4: Parameters of discretization for each tape of the YBCO 2G Coil.

	Δz	n_z elements	Δx	n_x elements	Total
Silver-t	1.3×10^{-4} cm	3	1.0 cm	430	1290
YBCO	1.0×10^{-6} cm	1			430
Hastelloy	0.0025 cm	4			1720
Silver-b	3.3×10^{-5} cm	3			1290
S. Steel	0.048 cm	5			3000
Total of the coil = $(1290 + 430 + 1720 + 1290) \times 8 + 3000 = 40840$ elements					

The parameters of discretization for the tapes of the Air Coil SFCL are presented in table 6.5.

Table 6.5: Parameters of discretization for each tape of the Air Coil SFCL.

	Δz	n_z elements	Δx	n_x elements	Total
Copper-t	13.3×10^{-4} cm	3	1.0 cm	147	441
Silver	2×10^{-6} cm	1			147
YBCO	1.0×10^{-6} cm	1			147
Hastelloy	0.0025 cm	4			588
Copper-b	13.3×10^{-4} cm	3			441
Total of the device = $(441 + 147 + 147 + 588 + 441) \times 22 = 38808$ elements					

The routines were performed under OS Windows 7 by means of a MATLAB® Script-File (m-file) using a conventional machine (3.4GHz, i4 processor, 8Gb RAM).

6.6 Results

Simulated results obtained by means of finite differences via ADI solution method are now compared with the experimental data presented in chapter 3, as have been done with simulated results via TEA method. Comparisons between measured and simulated data for limited current and voltage drop are done, as well as comparisons between models FDM-MB and FDM-MC.

Once again, curves will be evaluated only regarding peak values using the percentage error %E, repeated here for convenience.

$$\%E = \frac{|Measured - Simulated|}{Measured} \times 100 \quad (6.47)$$

Errors regarding phase shift between the curves are quite difficult to be evaluated, since unknown parameters and effects in the test circuits may exist.

Temperature values are shown for all modules and tapes at 4 distinct time instants, defined according to each test. Supplementary multimedia files have been created, aiming to provide a better presentation of temperature rise during fault transient. These files are very helpful for illustrating the results ³.

Comparisons between equivalent resistances obtained by models FDM-MB and FDM-MC are also presented.

6.6.1 MCP-BSCCO-2212 Results

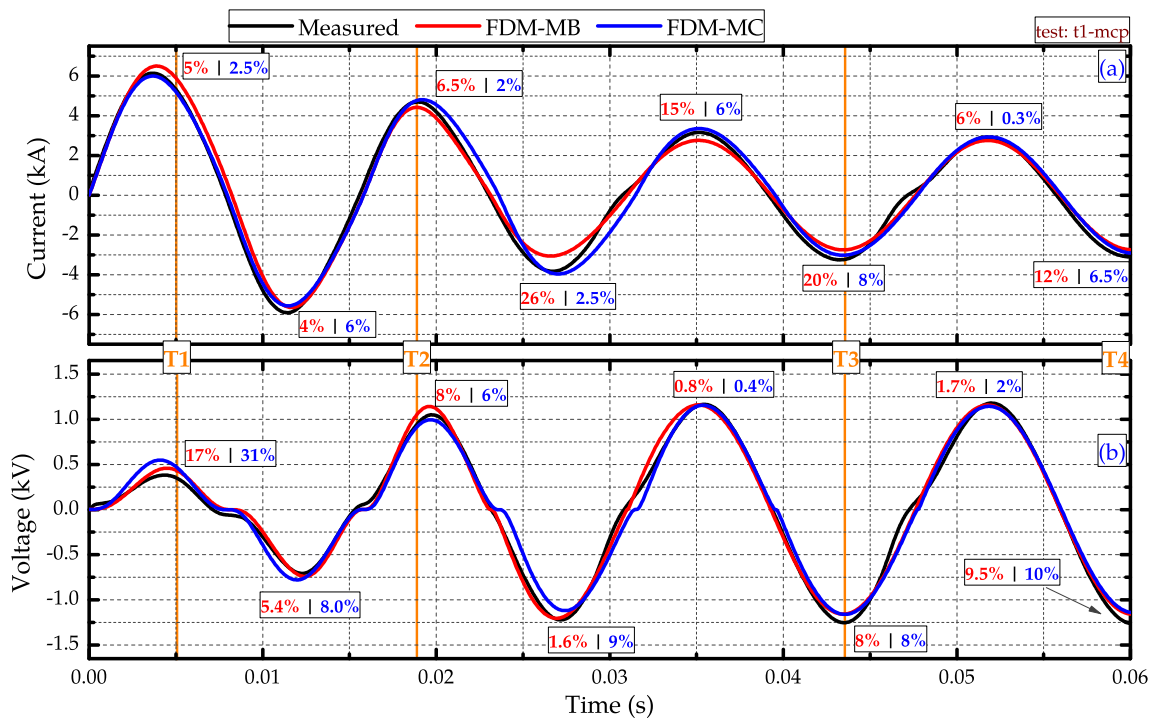


Figure 6.10: Comparison between measured and simulated results of the FDM-ADI model for a) limited current and b) voltage drop over the MCP-BSCCO-2212 assembly for test t1-mcp (fault current = 5.0 kA_{rms} under 1.0 kV_{rms}).

Figure 6.10 compares measured results with simulated ones for test t1-mcp. Excluding second peak of the limited current, errors of model FDM-MC are lower

³Supplementary files are labeled as the following example: t1-mcp_FDM-MB.mp4. In this example, the supplementary file refers to the temperature increase simulated by model FDM-MB for test t1-mcp. All supplementary files can be download by clicking [here](#).

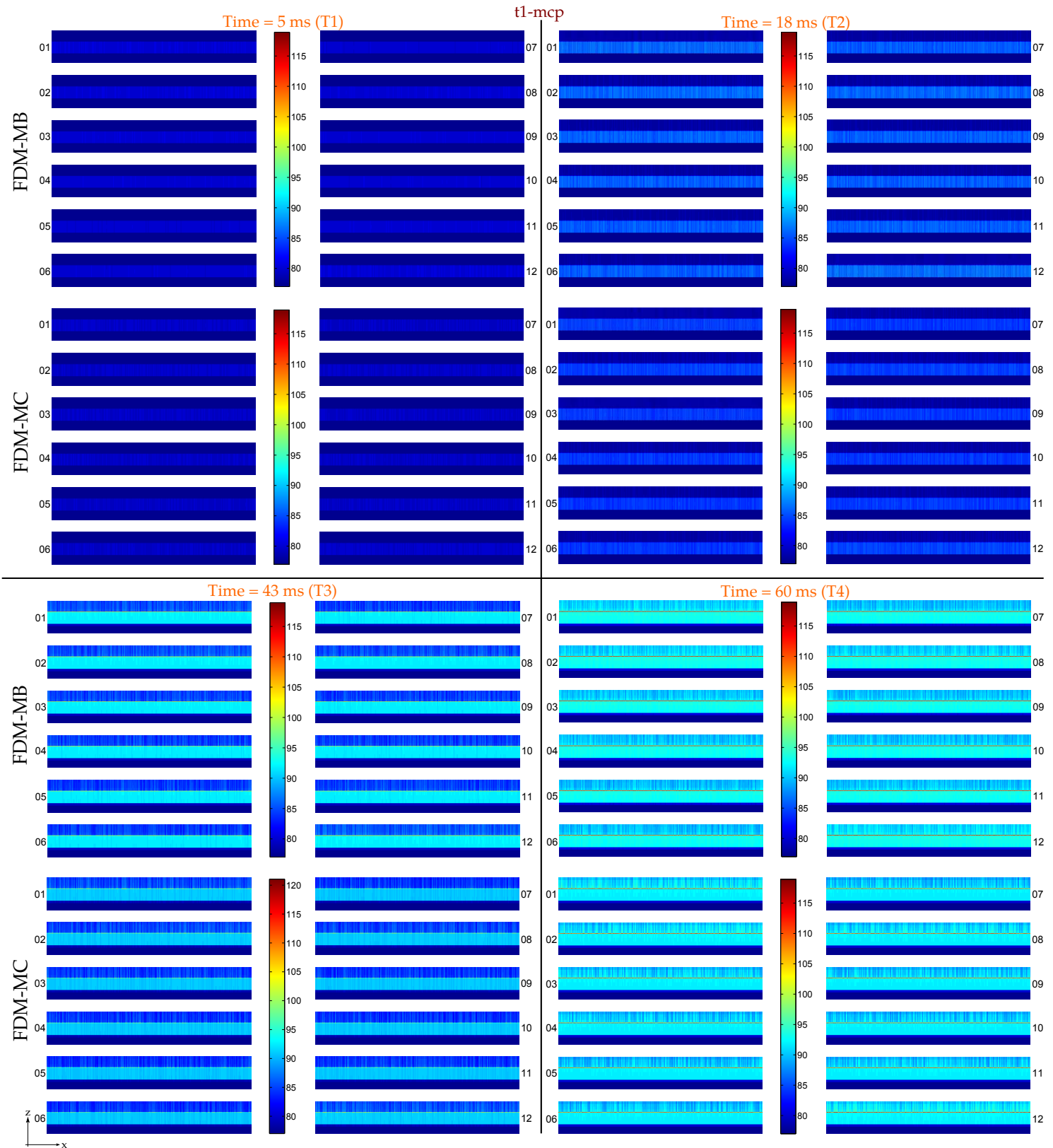


Figure 6.11: Temperature rise predicted by models FDM-MB and FDM-MC during the fault period for test t1-mcp. A longitudinal view is presented (thickness (z) \times length (x)). Figure out of scale.

than those of model FDM-MB. In the case of voltage drop curve, however, some errors committed by model FDM-MB are lower than those committed by model FDM-MC. Behaviors of simulated curves calculated by models FDM-MB and FDM-MC are similar to those of measurements.

Figure 6.11 illustrates temperature values for each MCP-BSCCO-2212 module of the assembly at four different instants of time, as defined in figure 6.10. Layers are disposed according to the sequence illustrated in figure 6.4a. Values obtained by models FDM-MB and FDM-MC at the four instants are compared; T1 at 5 ms, T2 at 18 ms, T3 at 43 ms and T4 at 60 ms. Supplementary files `t1-mcp_FDM-MB.mp4` and `t1-mcp_FDM-MC.mp4` present the heating process of test t1-mcp for all modules during the fault period.

Differences on the values calculated by both models are small. Both models provides approximately same temperature values for the same instants of time. Moreover, simulated results obtained by both models clear show temperature gradients inside the modules. Already at 5 ms (T1) the heating of the BSCCO-2212 layer can be noted. After the quench of the BSCCO-2212 layer, the heating rate of the solder layer increases, leading to higher temperatures at the end of the transient period, as shows figure 6.11 for instant T4 (60 ms). Moreover, because of modeling the modules with different I_c values, one also recognizes slightly temperature differences along a single layer. As shown, there is not an overheating of any particular region in relation to the others.

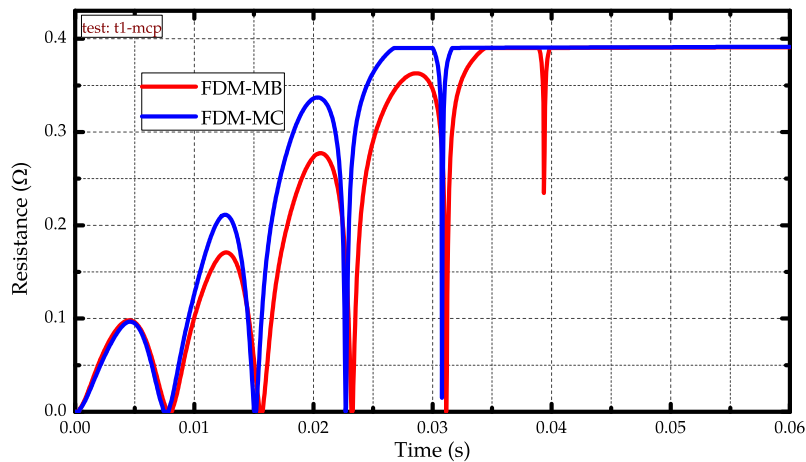


Figure 6.12: Comparison between equivalent resistances of the MCP-BSCCO-2212 assembly according to the models FDM-MB and FDM-MC during the fault period in test t1-mcp.

As shown in figure 6.12, resistance values calculated by model FDM-MC present higher peak values than those calculated by model FDM-MC during the transition of the BSCCO-2212 layer to normal state.

Figure 6.13 presents comparison between measured and simulated results for

test t2-mcp. Both models presents tolerable errors values, besides reproducing the same behavior of measured curves.

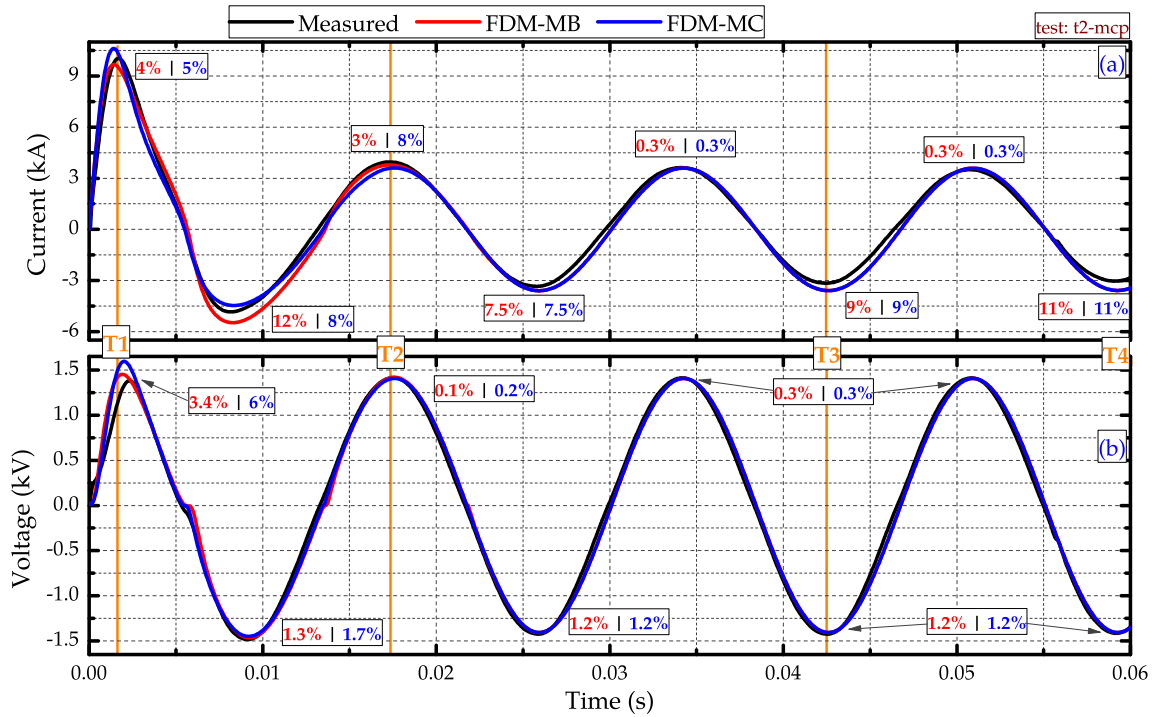


Figure 6.13: Comparison between measured and simulated results of the FDM-ADI model for a) limited current and b) voltage drop over the MCP-BSCCO-2212 assembly for test t2-mcp (fault current = 25.0 kA_{rms} under 1.0 kV_{rms}).

For this test, different instants of time have been taken to plot temperature values, in order to choose instants of peak current. Supplementary files t2-mcp_FDM-MB.mp4 and t2-mcp_FDM-MC.mp4 present the heating process of test t2-mcp for all modules during the fault period. As defined in figure 6.13, the instants of time are: T1 at 1 ms, T2 at 17 ms, T3 at 42 ms and T4 at 60 ms. Values obtained by models FDM-MB and FDM-MC at these instants are compared in figure 6.14. As in the previous test, it is possible recognize gradients of temperature along the thickness of the modules. The BSCCO-2212 layer heats up at the first moments of the transient, but after its quench, the solder layer presents highest values of temperature in relation to the others.

At the beginning of the fault period, resistance values calculated by means of model FDM-MC are higher than that calculated by model FDM-MB, as shown in figure 6.15. After the quench of the superconducting layer however (at approximately 22 ms), both models predicts equals values for the equivalent resistance of the assembly. For this reason, after 22 ms, both models presents equal errors values for limited current and voltage drop, as have been shown in figure 6.13.

Results of simulations performed with finite difference method for the last test performed with the MCP-BSCCO-2212 assembly (t3-mcp) are shown in the fol-

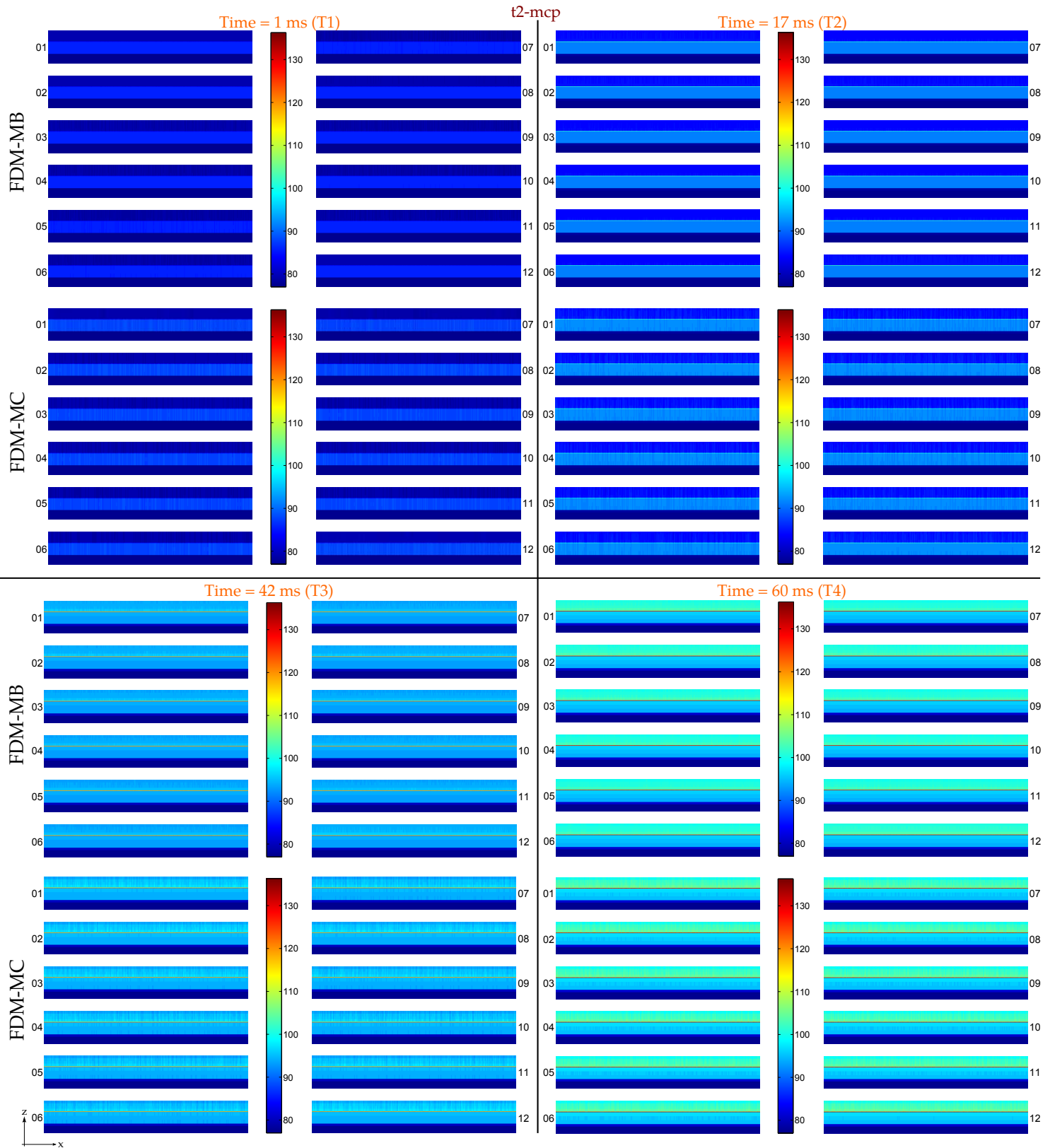


Figure 6.14: Temperature rise predicted by models FDM-MB and FDM-MC during the fault period for test t2-mcp. A longitudinal view is presented (thickness (z) \times length (x)). Figure out of scale.

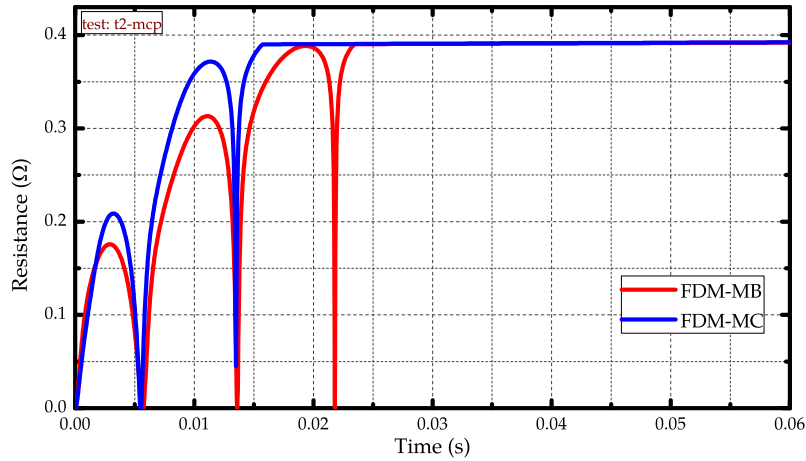


Figure 6.15: Comparison between equivalent resistances of the MCP-BSCCO-2212 assembly according to the models FDM-MB and FDM-MC during the fault period in test t2-mcp.

Following figures. Calculated data for limited current and voltage drop are shown in figure 6.16.

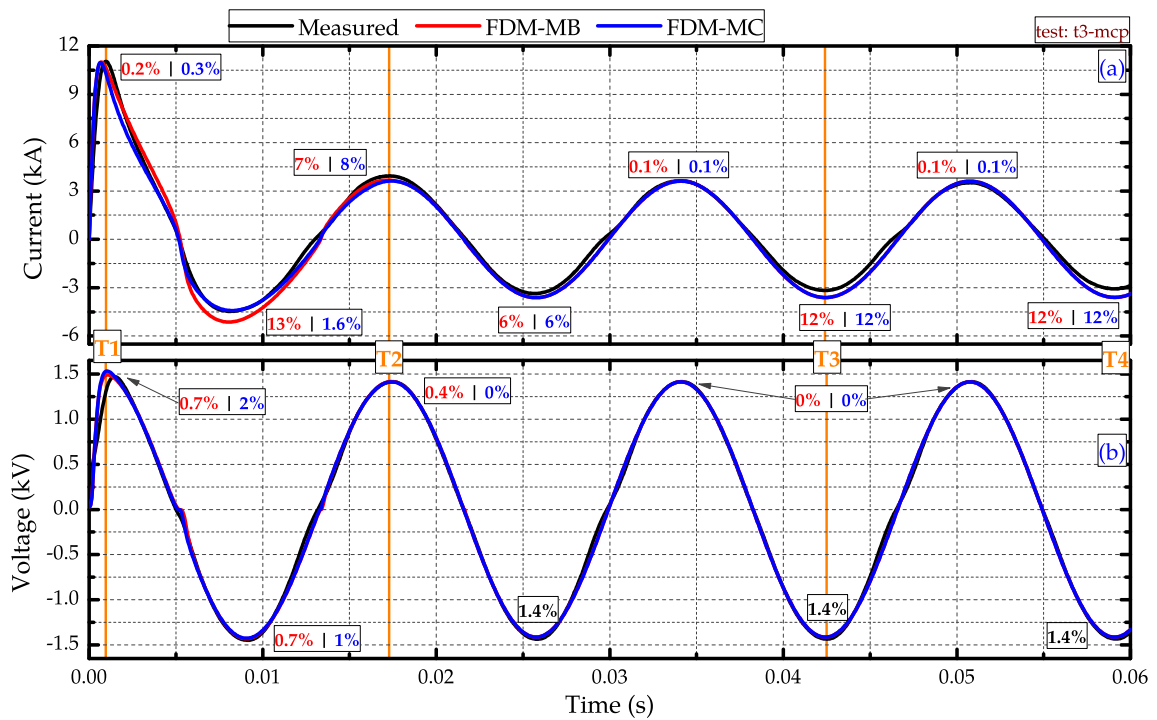


Figure 6.16: Comparison between measured and simulated results of the FDM-ADI model for a) limited current and b) voltage drop over the MCP-BSCCO-2212 assembly for test t3-mcp (fault current = 67.0 kA_{rms} under 1.0 kV_{rms}).

The highest error value belongs to the current peak calculated by model FDM-MB at the second current peak (13%). Errors in the voltage drop curve are lower than 1.5 % for both models.

Supplementary files t3-mcp_FDM-MB.mp4 and t3-mcp_FDM-MC.mp4 show the



Figure 6.17: Temperature rise predicted by models FDM-MB and FDM-MC during the fault period for test t3-mcp. A longitudinal view is presented (thickness (z) \times length (x)). Figure out of scale.

heating process for test t3-mcp for all modules during the fault period. This behavior can also be observed in figure 6.17. The instants of time T1, T2, T3 and T4 remains the same of those already defined in test t2-mcp (1 ms, 17 ms, 42 ms and 60 ms, respectively). Once again, one observes an early heating of the BSCCO-2212 layers at the beginning of the fault period, whereas at the end of the transient, highest values belong to the solder layers.

Furthermore, as in the previous tests, temperature gradients are noticeable inside the modules. It is worth mentioning that the solder layer is mainly heated by the heat transfer between the superconducting layer (BSCCO-2212) and the CuNi alloy.

Figure 6.18 presents the calculated equivalent resistance of the MCP-BSCCO-2212 assembly. It is highly non linear and after 22 ms both models predicts equals values of resistance.

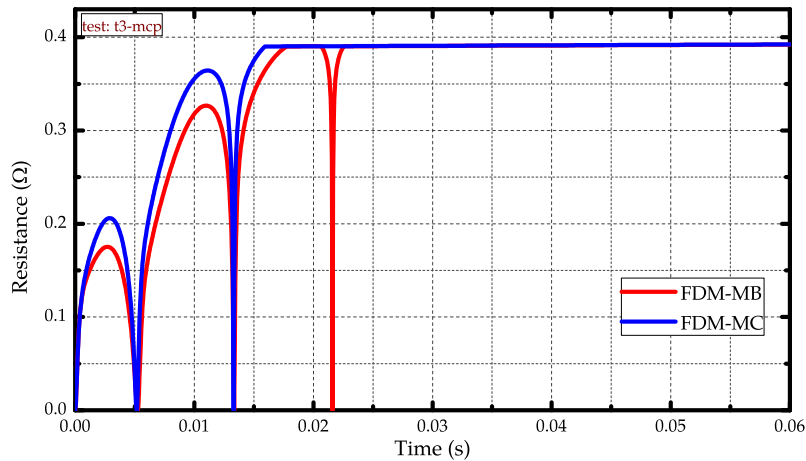


Figure 6.18: Comparison between equivalent resistances of the MCP-BSCCO-2212 assembly according to the models FDM-MB and FDM-MC during the fault period in test t3-mcp.

6.6.2 YBCO 2G coil Results

Figure 6.19 shows comparisons between measured results and simulated ones for test t1-coil. In comparison to simulations of the MCP-BSCCO-2212 modules, errors are lower. The highest error value in the limited current was committed by model FDM-MB at the first current peak (4%). For the voltage drop curve, the highest error value was also committed at the first peak by model FDM-MB (7%). Nevertheless, simulated curves for limited current and voltage drop follows the same behavior of the measured ones.

Figure 6.20 and supplementary multimedia files t1-coil_FDM-MB.mp4 and t1-coil_FDM-MC.mp4 present the simulated heating process during the fault period. Layers are disposed according to the sequence illustrated in figure 6.4b. An

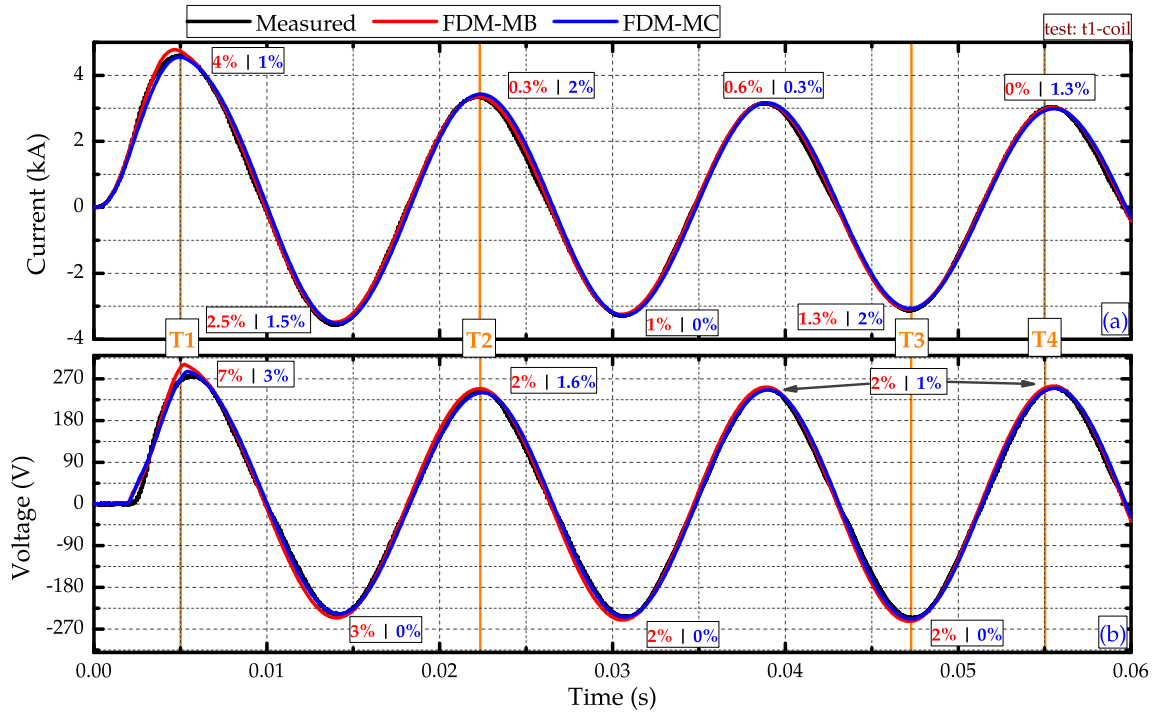


Figure 6.19: Comparison between measured and simulated results of the FDM-ADI model for a) limited current and b) voltage drop over the YBCO 2G coil for test t1-coil (fault current = 5.0 kA_{rms} under 1.0 kV_{rms}).

extra layer is shown, referring to the stack of stainless steel tapes. The instants of time shown in figure 6.20 are those defined in figure 6.19; T1 at 5 ms, T2 at 22 ms, T3 at 47 ms and T4 at 60 ms.

As figure 6.20 shows, gradients of temperature inside of tapes are small, that is, all layers present almost same values of temperature at any instant. There are only slightly variations regarding the early heating of the YBCO layer in relation to the others at the upper side. However, there is not temperature variations higher than 2 K between the layers.

There are also small variations of temperature regarding differences of I_c along the x -direction (length), that is, regarding the tapes inhomogeneity. However, no significant gradients along this direction have been identified.

Differences regarding temperature calculated by models FDM-MB and FDM-MC are apparent. As previously stated in chapter 5, the heating process of tapes are strongly dependent on the initial conditions as well as variations on the convective heat exchange coefficient h_c . Since values of the h_c coefficient quickly reaches its lowest value at the film boiling regime, the convective heat transfer to the liquid nitrogen bath becomes hampered, leading to higher values of temperature calculated by model FDM-MC.

The resistance development in the fault transient for test t2-coil is shown in figure 6.21. Values calculated by model FDM-MC are lower than those ones cal-

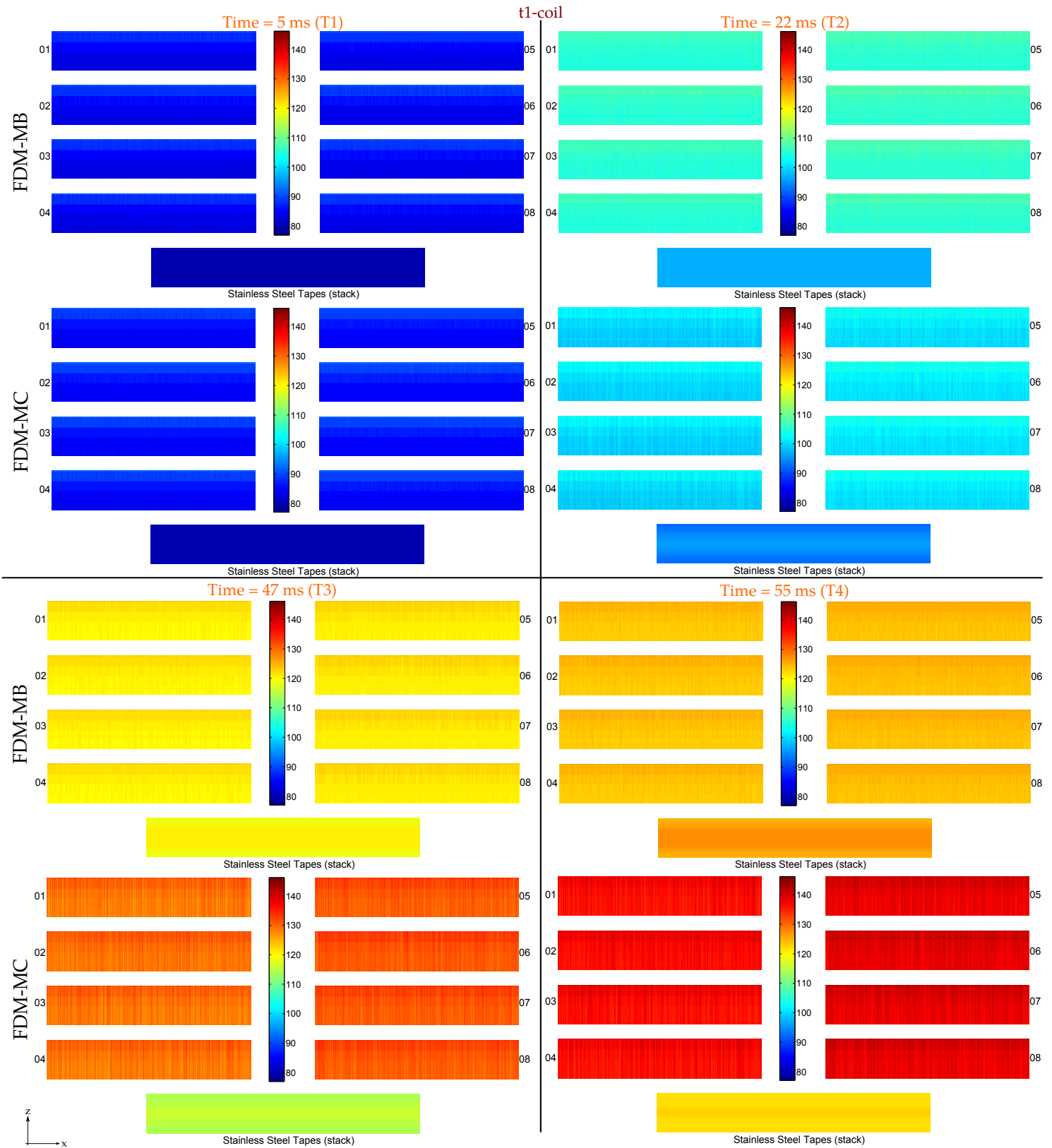


Figure 6.20: Temperature rise predicted by models FDM-MB and FDM-MC during the fault period for test t1-coil. A longitudinal view is presented (thickness (z) \times length (x)). Figure out of scale.

culated by model FDM-MB just after the quench of the YBCO layer (at approximately 5.5 ms). But, because of influence of the h_c coefficient, resistance values calculated by model FDM-MC are slightly higher at the end of fault period.

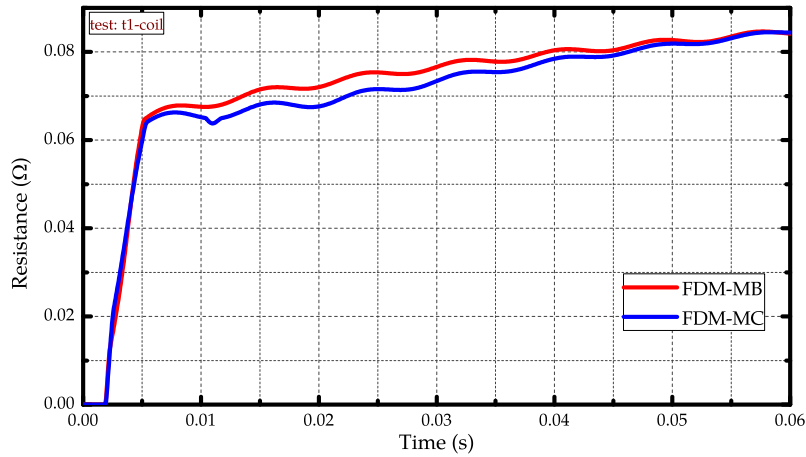


Figure 6.21: Comparison between equivalent resistances of the YBCO 2G coil according to the models FDM-MB and FDM-MC during the fault period in test t1-coil.

Comparisons between simulated results and measured ones for test t2-coil are shown in figure 6.22. A good agreement of simulated results with measured ones can be noted.

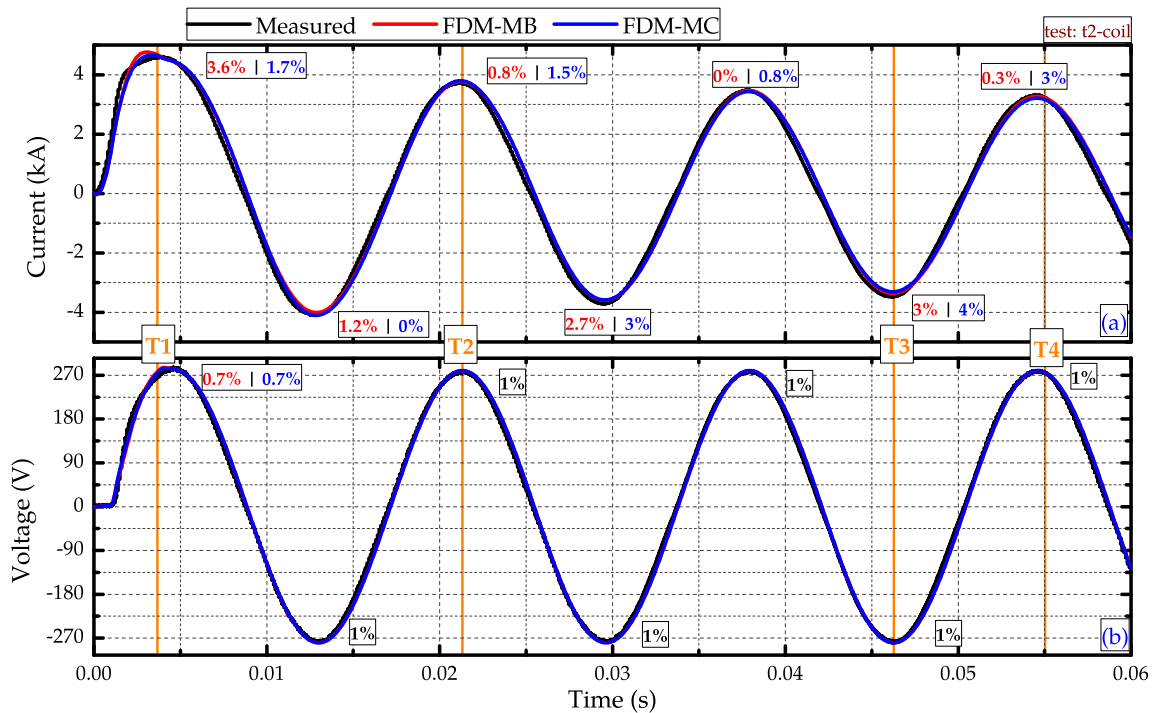


Figure 6.22: Comparison between measured and simulated results of the FDM-ADI model for a) limited current and b) voltage drop over the YBCO 2G coil for test t2-coil (fault current = 20.0 kA_{rms} under 1.0 kV_{rms}).

Excluding the first current peak, where model FDM-MB presented 3.6%, both models present similar results, besides reproducing quite well the behavior of measurements.

Points T1, T2, T3 and T4 in figure 6.22 define the following instants of time: 3 ms, 22 ms, 47 ms and 60 ms. Figure 6.23 shows temperature values for all tapes at these instants. Supplementary files `t2-coil_FDM-MB.mp4` and `t2-coil_FDM-MC.mp4` present the heating for all instants of time during the fault period.

All tapes illustrated in figure 6.23 present small internal temperature gradients along thickness (z -direction) and length (x -direction). Small differences on temperature along length are related to the inhomogeneity of tapes. However, there is not an overheating of a region over the others.

A careful observation of figure 6.23 let one observes temperature values slightly higher at the top of tapes. This occurs due the early heating of the superconducting layer (YBCO) which is closer to the top than to the bottom. However, as already stated, great temperature gradients should not exist inside tapes since they are very thin.

Figure 6.24 illustrates the resistance evolution calculated by models FDM-MB and FDM-MC. As in the previous text, values calculated by model FDM-MC are lower just after the quench of YBCO layer (approximately at 4 ms in this test), but becomes higher at the end of the fault period due to variations of the h_c coefficient.

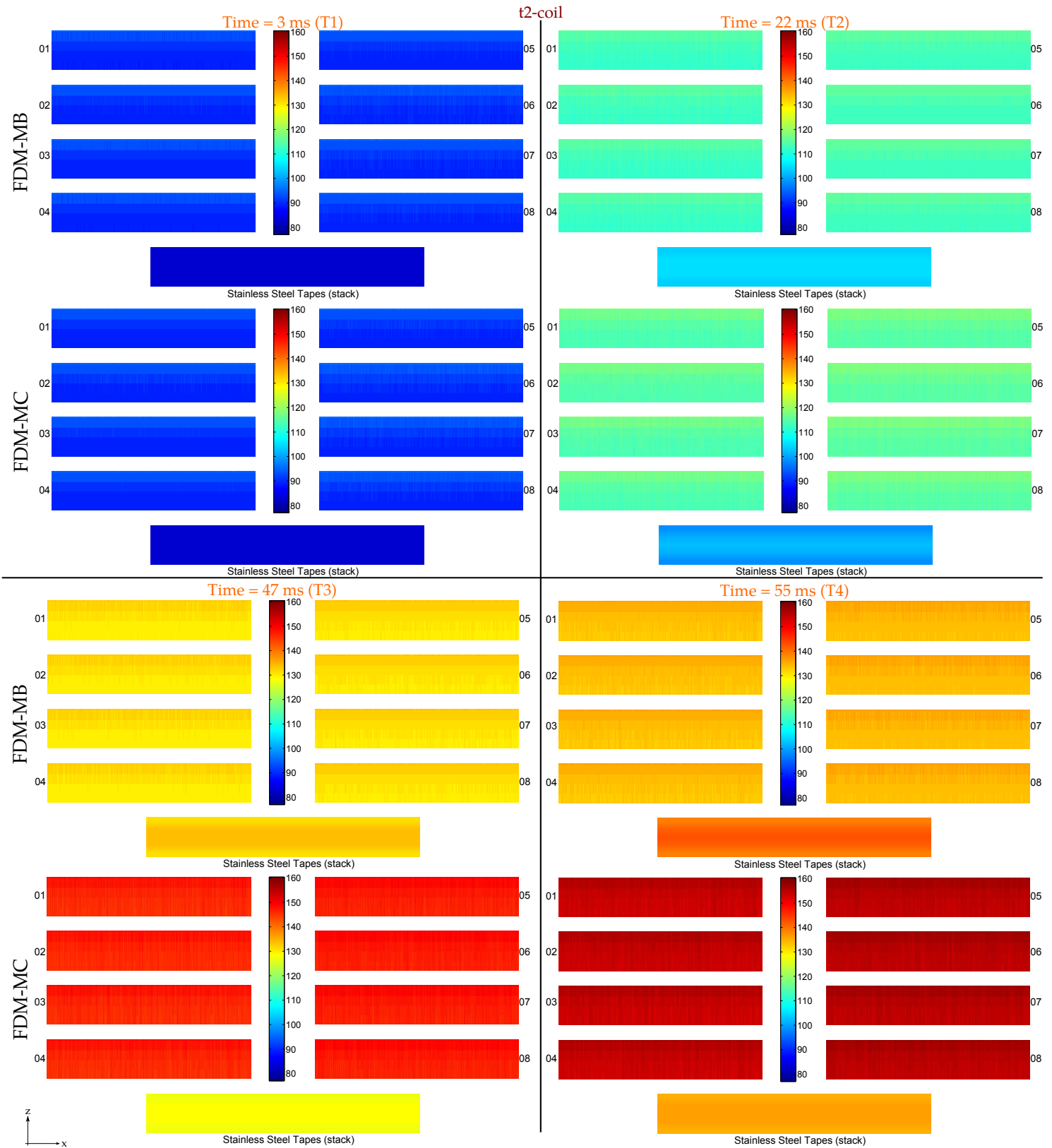


Figure 6.23: Temperature rise predicted by models FDM-MB and FDM-MC during the fault period for test t2-coil. A longitudinal view is presented (thickness (z) \times length (x)). Figure out of scale.

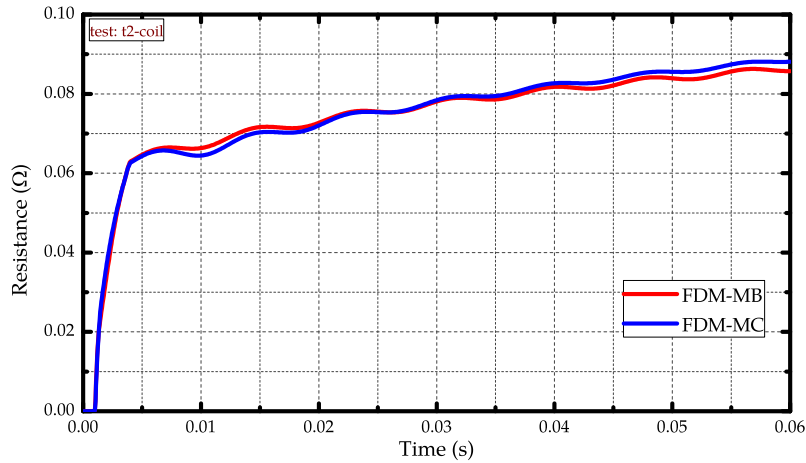


Figure 6.24: Comparison between equivalent resistances of the YBCO 2G coil according to the models FDM-MB and FDM-MC during the fault period in test t2-coil.

Figure 6.25 compares measured data with simulated ones for the performed test with the YBCO 2G coil (t3-coil). Models FDM-MB and FDM-MC present low error values besides reproducing quite well the limited current and voltage drop behavior.

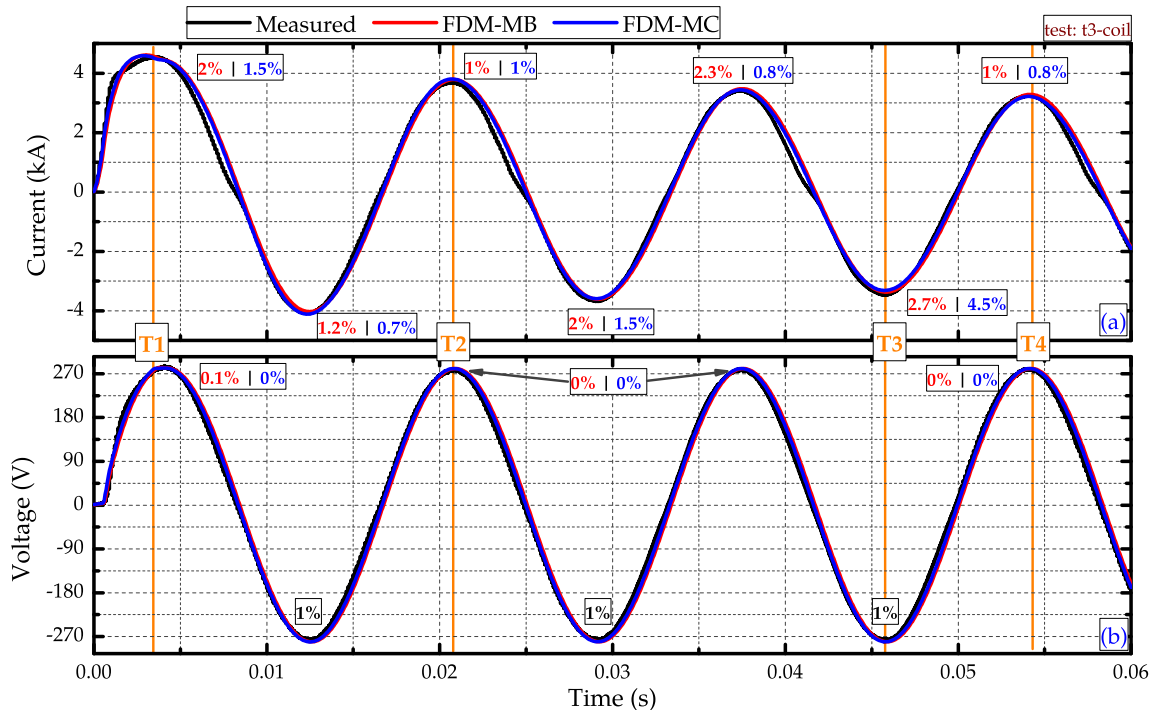


Figure 6.25: Comparison between measured and simulated results of the FDM-ADI model for a) limited current and b) voltage drop over the YBCO 2G coil for test t3-coil (fault current = 30.0 kA_{rms} under 1.0 kV_{rms}).

Figure 6.26 as well as multimedia files t3-coil_FDM-MB.mp4 and t3-coil_FDM-MC.mp4 present the heating during the fault period. In figure

6.26, the instants of time are: T1 at 3 ms, T2 at 22 ms, T3 at 47 ms and T4 at 54 ms.

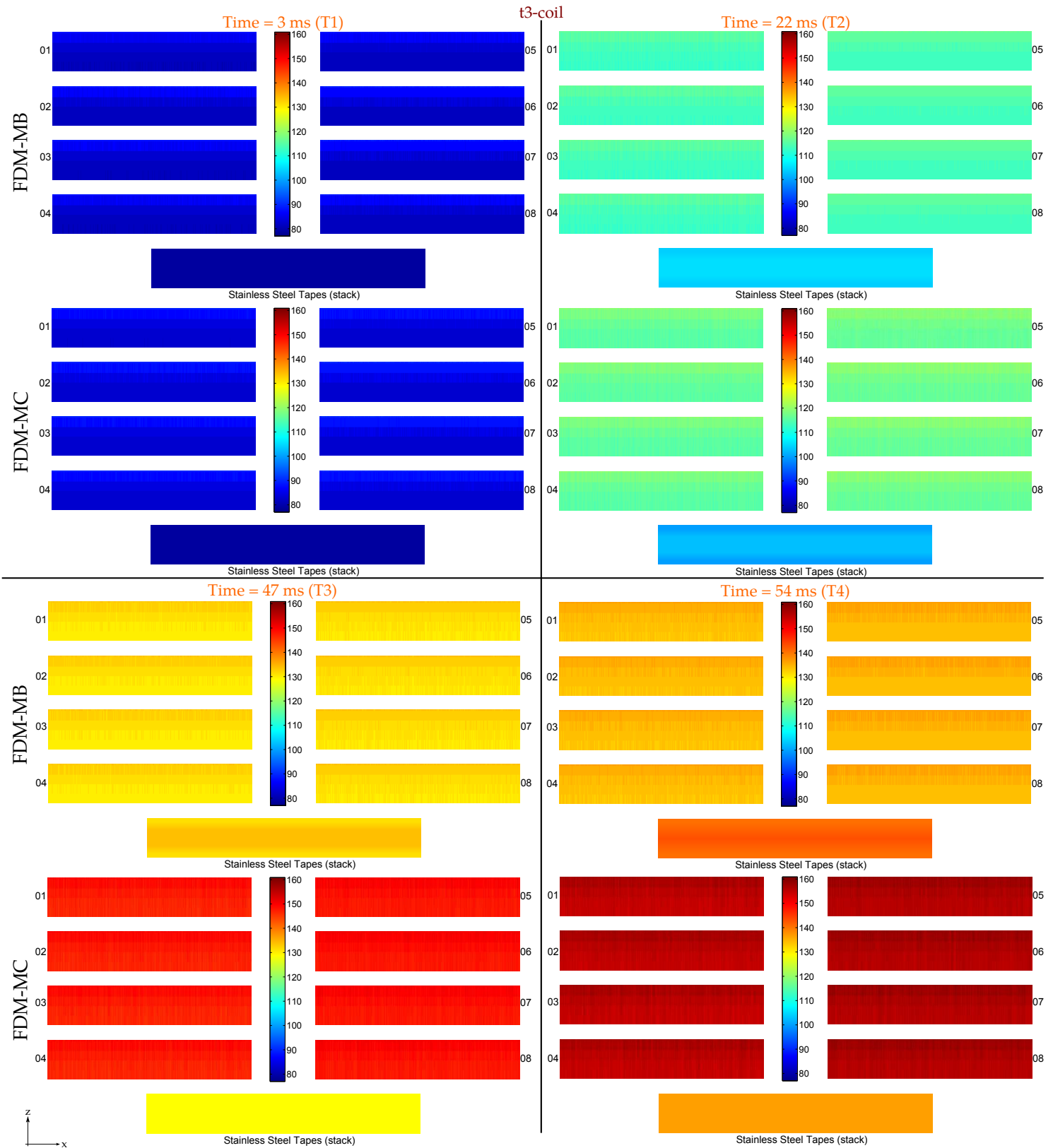


Figure 6.26: Temperature rise predicted by models FDM-MB and FDM-MC during the fault period for test t3-coil. A longitudinal view is presented (thickness (z) × length (x)). Figure out of scale.

One does not observe great temperature gradients along thickness and length, only small variations of temperature regarding the different I_c values along the x -direction. Temperature values calculated by model FDM-MC are higher than those ones obtained by model FDM-MB, since the film boiling regime of h_c coefficient is fast reached.

The characteristic behavior of resistance presented by the YBCO 2G coil in the previous tests repeats itself in test t3-coil, as shown in figure 6.27.

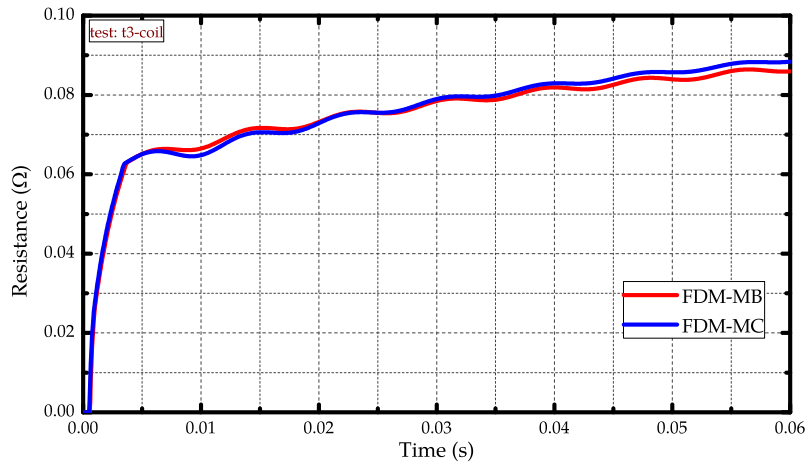


Figure 6.27: Comparison between equivalent resistances of the YBCO 2G coil according to the models FDM-MB and FDM-MC during the fault period in test t3-coil.

6.6.3 Air Coil SFCL Results

Results of simulations for test t1-acsfcl performed with the Air Coil SFCL are shown in the next figures.

Figure 6.28 compares measured data of limited current and voltage drop with simulated ones. Errors lower than 1% are identified in the limited current curve. For simulated voltage drop, the highest error observed was committed by model FDM-MB at the first peak (3.7%).

Some deviations of simulated data in relation to the measured ones for the voltage drop curve can be also noted. However, it may be related to the measurement setup and not with superconducting behavior or effects. For this reason simulations and measurements do not match at some points.

The heating process of tapes in test t1-acsfcl is illustrated in figure 6.29 at the instants T1 (5 ms), T2 (15 ms), T3 (25 ms) and T4 (35 ms). Layers are disposed according to the sequence illustrated in figure 6.4c. Supplementary files t1-acsfcl_FDM-MB.mp4 and t1-acsfcl_FDM-MC.mp4 show the complete heating process of test t1-acsfcl over the time.

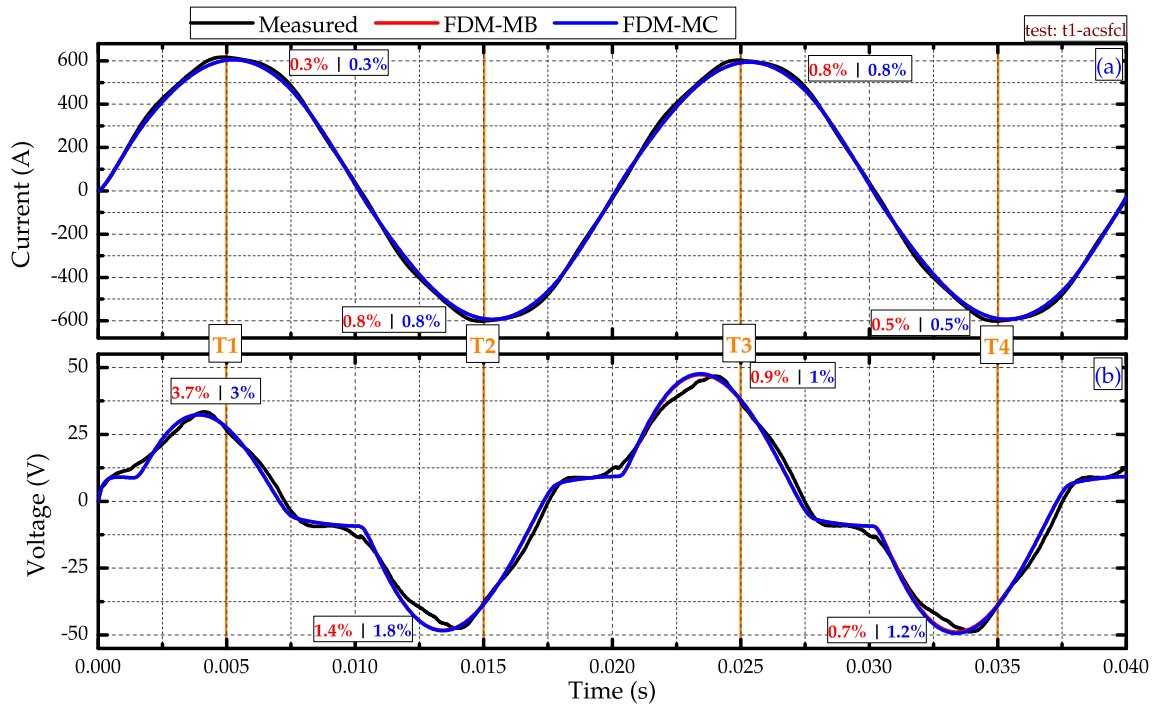


Figure 6.28: Comparison between measured and simulated results of the FDM-ADI model for a) limited current and b) voltage drop over the Air Coil SFCL for test t1-acsfcl (fault current = $450 A_{rms}$ under $400V_{rms}$).

As shown in figure 6.29, small temperature gradients are present inside the tapes, what is completely expected since the tapes are very thin. Variations along the length are related to inhomogeneities.

It is possible to observe higher temperatures at the top of tapes. As in the case of the YBCO 2G coil, the top heats up more than bottom because of the position of the superconducting layer close to the top. Moreover, the hastelloy layer has low thermal conductivity, what hampers the heat conduction to the layers at bottom.

Still on figure 6.29, one notes that the tapes 05, 06, 07, 16, 17, and 18 start to heat before the others since these tapes have a lower average value of critical current I_c . Furthermore, none of the used models predicts tapes quenching in this test.

Figure 6.30 illustrates calculated behaviors of equivalent resistance of the HTS tapes at the secondary of the Air Coil SFCL for test t1-acsfcl. Both models provides high non linear behaviors, suggesting that all tapes did not quench.

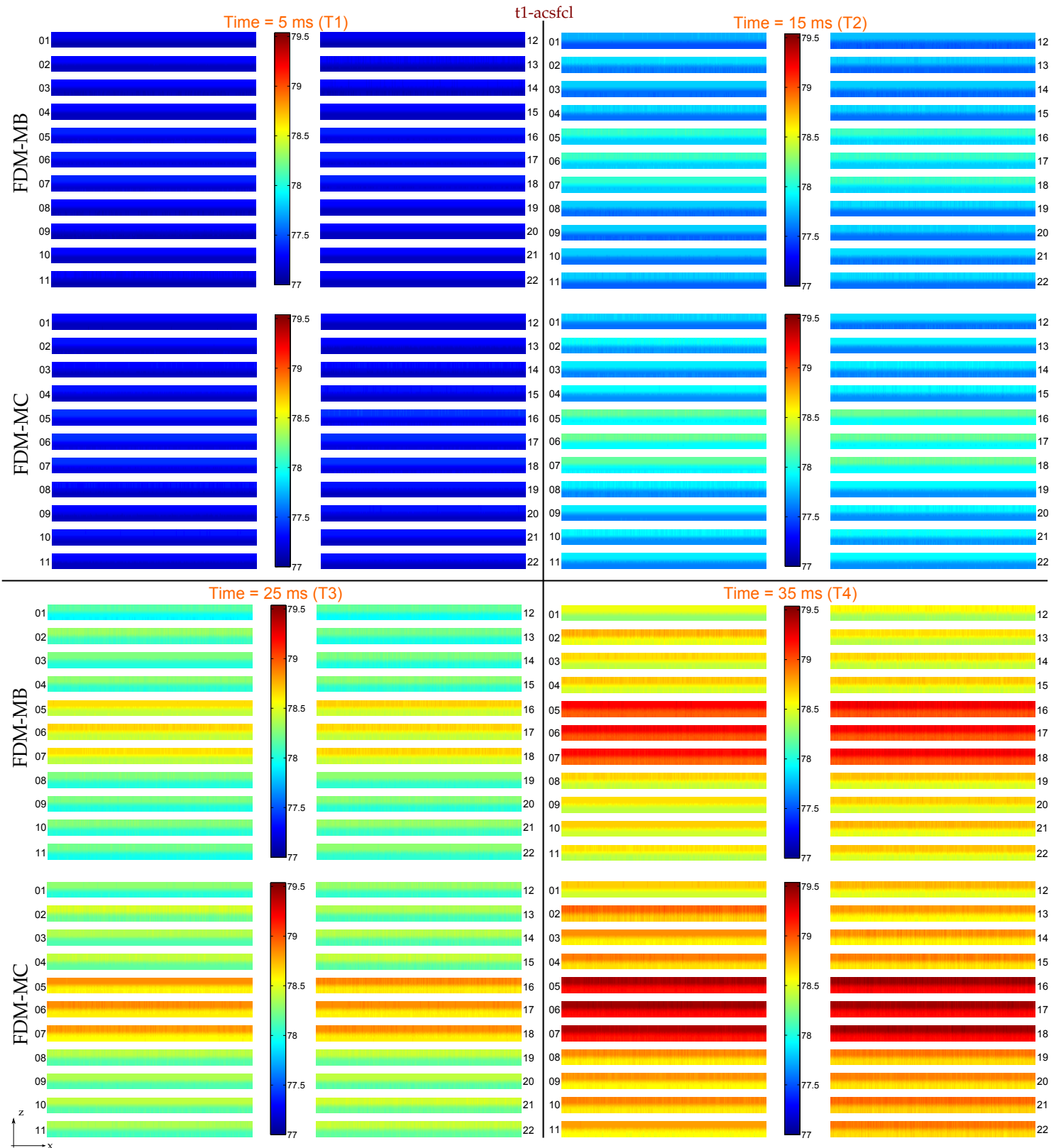


Figure 6.29: Temperature rise predicted by models FDM-MB and FDM-MC during the fault period for test t1-acsfcl. A longitudinal view is presented (thickness (z) × length (x)). Figure out of scale.

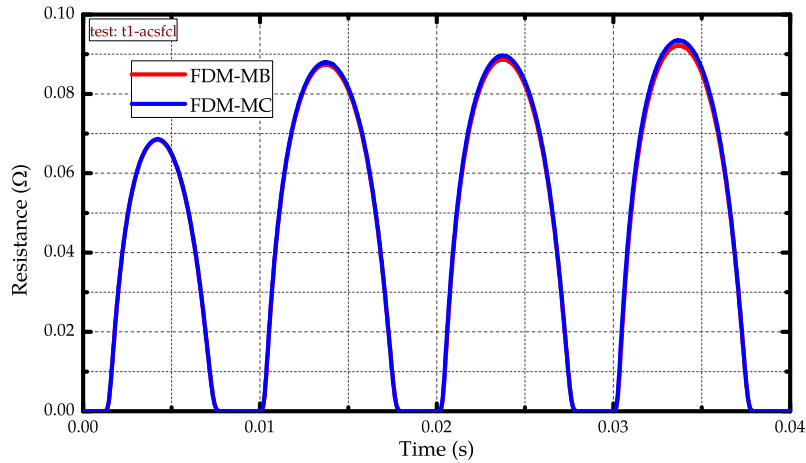


Figure 6.30: Comparison between equivalent resistances of the HTS tapes of the Air Coil SFCL according to the models FDM-MB and FDM-MC during the fault period in test t1-acsfcl.

Comparisons between measured and simulated results for test t2-acsfcl are shown in figure 6.31. Very small error values are found in the limited current curves. Model FDM-MB commits the highest error in this simulations at the second peak (0.3%).

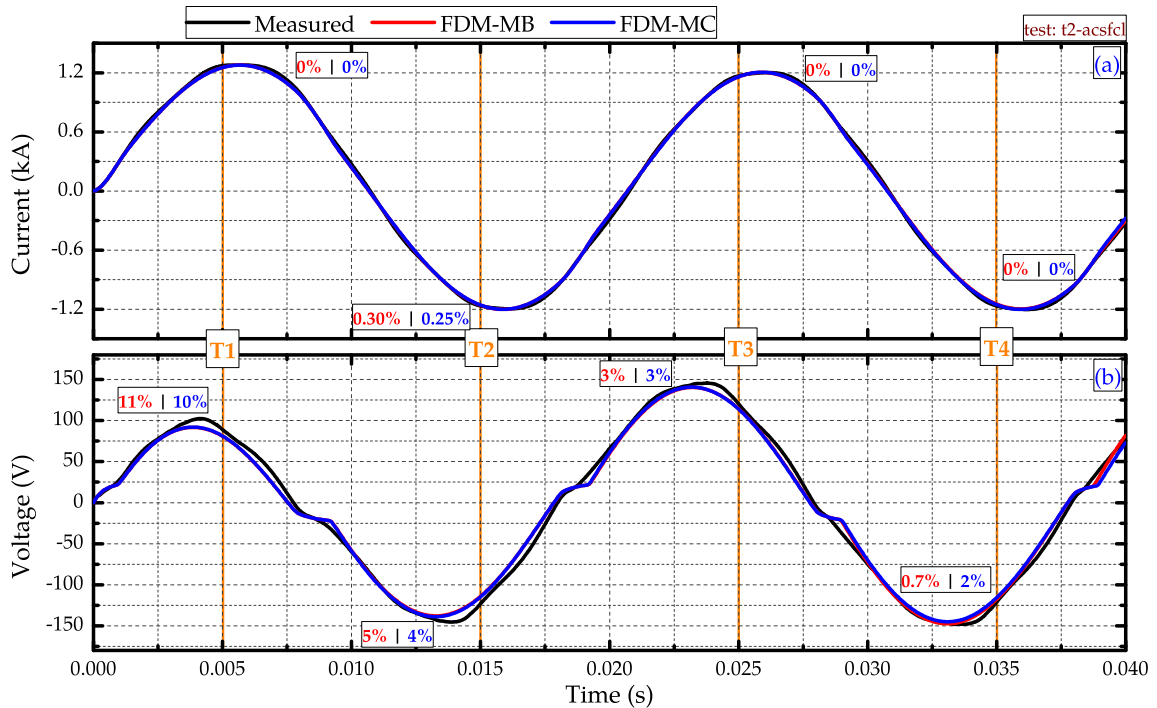


Figure 6.31: Comparison between measured and simulated results of the FDM-ADI model for a) limited current and b) voltage drop over the Air Coil SFCL for test t2-acsfcl (fault current = 1.05 kA_{rms} under 400 V_{rms}).

Supplementary files t2-acsfcl_FDM-MB.mp4 and t2-acsfcl_FDM-MC.mp4 as well figure 6.32 present the heating process for test t2-acsfcl during the transient.

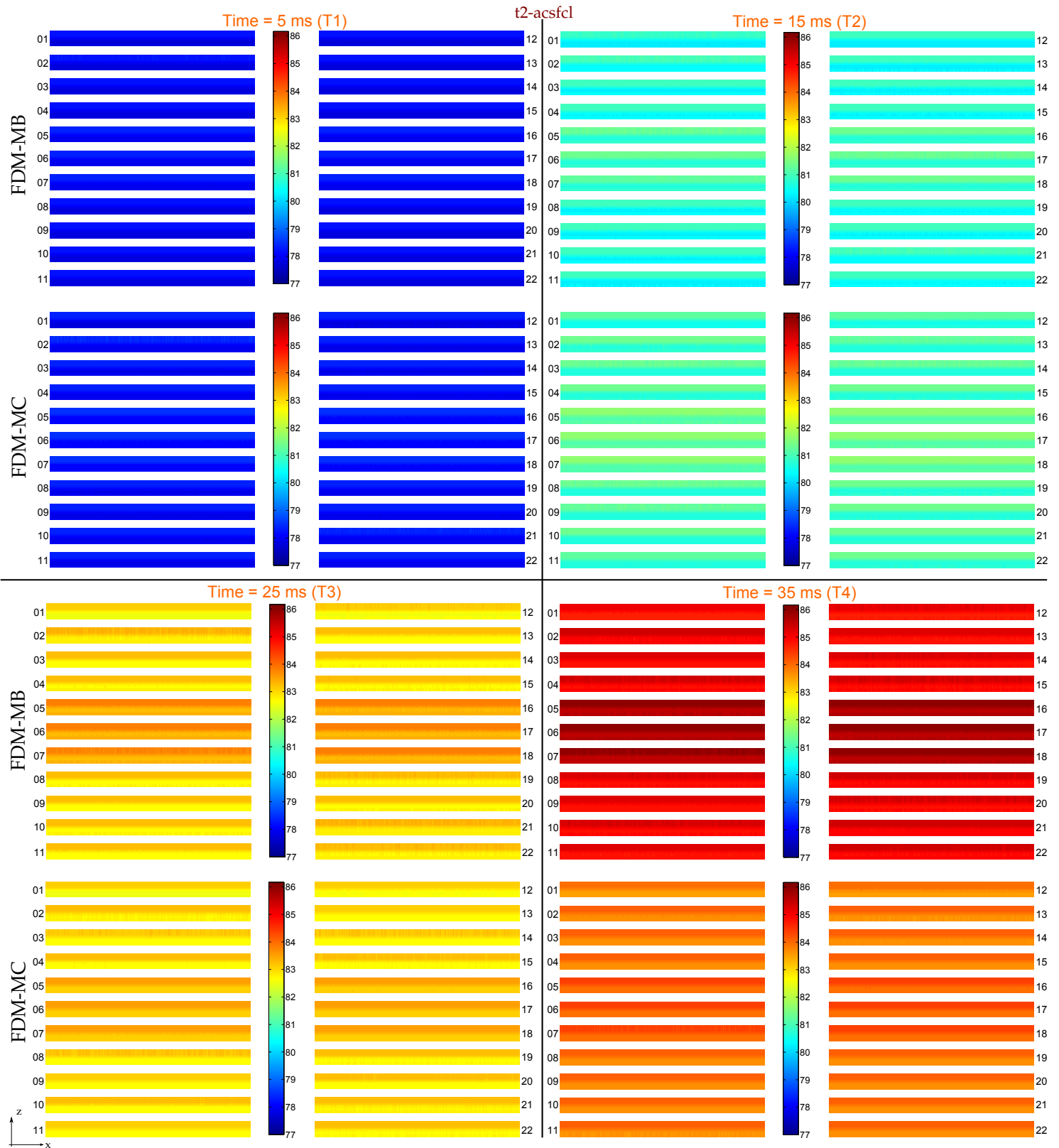


Figure 6.32: Temperature rise predicted by models FDM-MB and FDM-MC during the fault period for test t2-acsfcl. A longitudinal view is presented (thickness (z) \times length (x)). Figure out of scale.

According with the multimedia files and figure 6.32, there are no significant temperature gradients inside the tapes, neither along z -direction (thickness), nor along x -direction (length). Since tapes 05, 06, 07, 16, 17, and 18 have a lower average value of critical current I_c , they present a earlier heating in relation to the others. Nevertheless, it is also worth mentioning that there is no prediction of quenching in this test for all simulated tapes either by model FDM-MB or by model FDM-MC.

Temperature values calculated by model FDM-MC are lower than those calculated by means of model FDM-MB since the convective heat transfer coefficient h_c strongly affects the behavior of heating in model FDM-MC by its entrance in the bubble boiling regime.

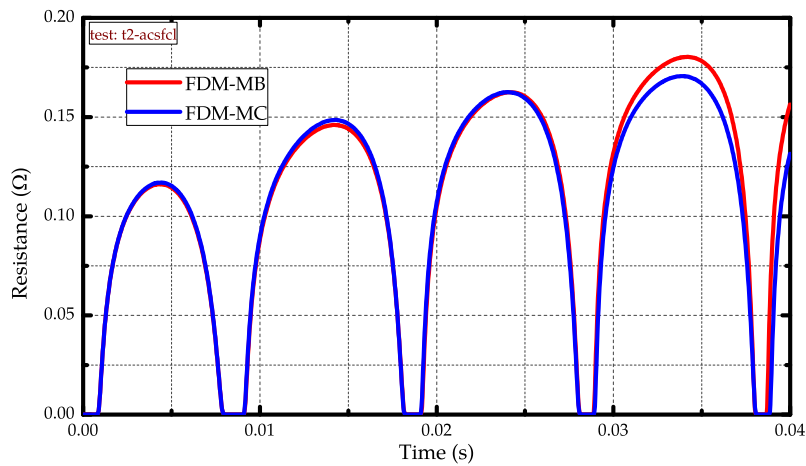


Figure 6.33: Comparison between equivalent resistances of the HTS tapes of the Air Coil SFCL according to the models FDM-MB and FDM-MC during the fault period in test t2-acsfcl.

Figure 6.33 illustrates the high non linear resistance behavior of the HTS tapes during the transient. As in the previous test, the non linear behaviors are related to the absence of quenching of the superconducting layer.

Errors regarding comparisons between measured and simulated results of test t3-acsfcl are also small, as shown in figure 6.34. Either in the limited current curve or in voltage drop one, both models provides good agreement with measurements. Errors above 3% were not committed.

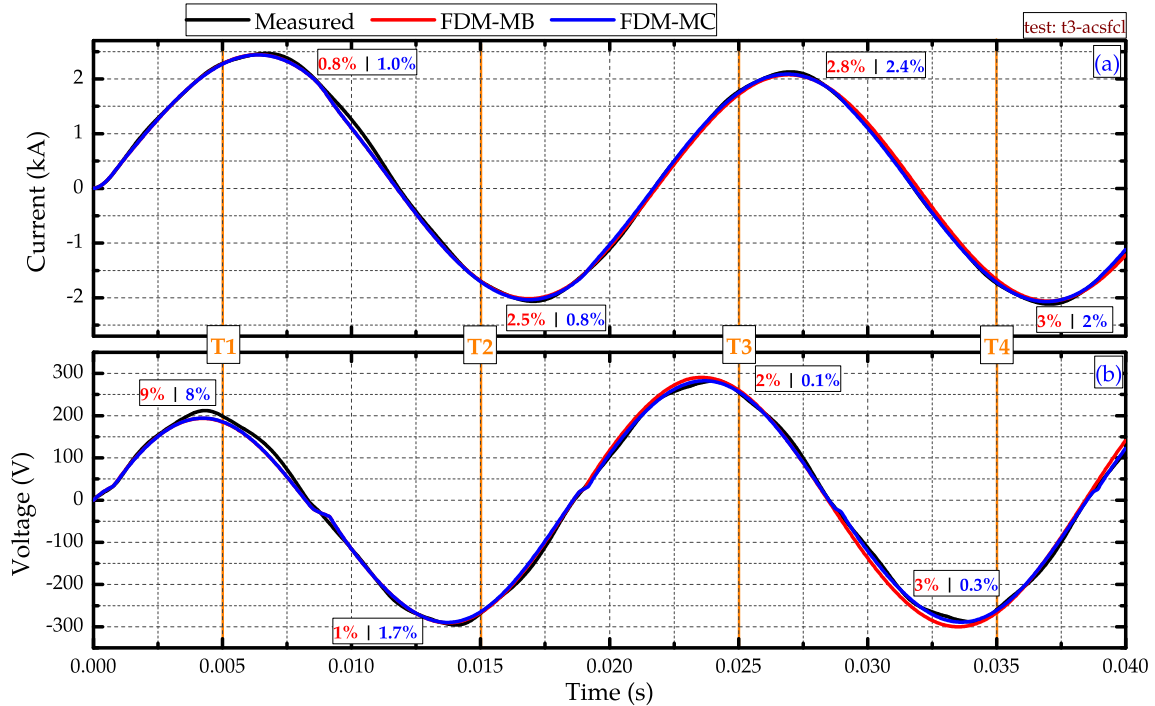


Figure 6.34: Comparison between measured and simulated results of the FDM-ADI model for a) limited current and b) voltage drop over the Air Coil SFCL for test t3-acsfcl (fault current = 2.55 kA_{rms} under 400 V_{rms}).

Instants of time defined in figure 6.34 are the same previously defined in tests t1-acsfcl and t2-acsfcl. Figure 6.35 shows temperature values for all simulated tapes in test t3-acsfcl at these instants. Supplementary files t3-acsfcl_FDM-MB.mp4 and t3-acsfcl_FDM-MC.mp4 show the complete heating process of test t3-acsfcl over the time.

Temperature values are strongly influenced by the h_c coefficient in model FDM-MB. For this reason, temperatures values calculated by model FDM-MB are higher than those obtained by model FDM-MC at the end of the fault period. In model FDM-MB the h_c value is constant.

In contrast to the tests t1-acsfcl and t2-acsfcl, the quenching of the superconducting material is predicted by model FDM-MB in test t3-acsfcl. As shown at instant T4, in figure 6.35, all tapes reach temperature values above T_c (92 K).

In case of model FDM-MC, however, the quench does not occurs. As shown in instant T4 in figure 6.35, none tape present temperature values higher than 92 K.

This fact is confirmed by analyzing resistance behaviors in figure 6.36. Model FDM-MB predicts a linear behavior at about 20 ms, indicating that a full quench

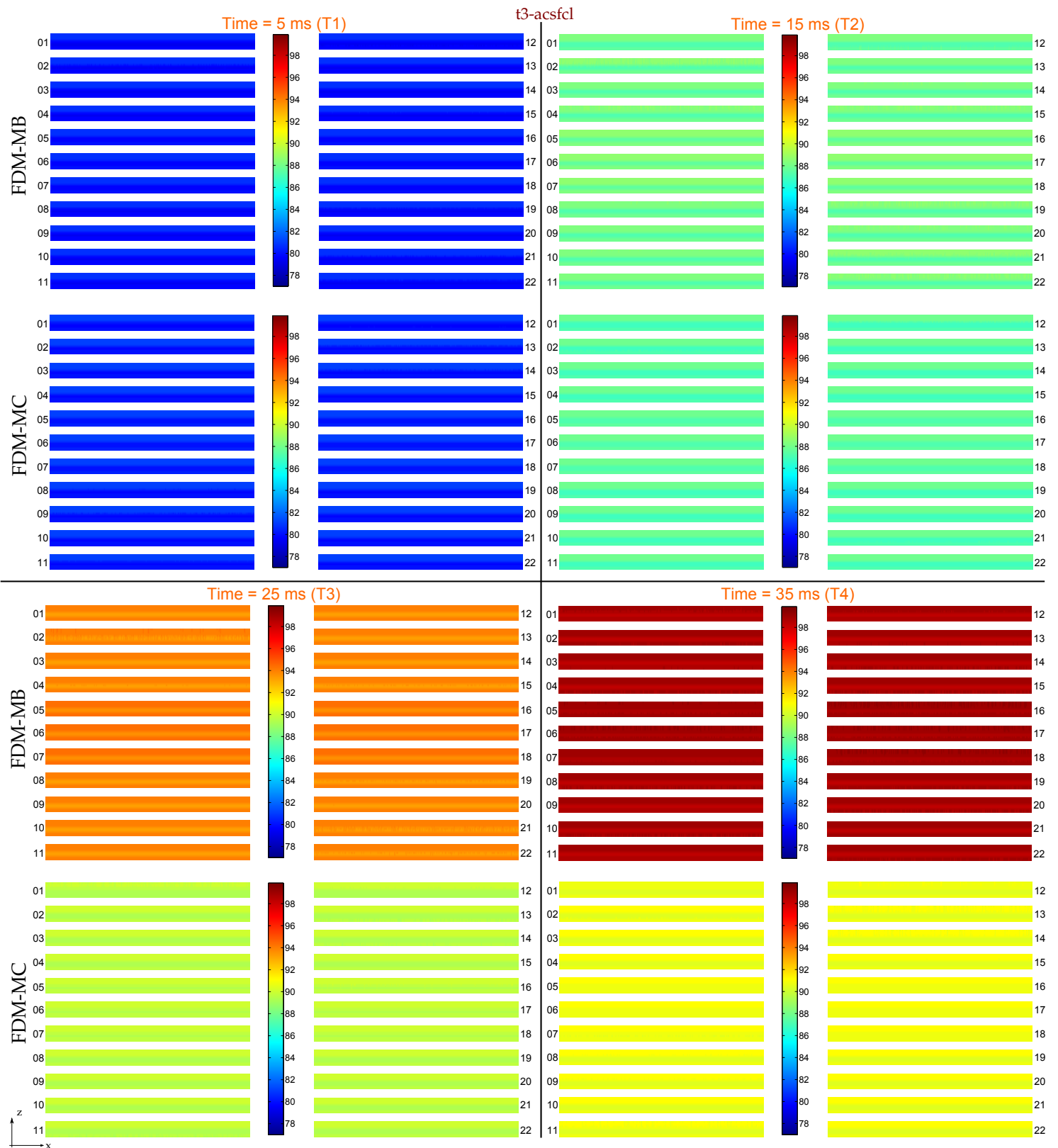


Figure 6.35: Temperature rise predicted by models FDM-MB and FDM-MC during the fault period for test t3-acsfcl. A longitudinal view is presented (thickness (z) \times length (x)). Figure out of scale.

occurred, whereas model FDM-MC predicts a non linear behavior during the entire period of fault.

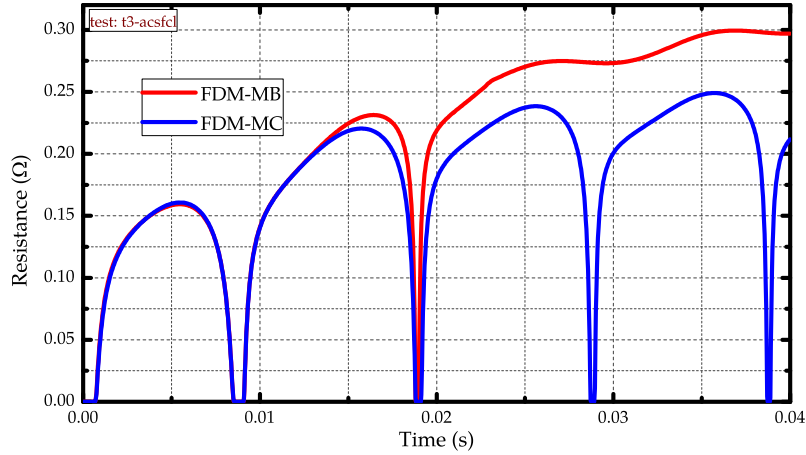


Figure 6.36: Comparison between equivalent resistances of the HTS tapes of the Air Coil SFCL according to the models FDM-MB and FDM-MC during the fault period in test t3-acsfcl.

6.7 Summary and Discussions

This chapter has introduced the Finite Difference Method (FDM) for simulations of tapes and modules constituting a SFCL device. Traditional solution routines may lead to huge times of simulation. As will be shown in chapter 7, the time of simulation can be significantly reduced by applying the alternating direction implicit (ADI) routine to solve systems of differential equations of the FDM method. The ADI method consists of an implicit method, what makes possible using larger values of timestep Δt besides ensuring stability.

Long tapes and modules could also be simulated by means of the FDM-ADI method. Conventional methods, as finite elements method, may not be able to simulate long lengths since such simulations would require super-computers to be performed besides resulting in huge times of simulation. Simulations presented in this work, performed with FDM-ADI, were run in a conventional computer.

The FDM-ADI method allows insertion of different values of critical current along the length of the superconducting layer, enabling further studies of inhomogeneities effects on current limitation. In this work, only inhomogeneities regarding values of critical current have been inserted, but it is also possible extending the present concept to insert different values of critical temperature T_c and index of transition n . Furthermore, based on data found in literature, it was decided to apply a Gaussian distribution to represent inhomogeneities of the tapes. However, other kinds of distribution can be used to represent inhomogeneities. As

example, in references [29, 149], an exponential distribution was employed.

As in the case of the TEA method, the FDI-ADI method was wearily tested under different conditions for three distinct SFCL concepts. Simulated results were verified against experimental results. Both developed models (FDM-MB and FDM-MC) have provided good accordance with measured data, since all simulated results follows similar behaviors of measured ones. In most of cases, errors committed by both models are lower than 10%. Moreover, they can be very helpful in providing estimations of properties of hard experimental access. For example, it would be quite complicated measuring temperature values of layers in modules and tapes during the fault transient. Measuring local values of temperature can be more complicated, or even impossible. Thus, if a study of local values of physical properties is desired, the FDM-ADI method can be an ideal choice.

Comparing models FDM-MB and FDM-MC, one observes no big differences between them regarding limited current and voltage drop curves. However, as already discussed in chapter 5, the convective heat transfer coefficient h_c plays an important role in simulations of tapes. Different regimes of the h_c coefficient, employed in model FDM-MC, are the main factor responsible for differences on temperature values provided by both models.

An important feature of temperature profiles generated by model FDM-MC, is that different heating rates along the length are not only due to inhomogeneity representation of I_c , but also due to local variations of physical properties (specific heat ς and thermal conductivity k). Models FDM-MB and FDM-MC calculate temperature values for each centimeter of tape. Thus, it is expected to obtain variations of temperature along length since at each centimeter a new value of critical current is inserted. However, when making use of model FDM-MC, calculations of temperature are also affected by variable physical properties, i.e, not only variations of I_c along the x -direction generates different heating rates, but also local variations of specific heat and thermal conductivity provides differences on thermal profiles provided by model FDM-MC in comparison with those provided by model FDM-MB. For example, in test t3-acsfcl, there was a prediction of quenching by model FDM-MB whereas no quenching was predicted by model FDM-MC.

Temperature profiles strongly affects outputted resistance behaviors. In the example above mentioned (t3-acsfcl), the resistance curve predicted by model FDM-MC presents a non linear behavior until the end of the fault period whereby the resistance curve predicted by model FDM-MB shows a linear behavior after 20 ms.

Since the existing variations between the models are small, both of them are able to provide satisfactory results, as have been verified by comparisons with measurements of limited and voltage drop curves. Although model FDM-MB

does not take into account local variations of physical properties as well as variations of the h_c coefficient, it has predicted results agreeing with experimental results. Model FDM-MC is the more realistic model developed in this work and has also provided good results. A major drawback of the model FDM-MC is its simulation algorithm. As shown in figure 6.9, model FDM-MC requires an additional task (box 11a), in order to update values of specific heat and thermal conductivity for each element of the mesh as well as to update values of the convective heat transfer coefficient. It must be done for all tapes and modules constituting the SFCL device. Such additional task does not only make the simulation algorithm more complex, but also considerably increases the simulation time, as will be shown in the next chapter (see table 7.1).

Chapter 7

Final Comparisons

In previous chapter one has introduced the main concepts of the thermal-electrical analogy (chapter 5) and finite difference method (chapter 6) in order to perform transient simulations of SFCL devices. Now, results obtained by means of these methods are compared. Error values committed in comparisons between limited current and voltage drop curves are analyzed. Resistance curves are also compared. A particular consideration is given to correlated models, that is, direct comparisons between models TEA-MB and FDM-MB as well as TEA-MC and FDM-MC.

7.1 MCP-BSCCO-2212 - TEA \times FDM Results

Figure 7.1 summarizes simulated results obtained by models TEA-MB, TEA-MC, FDM-MB and FDM-MC. As can be observed, the insertion of inhomogeneities in the modules have not reduced errors committed by models TEA in limited current and voltage drop curves. In some cases, error values were even considerably worsened.

These results suggest that the inhomogeneity representation employed for the modules may be not the more suitable one. In this sense, the parameter ϵ ¹ could be better adjusted in order to obtain better results. It is worth to remember that the standard deviation σ for the modules was retrieved from literature and may not correspond to real values of the employed modules. Furthermore, as already mentioned before, the inhomogeneity representation can be built not only for values of critical current, but also for critical temperature and index of transition values.

Although some errors exhibited by FDM models are higher than those exhibited by TEA models, it is worth noting that most errors are under 10%. In addi-

¹Defined in chapter 3 to select the most probable values of critical current I_c

tion, a comparison between temperature increase presented by models TEA-MB and TEA-MC (figures 5.14b and 5.14c, respectively) with temperature profiles presented in figure 6.11 by models FDM-MB and FDM-MC, indicates temperatures of the same magnitude for the selected instants of time.

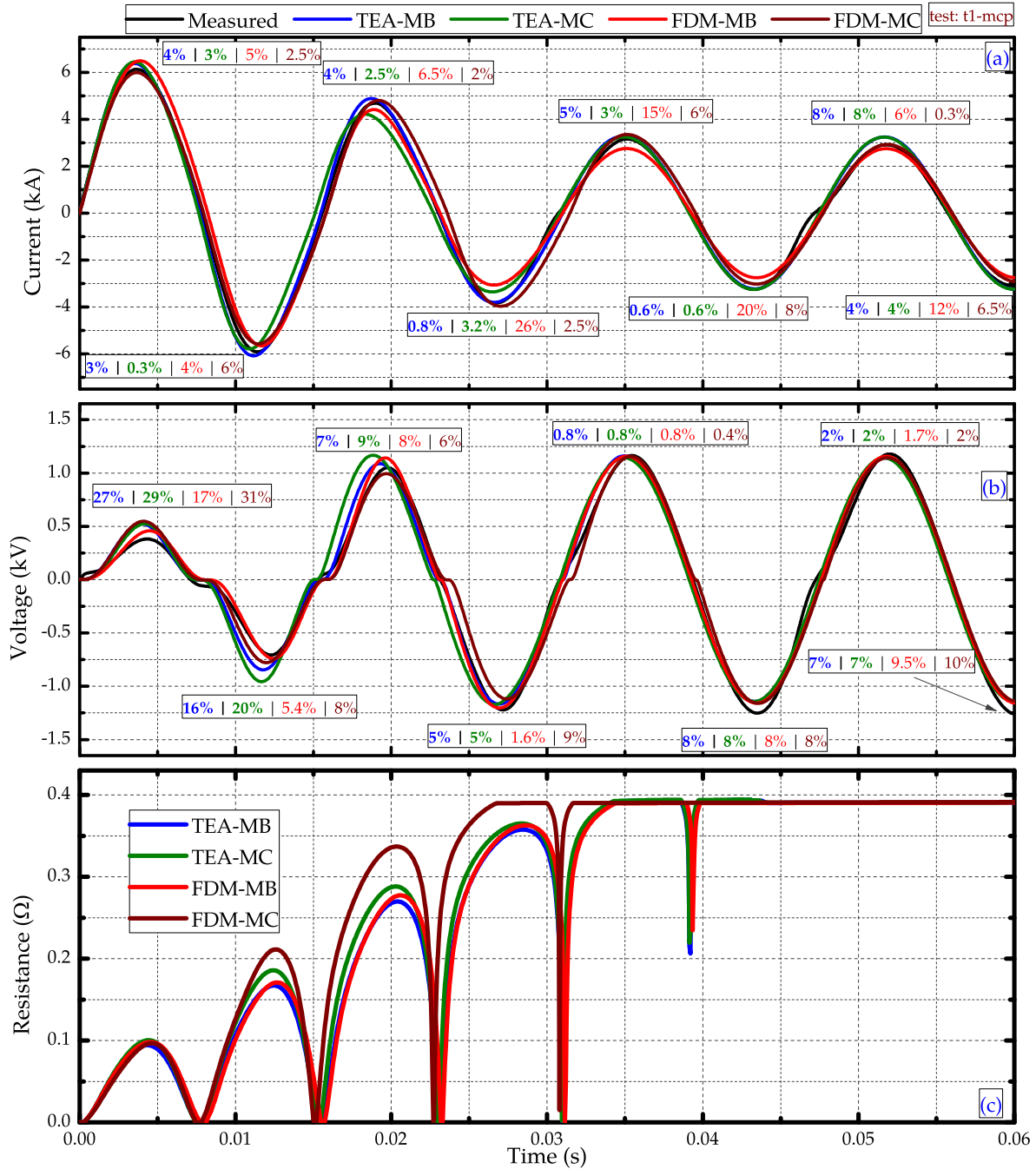


Figure 7.1: Comparison between measured and simulated results of the TEA and FDM-ADI models for a) limited current, b) voltage drop and c) equivalent resistances of the MCP-BSSCO-2212 assembly for test t1-mcp (fault current = 5.0 kA_{rms} under 1.0 kV_{rms}).

By observing resistance behaviors in figure 7.1c, one clearly notes the non linear behavior outputted by TEA and FDM models, originated from the E-J charac-

teristic curve of BSCCO-2212 material.

Figure 7.2 compares results of TEA and FDM models for test t2-mcp.

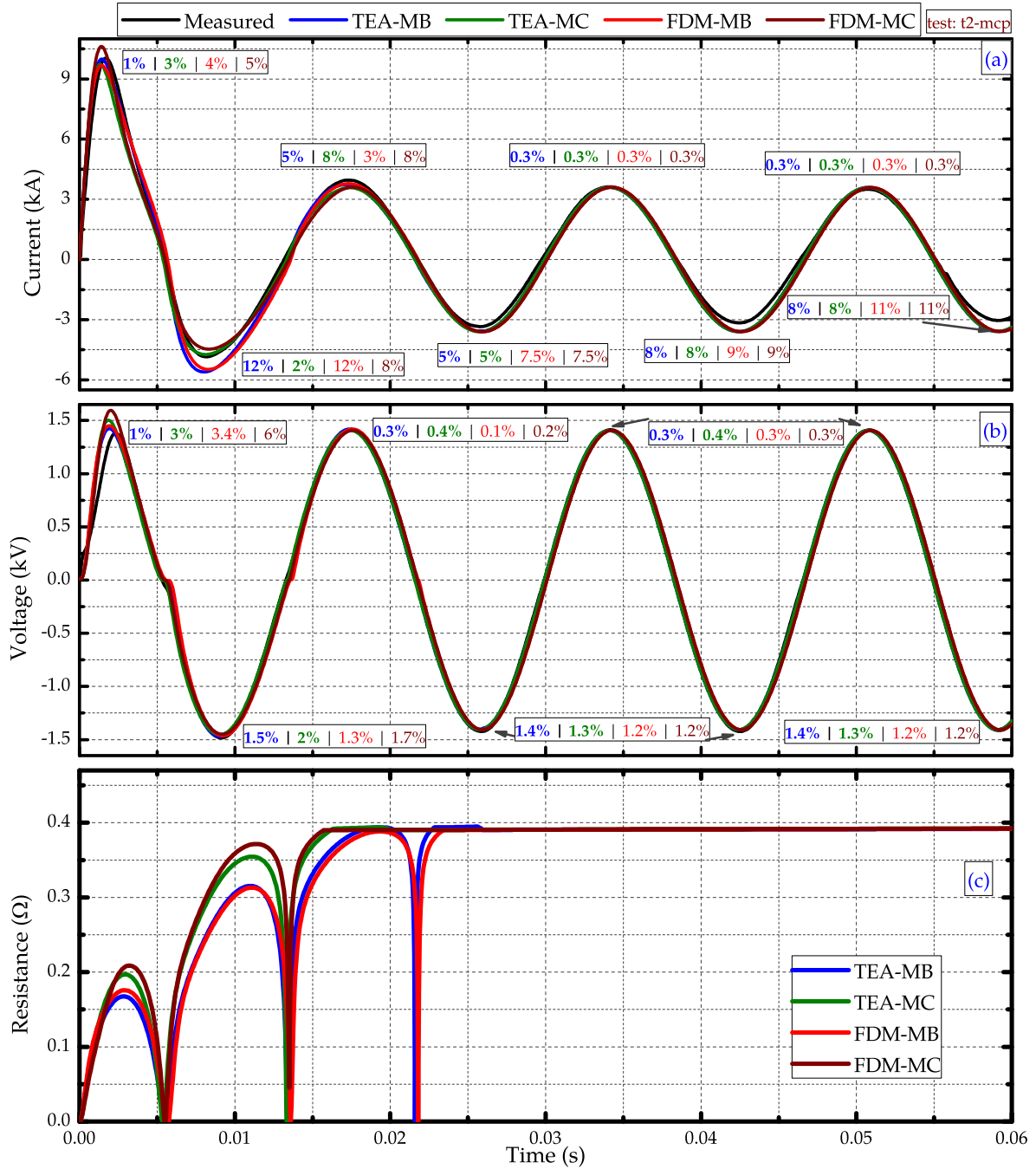


Figure 7.2: Comparison between measured and simulated results of the TEA and FDM-ADI models for a) limited current, b) voltage drop and c) equivalent resistances of the MCP-BSCCO-2212 assembly for test t2-mcp (fault current = 25.0 kA_{rms} under 1.0 kV_{rms}).

As in the previous test, no significant improvements can be observed by inserting the inhomogeneity representation. TEA and FDM models have committed errors in the same magnitude. It is worth to observe the behavior predicted by correlated models: models TEA-MB and FDM-MB (without local variations of

physical properties, as well as variations on the h_c coefficient) show similar behaviors not only in the limited current and voltage drop curves, but also in the resistance development curve (figure 7.2c)

Temperature values presented at instants T1, T2, T3 and T4 in figure 6.14 are similar in magnitude to those ones presented at the same instants in figures 5.17b and 5.17c. In other words, models TEA-MB and TEA-MC provide similar results of models FDM-MB and FDM-MC, respectively

A final comparison for the MCP-BSCCO-2212 modules is done in figure 7.3, for test t3-mcp. As in the previous tests, no huge differences have been found between TEA and FDM models. It is worth noting behavior of correlated methods. Models TEA-MB and FDM-MB present very similar behaviors, as well as models TEA-MC and FDM-MC are similar to each other. This characteristic can be corroborated by analyzing resistance curves, presented in figure 7.3c.

Finally, comparing temperature values of correlated models shown in figures 5.20b and 5.20c with those illustrated in figure 6.17, one can identify similar values at the indicated instants of time (T1, T2, T3 and T4).

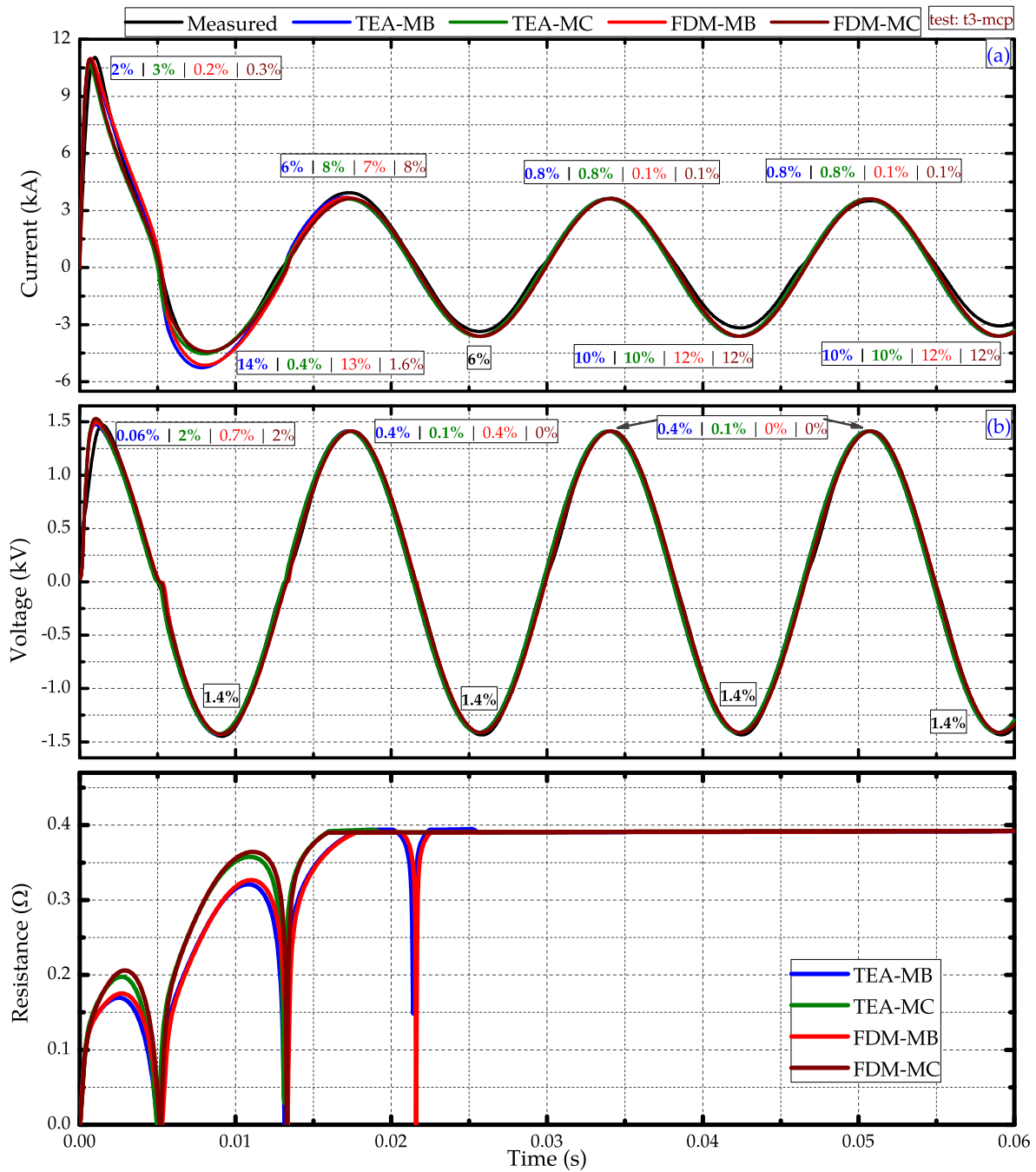


Figure 7.3: Comparison between measured and simulated results of the TEA and FDM-ADI models for a) limited current, b) voltage drop and c) equivalent resistances of the MCP-BSCCO-2212 assembly for test t3-mcp (fault current = 67.0 kA_{rms} under 1.0 kV_{rms}).

7.2 YBCO 2G Coil - TEA \times FDM Results

Simulated results outputted by TEA and FDM models for test t1-coil are quite similar, as shown in figure 7.4. As in the case of MCP-BSCCO-2212 modules, errors were not reduced by inserting inhomogeneities in the modules. However, errors higher than 10% have not been committed in this test by none model. Besides that,

all simulated curves behave similarly to the measured ones.

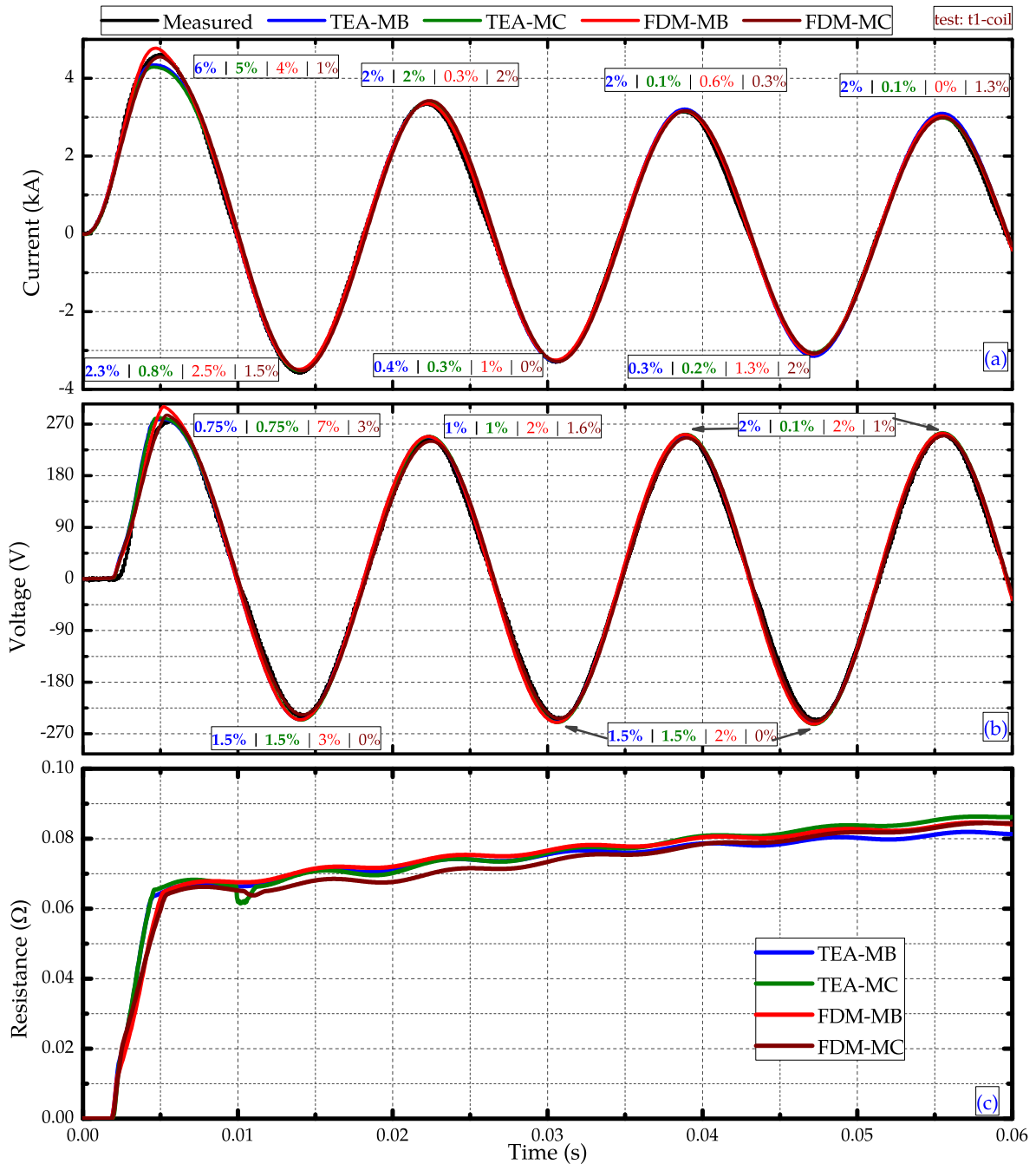


Figure 7.4: Comparison between measured and simulated results of the TEA and FDM-ADI models for a) limited current, b) voltage drop and c) equivalent resistances of the YBCO 2G coil for test t1-coil (fault current = 5.0 kA_{rms} under 200 V_{rms}).

Simulation results of different models are close to each other, but results of correlated models are even closer, what can be observed at figure 7.4c

Temperature values predicted by TEA models (figure 5.23) present a good agreement with those ones calculated by FDM models presented in figure 6.20. Temperature behavior presented by model TEA-MC in figure 5.23c emphasizes

the differences between tapes 06 and 01 (tapes with highest and lowest values of I_c , respectively). Nevertheless, model TEA-MC does not consider inhomogeneities of critical current. That is, by inserting different values of I_c in model TEA-MC, different heating rates are generated along the length. This effect is reinforced by local variations of physical properties. The early heating of a certain region of the tape with lower value of I_c is propagated along the x -direction by the metallic layers, leading to a more homogeneous temperature profile. Since model TEA-MC does not consider inhomogeneities of critical current, the heat propagation along the tapes length can not be considered, causing higher differences between the tapes.

Figure 7.5 shows comparisons between models TEA and FDM for test t2-coil. As can be observed, small errors have been committed by the studied models. There was not any error above 5%. Furthermore, all models present same value of error from second peak for the voltage drop curve, indicating a similar behavior which can be confirmed in figure 7.5c by comparing resistances curves.

Temperature values calculated by models TEA at instants T1, T2, T3 and T4 (figure 5.26) are similar to those presented by models FDM (figure 6.23).

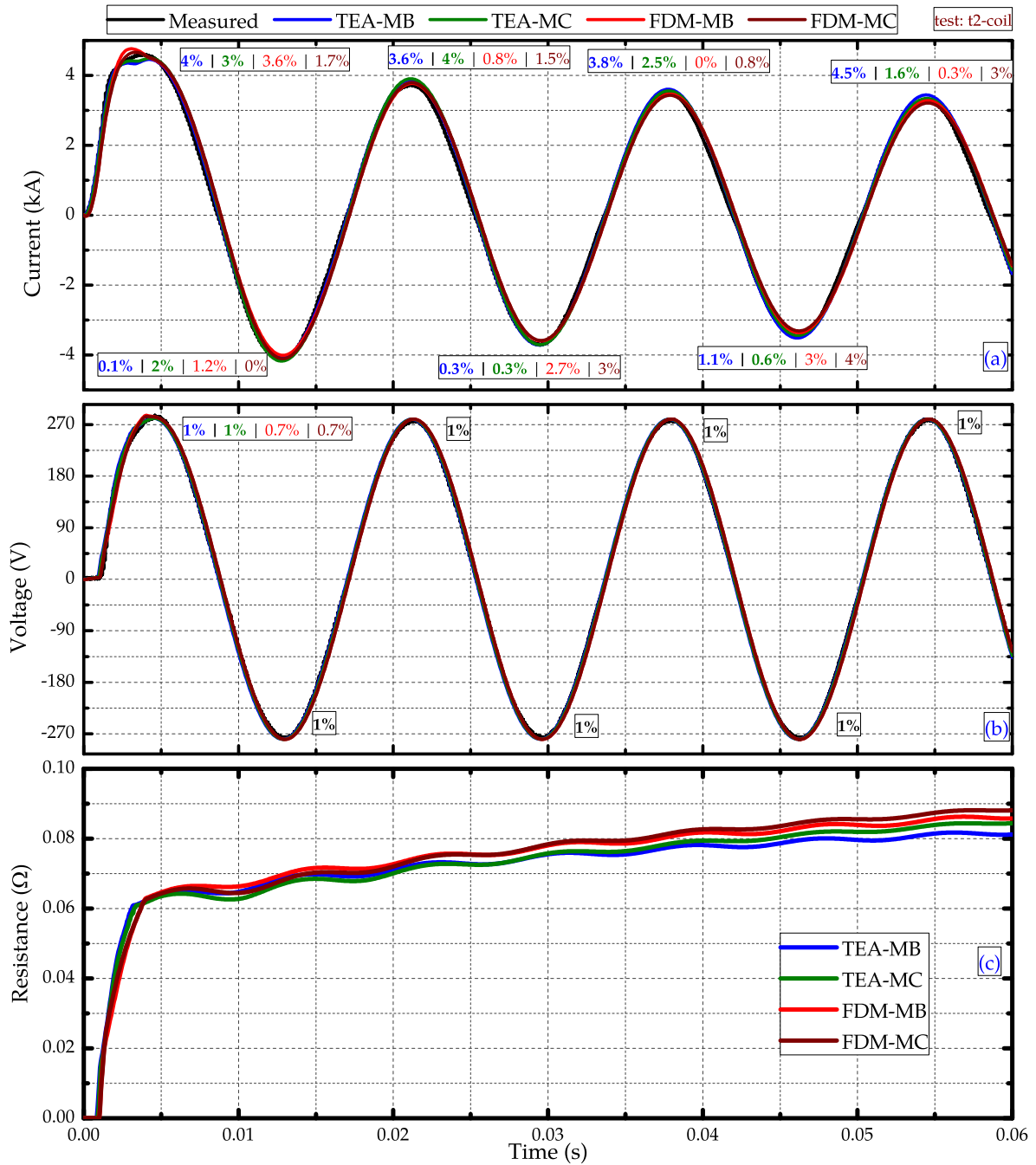


Figure 7.5: Comparison between measured and simulated results of the TEA and FDM-ADI models for a) limited current, b) voltage drop and c) equivalent resistances of the YBCO 2G coil for test t2-coil (fault current = 20.0 kA_{rms} under 200 V_{rms}).

Simulations of the last test performed with the YBCO 2G coil (t3-coil) also presents good concordance with measurements, as can be seen in figure 7.6. The highest error value (4.4%) was committed by model TEA-MC at the third current peak (figure 7.6a). Besides that, all models provide similar resistance curves, as shown in figure 7.6c.

Similar behaviors are also exhibited for temperatures calculated by models

TEA (figure 5.29) at the instants of time T1, T2, T3 and T4 defined in figure 6.26.

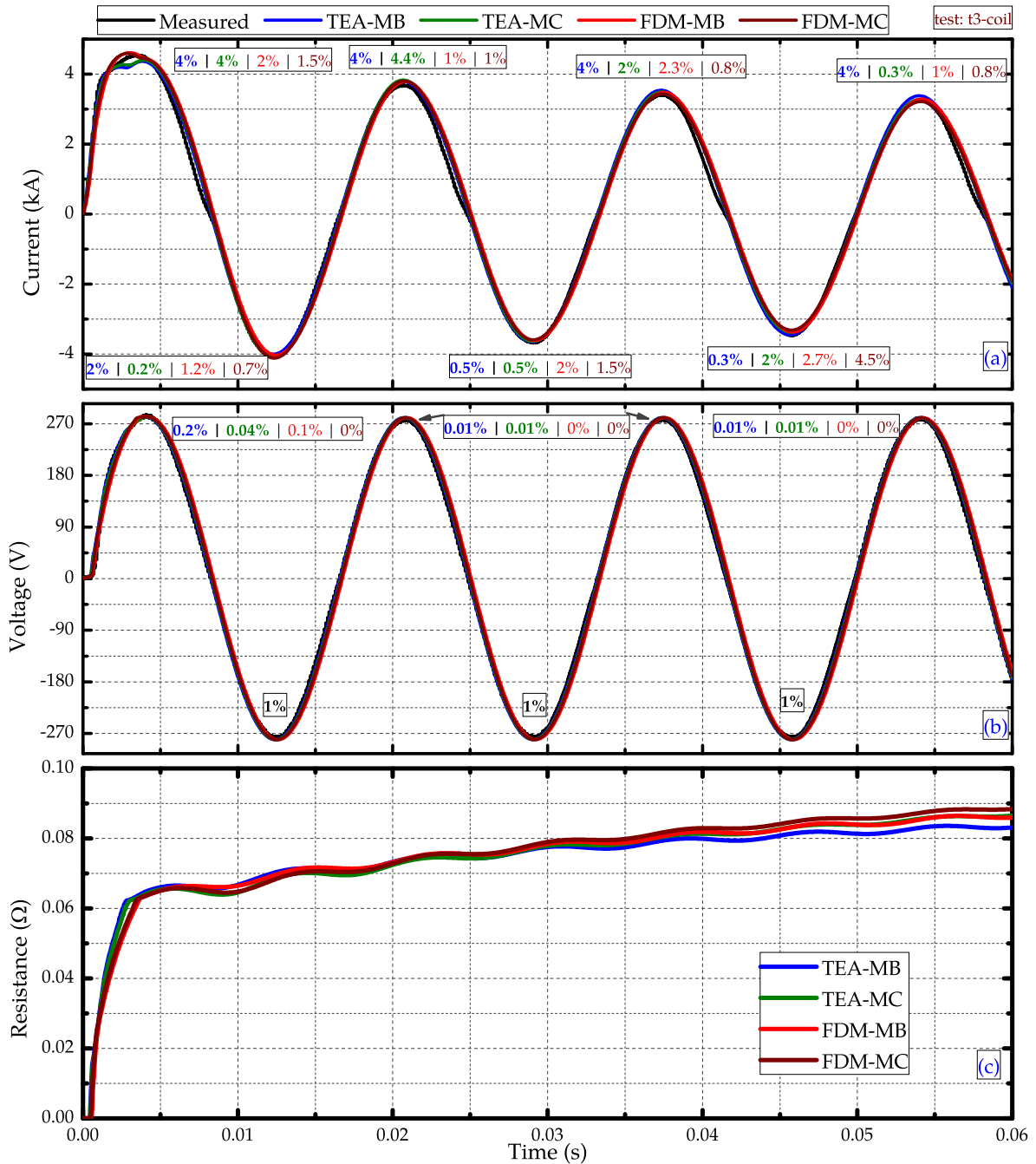


Figure 7.6: Comparison between measured and simulated results of the TEA and FDM-ADI models for a) limited current, b) voltage drop and c) equivalent resistances of the YBCO 2G coil for test t3-coil (fault current = 30.0 kA_{rms} under 200 V_{rms}).

7.3 Air Coil SFCL - TEA × FDM Results

Differences between results of TEA and FDM models for test t1-acsfcl are small. The highest error (4.5%) value was committed by model TEA-MB at second volt-

age peak (figure 7.7b). It is worth to observe that quenching was not predicted by all models (TEA-MB, TEA-MC, FDM-MB and FDM-MC). For this reason, the proposed models outputted a highly non linear resistance during the fault period (figure 7.7c).

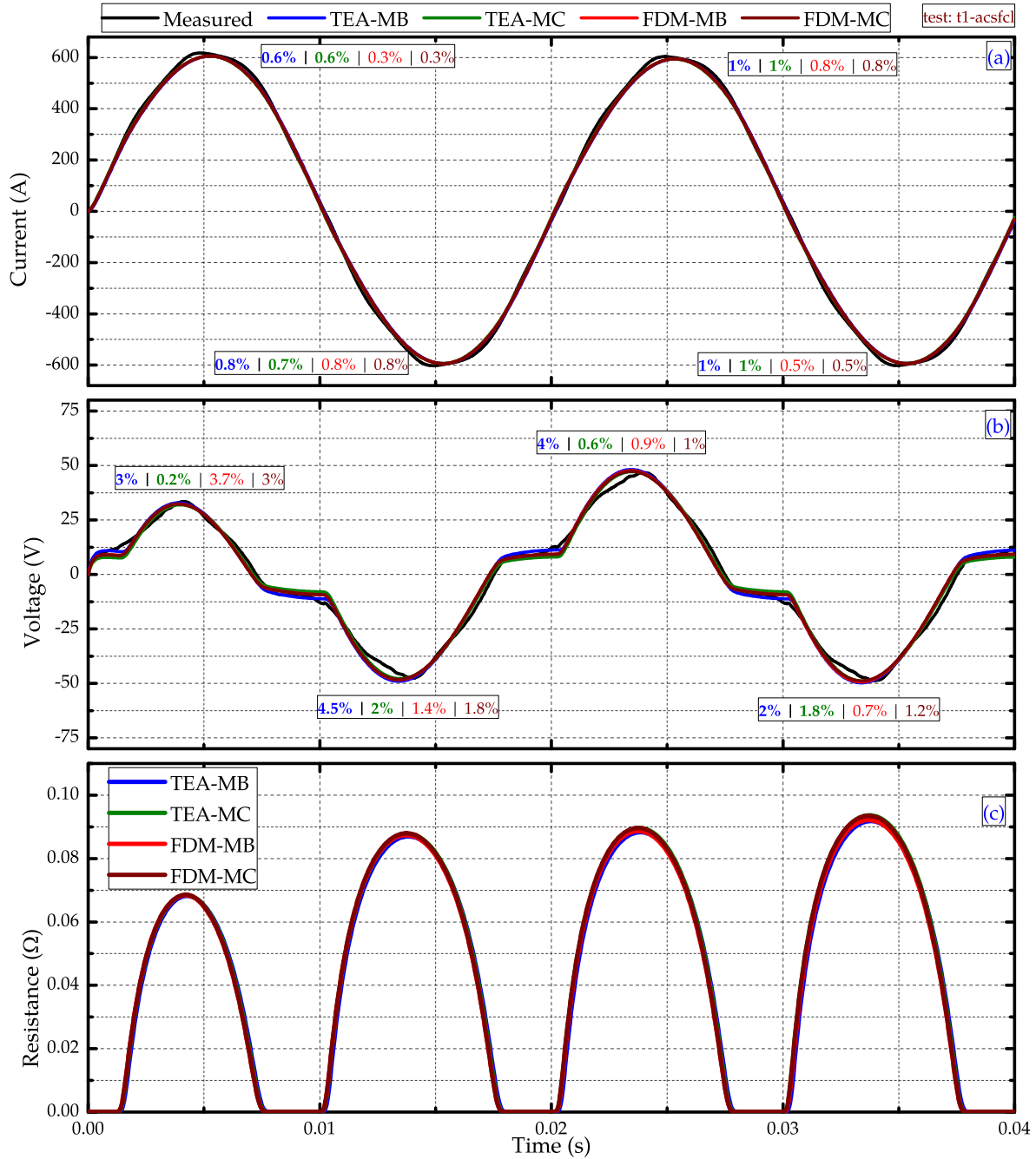


Figure 7.7: Comparison between measured and simulated results of the TEA and FDM-ADI models for a) limited current, b) voltage drop and c) equivalent resistances of the HTS tapes of the AC-SFCL for test t1-acsfcl (fault current = $450 A_{rms}$ under $400 V_{rms}$).

Temperature values calculated by FDM models at instants of time defined in figure 6.29 matches those calculated by TEA models at the same instants.

Errors committed by TEA and FDM models for current limitation in test t2-acsfc1 are very small, as shown in figure 7.8. The highest value found is 0.3% at the first current peak. However, for the voltage drop curve, errors of 10% can be observed at the first peak.

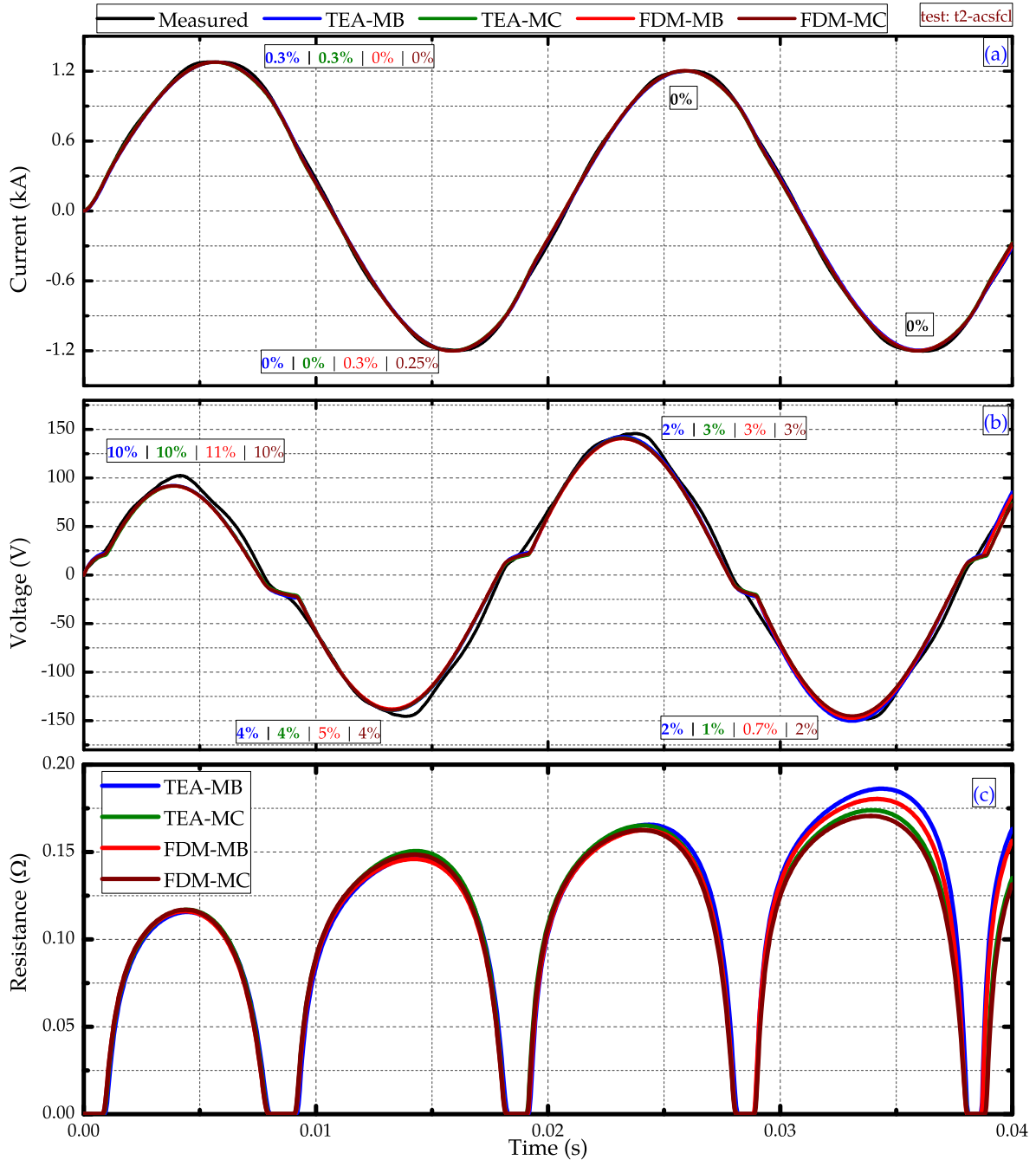


Figure 7.8: Comparison between measured and simulated results of the TEA and FDM-ADI models for a) limited current, b) voltage drop and c) equivalent resistances of the HTS tapes of the AC-SFCL for test t2-acsfc1 (fault current = 1.05 kA_{rms} under 400 V_{rms}).

All models provide similar behaviors for this case. Only small differences can be noted at the end of the fault period, what can be confirmed by observing figure

7.8c. Once again, the quench is not predicted by none of the proposed models since resistance curves present highly non linear behavior until the end of the fault period. That can also be confirmed through comparisons between figures 5.35 and 6.32. According to these figures, none model has predicted temperature values higher than 92 K for any of simulated tapes.

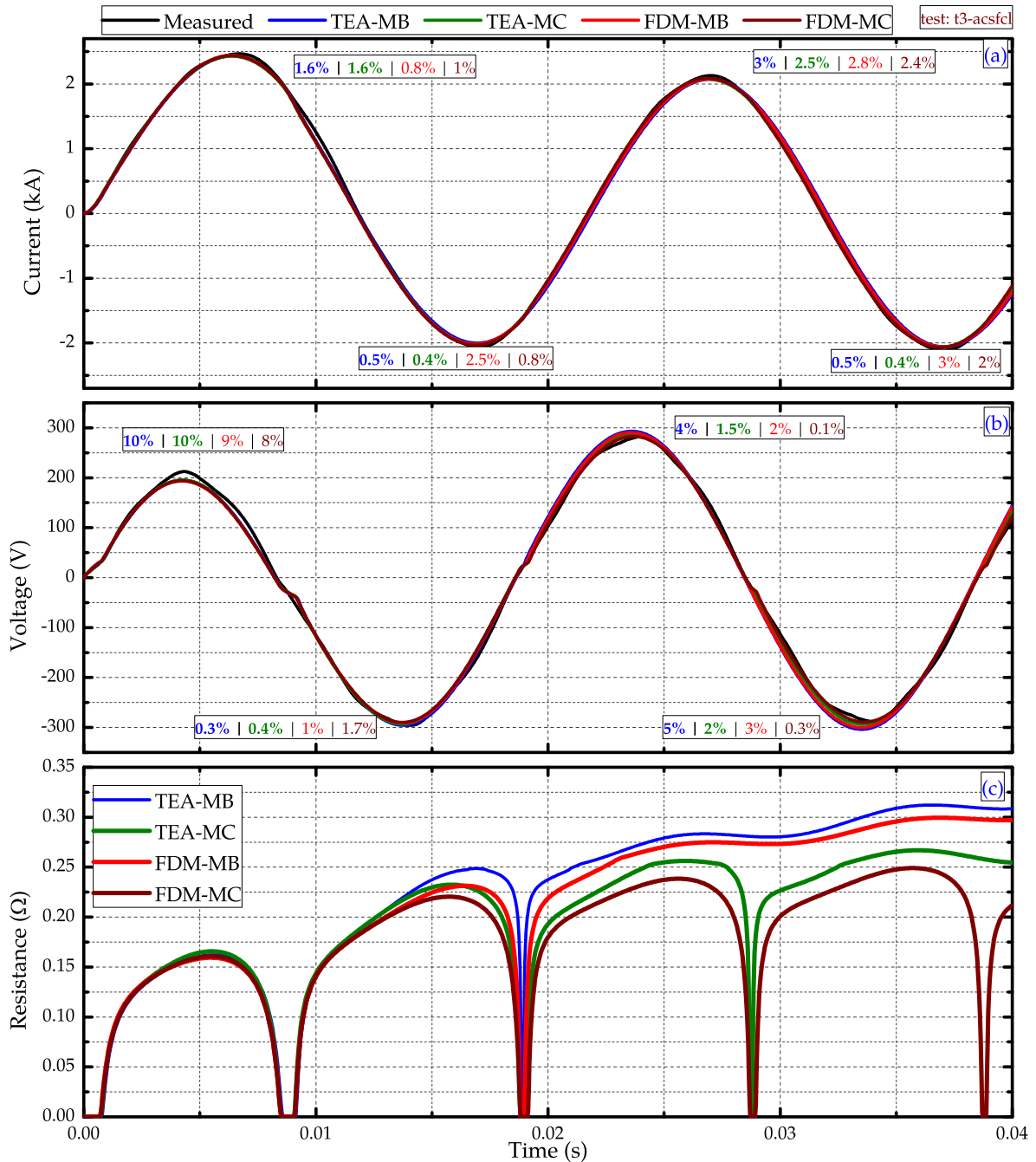


Figure 7.9: Comparison between measured and simulated results of the TEA and FDM-ADI models for a) limited current, b) voltage drop and c) equivalent resistances of the HTS tapes of the AC-SFCL for test t3-acsfcl (fault current = 2.55 kA_{rms} under 400 V_{rms}).

Differences between results of TEA and FDM models for test t3-acsfcl are

small. According to simulated data presented in figure 7.9c, correlated models TEA-MB and FDM-MB have similar behaviors. Behaviors of models TEA-MC and FDM-MC differs from each other after 30 ms; according to model FDM-MC the superconducting layer does not quench (what can be observed in figure 6.35 since all temperature values are under T_c). Model TEA-MC however predicts quench, but temperature values remains close to the critical temperature value (figure 5.38).

7.4 Computational Efforts and Error Values

In order to verify the performance of simulations proposed in this work, the time of simulation spent by each algorithm are now summarized. For a consistent comparison, the time of simulation was measured between 0 and 40 ms for all models. Furthermore, the same timestep was applied in all algorithms ($\Delta t = 5 \times 10^{-5}$ s). Table 7.1 summarizes simulation times of the presented models.

Table 7.1: Time of Simulation

		Devices								
		MCP-BSCCO-2212			YBCO 2G Coil			Air Coil SFCL		
		t1-mcp	t2-mcp	t3-mcp	t1-coil	t2-coil	t3-coil	t1-acsfcl	t2-acsfcl	t3- acsfcl
TEA	TEA-MA	16 s	17 s	17 s	7 s	7 s	7 s	24 s	22 s	20 s
	TEA-MB	8 s	9 s	9 s	3 s	3 s	3 s	7 s	14 s	12 s
	TEA-MC	9 s	11 s	11 s	4 s	3 s	3 s	9 s	15 s	17 s
FDM	FDM-MB	90 min	58 min	60 min	21 min	21 min	20 min	29 min	56 min	51 min
	FDM-MC	8 h	6.5 h	6 h	11 h	10 h	10 h	8 h	11 h	12 h

As shown to table 7.1, models based on the thermal electrical analogy (TEA) were performed in less than 20 s. Model TEA-MA requires more time to be carried out; as explained in chapter 5, this model does not consider heat transfer effects in its algorithm. Thus, the temperature of each layer must be calculated independently of each other at each timestep, that is, a set of η_θ equations must be solved at each new iteration to obtain solutions of the thermal problem in this model.

In the case of models TEA-MB and TEA-MC only one matrix of differential equations must be solved (such as for example equation 5.45 for the Air Coil SFCL), and therefore simulations run faster.

Considering temperature dependency of physical properties of materials in models based on TEA methodology does not increase significantly the simulation

time. In a general way, model TEA-MC spends just few seconds more than model TEA-MB to be performed.

Models FDM however requires higher simulation times than TEA models. Worth to remember that, according to [149], simulations of the Air Coil SFCL took long time of simulation to be performed (≈ 30 h). However, as can be seen in table 7.1, implementing ADI routine with variable mesh (as proposed in chapter 6) reduces drastically the time of simulation. In case of not considering dependency on temperature of materials, FDM simulations were carried out in minutes.

If the FDM-MC is used (considering local variations of physical properties), the time of simulation substantially increases. It can be noted that some hours are required to perform FDM-MC simulations since this model must update physical properties of all elements at each iteration. But even so, the ADI routine combined with variable mesh speeds up the simulation (if compared with an algorithm without variable mesh which requires 30 h).

Simulation time depends not only on the computer used, but also on the number of superconducting elements defined by the user. A great amount of elements representing the superconducting layer increases the simulation time since the current iteration process must run for each superconducting element at each timestep.

It is also worthwhile mentioning that no crashes of operational system were identified during the execution of simulations, indicating low use of the available processor capacity and RAM memory.

Table 7.2: Maximum Error values - Current error | Voltage error (%)

		Devices								
		MCP-BSCCO-2212			YBCO 2G Coil			Air Coil SFCL		
		t1-mcp	t2-mcp	t3-mcp	t1-coil	t2-coil	t3-coil	t1-acsfcl	t2-acsfcl	t3- acsfcl
TEA	TEA-MA	8 30	12 2	15 1.4	36 6	33 1	36 1	4 45	2.4 13	3.8 11
	TEA-MB	8 27	12 1.5	14 1.4	6 1.5	4.5 1	4 1	1 4.5	0.3 10	3 10
	TEA-MC	8 29	8 3	10 1.4	5 1.5	4 1	4.4 1	1 2	0.3 10	2.5 10
FDM	FDM-MB	26 17	12 3.4	13 1.4	4 7	3.6 1	2.7 1	0.8 3.7	0.3 11	3 9
	FDM-MC	8 10	11 6	12 2	2 3	4 1	4.5 1	0.8 3	0.25 10	2.4 8

To close up this section, table 7.2 summarizes the maximum error committed by each model for each performed test. As can be noted, there are no huge difference between errors committed by models with constant physical properties and models with variable physical properties.

7.5 Discussions

This chapter has presented comparisons between models based on TEA and FDM methods.

As mentioned before (chapter 4), predicting the behavior of SFCL devices may be a complex task. However, all models proposed in this work have provided errors within a tolerable margin, as can be substantiated by table 7.2.

It is quite natural to exist small deviations between results calculated by different methods. Each model deals with the problem by a particular manner, although fundamental equations remains the same. But, in general, differences between TEA and FDM results are small. All models have outputted behaviors quite similar to measurements. For example, both the TEA as FDM models predicted that the superconducting layer would not quench in tests t1-acsfcl and t2-acsfcl.

The only difference between TEA and FDM behaviors occurred for test t3-acsfcl; model TEA-MC has predict quench after 1.5 current cycle whereas no quench prediction has been made by model FDM-MC.

Simulated curves present a remarkable feature during quench. Most of major deviations between measurements and simulations occurs at the first moments of the transient period. That is strongly related to inhomogeneities effects of HTS materials composing tapes and modules. Hence, it is expected to observe deviations between measurements and simulations results during the quench.

It can not be stated that the inclusion of inhomogeneities representation by models FDM significantly improves results obtained by means of TEA method. In some cases, errors committed by TEA methods are quite lower than errors of FDM model, specially in the case of MCP-BSCCO-2212 modules. Hence, the inhomogeneity distribution used to simulate different values of I_c along modules and tapes length may be not the more suitable one. Nevertheless, such representations can be easily adjusted by increasing parameter ϵ in order to select further I_c values on the probability curve (see figure 3.14).

Regarding to the time spent on simulations, one can state that the proposed models do not require high computational efforts. All models have been run in a conventional computer, not requiring the use of super computers. Models based on TEA method were performed in less than 20 seconds and can be considered as fast algorithms.

Algorithms of FDM method can also be considered as being relatively fast. In case of model FDM-MB, 20 to 30 minutes were necessary to conclude the complete simulation. It is a huge time reduction in relation to the previous version, published in [149]. This reduction was possible since the ADI routine combined with variable mesh was employed.

Model FDM-MC also runs faster than the published work, since it employs the ADI routine with variable mesh too. However, by considering local changes of physical properties a considerable increase on time of simulation was identified (if compared with FDM-MB model). One must attempt to the fact that the FDM-MC model posses a complex algorithm, higher simulation times and provides similar results to those provided by model FDM-MB, besides presenting error values in same magnitude of the FDM-MB model.

It is worthwhile mentioning that the current iteration process plays a important role on the simulation time. The higher the number of elements representing the superconducting layer, the higher will be the number of times the process will run, since it must deal with the dependency on current for each element.

Chapter 8

Conclusions

At present, a variety of techniques to simulate SFCLs can be found in the literature. Some of them have been summarized in chapter 4. The main goal of this work was to present new simulation approaches starting from basic concepts regarding fault current limitation and expanding it to more sophisticated methods.

The first presented method, the time dependent model, is a very elementary method. As have been show, this method can be employed, but it may require a trial and error process if there is no experimental information available. Conversely, if informations of current limitation and voltage drop extracted from performed tests are available, the time dependent model can be an alternative for a simple power system study. For example, chapters 5 and 6 presented resistance behaviors during fault period for the YBCO 2G coil device. Those behaviors can easily be described by a time dependent function. In that way, one can model a SFCL device just by setting the resistance curve along the time. The model is thereby effective for estimating the reduction of fault current, avoiding complexities of thermal-electric models.

The time dependent model, however, is not able to provide any further information. Temperature values, inhomogeneity effects or recovery time can not be estimated by means of this approach. A more detailed model, as the two branches model, takes into account main characteristics of HTS materials, but it also does not handle with heat transfer phenomena in a proper way. Hence, models based on the analogy between electrical and thermal equivalents were proposed (TEA). Furthermore, it is remarkable the employment of the current iteration process in the two branches model.

The current iteration process allows developing more sophisticated methods, since solutions of stiffness equations are easily obtained. For example, if the current iteration method is not used in the solution process of FDM problems, at each timestep a complex numerical method must be employed in order to obtain the solution for each element forming the mesh. Certainly, it would lead to very com-

plex algorithms and long times of simulation. Thus, it is strongly recommended including the current iteration process in the future methods.

By means of the thermal-electrical analogy, the thermal behaviors of each layer of tapes and modules have been simulated. Results of simulated limited currents and voltages were compared with measured data and a good agreement between simulations and measurements can be observed. Also, solutions for the temperature rise and development of the resistances are within the expected and are comparable to those often found in the literature.

A deep investigation of adiabatic conditions was performed by employing the TEA model (TEA-MA), since it is a very common approach found in literature. Results of TEA-MA model have shown that the adiabatic considerations are not the best approach to be taken since wrong values and behaviors of temperature may be obtained during the fault regime. Besides that, model TEA-MA will always predict temperature gradient along thickness of tapes and modules. Results of models TEA-MB and TEA-MC show that it is not a correct assumption, especially if simulating tapes.

Models based on FDM method were solved by means of ADI routine with variable mesh. Such technique makes possible the insertion of any kind of inhomogeneity representation in tapes and modules. The use of the ADI method with variable mesh to solve systems of differential equations obtained from FDM discretization enables simulations of long lengths of tapes and modules with inhomogeneities. It also provides a unique simulation program, i.e., there is no need of combining two different softwares to perform simulations since electrical and thermal equations are solved together by means of one single algorithm. Combining two different softwares is a usual practice when simulating with finite elements method [20].

Results of FDM method also present a good accordance with measured ones. Obtained temperature profiles allows a local study of tapes and modules. Because of the good performance and results presented by FDM models in this work, it may be worth mentioning that the FDM method (combined with ADI routine and variable mesh) can be applied to study other technological applications of superconductivity, not only to SFCL devices. It can be an attractive method when the interest is a deep study of local phenomena.

Both TEA and FDM method have provided similar results for all performed tests with the considered SFCL devices. From a certain point of view, it can be understood as a proof of effectiveness of the proposed models. In case of some wrong assumption in any of both models, final results would not be similar to each other. In other words, very distinct model would not provide similar results if one of them were unsuitable.

Some important conclusions can be achieved by analyzing similarities between results outputted by FDM and TEA models. Since they are similar, it indicates that assuming average values of critical current I_c serves as a good approach to simulate tapes and modules besides providing results as good as those provided by FDM models (if the HTS material does not exhibit great inhomogeneity).

Another important conclusion concerns future considerations on SFCL modeling. As have been show by results of models FDM and TEA (excluding TEA-MA), small temperature gradients along thickness exists within tapes during the fault period. Therefore, another approach can be used by setting temperature of the tape to a common value if a fast algorithm is desired (for example, by setting the temperature of all layers with the temperature of the HTS layer). In case of simulating MCP-BSCCO-2212 modules such approximation can not be done, since there is considerable temperature gradient along thickness.

This work has also studied influences of dependency on temperature of physical properties in transient simulations of SFCL devices. In a general view, no huge differences between models with constant physical properties were detected in relation to those considering variable properties. Thus, it is a important feature to be considered when simulating SFCL devices. Models considering variable physical properties tends to present more complex algorithms and its results may not differs so much of those with constant properties.

The external influence of the convective heat transfer coefficient h_c has been also analyzed. TEA and FDM models show that it is a very important external influence to be taken into account, since it can considerably change the temperature behavior during the transient time, mainly if simulating SFCL based on coated conductors (2G tapes)

Finally, simulations results predicted by TEA and FDM models can be considered as satisfactory and suitable to predict the transient behavior of SFCL devices. TEA models present fast algorithm and are more suitable to simulating the influence of SFCL installed in power systems. Besides predicting how the electrical network will react to the installed SFCL, the model will also provide important informations concerning the SFCL itself (temperature increase and resistance development). Due its relative simplicity, TEA models can be easily adapted in conventional power system analysis softwares. FDM models, however, are not indicated to power system analyzes because of its relative complex algorithm. However, if a study of local properties of tapes and modules during the fault transient is necessary, FDM models are the more suitable ones. By means of FDM models, it is possible to investigate inhomogeneity effects, as have been done in this work.

Although it was not performed in this work, further studies with TEA and FDM models can be done. One of them regards studies of the recovery time.

Since both models have been developed from fundamental laws of heat transfer, it is natural that they can predict not only heating, but also cooling after the fault period.

All presented algorithms are versatile, i.e., they can be easily changed in order to satisfy particular considerations. For example, as already mentioned, it is of significant importance considering changes on the h_c coefficient if simulating tapes. Taking model FDM-MC as example, it would take about 10 h to run a single simulation. If time is an important factor in this case, the FDM-MC algorithm can be modified in order to not consider dependencies on temperature of physical properties (what increases simulation time) and keep the main characteristics of the h_c curve behavior (shown in figure 5.11).

To close this section, it is remarkable to cite table 7.1. Times of simulations presented in this table are very low compared with simulation times found in literature. Considering conventional methods of simulation (e.g., finite elements method), simulations of one single tape could spend many hours. At this work, one has simulated many tapes (22 in the heaviest case) at once using a conventional computer.

Hence, the final conclusion is that models TEA and FDM presented in this work can serve as interesting and useful options to be considered by the scientific community and power system experts if studies concerning SFCL devices are intended.

Bibliography

- [1] ONNES, H. K. "Further experiments with liquid helium. G. On the electrical resistance of pure metals, etc. VI. On the sudden change in the rate at which the resistance of mercury disappears." *Koninklijke Nederlandse Akademie van Wetenschappen Proceedings Series B Physical Sciences*, v. 14, n. 14, pp. 818–821, 1911.
- [2] ASHCROFT, N., MERMIN, D. *Solid State Physics*. USA, Saunders College Publishing, 1976.
- [3] BEDNORZ, J. G., MÜLLER, K. A. "Possible High Tc Superconductivity in the Ba-La-Cu-O System", *Z. Physik, B*, v. 64, n. 2, pp. 189–193, 1986.
- [4] WU, M. K., CHU, C. W., ASHBURN, J. R., et al. "Superconductivity at 93 K in a new mixed-phase Y-Ba-Cu-O compound system at ambient pressure", *Phys. Rev. Lett.*, v. 58, n. 9, pp. 908–910, March 1987.
- [5] MICHEL, C., HERVIEU, M., BOREL, M. M., et al. "Superconductivity in Bi-Sr-Cu-O system", *Z. Physik, B*, v. 68, n. 4, pp. 421–423, 1987.
- [6] MAEDA, H., TANAKA, Y., FUKUTOMI, M., et al. "A New High-Tc Oxide Superconductor without a Rare Earth Element", *Jpn. J. Appl. Phys.*, v. 27, n. 2, pp. 209 – 210, February 1988.
- [7] KONDOH, S., ANDO, Y., ONODA, M., et al. "Superconductivity in Tl-Ba-Cu-O System", *Solid State Commun.*, v. 65, n. 11, pp. 1329–1331, March 1988.
- [8] MEISSNER, W., OCHSENFELD, R. "Ein neuer Effekt bei Eintritt der Supraleitfähigkeit", *Naturwissenschaften*, v. 21, n. 44, pp. 787–788, November 1933.
- [9] BARDEEN, J., COOPER, L. N., SCHRIEFFER, J. R. "Microscopic Theory of Superconductivity", *Phys. Rev.*, v. 106, pp. 162–164, April 1957.
- [10] MAROUCHKINE, A. *Room-Temperature Superconductivity*. England, Cambridge International Science Publishing, 2004.

Bibliography

- [11] ROSE-INNES, A. C. *Introduction to Superconductivity*. 2 ed. London, Pergamon Press, January 1978. 1.
- [12] TINKHAM, M. *Introduction to Superconductivity*. 2 ed. New York, McGraw-Hill Science / Engineering/Math, October 1995.
- [13] SCHUBNIKOW, L., RJABININ, J. N. "Magnetic properties and critical currents of supra-conducting alloys", *Nature*, v. 135, n. 3415, pp. 581–582, April 1935.
- [14] ABRIKOSOV, A. A. "The magnetic properties of superconducting alloys", *J. Phys. Chem. Solids*, v. 2, n. 3, pp. 199–208, 1957.
- [15] SHEAHEN, T. P. *Introduction to High-Temperature Superconductivity*. New York, Plenum Press, 1994.
- [16] SAXENA, A. K. *High-Temperature Superconductors*. 2 ed. Heidelberg Dordrecht London New York, Springer, July 2012.
- [17] FOSSHEIN, K., SUDBO, A. *Superconductivity - Physics and Applications*, v. 1. 1 ed. West Sussex, England, John Wiley and Sons Ltd, 2004.
- [18] SHIMIZU, H., YOKOMIZU, Y., MATSUMURA, T., et al. "Proposal of Flux Flow Resistance Type Fault Current Limiter using Bi2223 High Tc Superconducting Bulk", *IEEE Trans. Appl. Supercond.*, v. 12, n. 1, pp. 876–879, March 2002.
- [19] SHI, D. *High-Temperature Superconducting Materials Science and Engineering: New Concepts and Technology*. 1, Pergamon, March 1995.
- [20] COLANGELO, D. *Modelling of 2G HTS Coated Conductors for Fault Current Limiter Applications*. PhD thesis, École Polytechnique Fédérale de Lausanne, Lausanne, September 2013.
- [21] SUTHERLAND, P. E. "Analytical Model of Superconducting to Normal Transition of Bulk High Tc Superconductor BSCCO-2212", *IEEE Trans. Appl. Supercond.*, v. 16, n. 1, pp. 43 – 48, March 2006.
- [22] ELSCHNER, S., BREUER, F., WOLF, A., et al. "Characterization of BSCCO 2212 Bulk Material for Resistive Current Limiters", *IEEE Trans. Appl. Supercond.*, v. 11, n. 1, pp. 2507–2510, March 2001.
- [23] PAUL, W., CHEN, M., LAKNER, M., et al. "Fault Current Limiter Based on High Temperature Superconductors - Different Concepts, Test Results,

Bibliography

- Simulations, Applications”, *Phys. C Supercond.*, v. 354, n. 14, pp. 27 – 33, May 2001.
- [24] DURON, J., DUTOIT, B., GRILLI, F., et al. “Computer Modeling of YBCO Fault Current Limiter Strips Lines in Over-Critical Regime With Temperature Dependent Parameters”, *IEEE Trans. Appl. Supercond.*, v. 17, n. 2, pp. 1839–1842, June 2007.
- [25] RETTELBACH, T., SCHMITZ, G. J. “3D Simulation of Temperature, Electric Field and Current Density Evolution in Superconducting Components”, *Supercond. Sci. Technol.*, v. 16, n. 5, pp. 645–653, May 2003.
- [26] PAUL, W., CHEN, M., LAKNER, M., et al. “Superconducting Fault Current Limiter - Applications, Technical and Economical Benefits, Simulations and Test Results”. In: *CIGRÉ*, pp. 13–201, Paris, 2000.
- [27] CHA, Y. S. “An empirical correlation for E(J,T) of a melt-cast-processed BSCCO-2212 superconductor under self field”, *IEEE Trans. Appl. Supercond.*, v. 13, n. 2, pp. 2028–2031, June 2003.
- [28] GRUNDMANN, J. *Kennlinienfeldmessung und Modellierung der Auslösung und Quenchausbreitung in HTSL Strombegrenzern*. PhD thesis, Techn. Univ. Carolo-Wilhelmina zu Braunschweig, Göttingen, March 2007.
- [29] MÄDER, O. *Simulationen und Experimente zum Stabilitätsverhalten von HTSL-Bandleitern*. PhD thesis, Karlsruher Institut für Technologie, Fakultät für Elektrotechnik und Informationstechnik, May 2012.
- [30] THERASSE, M., DECROUX, M., ANTOGNAZZA, L., et al. “Electrical Characteristics of DyBCO Coated Conductors at High Current Densities for Fault Current Limiter Application”, *Phys. C Supercond.*, v. 21, n. 1, pp. 2191–2196, October 2008.
- [31] DE SOUSA, W. T. B., POLASEK, A., SILVA, F. A., et al. “Simulations and Tests of MCP-BSCCO-2212 Superconducting Fault Current Limiters”, *IEEE Trans. Appl. Supercond.*, v. 22, n. 2, pp. 5600106, April 2012.
- [32] LANGSTON, J., STEURER, M., WOODRUFF, S., et al. “A Generic Real-time Computer Simulation Model for Superconducting Fault Current Limiters and its Application in System Protection Studies”, *IEEE Trans. Appl. Supercond.*, v. 15, n. 2, pp. 2090–2093, June 2005.
- [33] PAITHANKAR, Y. G. *Transmission Network Protection: Theory and Practice*, v. 1. New York, Marcel Dekker INC, 1997.

Bibliography

- [34] NOE, M., STEURER, M. "High-Temperature Superconductor Fault Current Limiters: Concepts, Applications, and Development Status", *Supercond. Sci. Technol.*, v. 20, n. 3, pp. 15–29, January 2007.
- [35] WOLSKY, A. *HTS from Precommercial to Commercial: A Roadmap to Future use of HTS by the Power Sector*. Tech. Report, International Energy Agency, August 2013.
- [36] KURUPAKORN, C., KOJIMA, H., HAYAKAWA, N., et al. "Recovery Characteristics After Current Limitation of High Temperature Superconducting Fault Current Limiting Transformer (HTc-SFCLT)", *IEEE Trans. Appl. Supercond.*, v. 15, n. 2, pp. 1859–1862, June 2005.
- [37] HOBL, A., ELSCHNER, S., BOCK, J., et al. "Superconducting Fault Current Limiters - A New Tool for the Grid of the Future". In: *CIREN Workshop*, p. 0296, Lisbon, May 2012. CIREN.
- [38] DE SOUSA, W. T. B., POLASEK, A., MATT, C. F. T., et al. "Recovery of Superconducting State in an R-SCFCL MCP-BSCCO-2212 Assembly", *IEEE Trans. Appl. Supercond.*, v. 23, n. 1, pp. 5601407, February 2013. doi: 10.1109/TASC.2012.2232915.
- [39] BERGER, A., NOE, M., KUDYMOW, A. "Test Results of 60 kVA Current Limiting Transformer with Full Recovery Under Load", *IEEE Trans. Appl. Supercond.*, v. 21, n. 3, pp. 1384–1387, June 2011.
- [40] NOE, M., OSWALD, B. R. "Technical and Economical Benefits of Superconducting Fault Current Limiters in Power Systems", *IEEE Trans. Appl. Supercond.*, v. 9, n. 9, pp. 1347–1350, June 1999.
- [41] KALSI, S. S., MALOZEMOFF, A. "HTS Fault Current Limiter Concept", *IEEE Trans. Appl. Supercond.*, v. 2, n. 1, pp. 1426 – 1430, June 2004.
- [42] BOCK, J., BREUER, F., WALTER, H., et al. "CURL10 - Development and Field-Test of a 10 kV-10 MVA Resistive Current Limiter Based on Bulk BSCCO 2212", *IEEE Trans. Appl. Supercond.*, v. 15, n. 2, pp. 1955–1960, June 2005.
- [43] ELSCHNER, S., STEMMLE, M., BREUER, F., et al. "Coil in coil - Components for the high voltage superconducting resistive current limiter CULT 110", *J. Phys.: Conf. Ser.*, v. 97, n. 1, pp. 012309, January 2008.
- [44] NOE, M., KUDYMOW, A., FINK, S., et al. "Conceptual Design of a 110 kV Resistive Superconducting Fault Current Limiter Using MCP-BSCCO

Bibliography

- 2212 Bulk Material", *IEEE Trans. Appl. Supercond.*, v. 17, n. 2, pp. 1784–1787, June 2007.
- [45] GRAY, K. E., FOWLER, D. E. "A superconducting fault current limiter", *J. Appl. Phys.*, v. 49, n. 4, pp. 4, April 1978.
- [46] NOE, M. *Supraleitende Strombegrenzer als neuartige Betriebsmittel in Elektroenergiesystemen*. PhD thesis, Universität Hannover, June 1998.
- [47] PETRANOVIC, R. *Untersuchungen des transienten Verhaltens von Strombegrenzern mit Hochtemperatur-Supraleitern*. PhD thesis, Karlsruher Institut für Technologie - Institut für Elektroenergiesysteme und Hochspannungstechnik, May 2004.
- [48] STEMMLE, M. *Supraleitende Strombegrenzer in Hochspannungsnetzen*. PhD thesis, Universität Hannover, July 2009.
- [49] TAKASHIMA, H., ICHI SASAKI, K., ONISHI, T. "Thermal stress analysis for the meander-shape YBCO fault current limiter", *Phys. C Supercond.*, v. 411, n. 2, pp. 25–31, September 2004.
- [50] NOE, M., HOBL, A., TIXADOR, P., et al. "Conceptual Design of a 24 kV, 1 kA Resistive Superconducting Fault Current Limiter", *IEEE Trans. Appl. Supercond.*, v. 22, n. 3, pp. 5600304, June 2012.
- [51] ELSCHNER, S., KUDYMOW, A., BRAND, J., et al. "ENSYSTROB - Design, Manufacturing and Test of a 3-Phase Resistive Fault Current Limiter Based on Coated Conductors for Medium Voltage Application", *Phys. C Supercond.*, v. 1, pp. 1–7, May 2012.
- [52] ELSCHNER, S., KUDYMOW, A., FINK, S., et al. "ENSYSTROB - Resistive Fault Current Limiter Based on Coated Conductors for Medium Voltage Application", *IEEE Trans. Appl. Supercond.*, v. 21, n. 3, pp. 1209 – 1212, June 2011.
- [53] ELSCHNER, S., BREUER, F., NOE, M., et al. "Manufacturing and Testing of MCP 2212 Bifilar Coils for a 10 MVA Fault Current Limiter", *IEEE Trans. Appl. Supercond.*, v. 13, n. 2, pp. 1980 – 1983, June 2003.
- [54] BOCK, J., ELSCHNER, S., HERRMANN, P. F. "Melt cast processed (MCP)-BSCCO 2212 tubes for power applications up to 10 kA", *IEEE Trans. Appl. Supercond.*, v. 5, n. 2, pp. 1409 – 1412, June 1995.
- [55] PARK, Y. M., JANG, G. E. "Characteristics of HTS tube depending on heat-treatment conditions", *Cryogenics*, v. 3, pp. 169–173, March 2001.

Bibliography

- [56] XIE, Y., SELVAMANICKAM, V., MARCHEVSKY, M., et al. "Second-generation HTS wire manufacturing and technology advancement at SuperPower". In: *International Conference on Applied Superconductivity and Electromagnetic Devices*, p. ID1180, Chengdu, China, September 2009.
- [57] XIE, Y.-Y., MARCHEVSKY, M., ZHANG, X., et al. "Second-Generation HTS Conductor Design and Engineering for Electrical Power Applications", *IEEE Trans. Appl. Supercond.*, v. 19, n. 3, pp. 3009 – 3013, June 2009.
- [58] KREISKOTT, S., ARENDT, P. N., COULTER, J. Y., et al. "Reel-to-reel preparation of ion-beam assisted deposition (IBAD)-MgO based coated conductors", *Supercond. Sci. Technol.*, v. 17, n. 5, pp. S132–S134, 2004.
- [59] PARK, D. K., YANG, S. E., KIM, Y. J., et al. "Experimental and Numerical Analysis of High Resistive Coated Conductor for Conceptual Design of Fault Current Limiter", *Cryogenics*, v. 49, n. 6, pp. 249 – 253, June 2009.
- [60] ELSCHNER, S., KUDYMOW, A., FINK, S., et al. "ENSYSTROB - Resistive Fault Current Limiter based on Coated Conductors for Medium Voltage Application". Apresentação Oral, September 2011. EUCAS-ISEC-ICMC: Superconductivity Centennial Conference, Den Haag, Holanda.
- [61] BOENIG, H. J., MIELKE, C. H., BURLEY, B. L., et al. "The bridge-type fault current controller - a new FACTS controller". In: *IEEE Power Engineering Society Summer Meeting*, v. 1, pp. 455–460, July 2002.
- [62] BOENIG, H. J., PAICE, D. A. "Fault current limiter using a superconducting coil", *IEEE Trans. Magn.*, v. 19, n. 3, pp. 1051–1053, May 1983.
- [63] HUI, D., WANG, Z. K., ZHANG, J. Y., et al. "Development and Test of 10.5 kV/1.5 kA HTS Fault Current Limiter", *IEEE Trans. Appl. Supercond.*, v. 16, n. 2, pp. 687–690, June 2006.
- [64] RAJU, B. P., PARTON, K. C., BARTRAM, T. C. "A Current Limiting Device Using Superconducting D.C. Bias Applications and Prospects", *IEEE Trans. Power Appar. Syst.*, v. PER-2, n. 9, pp. 34–35, September 1982.
- [65] ABBOTT, S. B., ROBINSON, D. A., PERERA, S., et al. "Simulation of HTS saturable core-type FCLs for MV distribution systems", *IEEE Trans. Power Deliv.*, v. 21, n. 2, pp. 1013–1018, April 2006.

Bibliography

- [66] ROZENSHTAIN, V., FRIEDMAN, A., WOLFUS, Y., et al. "Saturated Cores FCL - A New Approach", *IEEE Trans. Appl. Supercond.*, v. 17, n. 2, pp. 1756–1759, June 2007.
- [67] HASSENZAHL, W., YOUNG, M. *Superconducting Fault Current Limiters*. Tech. Report 1017793, Electric Power Research Institute (EPRI), December 2009.
- [68] NÄCKEL, O., NOE, M. "Conceptual Design Study of an Air Coil Fault Current Limiter", *IEEE Trans. Appl. Supercond.*, v. 23, n. 3, pp. 5602404, June 2013.
- [69] NAECKEL, O., NOE, M. "Design and Test of an Air Coil Superconducting Fault Current Limiter Demonstrator", *IEEE Trans. Appl. Supercond.*, v. 24, n. 3, pp. 5601605, October 2013.
- [70] DE SOUSA, W. T. B., NÄCKEL, O., NOE, M. "Transient Simulations of an Air-Coil SFCL", *IEEE Trans. Appl. Supercond.*, v. 24, n. 4, pp. 5601807, August 2014.
- [71] WANGA, Y., XIAOA, L., LINA, L., et al. "Effects of Local Characteristics on the Performance of Full Length Bi2223 Multifilamentary Tapes", *Cryogenics*, v. 43, n. 2, pp. 71–77, February 2003.
- [72] TIXADOR, P., NGUYEN-NHAT, T., OKADA-VIEIRA, H. G., et al. "Impact of Conductor Inhomogeneity on FCL Transient Performance", *IEEE Trans. Appl. Supercond.*, v. 21, n. 3, pp. 1194–1197, June 2011.
- [73] COLANGELO, D., DUTOIT, B. "Inhomogeneity Effects in HTS Coated Conductors Used as Resistive FCLs in Medium Voltage Grids", *Supercond. Sci. Technol.*, v. 25, n. 9, pp. 095005, September 2012.
- [74] HOBL, A., GOLDACKER, W., DUTOIT, B., et al. "Design and Production of the ECCOFLOW Resistive Fault Current Limiter", *IEEE Trans. Appl. Supercond.*, v. 23, n. 3, pp. 5601804, June 2013.
- [75] SCHACHERER, C. *Theoretische und experimentelle Untersuchungen zur Entwicklung supraleitender resistiver Strombegrenzer*. PhD thesis, Universität Karlsruhe (TH), Fakultät für Elektrotechnik und Informationstechnik, July 2009.
- [76] BERGER, A. *Entwicklung supraleitender, strombegrenzender Transformatoren*. PhD thesis, Karlsruher Institut für Technologie - Fakultät für Elektrotechnik und Informationstechnik, January 2011.

Bibliography

- [77] BUTCHER, J. C. *Numerical Methods for Ordinary Differential Equations*. 2 ed. West Sussex, England, John Wiley & Sons, March 2008.
- [78] SADIKU, A. *Fundamental of Electric Circuits*. 1 ed. New York, McGraw-Hill, 2007.
- [79] HAIRER, E., WANNER, G. *Solving Ordinary Differential Equations II*. 2 ed. Switzerland, Springer, 1996.
- [80] DHARMARAJA, S. *An analysis of the TR-BDF2 integration scheme*. Master's Thesis , Massachusetts Institute of Technology, September 2007.
- [81] BUTZKE, U. "Simulationen resistiver hochtemperatur-supraleitender Strombegrenzer mit Hilfe der Finiten-Differenzen Methode". January 1996. Diplomarbeit, Universität Hannover - Institut für Elektrische Energieversorgung.
- [82] MÄURER, A. "Simulation eines induktiven Strombegrenzers mit hochtemperatur-supraleitenden Dünnschichten". February 1997. Studienarbeit, Universität Hannover - Institut für Elektrische Energieversorgung.
- [83] WELLER, R., CAMPBELL, A., COOMBS, T., et al. "Computer Modelling of Superconductive Fault Current Limiters", *Mater. Sci. Eng. B*, v. 53, n. 1-2, pp. 229–233, May 1998.
- [84] GOTO, Y., YUKITA, K., MIZUNO, K., et al. "Experimental Studies on Power System Transient Stability due to Introduction of Superconducting Fault Current Limiters", *IEEE Trans. Appl. Supercond.*, v. 2, n. 4, pp. 1129 – 1134, January 2000.
- [85] MUTA, I., DOSHITA, T., NAKAMURA, T., et al. "Influences of Superconducting Fault Current Limiter (SFCL) on Superconducting Generator in One-Machine Double-Line System", *IEEE Trans. Appl. Supercond.*, v. 13, n. 2, pp. 2206 – 2209, June 2003.
- [86] YE, L., LIN, L. Z., JUENGST, K.-P. "Application Studies of Superconducting Fault Current Limiters in Electric Power Systems", *IEEE Trans. Appl. Supercond.*, v. 12, n. 1, pp. 900 – 903, March 2002.
- [87] A. S. EMHEMED AND, R. M. T., SINGH, N. K., BURT, G. M., et al. "Improving the Transient Performance of a High Penetration of LV Connected Microgeneration". In: *Power & Energy Society General Meeting*, pp. 1–6, Calgary, AB, July 2009. IEEE.

Bibliography

- [88] KAMEDA, H., TANIGUCHI, H. "The Setting Method of the Specific Parameters of a Superconducting Fault Current Limiter Installed at the Bus-Tie and Response of Protective Relays at Operation of the SFCL", *Phys. C Supercond.*, v. 372-376, pp. 1673–1679, August 2002.
- [89] MARTINI, L., BOCCHI, M., LEVATI, M., et al. "Simulations and Electrical Testing of Superconducting Fault Current Limiter Prototypes", *IEEE Trans. Appl. Supercond.*, v. 15, n. 2, pp. 2067 – 2070, June 2005.
- [90] NOGUCHI, S., TANIKAWA, T., IGARASHI, H. "Operating Property Analysis of Parallelized Resistive Fault Current Limiter Using YBCO Thin Films", *IEEE Trans. Appl. Supercond.*, v. 17, n. 2, pp. 1835 – 1838, June 2007.
- [91] NAM, K., LEE, C., PARK, D. K., et al. "Thermal and Electrical Analysis of Coated Conductor Under AC Over-Current", *IEEE Trans. Appl. Supercond.*, v. 17, n. 2, pp. 1923 – 1926, June 2007.
- [92] YE, Y., XIAO, L., WANG, H., et al. "Research on Resistor Type Superconducting Fault Current Limiter in Power System". In: *IEEE/PES Transmission and Distribution*, pp. 1–6, Dalian, China, 2005. IEEE.
- [93] YE, L., CAMPBELL, A. "Case Study os HTS Resistive Superconducting Fault Current Limiter in Electrical Distribution Systems", *Electr. Pow. Syst. Res.*, v. 77, n. 5-6, pp. 534 – 539, April 2007.
- [94] DE SOUSA, W. T. B., POLASEK, A., DIAS, R., et al. "Short-Circuit Tests and Simulations with a SCFCL Modular Assembly", *Physics Procedia*, v. 36, pp. 1242 – 1247, September 2012.
- [95] YE, L., JUENGST, K.-P. "Modeling and Simulation of High Temperature Resistive Superconducting Fault Current Limiters", *IEEE Trans. Appl. Supercond.*, v. 14, n. 2, pp. 839–842, June 2004.
- [96] HEYDARI, H., HOOSHYAR, H., SAVAGHEBI, M., et al. "Proper Dimension of HTS Material for a Resistive Type SFCL in an 11kV Distribution System". In: *IEEE PES PowerAfrica 2007 Conference and Exposition*, pp. 1–4, Johannesburg, South Africa, July 2007. IEEE.
- [97] SHARIFI, R., HEYDARI, H. "Multiobjective Optimization for HTS Fault-Current Limiters Based on Normalized Simulated Annealing", *IEEE Trans. Appl. Supercond.*, v. 19, n. 4, pp. 3675 – 3682, August 2009.

Bibliography

- [98] SHARIFI, R., HEYDARI, H. "Electro-Thermal Modeling and Optimization Algorithm of Resistive Superconducting Fault Current Limiters". In: *Energy Conference and Exhibition (EnergyCon)*, pp. 814 – 819, Manama, December 2010. IEEE International.
- [99] YEW, P. J., SELAMAT, N. S., WAI, S. K., et al. "Modeling of Resistive Type Superconducting Fault Current Limiter in Power System", *J. Solid St. Sci. and Technol. Letters*, v. 12, n. 1, pp. 171–179, 2005.
- [100] BLAIR, S. M., BOOTH, C. D., BURT, G. M. "Current-Time Characteristics of Resistive Superconducting Fault Current Limiters", *IEEE Trans. Appl. Supercond.*, v. 22, n. 2, pp. 5600205, April 2012.
- [101] NEMDILI, S., BELKHIAT, S. "Modeling and Simulation of Resistive Superconducting Fault-Current Limiters", *J. Supercond. Nov. Magn.*, v. 25, n. 7, pp. 2351 – 2356, October 2012.
- [102] NEMDILI, S., BELKHIAT, S. "Electrothermal Modeling of Coated Conductor for a Resistive Superconducting Fault-Current Limiter", *J. Supercond. Nov. Magn.*, v. 26, pp. 2713 – 2720, August 2013.
- [103] HAUSER, F. *Entwicklung eines elektrischen Netzwerkmodells zur Nachbildung des thermodynamischen Verhaltens heliumgekulter supraleitender Vielkernleiter*. Diplomarbeit, Institut für Elektroenergiesysteme und Hochspannungstechnik, Universität Karlsruhe, Karlsruhe, 2000.
- [104] CAVE, J., ANDR. NADI, D. W., BRISSETTE, Y. "Development of Inductive Fault Current Limiters up to 100 kVA Class Using Bulk HTS Materials", *IEEE Trans. Appl. Supercond.*, v. 9, n. 2, pp. 1335–1338, June 1999.
- [105] PECHER, R., MCCULLOCH, M., CHAPMAN, S., et al. "3D Modelling of Bulk type-II Superconductors Using Unconstrained H-Formulation". In: *EUCAS 2003: 6th European Conf. on Applied Superconductivity*, 2003.
- [106] DURON, J., ANTOGNAZZA, L., DECROUX, M., et al. "3D Finite Element Simulations of Strip Lines in a YBCO/Au Fault Current Limiter", *IEEE Trans. Appl. Supercond.*, v. 15, n. 2, pp. 1998–2002, June 2005.
- [107] KIM, C. H., LEE, K. M., RYU, K. W. "A Numerical Study on Temperature Increase in the Resistive SFCL Element due to the Quench Condition", *IEEE Trans. Appl. Supercond.*, v. 16, n. 2, pp. 636–641, June 2006.
- [108] BADEL, A., ANTOGNAZZA, L., DECROUX, M., et al. "Hybrid Model of Quench Propagation in Coated Conductors Applied to Fault Current

Bibliography

- Limiter Design”, *IEEE Trans. Appl. Supercond.*, v. 23, n. 3, pp. 5603705, June 2013.
- [109] BADEL, A., ANTOGNAZZA, L., THERASSE, M., et al. “Hybrid Model of Quench Propagation in Coated Conductors for Fault Current Limiters”, *Supercond. Sci. Technol.*, v. 9, n. 9, pp. 095015, July 2012.
- [110] ROY, F. *Modeling and Characterization of Coated Conductors Applied to the Design of Superconducting Fault Current Limiters*. PhD thesis, École Polytechnique Fédérale de Lausanne, Lausanne, June 2010.
- [111] SUGITA, S., OHSAKI, H. “FEM Analysis of Resistive Superconducting Fault Current Limiter Using Superconducting Thin Films by Current Vector Potential Method”, *Phys. C Supercond.*, v. 378-381, pp. 196–1201, October 2002.
- [112] KOZAK, S., JANOWSKI, T., KONDRATOWICZ-KUCEWICZ, B., et al. “Experimental and Numerical Analysis of Energy Losses in Resistive SFCL”, *IEEE Trans. Appl. Supercond.*, v. 15, n. 2, pp. 2098 – 2101, June 2005.
- [113] ICHIKI, Y., OHSAKI, H. “Numerical Analysis and Design of Fault Current Limiting Elements Using Large-size YBCO Thin Films”, *Phys. C Supercond.*, v. 463-465, n. 1, pp. 1168–1171, October 2007.
- [114] ROY, F., PÉREZ, S., THERASSE, M., et al. “Quench Propagation in Coated Conductors for Fault Current Limiters”, *Phys. C Supercond.*, v. 469, n. 15 - 20, pp. 1462 – 1466, October 2009.
- [115] HONG, Z., JIN, Z., AINSLIE, M., et al. “Numerical Analysis of the Current and Voltage Sharing Issues for Resistive Fault Current Limiter Using YBCO Coated Conductors”, *IEEE Trans. Appl. Supercond.*, v. 21, n. 3, pp. 1198–1201, December 2011.
- [116] H. S. RUIZ, Z. Z., COOMBS, T. A. “Resistive Type Superconducting Fault Current Limiters: Concepts, Materials and Numerical Modelling”, *IEEE Trans. Appl. Supercond.*, p. 1952410, January 2015.
- [117] GRILLI, F., MARTINI, L., STAVREV, S., et al. “Analysis of Magnetic Field and Geometry Effects for the Design of HTS Devices for AC Power Applications”, *IEEE Trans. Appl. Supercond.*, v. 15, n. 2, pp. 2074 – 2077, June 2005.

Bibliography

- [118] GRILLI, F. *Numerical Modelling of High Temperature Superconducting Tapes and Cable*. PhD thesis, École Polytechnique Fédérale de Lausanne, Lausanne, 2004.
- [119] STAVREV, S. *Modelling of High Temperature Superconductors for AC Power Applications*. PhD thesis, École Polytechnique Fédérale de Lausanne, Lausanne, 2002.
- [120] FABBRICATORE, P., FARINON, S., GÖMÖRY, F., et al. "Ac Losses in Multifilamentary High-TC Tapes due to a Perpendicular AC Magnetic Field", *Supercond. Sci. Technol.*, v. 13, pp. 1327 – 1337, June 2000.
- [121] GÖMÖRY, F., INANIR, F. "AC Losses in Coil Wound from Round Wire Coated by a Superconducting Layer", *IEEE Trans. Appl. Supercond.*, v. 22, n. 3, pp. 4704704, June 2012.
- [122] SUGITA, S., OHSAKI, H. "Numerical Analysis of AC Losses in REBCO Thin Film for Coated Conductor and Fault Current Limiter", *Phys. C Supercond.*, v. 392-396, n. 2, pp. 1150–1155, October 2003.
- [123] KOZAK, S., JANOWSKI, T., WOJTASIEWICZ, G., et al. "The 15 kV Class Inductive SFCL", *IEEE Trans. Appl. Supercond.*, v. 20, n. 3, pp. 1203 – 1206, June 2010.
- [124] ROY, F., DUTOIT, B., GRILLI, F., et al. "Magneto-Thermal Modeling of Second-Generation HTS for Resistive Fault Current Limiter Design Purposes", *IEEE Trans. Appl. Supercond.*, v. 18, n. 1, pp. 29 – 35, March 2008.
- [125] MARTINI, L., ARCOS, I., BOCCHI, M., et al. "Resistive Fault Current Limiter Prototypes: Mechanical and Electrical Analyses", *J. Phys.: Conf. Ser.*, v. 43, pp. 925–928, 2006.
- [126] ZHU, G., SONG, M., WANG, Z., et al. "Design of LTS Coil Used for the Combined Device of SMES-SFCL", *IEEE Trans. Appl. Supercond.*, v. 16, n. 2, pp. 674 – 677, June 2006.
- [127] MAKKI, B., SADATI, N., SOHANI, M. "Simulation of Superconductive Fault Current Limiter (SFCL) Using Modular Neural Networks". In: *IECON 2006 - 32nd Annual Conference of IEEE Industrial Electronics*, pp. 4415 – 4419, Paris, November 2006. IEEE Industrial Electronics.
- [128] DE SOUSA, W. T. B., POLASEK, A., DIAS, R., et al. "Thermal-Electrical Analogy for Simulations of Superconducting Fault Current Limiters", *Cryogenics*, v. 62, pp. 97 – 109, July 2014.

Bibliography

- [129] BRAEGGER, R. A. B. "Modeling of the Electrical- and Thermal Behaviour of a 10 kV Resistive Type Superconducting Fault Current Limiter and its Implementation in Electric Powers Systems". 2002. Diploma Thesis, Karlsruher Institut für Technologie - Institut für Elektroenergiesysteme und Hochspannungstechnik.
- [130] BRANCO, P. C., ALMEIDA, M., DENTE, J. "Proposal for an RMS Thermoelectric Model for a Resistive-Type Superconducting Fault Current Limiter (SFCL)", *Electr. Pow. Syst. Res.*, v. 80, n. 10, pp. 1229 – 1239, October 2010.
- [131] MASANA, F. "A New Approach to the Dynamic Thermal Modelling of Semiconductor Packages", *Microelectron. Reliab.*, v. 41, n. 6, pp. 901–912, October 2001.
- [132] DAJAKU, G., GERLING, D. "An Improved Lumped Parameter Thermal Model for Electrical Machines". In: *17th International Conference on Electrical Machines (ICEM2006)*, September 2006.
- [133] FRAISSE, G., VIARDOT, C., LAFABRIE, O., et al. "Development of a Simplified and Accurate Building Model Based on Electrical Analogy", *Energ. Buildings*, v. 34, n. 10, pp. 1017–1031, November 2002.
- [134] BAGNOLI, P. E., CASAROSA, C., CIAMPI, M., et al. "Thermal Resistance Analysis by Induced Transient (TRAIT) Method for Power Electronic Devices Thermal Characterization. I. Fundamentals and Theory", *IEEE Trans. Power Electron.*, v. 13, n. 6, pp. 1208–1219, November 1998.
- [135] LAWSON, D. I., MCGUIRE, J. H. "The Solution of Transient Heat-Flow Problems by Analogous Electrical Networks", *P. I. Mech. Eng.*, v. 167, n. 1, pp. 275 – 290, June 1956.
- [136] ROBERTSON, A. F., GROSS, D. "An Electrical-Analog Method for Transient Heat-Flow Analysis", *J. Res. Natl. Bur. Stand.*, v. 61, n. 2, pp. 105 – 115, August 1958.
- [137] REIF, F. *Fundamentals of Statistical and Thermal Physics*. New York, Waveland Press Inc., 2008.
- [138] JUHA PYRHÖNEN, T. J., HRABOVCOVÁ, V. *Design of Rotating Electrical Machines*. 1st ed. New Delhi, India, John Wiley & Sons, Ltd., 2008.

Bibliography

- [139] FISCHER, S. *Transiente Wärmeentwicklung und Wärmeabfuhr an supraleitenden Strombegrenzern in Flüssigstickstoff*. PhD thesis, Universität Carolus-Wilhelmina zu Braunschweig, June 1999.
- [140] FASTOWSKI, W., PETROWSKI, J., ROWINSKI, A. *Kryotechnik*, v. 1. Berlin, Akademie-Verlag, 1970.
- [141] DE SOUSA, W. T. B., POLASEK, A., ASSIS, T. M. L., et al. "Simulations of Resistive and Air Coil SFCLs in a Power Grid", *IEEE Trans. Appl. Supercond.*, v. 25, n. 3, pp. 1 – 5, January 2015.
- [142] CRANK, J. *The Mathematics of Diffusion*, v. 1. 2 ed. Oxford, Clarendon Press, March 1975.
- [143] OZISIK, M. N. *Heat Conduction*. 2^o ed. New York, John Wiley & Sons, February 1993.
- [144] CROFT, D. R., LILLEY, D. G. *Heat Transfer Calculations Using Finite Difference Equations*. N. 283, 1. London, Applied Science Publishers, 1977.
- [145] COURANT, R., FRIEDRICHS, K., LEWY, H. "Über die partiellen Differenzgleichungen der mathematischen Physik", *Mathematische Annalen*, v. 100, n. 1, pp. 32 – 74, December 1928.
- [146] JR., J. D. "Alternating direction iteration for mildly nonlinear elliptic difference equations", *Numerische Mathematik*, v. 3, n. 1, pp. 92–98, 1961.
- [147] PEACEMAN, D. W., JR., H. H. R. "The Numerical Solution of Parabolic and Elliptic Differential Equations", *J. Soc. Indust. Appl. Math.*, v. 3, n. 3, pp. 28–41, March 1955.
- [148] WANG, T.-Y., CHEN, C. C.-P. "Thermal ADI - A Linear-Time Chip-Level Dynamic Thermal-Simulation Algorithm Based on ADI Method", *IEEE Trans. Very Large Scale Integr. (VLSI) Syst.*, v. 11, n. 4, pp. 691–700, August 2003.
- [149] DE SOUSA, W. T. B., NOE, M. "The ADI Method for Simulations of SFCL", *IEEE Trans. Appl. Supercond.*, v. 25, n. 2, pp. 5600309, April 2015.
- [150] POLIFKE, W., KOPITZ, J. *Wärmeübertragung - Grundlagen, analytische und numerische Methoden*. 2 ed. München, Pearson, 2009.
- [151] DE SOUSA, W. T. B. *Simulações e Ensaio com Limitadores de Corrente de Curto-Circuito Supercondutores do Tipo Resistivo*. Master's Thesis , COPPE/UFRJ, March 2011.

Bibliography

- [152] NAITO, T., FUJISHIRO, H., YAMAMURA, Y., et al. "Thermal Conductivity of YBCO Coated Conductors Reinforced by Metal Tape", *IEEE Trans. Appl. Supercond.*, v. 21, n. 3, pp. 3037 – 3040, June 2011.
- [153] NAITO, T., FUJISHIRO, H., OKAMOTO, H., et al. "Thermal Conductivity of YBCO Coated Conductors Fabricated by IBAD-PLD Method", *Supercond. Sci. Technol.*, v. 23, pp. 105013, September 2010.
- [154] YANG, S., CHEN, B., HELLSTROM, E. E., et al. "Thermal Conductivity and Contact Conductance of BSCCO-2212 Material", *IEEE Trans. Appl. Supercond.*, v. 5, n. 2, pp. 1471 – 1474, June 1995.

Appendix A

Critical Current Measurements

A.1 MCP-BSCCO-2212 Modules

In this section the results of critical current measurements of the MCP-BSCCO-2212 components are shown.

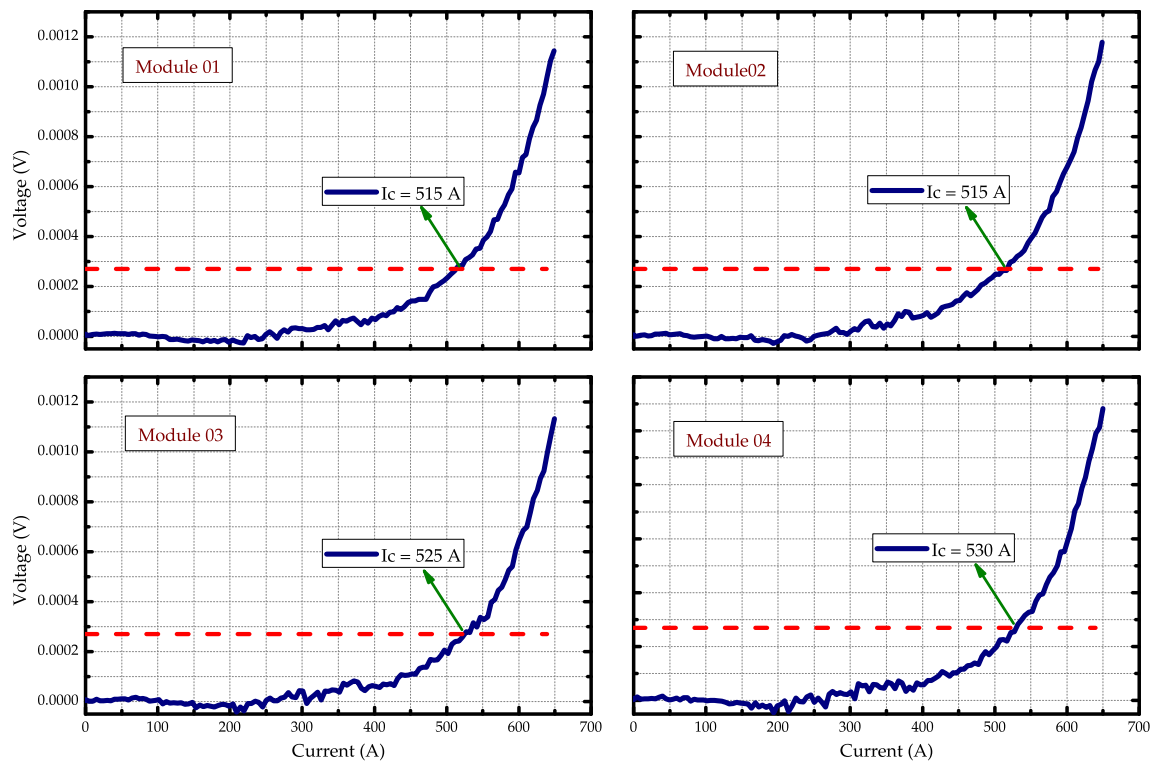


Figure A.1: Critical current measurement of the whole component. The horizontal dashed line indicates the $1 \mu\text{V}/\text{cm}$ criteria. Graphs from modules 01 to module 04.

Appendix A - Critical Current Measurements

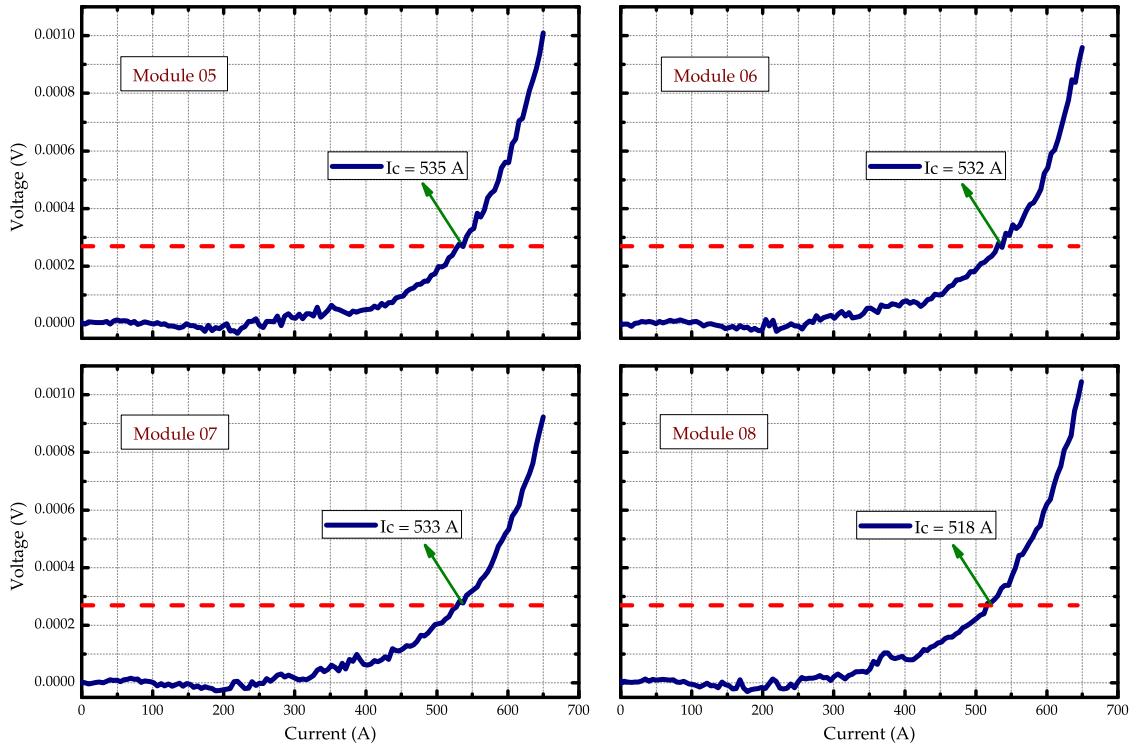


Figure A.2: Critical current measurement of the whole component. The horizontal dashed line indicates the $1 \mu\text{V}/\text{cm}$ criteria. Graphs from module 05 to module 08.

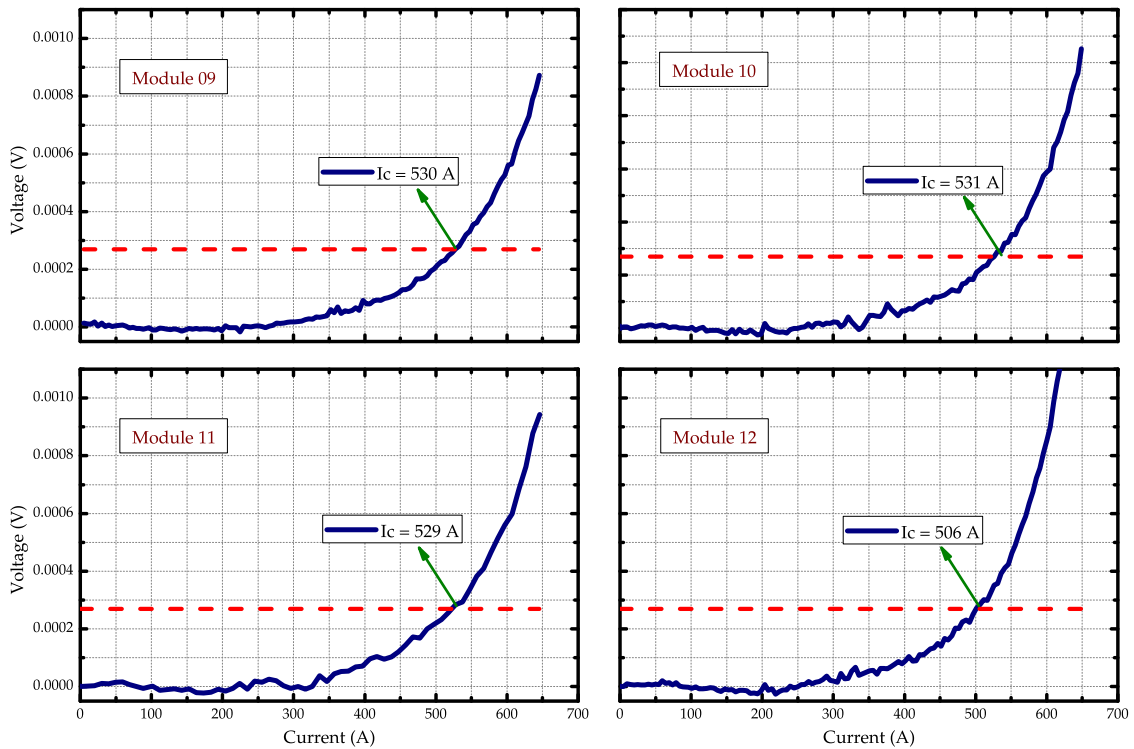


Figure A.3: Critical current measurement of the whole component. The horizontal dashed line indicates the $1 \mu\text{V}/\text{cm}$ criteria. Graphs from module 09 to module 12.

A.2 Air Coil SFCL tapes

In this section the results of critical current measurements of the tapes of the Air Coil SFCL are shown. At the end, table A.1 summarizes all the measured voltages over each region of the tapes. Table A.1 also shows the calculated I_{cm} and σ values for each tape respectively.

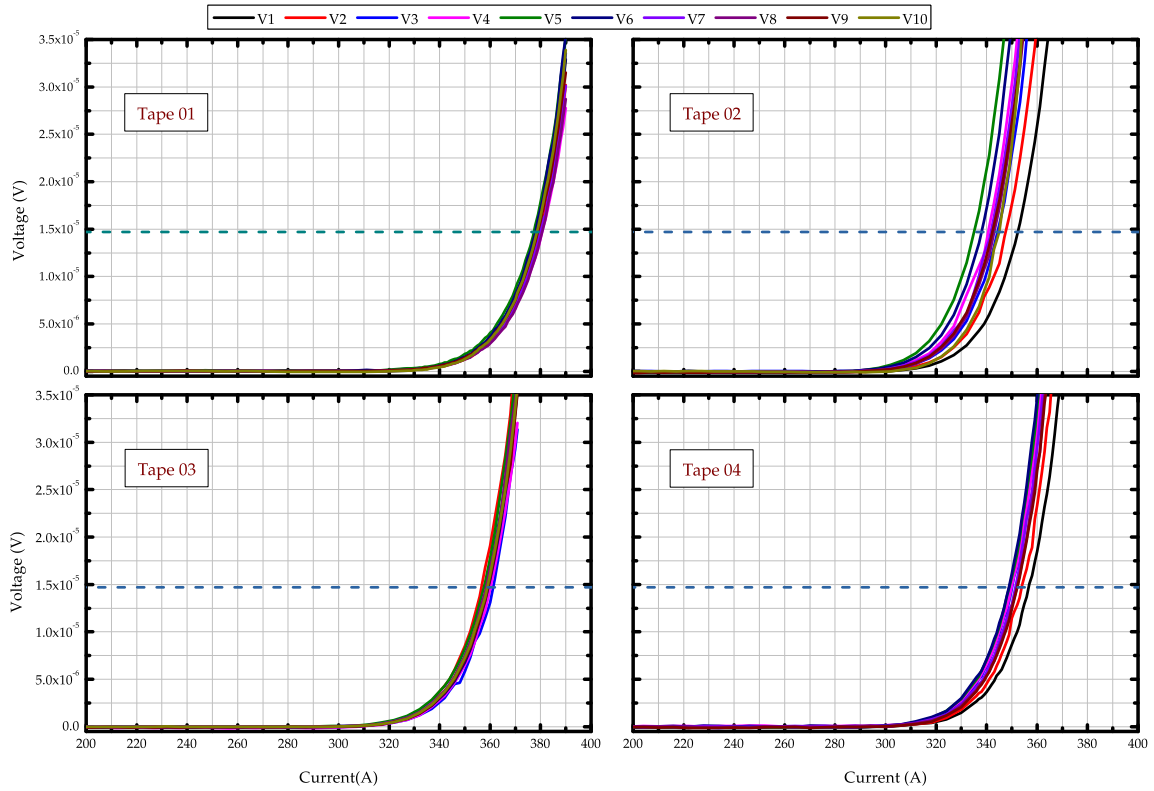


Figure A.4: Critical current measurements along the tapes length. The horizontal dashed line indicates the $1 \mu\text{V}/\text{cm}$ criteria. Graphs from tape 01 to tape 04.

Appendix A - Critical Current Measurements

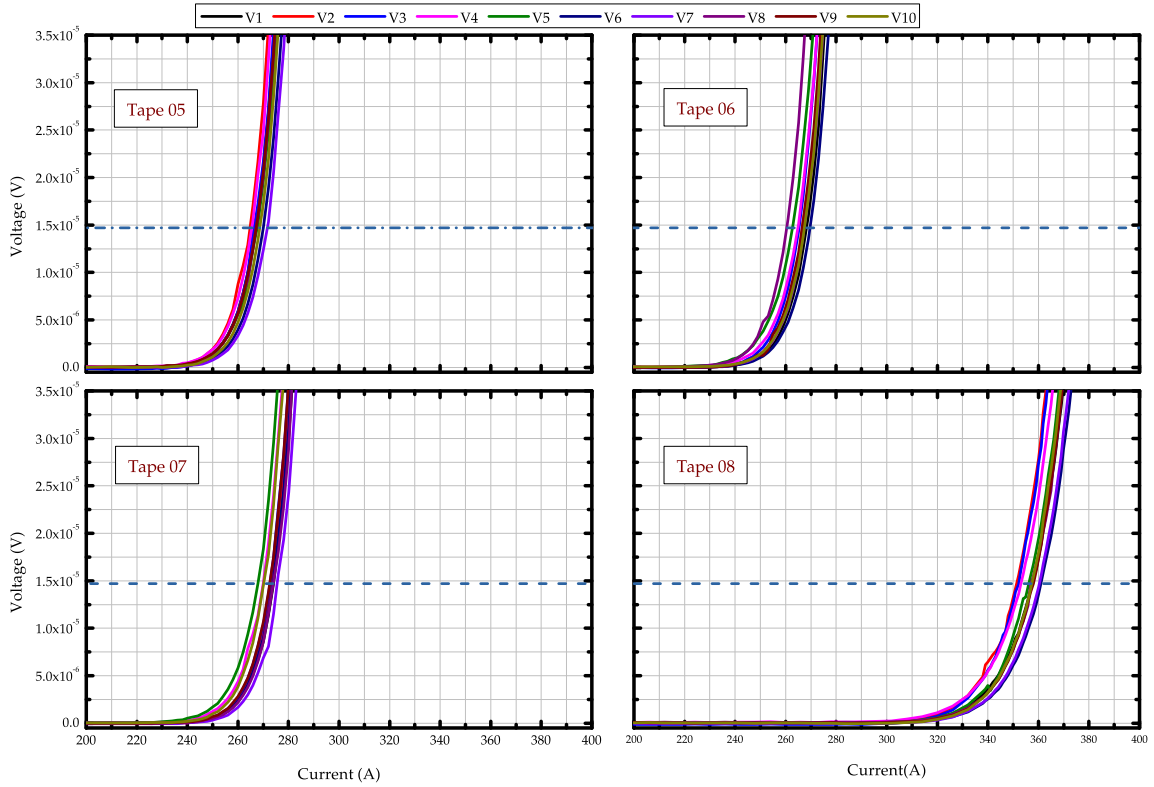


Figure A.5: Critical current measurements along the tapes length. The horizontal dashed line indicates the $1 \mu\text{V}/\text{cm}$ criteria. Graphs from tape 05 to tape 08.

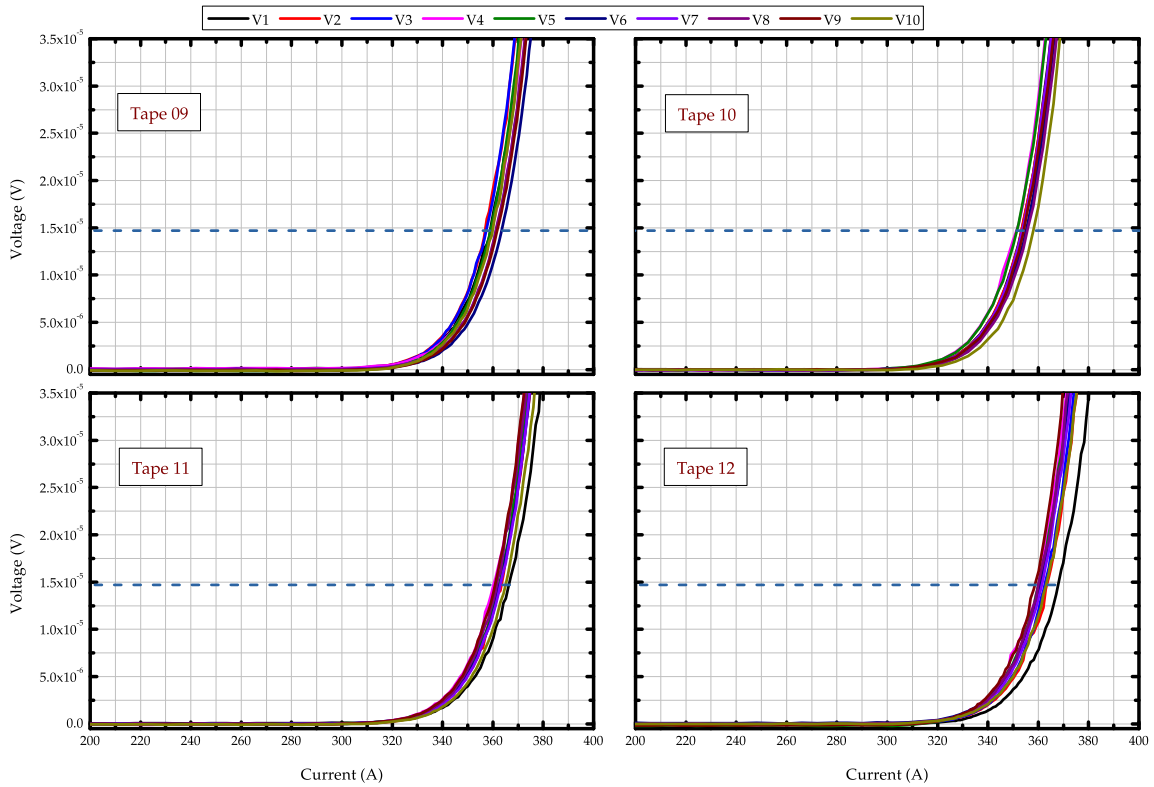


Figure A.6: Critical current measurements along the tapes length. The horizontal dashed line indicates the $1 \mu\text{V}/\text{cm}$ criteria. Graphs from tape 09 to tape 12.

Appendix A - Critical Current Measurements

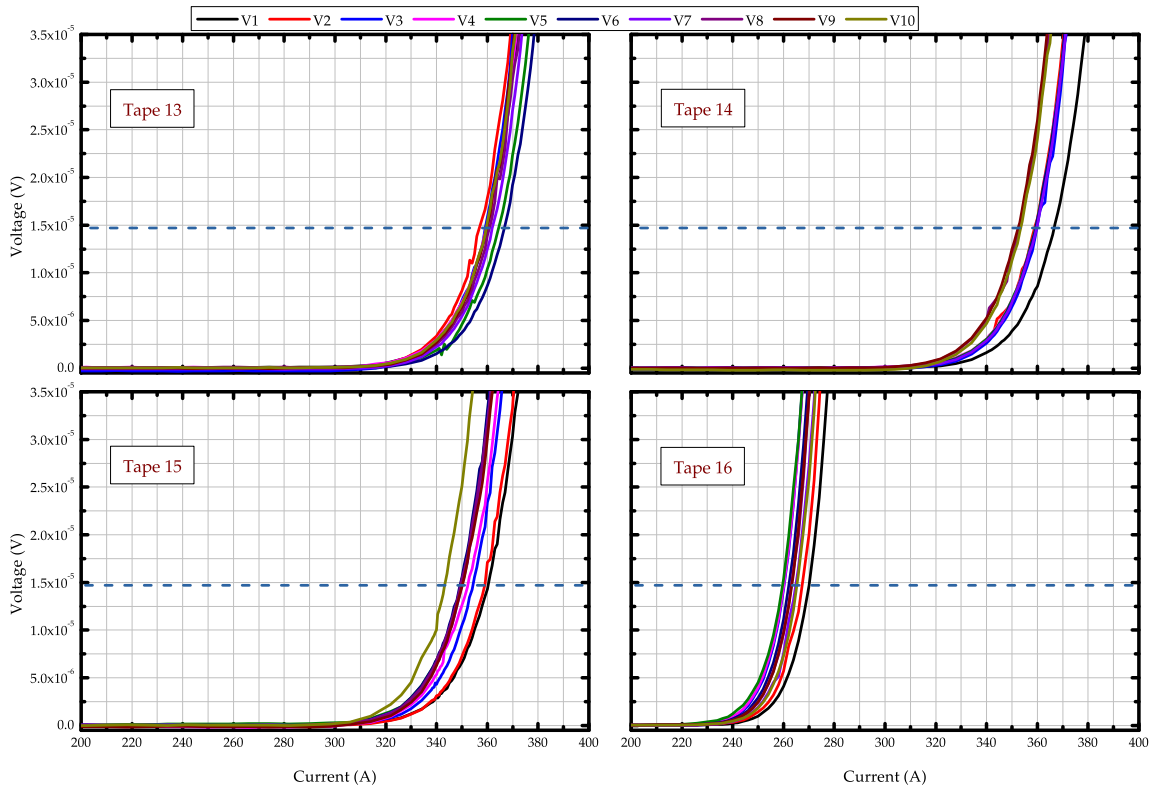


Figure A.7: Critical current measurements along the tapes length. The horizontal dashed line indicates the $1 \mu\text{V}/\text{cm}$ criteria. Graphs from tape 13 to tape 16.

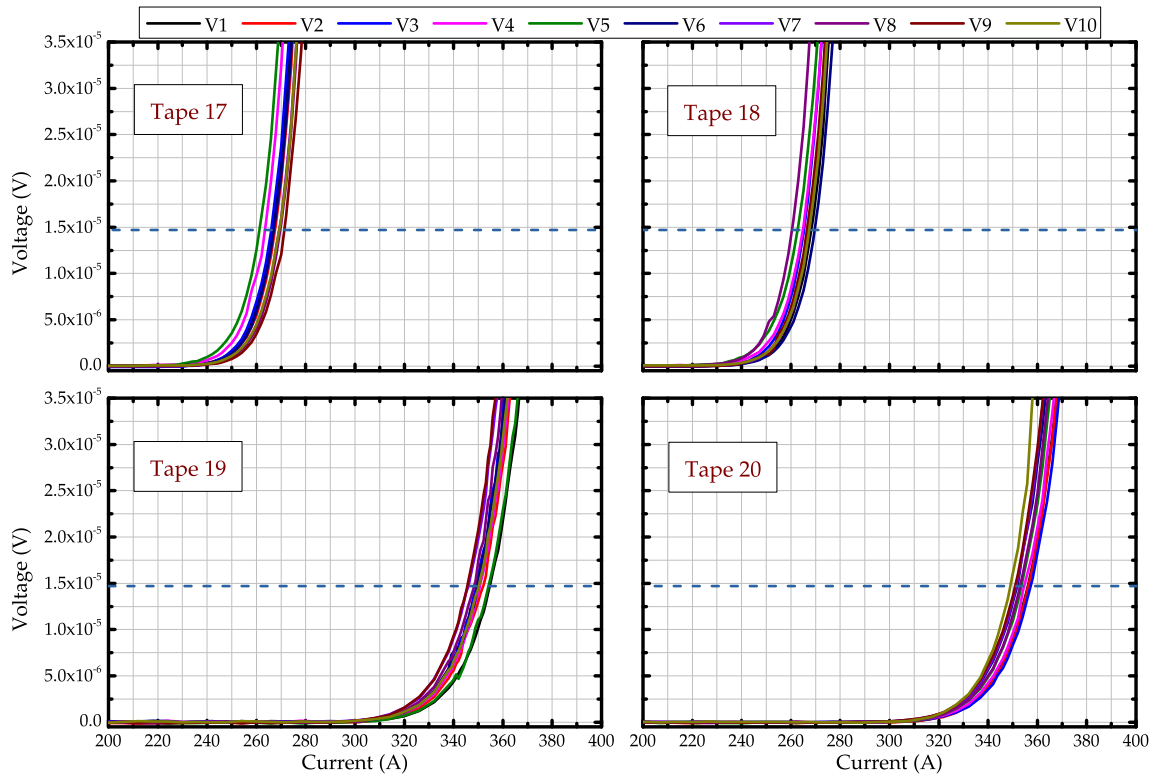


Figure A.8: Critical current measurements along the tapes length. The horizontal dashed line indicates the $1 \mu\text{V}/\text{cm}$ criteria. Graphs from tape 17 to tape 20.

Appendix A - Critical Current Measurements

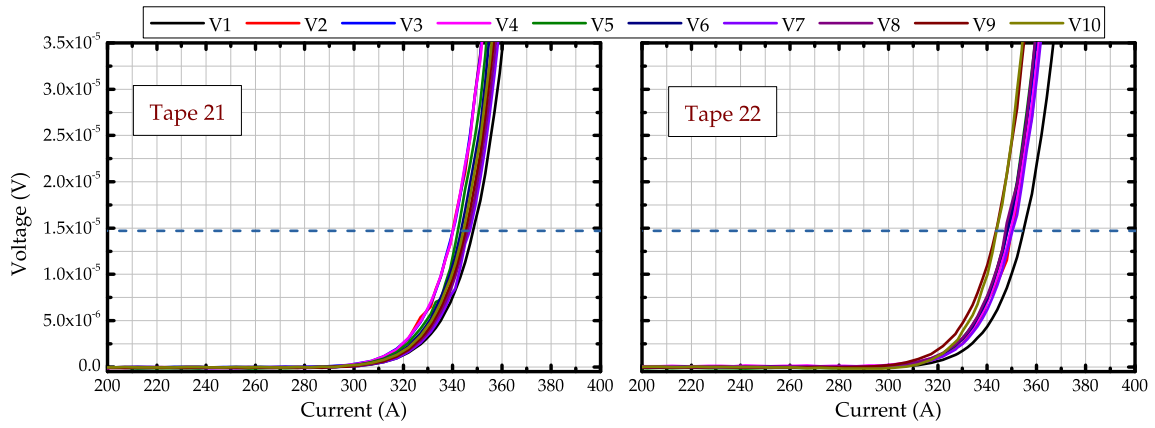


Figure A.9: Critical current measurements along the tapes length. The horizontal dashed line indicates the $1 \mu\text{V}/\text{cm}$ criteria. Tapes 21 and 22.

Table A.1: Measured critical current values for the tapes of the Air Coil SFCL.

Tape	I_{c1}	I_{c2}	I_{c3}	I_{c4}	I_{c5}	I_{c6}	I_{c7}	I_{c8}	I_{c9}	I_{c10}	I_{cm}	σ (A)
01	378.5	379.8	378.4	380.4	377.4	378.0	379.6	380.6	378.8	378.6	379.0	0.9
02	352.4	347.6	344.2	340.6	335.0	338.0	341.7	343.0	342.3	345.0	342.9	4.6
03	358.7	356.5	361.1	360.1	357.4	359.2	358.7	358.4	359.1	358.8	358.8	1.2
04	356.7	353.8	350.1	349.9	349.0	348.8	351.4	352.0	352.1	352.2	351.6	2.2
05	266.9	264.8	266.3	265.4	267.6	270.0	271.5	267.1	267.2	268.6	267.5	1.9
06	268.2	266.6	265.2	264.8	262.7	269.6	267.3	260.4	266.5	267.4	265.8	2.5
07	274.0	273.3	272.6	269.9	267.9	273.8	275.5	273.9	272.5	270.0	272.3	2.2
08	357.5	351.4	352.1	353.0	356.2	360.9	360.3	357.0	357.9	357.4	356.3	3.0
09	358.9	356.8	357.3	359.6	359.0	361.3	361.2	361.2	361.7	359.9	359.7	1.6
10	353.3	353.3	353.9	351.3	351.5	355.1	353.6	355.6	354.2	357.9	354.0	1.8
11	366.3	363.4	362.7	360.2	362.4	362.7	363.0	361.5	360.8	365.0	362.8	1.7
12	367.9	363.4	362.6	360.1	360.0	360.7	361.4	359.9	358.6	363.1	361.7	2.5
13	359.7	356.8	359.1	359.6	364.4	366.6	361.9	360.8	359.7	359.5	360.8	2.7
14	366.5	358.8	359.7	359.2	359.2	359.3	359.6	352.9	352.4	353.4	358.1	4.0
15	360.3	358.9	354.3	352.2	349.5	349.2	349.9	349.5	350.2	343.2	351.7	4.7
16	270.0	267.3	260.2	260.0	259.6	262.1	264.8	263.1	263.3	265.2	263.5	3.2
17	266.6	267.5	265.9	263.5	261.2	267.0	269.2	269.5	271.2	269.2	267.1	2.8
18	268.2	266.6	265.2	264.8	262.7	269.6	267.3	260.4	266.5	267.4	265.8	2.6
19	354.6	351.9	349.2	350.7	354.1	349.6	345.9	348.3	345.5	350.2	350.0	2.8
20	356.1	356.3	357.2	354.6	353.4	351.7	351.3	352.9	350.9	349.0	353.3	2.5
21	348.2	340.0	340.0	340.1	342.1	343.5	346.9	345.9	345.2	344.3	343.6	2.8
22	354.7	349.9	348.1	349.5	347.9	348.2	350.3	347.4	343.7	343.8	348.3	3.0

Appendix B

Physical Properties

B.1 Electrical Resistivity ρ

This section shows the temperature dependence of the resistivity ρ (Ωm) of each material studied in the present work. All values are plotted in figure B.1. These data have been extracted from [29, 48, 107, 151].

Copper:

$$\rho_{cu} = -3.06 \times 10^{-9} + 6.841 \times 10^{-11}T \quad (\text{B.1})$$

Silver:

$$\rho_{ag} = -2.082 \times 10^{-9} + 6.17 \times 10^{-11}T \quad (\text{B.2})$$

YBCO (above T_c):

$$\rho_{yb} = -10 \times 10^{-4} + 1 \times 10^{-4}T \quad (\text{B.3})$$

Hastelloy:

$$\rho_{hy} = 1.103 \times 10^{-6} + 8.958 \times 10^{-11}T \quad (\text{B.4})$$

CuNi Alloy:

$$\rho_{alloy} = 0.000001255T + 0.0067967 \quad (\text{B.5})$$

Solder:

$$\rho_{solder} = 5 \times 10^{-3} \quad (\text{B.6})$$

BSCCO-2212 (above T_c):

$$\rho_{bscco} = \{0.087(1 + 0.0092(T - T_c))\} \quad (\text{B.7})$$

FRP:

$$\rho_{frp} = (0.1255T + 0.7) \times 10^2 \quad (\text{B.8})$$

Stainless Steel:

$$\rho_{ss} = 1.193 \times 10^{-6} - 7.529 \times 10^{-7} e^{-T/647.113} \quad (\text{B.9})$$

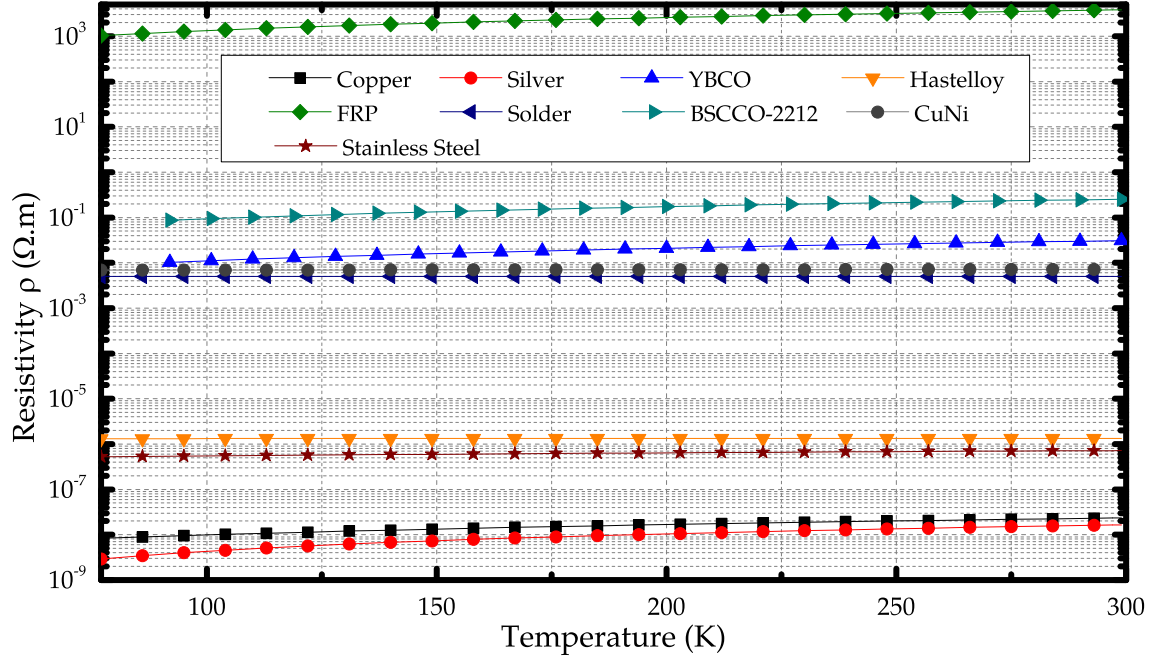


Figure B.1: Electrical resistivity ρ of the materials composing the studied SFCL devices.

B.2 Specific Heat ς

The following equations were used to calculate the specific heat ς (J/kg.K) of the materials. All values are plotted in figure B.2. These data have been extracted from [29, 48, 129, 152].

Copper:

$$\varsigma_{cu} = 390.9 - 593.4e^{-0.014T} \quad (\text{B.10})$$

Silver:

$$\varsigma_{ag} = 220.5 + 0.046T \quad (\text{B.11})$$

YBCO:

$$\varsigma_{yb} = 0.39 \left(\frac{250}{T} \right)^2 \frac{e^{(250/T)}}{[e^{(250/T)} - 1]^2} \times 10^3 \quad (\text{B.12})$$

Hastelloy:

$$\varsigma_{hy} = 1 \times 10^3 \left\{ 0.19 + 2 \left[0.194 \left(1 - e^{-\frac{T}{310}} \right) \right] \right\} \quad (\text{B.13})$$

CuNi Alloy:

$$\varsigma_{alloy} = 396.4 - 546.6e^{-0.013T} \quad (\text{B.14})$$

Solder:

$$\zeta_{solder} = 0.109 \times 10^3 \quad (B.15)$$

BSCCO-2212:

$$\zeta_{bscco} = 0.421 \left(\frac{300}{T} \right)^2 \frac{e^{(300/T)}}{[e^{(300/T)} - 1]^2} \times 10^3 \quad (B.16)$$

FRP:

$$\zeta_{frp} = 1 \times 10^3 \quad (B.17)$$

Stainless Steel:

$$\zeta_{ss} = 0.2 \times 10^3 \quad (B.18)$$

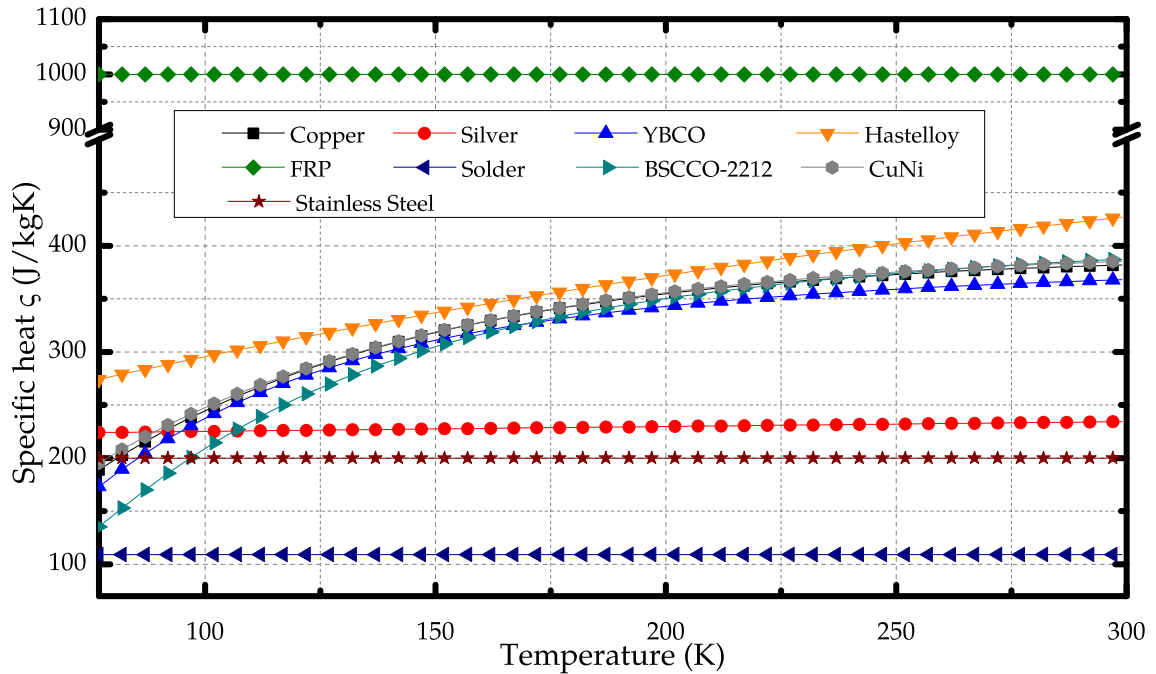


Figure B.2: Specific Heat ζ of the materials composing the studied SFCL devices.

B.3 Thermal Conductivity k

The following equations were used to calculate the thermal conductivity k (W/m.K) of the materials. All values are plotted in figure B.3. These data have been extracted from [29, 152–154].

Copper:

$$k_{cu} = 402.7 + (2076 \times 0.965^T) \quad (B.19)$$

Silver:

$$k_{ag} = 420.9 + (501.8 \times 0.956^T) \quad (B.20)$$

Appendix B - Physical Properties

YBCO:

$$k_{yb} = 5.0 \quad (\text{B.21})$$

Hastelloy:

$$k_{hy} = 3.873 + 0.017T \quad (\text{B.22})$$

CuNi Alloy:

$$k_{alloy} = 18 + 0.076T - 3.3 \times 10^{-4}T^2 + 6.7 \times 10^{-7}T^3 \quad (\text{B.23})$$

Solder:

$$k_{solder} = 0.005 \times 10^2 \quad (\text{B.24})$$

BSCCO-2212:

$$k_{bscco} = 2.3 - 0.011T + 7 \times 10^{-5}T^2 - 6.6 \times 10^{-8}T^3 \quad (\text{B.25})$$

FRP:

$$k_{frp} = 0.67(1 + 0.0033T) \quad (\text{B.26})$$

Stainless Steel:

$$k_{ss} = 15 \quad (\text{B.27})$$

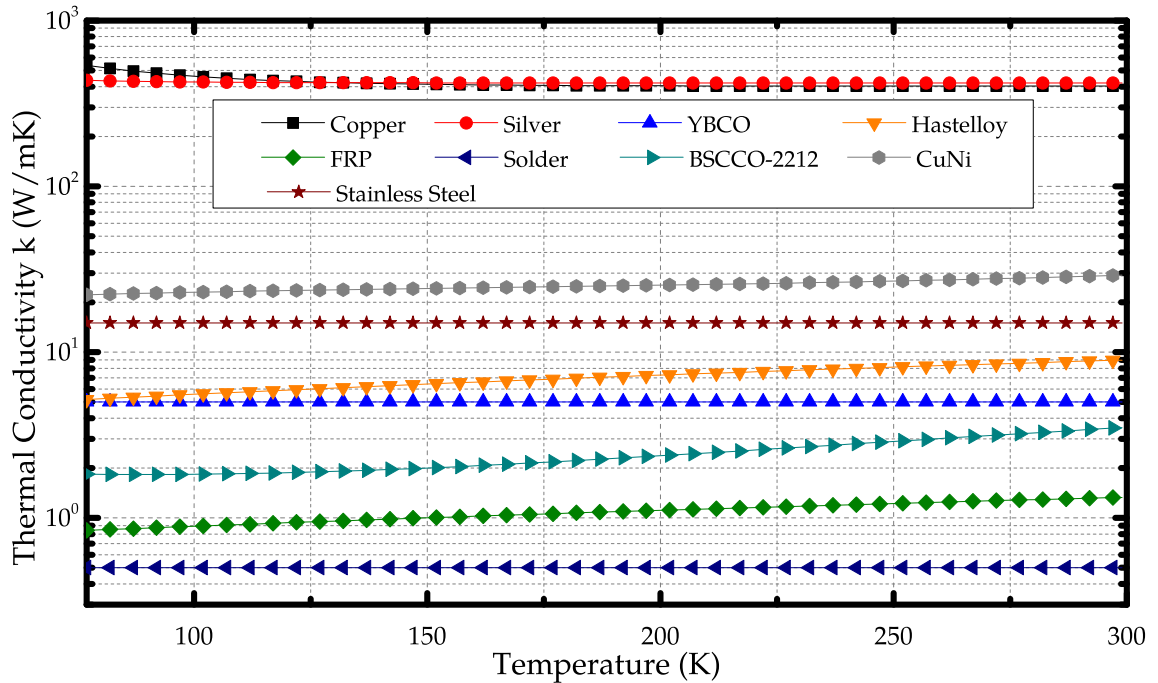


Figure B.3: Thermal Conductivity k of the materials composing the studied SFCL devices.

B.4 Convective heat transfer h_c

The following equation describes the mathematical model for the temperature dependence of the convective heat transfer shown in figure 5.11.

$$h_c(\Delta T) = \begin{cases} 0.18, & \text{if } \Delta T < 2 \\ [a_0 + a_1\Delta T + a_2\Delta T^2 + a_3\Delta T^3 + a_4\Delta T^4 + a_5\Delta T^5] / \Delta T, & \text{if } 2 > \Delta T > 26.5 \\ 0.03, & \text{if } \Delta T > 26.5 \end{cases} \quad (\text{B.28})$$

where:

$$a_0 = 3.8147 \quad (\text{B.29})$$

$$a_1 = -2.8209 \quad (\text{B.30})$$

$$a_2 = 0.72328 \quad (\text{B.31})$$

$$a_3 = -0.049438 \quad (\text{B.32})$$

$$a_4 = 1.325 \times 10^{-3} \quad (\text{B.33})$$

$$a_5 = -12.773 \times 10^{-6} \quad (\text{B.34})$$

Appendix C

Mathematical Procedures - ADI parameters

C.1 Boundary Conditions at the First half-timestep

In the first half-timestep one applies only the boundary conditions related to the heat exchange with the metal parts of the electrical contacts. Thus, consider equation (6.30) for a layer η , repeated here for convenience:

$$\underbrace{-Fo_x T_{j-1,m}^{\tau+\frac{1}{2}} + (1 + 2Fo_x) T_{j,m}^{\tau+\frac{1}{2}} - Fo_x T_{j+1,m}^{\tau+\frac{1}{2}}}_{X_\eta} = \underbrace{Fo_z T_{j,m-1}^\tau + (1 - 2Fo_z) T_{j,m}^\tau + Fo_z T_{j,m+1}^\tau}_{SZ_j} + k_{j,m} \frac{\dot{g}_{j,m}}{\alpha_{j,m}} \frac{\Delta t}{2} \quad (\text{C.1})$$

As stated in section 6.4.2, the value of Θ is obtained only when $j = 1$ and $j = n_x$, since its is related to the boundary conditions $x = 0$ and $x = \ell$. For both studied resistive SFCL, one has $T = T_{LN_2}$ at the borders. Thus, one can use the fictitious node concept, as described in section 6.4.2 to create the nodes $T_{0,m}$ and $T_{n_x+1,m}$ at $x = 0$ and $x = \ell$, respectively. When $j = 1$ ¹, equation (C.1) becomes

$$\underbrace{-Fo_x T_{0,m}^{\tau+\frac{1}{2}} + (1 + 2Fo_x) T_{1,m}^{\tau+\frac{1}{2}} - Fo_x T_{2,m}^{\tau+\frac{1}{2}}}_{X_1} = \underbrace{Fo_z T_{1,m-1}^\tau + (1 - 2Fo_z) T_{1,m}^\tau + Fo_z T_{1,m+1}^\tau}_{SZ_1} + k_{1,m} \frac{\dot{g}_{1,m}}{\alpha_{1,m}} \frac{\Delta t}{2} \quad (\text{C.2})$$

Replacing $T_{0,m}$ by T_{LN_2} , yields

$$-Fo_x T_{LN_2} + (1 + 2Fo_x) T_{1,m}^{\tau+\frac{1}{2}} - Fo_x T_{2,m}^{\tau+\frac{1}{2}} = \Upsilon_{1,m}^\tau \quad (\text{C.3})$$

¹ $j = 1$ indicates the first row of the discretized geometry, hence the properties of the top layer ($\eta = 1$) must be taken into account.

where

$$\Upsilon_{1,m}^\tau = Fo_z T_{1,m-1}^\tau + (1 - 2Fo_z) T_{1,m}^\tau + Fo_z T_{1,m+1}^\tau + k_{1,m} \frac{\dot{g}_{1,m}}{\alpha_{1,m}} \frac{\Delta t}{2}$$

Rewriting equation (C.3) to separate the unknown quantities one becomes

$$(1 + 2Fo_x) T_{1,m}^{\tau+\frac{1}{2}} - Fo_x T_{2,m}^{\tau+\frac{1}{2}} - \Theta = \Upsilon_{1,m}^\tau \quad (\text{C.4})$$

Being $\Theta = Fo_x T_{LN2}$ for all values of m , i.e, for all layers η . Proceeding in the same way to satisfy the boundary conditions at $x = \ell$, or when $j = n_x$ ², yields

$$- Fo_x T_{n_x-1,m}^{\tau+\frac{1}{2}} + (1 + 2Fo_x) T_{n_x,m}^{\tau+\frac{1}{2}} - Fo_x T_{n_x+1,m}^{\tau+\frac{1}{2}} = \Upsilon_{n_x,m}^\tau \quad (\text{C.5})$$

Replacing $T_{n_x+1,m}$ by T_{LN2} , yields

$$- Fo_x T_{n_x-1,m}^{\tau+\frac{1}{2}} + (1 + 2Fo_x) T_{n_x,m}^{\tau+\frac{1}{2}} - \Theta = \Upsilon_{n_x,m}^\tau \quad (\text{C.6})$$

Equations (C.4) and (C.6) define the rule to form the first and last rows, respectively, of matrix X_η in equation (6.33), for the resistive devices. As can be seen the parameter Θ is independent of temperature of any element of the discretized geometry. For this reason, in the case of resistive SFCL, a independent matrix with the values of Θ is necessary in equation (6.33).

In the case of the AC-SFCL, the boundary conditions at $x = 0$ and $x = \ell$ are quite different since the tapes are short-circuited. Because of that, the fictitious nodes at the borders can be defined as the temperature of the opposite border. Considering equation (C.1) for the AC-SFCL in the case of $j = 1$ results

$$- Fo_x T_{n_x,m}^{\tau+\frac{1}{2}} + (1 + 2Fo_x) T_{1,m}^{\tau+\frac{1}{2}} - Fo_x T_{2,m}^{\tau+\frac{1}{2}} = \Upsilon_{1,m}^\tau \quad (\text{C.7})$$

Defining $\Gamma = Fo_x$ and rewriting equation (C.7)

$$(1 + 2Fo_x) T_{1,m}^{\tau+\frac{1}{2}} - Fo_x T_{2,m}^{\tau+\frac{1}{2}} - \Gamma T_{n_x,m}^{\tau+\frac{1}{2}} = \Upsilon_{1,m}^\tau \quad (\text{C.8})$$

One can promptly recognize that at the first row of matrix (6.33) for the AC-SFCL a temperature dependent term in the last element of the discretized geometry is necessary. Proceeding in the same way for $j = n_x$ yields

$$- Fo_x T_{n_x-1,m}^{\tau+\frac{1}{2}} + (1 + 2Fo_x) T_{n_x,m}^{\tau+\frac{1}{2}} - Fo_x T_{1,m}^{\tau+\frac{1}{2}} = \Upsilon_{n_x,m}^\tau \quad (\text{C.9})$$

² $j = n_x$ indicates the last row of the discretized geometry, hence the properties of the bottom layer ($\eta = \eta_\ell$) must be taken into account.

Replacing Γ

$$-\Gamma T_{1,m}^{\tau+\frac{1}{2}} - Fo_x T_{n_x-1,m}^{\tau+\frac{1}{2}} + (1 + 2Fo_x) T_{n_x,m}^{\tau+\frac{1}{2}} = \Upsilon_{n_x,m}^{\tau} \quad (C.10)$$

In this case, one notes a temperature dependent term on the first element of the discretized geometry.

C.2 Boundary Conditions at the Second half-timestep

Convective heat transfer - In the second half-timestep one must deal with the boundary conditions related to the heat exchange with the liquid nitrogen bath and the heat exchange at the interface between two adjoining layers.

The parameters β and γ rises from the discretization of the boundary conditions described in equations (6.23) and (6.24). To discretize these boundary conditions, the fictitious node concept has been used, as already show in equations (6.41) and (6.42). From this procedures one has obtained the values of $T_{j,0}$ and T_{j,n_z+1} (equations (6.43) and (6.44), respectively).

Consider now the case when $m = 1$ ³, for any value of j . In this case, equation (6.35) for the second half-step is:

$$\underbrace{-Fo_z T_{j,0}^{\tau+1} + (1 + 2Fo_z) T_{j,1}^{\tau+1} - Fo_z T_{j,2}^{\tau+1}}_Z = \underbrace{Fo_x T_{j-1,1}^{\tau+\frac{1}{2}} + (1 - 2Fo_x) T_{j,1}^{\tau+\frac{1}{2}} + Fo_x T_{j+1,1}^{\tau+\frac{1}{2}}}_{SX_1} + k_{j,1} \frac{\dot{g}_{j,1}}{\alpha_{j,1}} \frac{\Delta t}{2} \quad (C.11)$$

Now, placing expression (6.43) in $T_{j,0}$ yields

$$-Fo_z \left[2 \frac{h_c \Delta z}{k_{j,1}} (T_{LN_2} - T_{j,1}^{\tau+1}) + T_{j,2}^{\tau+1} \right] + (1 + 2Fo_z) T_{j,1}^{\tau+1} - Fo_z T_{j,2}^{\tau+1} = \Upsilon_{j,1}^{\tau+\frac{1}{2}} \quad (C.12)$$

being,

$$\Upsilon_{j,1}^{\tau+\frac{1}{2}} = Fo_x T_{j-1,1}^{\tau+\frac{1}{2}} + (1 - 2Fo_x) T_{j,1}^{\tau+\frac{1}{2}} + Fo_x T_{j+1,1}^{\tau+\frac{1}{2}} + k_{j,1} \frac{\dot{g}_{j,1}}{\alpha_{j,1}} \frac{\Delta t}{2}$$

Rearranging the terms in equation (C.12) results

$$\left[1 + 2Fo_z + 2Fo_z \frac{h_c \Delta z}{k_{j,1}} \right] T_{j,1}^{\tau+1} - 2Fo_z T_{j,2}^{\tau+1} - 2Fo_z \frac{h_c \Delta z}{k_{j,1}} T_{LN_2} = \Upsilon_{j,1}^{\tau+\frac{1}{2}} \quad (C.13)$$

³ $m = 1$ indicates the first column of the discretized geometry.

Using the definition of β and γ (equation (6.45))

$$[1 + 2Fo_z\beta] T_{j,1}^{\tau+1} - 2Fo_z T_{j,2}^{\tau+1} - 2Fo_z\gamma = \Upsilon_{j,1}^{\tau+\frac{1}{2}} \quad (\text{C.14})$$

Equation (C.14) defines the formation of the first row of all matrices in equation (6.46), mainly the first row of matrices Z and H . In the case of the last row, where there are also heat exchanges with the liquid nitrogen bath, one must repeat the same procedure for $m = n_z$. Thus, considering equation (C.11) again for the case $m = n_z$ ⁴ and any value of j results

$$\underbrace{-Fo_z T_{j,n_z-1}^{\tau+1} + (1 + 2Fo_z) T_{j,n_z}^{\tau+1} - Fo_z T_{j,n_z+1}^{\tau+1}}_Z = \underbrace{Fo_x T_{j-1,n_z}^{\tau+\frac{1}{2}} + (1 - 2Fo_x) T_{j,n_z}^{\tau+\frac{1}{2}} + Fo_x T_{j+1,n_z}^{\tau+\frac{1}{2}}}_{SX_{n_z}} + k_{j,n_z} \frac{\dot{g}_{j,n_z} \Delta t}{\alpha_{j,n_z} 2} \quad (\text{C.15})$$

Now, placing expression (6.44) in T_{j,n_z+1} yields

$$-Fo_z T_{j,n_z-1}^{\tau+1} + (1 + 2Fo_z) T_{j,n_z}^{\tau+1} - Fo_z \left[2 \frac{h_c \Delta z}{k_{j,n_z}} (T_{\text{LN}_2} - T_{j,n_z}^{\tau+1}) + T_{j,n_z-1}^{\tau+1} \right] = \Upsilon_{j,n_z}^{\tau+\frac{1}{2}} \quad (\text{C.16})$$

Rearranging the terms in equation (C.16) results

$$-2Fo_z T_{j,n_z-1}^{\tau+1} + \left[1 + 2Fo_z + 2Fo_z \frac{h_c \Delta z}{k_{j,n_z}} \right] T_{j,n_z}^{\tau+1} - 2Fo_z \frac{h_c \Delta z}{k_{j,n_z}} T_{\text{LN}_2} = \Upsilon_{j,n_z}^{\tau+\frac{1}{2}} \quad (\text{C.17})$$

Applying again the definition of β and γ (equation (6.45))

$$-2Fo_z T_{j,n_z-1}^{\tau+1} + [1 + 2Fo_z\beta] T_{j,n_z}^{\tau+1} - 2Fo_z\gamma = \Upsilon_{j,n_z}^{\tau+\frac{1}{2}} \quad (\text{C.18})$$

Equation (C.18) defines the formation of the last row all of matrices in equation (6.46), mainly the last row of matrices Z and H .

Heat transfer at interfaces - One concerns now about the heat transfer at the interfaces between two adjoining layers. For that, one takes the last row m of a layer η and the first row $m + 1$ of the next layer $\eta + 1$, as already shown in figure

⁴ $m = n_z$ indicates the last column of the discretized geometry.

6.7. Consider equation (C.11) for the last row m of the layer η :

$$\underbrace{-Fo_z T_{j,m-1}^{\tau+1} + (1 + 2Fo_z)T_{j,m}^{\tau+1} - Fo_z T_{j,m+1}^{\tau+1}}_Z = \underbrace{Fo_x T_{j-1,m}^{\tau+\frac{1}{2}} + (1 - 2Fo_x)T_{j,m}^{\tau+\frac{1}{2}} + Fo_x T_{j+1,m}^{\tau+\frac{1}{2}}}_{SX_m} + k_{j,m} \frac{\dot{g}_{j,m}}{\alpha_{j,m}} \frac{\Delta t}{2} \quad (C.19)$$

In order to satisfy the imposed boundary condition at the interface, one must replace the term $T_{j,m+1}$ by the auxiliary temperature T_{ha} , defined in equation (6.38). Hence

$$-Fo_z T_{j,m-1}^{\tau+1} + (1 + 2Fo_z)T_{j,m}^{\tau+1} - Fo_z \left(\left[\frac{2\psi}{1+\psi} \right] T_{j,m+1}^{\tau+1} + \left[\frac{1-\psi}{1+\psi} \right] T_{j,m}^{\tau+1} \right) = \Upsilon_{j,m}^{\tau+\frac{1}{2}} \quad (C.20)$$

where

$$\Upsilon_{j,m}^{\tau+\frac{1}{2}} = Fo_x T_{j-1,m}^{\tau+\frac{1}{2}} + (1 - 2Fo_x)T_{j,m}^{\tau+\frac{1}{2}} + Fo_x T_{j+1,m}^{\tau+\frac{1}{2}} + k_{j,m} \frac{\dot{g}_{j,m}}{\alpha_{j,m}} \frac{\Delta t}{2}$$

Rewriting equation (C.20) results

$$-Fo_z T_{j,m-1}^{\tau+1} + \left(1 + 2Fo_z - \left[\frac{1-\psi}{1+\psi} Fo_z \right] \right) T_{j,m}^{\tau+1} - \frac{2\psi Fo_z}{1+\psi} T_{j,m+1}^{\tau+1} = \Upsilon_{j,m}^{\tau+\frac{1}{2}} \quad (C.21)$$

Equation (C.21) describes the rule to form the last row of the layer η in contact with the layer $\eta + 1$, as has been already shown in the first highlighted row of matrix Z in equation (6.46).

Finally, for the first row of layer $\eta + 1$ one takes equation (C.11) for the case $m + 1$, thus

$$\underbrace{-Fo_z T_{j,m}^{\tau+1} + (1 + 2Fo_z)T_{j,m+1}^{\tau+1} - Fo_z T_{j,m+2}^{\tau+1}}_Z = \underbrace{Fo_x T_{j-1,m+1}^{\tau+\frac{1}{2}} + (1 - 2Fo_x)T_{j,m+1}^{\tau+\frac{1}{2}} + Fo_x T_{j+1,m+1}^{\tau+\frac{1}{2}}}_{SX_{m+1}} + k_{j,m+1} \frac{\dot{g}_{j,m+1}}{\alpha_{j,m+1}} \frac{\Delta t}{2} \quad (C.22)$$

Substituting the term $T_{j,m}$ by the auxiliary temperature T_{hb} , defined in equation (6.39), yields

$$-Fo_z \left(\left[\frac{2}{1+\psi} \right] T_{j,m}^{\tau+1} - \left[\frac{1-\psi}{1+\psi} \right] T_{j,m+1}^{\tau+1} \right) + (1 + 2Fo_z)T_{j,m+1}^{\tau+1} - Fo_z T_{j,m+2}^{\tau+1} = \Upsilon_{j,m+1}^{\tau+\frac{1}{2}} \quad (C.23)$$

Rewriting equation (C.23) results

$$-\frac{2Fo_z}{1+\psi}T_{j,m}^{\tau+1} + \left(1 + 2Fo_z + \left[\frac{1-\psi}{1+\psi}\right]\right)T_{j,m+1}^{\tau+1} - Fo_zT_{j,m+2}^{\tau+1} = \Upsilon_{j,m+1}^{\tau+\frac{1}{2}} \quad (\text{C.24})$$

One can note that equation (C.24) describes the first row of the layer $\eta + 1$, as has been already shown in the second highlighted row of matrix Z in equation (6.46).

Wescley T. B. de Sousa

Curriculum Vitae



PERSONAL DETAILS

Birth November 16, 1983
Place Santo André - São Paulo
Country Brazil
Mail wescley@daad-alumni.de

EDUCATION

D.Sc. **2011-2015**
Universidade Federal do Rio de Janeiro (UFRJ)

Development of simulations using the Thermal Electrical Analogy Method for simulation of Superconducting Fault Current Limiters (in special R-SFCL). Funded by Electric Power Research Center (ELETROBRAS CEPEL)

D.Sc. - Sandwich Period **2013-2014**
Karlsruher Institut für Technologie (KIT)

Development of simulations using Finite Differences method (FDM-ADI) for simulation of Superconducting Fault Current Limiters (in special AC-SFCL). Funded by Deutscher Akademischer Austauschdienst (DAAD) and Conselho Nacional de Desenvolvimento Científico e Tecnológico (CNPq)

M.Sc. of Electrical Engineering **2009-2011**
Universidade Federal do Rio de Janeiro (UFRJ)

First works and papers regarding transient simulations of Resistive Superconducting Fault Current Limiters. Funded by Electric Power Research Center (ELETROBRAS CEPEL)

B.Sc. of Physics **2005-2008**
Universidade Estadual de Ponta Grossa (UEPG)

Scientific Initiation Student - Processing, Characterizing, as well as Critical and Gaussian Conductivity Fluctuations studies in polycrystalline samples of $RE_{1-x}Pr_xBa_2Cu_3O_{7-\delta}$ Superconductor.

SKILLS

<i>Languages</i>	Portuguese (mother tongue) English (Advanced) German (B.2.1 Level)
<i>IT Skills</i>	Large experience with MatLab, EMTP, OriginLab and L ^A T _E X Familiarity with C++ programming, CorelDraw and Inkscape Knowledge of OS Windows, Office, COMSOL and ANSYS

PUBLISHED PAPERS

- Simulations of Resistive and Air Coil SFCLs in a Power Grid.** 2015
IEEE Transactions on Applied Superconductivity, v. 25, p. 1-1
de Sousa, W. T. B., Polasek, A., Assis, T. M. L., de Andrade Jr., R. and Noe, M
- The Alternating Direction Implicit (ADI) Method for Simulations of Superconducting Fault Current Limiters** 2014
IEEE Transactions on Applied Superconductivity, v. 24, p. 5600309
de Sousa, W. T. B. and Noe, M.
- Transient Simulations of an Air-Coil SFCL** 2014
IEEE Transactions on Applied Superconductivity, v. 24, p. 5601807
de Sousa, W. T. B., Näckel, O. and Noe, M.
- Thermal-Electrical Analogy for Simulations of Superconducting Fault Current Limiters** 2014
Cryogenics, v. 62, p. 97-109
de Sousa, W. T. B., Polasek, A., Matt. C. F. T. and de Andrade Jr., R.
- Investigation of 2G coil SCFCL - Modeling and Testing** 2014
Journal of Physics. Conference Series, v. 507, p. 032005
de Sousa, W. T. B., Polasek, A., Matt. C. F. T. and de Andrade Jr., R. and Silva, F. A.

Recovery of Superconducting State in an Resistive SCFCL MCP-BSCCO-2212 Assembly 2013

IEEE Transactions on Applied Superconductivity, v. 23, p. 5601407

de Sousa, W. T. B., Polasek, A., Matt. C. F. T. and de Andrade Jr., R.

Comparison Between the Fault Current Limiting Performance of Bi-2212 Bifilar Components and 2G YBCO Coils 2013

IEEE Transactions on Applied Superconductivity, v. 23, p. 5602204

de Sousa, W. T. B., Polasek, A., Dias, R., de Andrade Jr., R. and Silva, F. A.

Short-Circuit Tests and Simulations with a Superconducting Fault Current Limiter Modular Assembly 2012

Physics Procedia, v. 36, p. 1242-1247

de Sousa, W. T. B., Polasek, A., Dias, R., de Andrade Jr., R., Lopes, F. C., Silva, F. A. and Filho, O. O.

Simulations and Tests of MCP-BSCCO-2212 Superconducting Fault Current Limiters 2012

IEEE Transactions on Applied Superconductivity, v. 22, p. 5600106

de Sousa, W. T. B., Polasek, A., Dias, R., Andrade Jr., R., Jurelo, A.R. and Silva, F. A.

Limitadores de corrente de curto-circuito supercondutores: Principais Conceitos e Testes 2012

Revista Brasileira de Ensino de Física, v. 34, p. 1-8

de Sousa, W. T. B., Polasek, A., Dias, R. and Andrade Jr., R.

Critical and Gaussian Conductivity Fluctuations in Granular $\text{Ho}_{1-x}\text{Pr}_x\text{Ba}_2\text{Cu}_3\text{O}_{7-d}$ Superconductor 2010

Journal of Superconductivity and Novel Magnetism, v. 23, p. 1307-1312

de Sousa, W. T. B., Pinheiro, L. B. L. G., Jurelo, A. R., Menegotto Costa, R., Júnior, P.R., Cruz, G.K. and Dias, F. T.

Analysis of fluctuation conductivity of polycrystalline $\text{Er}_{1-x}\text{Pr}_x\text{Ba}_2\text{Cu}_3\text{O}_{7-\delta}$ Superconductors 2009

Brazilian Journal of Physics, v. 39, p. 667-672

Jurelo, A.R., de Sousa, W. T. B., Menegotto Costa, R., Andrade, A.V.C., Júnior, P.R., Cruz, G.K., Lopes, C.S. and Santos, M.